Geofluids

Multiphysics Coupling Simulation of Fluid Flow in Fractured Rock Mass

Lead Guest Editor: Long Yan
Guest Editors: Feng Xiong, Wenbo Zheng, and Jianping Sun

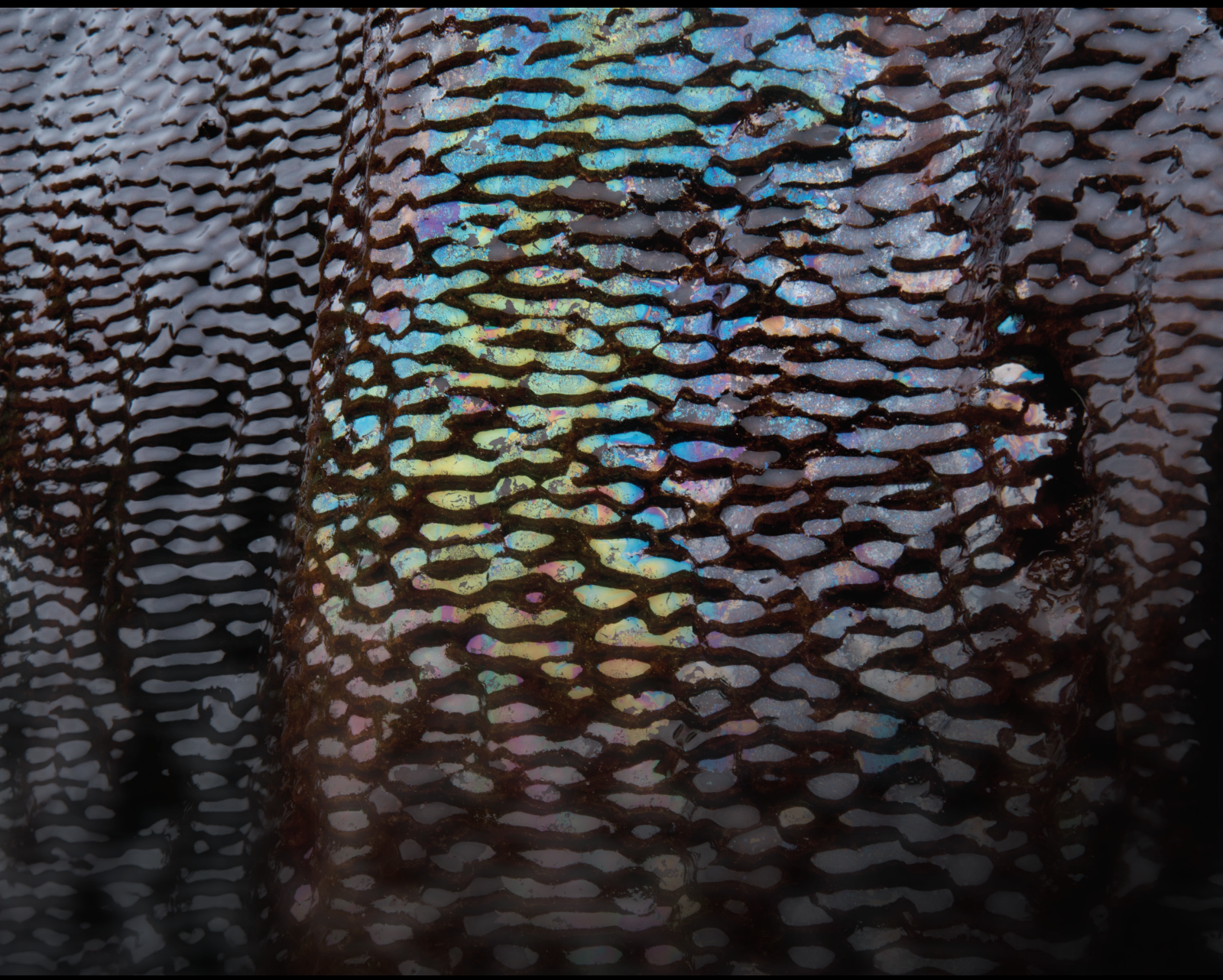

Multiphysics Coupling Simulation of Fluid Flow in Fractured Rock Mass

Geofluids

Multiphysics Coupling Simulation of Fluid Flow in Fractured Rock Mass

Lead Guest Editor: Long Yan
Guest Editors: Feng Xiong, Wenbo Zheng, and Jianping Sun

Chief Editor

Associate Editors

Academic Editors

Contents

Hindawi
Geofluids
Volume 2022, Article ID 1705985, 22 pages
https://doi.org/10.1155/2022/1705985

Review Article

On the Freeze-Thaw Instability of an Open Pit Slope Using Three-Dimensional Laser Scanning and Numerical Simulation

Juzhou Li, Changhong Li, Guoqing Li, Yongyue Hu, Xuefeng Yi, and Yu Wang

Beijing Key Laboratory of Urban Underground Space Engineering, Department of Civil Engineering, School of Civil & Resource Engineering, University of Science & Technology Beijing, Beijing 100083, China

Correspondence should be addressed to Yu Wang; wyzhou@ustb.edu.cn

Received 13 May 2022; Accepted 11 July 2022; Published 31 July 2022

Academic Editor: Long Yan

In order to reveal the instability law of open pit mine slope in high-cold and high-altitude area. Firstly, the slope structural plane is scanned by three-dimensional (3D) laser scanning technology, and the point cloud data is obtained to realize the intelligent identification of rock mass structural plane. The geometric parameters of rock mass are counted, and the physical structure model is established. Then, we carry out freeze-thaw cyclic tests on granite to obtain the corresponding mechanical parameters. Finally, according to the obtained mechanical parameters, we use RS2 finite element software to calculate the shear strength of structural plane and joint by generalized Hoek-Brown criterion and Barton-Bandis criterion, respectively, establish the geomechanical model, and use the finite element strength reduction method to calculate the safety factor of slope and judge the instability of slope. The results show that the physical and mechanical properties of granite deteriorate with the increase of the freeze-thaw cycle. Under the action of the freeze-thaw cycle, the pore water in the rock mass freezes and forms frost heaving force. The expansion of volume leads to the further development of joint fissures. The strength of rock slope decreases gradually with the increase of freeze-thaw cycle times, and the safety factor of slope decreases continuously. It shows that repeated freeze and thaw alternation makes the stability of mine slope worse and worse. The research results are helpful to prevent the occurrence of slope disasters in advance and are of great significance to effectively and safely manage the stability of slope, the treatment of open pit, and environmental treatment.

1. Introduction

With the development of science and technology, 3D laser scanning technology and finite element software are widely used in the analysis of rock slope stability [1–3]. At the same time, in order to satisfy the growing production demand, China's mineral resources development has gradually shifted to the northwest region, which is rich in mineral resources but as poor natural environment, with weak infrastructure, poor ecological environment, and extremely cold winter. The temperature variation and seasonal variation caused by the alternation of day and night will have a great impact on the mechanical properties of rock mass. Repeated freeze-thaw cycle will expand and increase the rock fissures, deteriorate the physical and mechanical properties of the rock, and reduce the strength of the slope rock mass, resulting in the sliding of the slope rock mass [4–6]. These issues have become increasingly prominent. Therefore, this paper puts forward the research on the safety and stability evaluation of open pit slope based on 3D laser scanning and numerical simulation.

3D laser scanning is the latest development of geological mapping [7], which has been proved to be an effective non-contact tool. It is used to collect rock mass information. Its application fields include surface geological data collection [8, 9], slope stability and displacement monitoring [10, 11], and 3D rock mass model creation [12, 13]. It has the advantages of high density, maneuverability, high precision, and noncontact. At present, many experts and scholars have carried out a series of scanning analysis on rock slope engineering with the help of this technology. Chen et al. [14] compared the difference between 3D laser scanning

technology and traditional window mapping technology. The results show that the average dip/dip direction discrepancy between the two methods is 1.5°/16°, which is due to the large amount of data collected by 3D laser scanning technology. It is proved that the 3D laser scanning technology has the advantages of higher efficiency and accuracy in underground mines. Wang et al. [15] used 3D laser scanning technology to scan the fragmentation of blast muck piles and provided high-precision point cloud data for calculating BFMP. They proposed an improved VCCS algorithm based on discrete characteristics. The results show that when the size of crushing block is 0.1 m ~0.5 m, the accuracy of calculation results are about 80%, and when the size of broken block exceeds 0.5 m, almost all bfmp can be calculated correctly. Kromer et al. [16] used a ground-based 3D laser scanning technology to test the Séchiienne landslide in France for six weeks to detect the flow, displacement, and prefailure deformation of discrete collapse events. Then, they proposed an automatic ground laser scanning system with near real-time automatic change detection and processing function. Ma et al. [17] introduced 3D laser scanning technology into the overall deformation monitoring of slope surface in landslide physical model test and comprehensively analyzed the deformation characteristics of landslide in different evolution stages through the example of landslide physical model test. The results show that on the premise of ensuring high-precision feature point monitoring, the overall deformation and displacement of the model slope can be obtained with the help of 3D laser scanning technology.

Similarly, RS2 software can carry out fluid structure coupling analysis and dynamic analysis and can automatically generate finite element meshes such as triangles, and material models have the advantages of diversified types. It is also widely used in numerical simulation under cyclic loading [18]. In order to analyze the yield failure of the open pit mine in Minas Gerais, Brazil, Pereira and Lana [19] established many representative slope hypothesis models by using RS2 finite element software, carried out elastic and plastic simulation, and evaluated the yield failure mechanism. Liu et al. [20] used numerical simulation software to study the main causes of coal mine roof accidents. The results show that as the coal seam continues to advance, the maximum settlement displacement remains basically unchanged, and the settlement displacement curve presents an asymmetric flat bottom distribution and the stress concentration in front of the coal wall is the source of the abutment pressure. Silva and Lana [21] used RS2 software to study the failure mechanism of flexural buckling that occurred in Pau Branco Mine, of Vallourec and Mannesman Group, in 2002. Through the back analysis of the failure mechanism, they obtained the representative values of in situ stress state, normal stiffness modulus, and shear stiffness modulus of foliation structure. The results are of great significance to further analyze the stability of phyllite slopes of Pau Branco Mine. Arslan et al. [22] used RS2 finite element software to analyze the stability of marble stope under static and dynamic conditions, built shear strength reduction (SSR) technology into the software to determine the failure mechanism, and put forward suggestions and carried out necessary control to ensure the stability of slope. Adach-Pawelus [23] used RS2 finite element software to conduct numerical simulation in the plane deformation state, combined with seismic activity analysis and numerical simulation methods to illustrate the impact of mine residues on the possibility of seismic events. The results show that undisturbed rock cuttings may have a negative impact on earthquake and rock burst disasters in the mining area.

Even though 3D laser scanning technology and RS2 finite element software have made great progress and application, there are few studies on high-cold and high-altitude areas with the help of and combination of these two technologies. In view of this, this paper uses Optech Polaris LR 3D laser scanner to scan the open pit slope in cold area, obtains the point cloud data, realizes the intelligent identification and information extraction of rock mass structural plane, obtains the rock mechanical parameters through the freeze-thaw cycle tests, and establishes the slope mechanical model combined with RS2 finite element software to calculate the safety factor of the slope under different times of freeze-thaw cycle. This has important guiding significance for in-depth understanding of the law of slope instability of open pit mines in high-cold and high-altitude areas and preventing slope disasters and accidents in advance [24].

2. Identification and Extraction of Rock Structure Plane

2.1. Study Area. The research object of this paper is located in Beizhan iron mine in Hejing County, Korla, Xinjiang, in Northwest China. Permanent Piedmont glaciers are located in the south and west of the mining area, and the altitude of the ore body is 3450-3723 m. The mining area is located in the alpine area with perennial snow, and the climate is extremely cold. The monthly average temperature from January to April and from September to December is lower than zero, and the minimum temperature can reach -40°C. The temperature rises from May to August, generally 5-15°C, and the maximum rise can be 20°C. The temperature at night is usually as low as about -3°C, so the temperature difference between day and night in the mining area is large. The mining area has frequent rain and snow throughout the year. It is the local rainy season from July to August, and it begins to snow in early October. Therefore, it is only suitable to carry out appropriate field operations from May to September every year. The deposit is located in the river valley, and the terrain of the mining area is conducive to natural drainage. The overall strike of the ore body is 97°, and the dip angle is 47°-74°. According to the prediction of landform, meteorology and hydrology, geological structure, human activities, and other conditions in the mining area, the risk of geological disasters such as landslide and debris flow is small, but the risk of collapse geological disasters caused by local high and steep mountains is high. The study area is shown in Figure 1.

2.2. 3D Laser Scanning Technique. Optech Polaris LR 3D laser scanner is used to conduct overall scanning and fine scanning of the research area, respectively. The instrument

Figure 1: Study area.

Figure 2: Placement of 3D laser scanner.

Table 1: Parameters of 3D laser scanner.

Parameters	Index
Maximum measuring distance (m)	2000
Minimum measuring distance (m)	1.5
Scanning vision angle (°)	360 × 120
Principle of distance measuring	Pulse
Laser head rotation mechanism	Swinging mirrors
Working temperature (°C)	-20~50

meets the long-distance fine test requirements of the project, as shown in Figure 2. The parameters are shown in Table 1.

2.3. Rock Structural Plane Geometric Characteristics. In order to have a preliminary understanding of the whole mining area, 11 3D laser scans were carried out, covering the whole mining pit, as shown in Figure 3(a). 3D laser scanning was carried out on each point to obtain the point cloud data of each point. After splicing and packaging, a complete 3D geometric model is obtained, as shown in Figure 3(b). At the same time, fine scanning is carried out for the mining area. The scanning point S8 is located on the east side of the pit, including 399020 points. The scanning range is 2044.0957 m^2, and the maximum size of the scanning area is $51.2365 \times 61.8522 \times 29.0181$ m. Combining the 3D laser scanning technology with the digital camera, the pixel points of the picture are matched with the point cloud, and the gray information or color information of the point cloud data can be obtained. The color information is helpful to display the scanning results, and the results are shown in Figure 3(c).

2.3.1. Processing of Point Cloud Data. The amount of point cloud data obtained by 3D laser scanning structural plane is large and dense will seriously affect the operation speed. Therefore, in order to realize the programming of the algorithm, it is necessary to divide the point cloud data into space and grid the point cloud data. In this study, for the point cloud data with high scanning accuracy, the 3D difference method is adopted. This method has little impact on the accuracy, and the impact can be ignored. The results are shown in Figure 4.

In order to obtain the optimal threshold, it is necessary to select the discrimination index of structural plane intelligent recognition. In this paper, the point normal vector is used as the discrimination index. The next step is to determine the flatness detection threshold of point cloud.

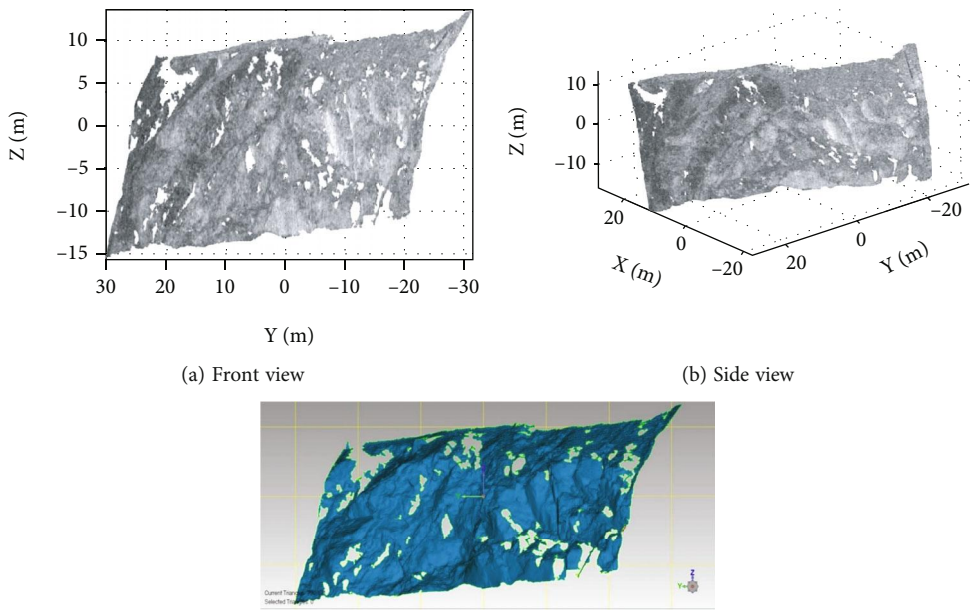

(a) Front view

(b) Side view

(c) Triangulation model

Figure 3: S8 station scanning slope point cloud data.

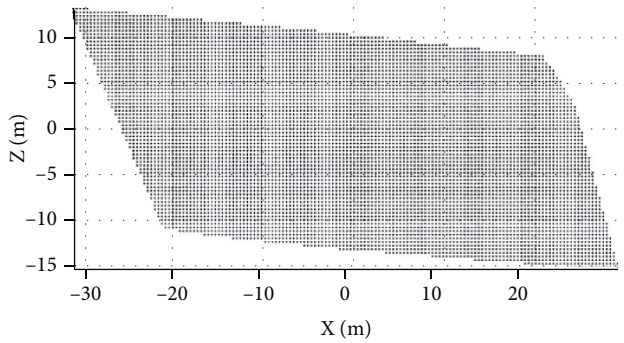

Figure 4: Result of grid processing.

According to the rules, when the value of ξ_1 is smaller, the more points are included in the BORDER matrix, which means that more points are regarded as boundary points and do not participate in the next image segmentation algorithm. Conversely, when the value of ξ_1 is too large, the number of points in the BORDER matrix decreases, which means that the edge recognition effect is weakened, indicating that some boundary points will not be recognized effectively. So, according to the actual situation of the mining area, the flatness detection threshold ξ_1 is set to 20°.

2.3.2. Selection of Optimal Threshold. Make the regional growth threshold ξ_2 between 5° and approximately 40°, and the value interval is 5°. The area threshold remains unchanged at 0.5 m^2. When the value of regional growth threshold is too small, the growth criteria is relatively severe, and many point cloud data are not identified as structural plane, which makes the regional division too fragmented and the number of structural plane identified is few. When the value of regional growth threshold is too large, the growth criteria is too loose, which leads to a part of the point cloud data located in uneven areas will also be divided into structural plane, and the number of structural plane identified is too large, so it is impossible to distinguish adjacent structural plane. According to visual judgment, when the regional growth threshold is between 20° and 30°, the recognition effect is more realistic. The results of structural plane recognitions are shown in Figures 5(a)–5(c).

Similarly, make the area threshold W_1 between 0.1 m^2 and approximately 10 m^2, and the value interval is 0.1 m^2. The regional growth threshold remains unchanged at 20°. When the area threshold W_1 is greater than 0.1 m^2, the recognition effect is more practical. When the area threshold is too large, more structural plane are eliminated, which leads to too few remaining structural plane and is not conducive to the later structural plane information extraction. The result of structural plane recognition is shown in Figure 5(d). In summary, the growth threshold is 20°, and the area threshold is 0.1 m^2.

2.4. Extraction of Structural Plane Information of Rock Mass

2.4.1. Acquisition of Structure Plane Occurrence Information. The least square method is used to fit all nodes of each rock mass structural plane obtained before. In this way, the plane equation of quasi plane shape can be obtained. The plane equation is shown in

$$ax + by + c = z. \tag{1}$$

It is assumed that the spatial coordinates of n points on the structural plane are (x_1, y_1, z_1), (x_2, y_2, z_2) ,…,(x_n, y_n, z_n), respectively, and the matrix equation can be expressed as

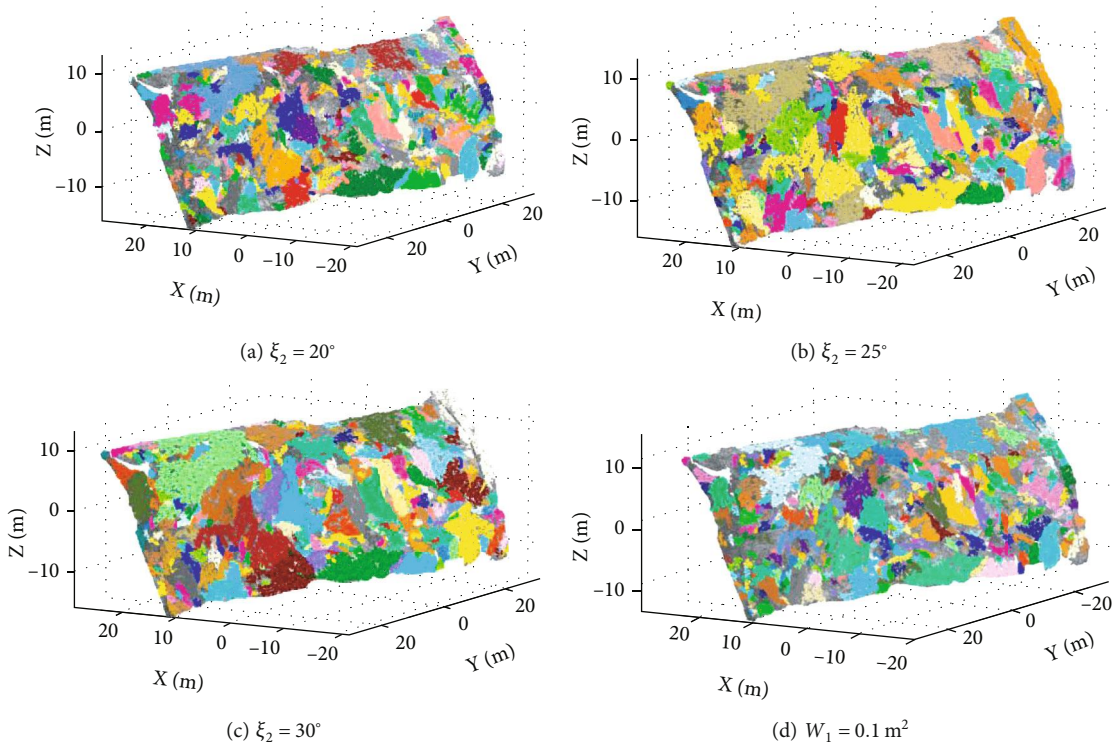

Figure 5: Intelligent identification results of rock structural plane under different growth and area thresholds.

$$\begin{bmatrix} x_1 & y_1 & 1 \\ x_2 & y_2 & 1 \\ \vdots & \vdots & \vdots \\ x_n & y_n & 1 \end{bmatrix} \begin{bmatrix} a \\ b \\ c \end{bmatrix} = \begin{bmatrix} z_1 \\ z_2 \\ \vdots \\ z_n \end{bmatrix}. \tag{2}$$

Let

$$D = \begin{bmatrix} a \\ b \\ c \end{bmatrix}, \tag{3}$$

$$X = \begin{bmatrix} x_1 & y_1 & 1 \\ x_2 & y_2 & 1 \\ \vdots & \vdots & \vdots \\ x_n & y_n & 1 \end{bmatrix}, \tag{4}$$

$$Z = \begin{bmatrix} z_1 \\ z_2 \\ \vdots \\ z_n \end{bmatrix}. \tag{5}$$

So, we need to find vector D and make $\phi(D) = \|DX - Z\|$ get the minimum value. Finally, the normal vector and plane equation of structural plane are obtained to complete the fitting of the structural plane.

This study mainly calculates the dip and dip angle in the occurrence information of structural plane. If the normal vector coordinate of structural plane is (x_0, y_0, z_0). According to the working principle of laser emission in 3D laser scanning technology, it can only scan the structural plane with good exposure on the side slope, so $z_0 > 0$. With the geodetic coordinate system, the due east and due north are defined as the positive directions of the X axis and Y axis, respectively, and the Z axis points to the elevation direction. Therefore, the occurrence information dip θ and dip angle δ of the rock mass structural plane can be expressed by the following equation:

$$\left.\begin{aligned} &\delta = \arccos(z_0) \\ &\text{if} \quad x_0 \geqslant 0, y_0 \geqslant 0, \ \theta = \arcsin\left(\frac{x_0}{\sin\delta}\right) \\ &\text{if} \quad x_0 < 0, y_0 > 0, \ \theta = 360° - \arcsin\left(-\frac{x_0}{\sin\delta}\right) \\ &\text{if} \quad x_0 < 0, y_0 > 0, \ \theta = 180° - \arcsin\left(\frac{x_0}{\sin\delta}\right) \\ &\text{if} \quad x_0 > 0, y_0 < 0, \ \theta = 180° + \arcsin\left(-\frac{x_0}{\sin\delta}\right) \end{aligned}\right\}. \tag{6}$$

The occurrence information of point cloud data of rock mass structural plane is shown in Figure 6.

2.4.2. Grouping of Rock Mass Structure Planes Based on Occurrence Information. Then, the K-means cluster analysis method is used to group these occurrence information and is combined with the field investigation of geological

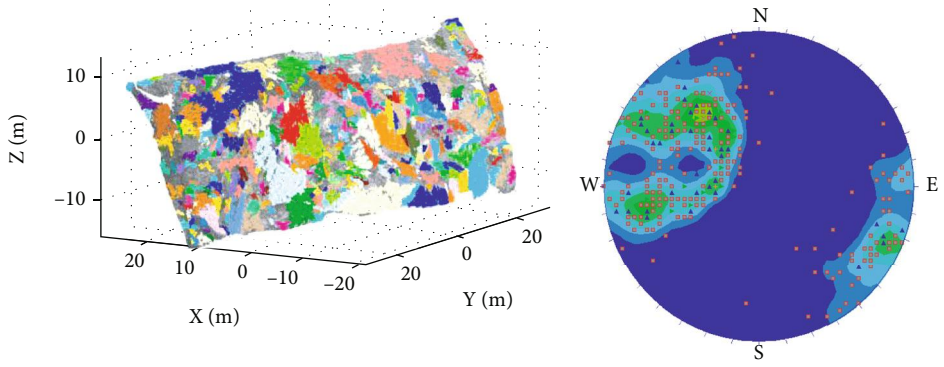

(a) Distribution characteristics of structural plane (b) The result of stereographic projection

Figure 6: Distribution characteristics of structural plane and the result of stereographic projection.

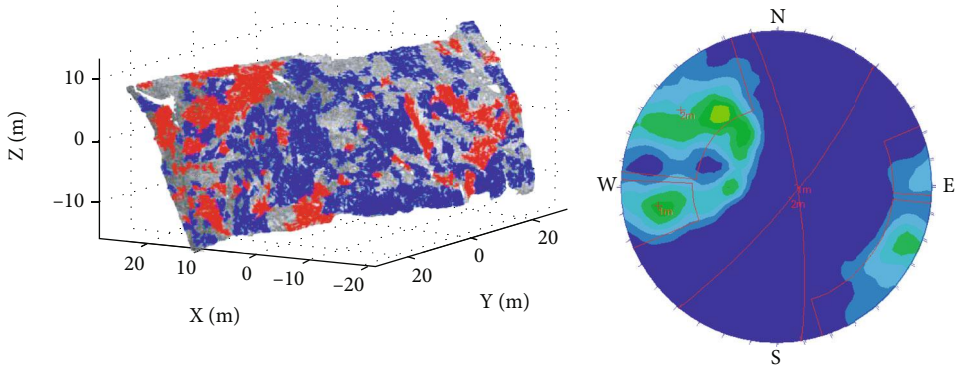

(a) Distribution characteristics of occurrence (b) The result of stereographic projection

Figure 7: Occurrence distribution characteristics of the rock mass structural plane after clustering and the result of stereographic projection.

information. It is obtained that the structural plane of the slope in the mining area can be divided into three groups, including a group of gently inclined plane and two groups of steeply inclined joints. Intelligent identification mainly finds two groups of steep joints. Finally, the cluster center and average occurrence are calculated. The average occurrence of the two groups of rock mass structural planes is $261^\circ < 75^\circ$ and $307^\circ < 77^\circ$, respectively. The results are shown in Figure 7.

In this study, the structural plane occurrence modeling method based on empirical probability distribution is adopted to truly reflect the actual structural plane occurrence distribution and then obtain the relative frequency of two groups of rock mass structural plane occurrence. The results are shown in Figure 8.

2.4.3. Calculation of Spacing between Rock Structural Planes. In order to obtain the spacing between adjacent structural planes, it is calculated according to the method shown in Figure 9. The dotted line in the figure is the initial state of the same group of structural planes, the solid line is the ideal state of the structural planes converted according to the above method, and the structural planes are parallel to each other in the same group. The vertical distance calculation equation is used to calculate the distance between adjacent structural planes.

$$l_1 : Ax + By + Cz + D_1 = 0, \tag{7}$$

$$l_2 : Ax + By + Cz + D_2 = 0, \tag{8}$$

$$d_{l_1 l_2} = \frac{|D_1 - D_2|}{\sqrt{A^2 + B^2 + C^2}}, \tag{9}$$

Where l_1 is plane 1 equation, l_2 is plane 2 equation, and $d_{l_1 l_2}$ is the vertical distance between two adjacent structural planes.

According to the equation, the distribution characteristics of the spacing information of the two groups of rock mass structural planes are calculated, as shown in Figure 10.

2.4.4. Calculation of Equivalent Trace Length of Rock Mass Structural Planes. Because the data obtained by the image segmentation method is point cloud data, the method of projection is used to calculate the area of the structural plane, as shown in

$$S = \frac{S_{xoy}}{\cos \gamma}, \tag{10}$$

where γ is the angle between the xoy plane and the structural plane, S is the area of the desired structural plane, and

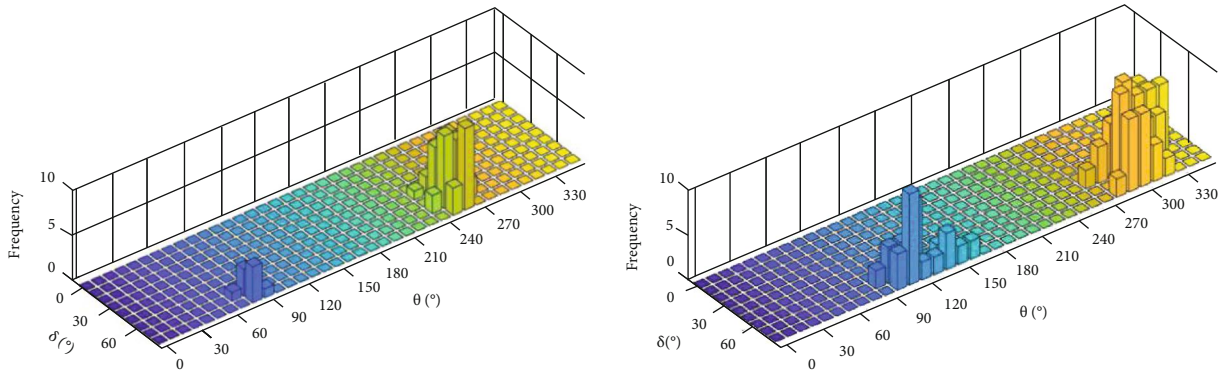

Figure 8: 3D histogram of the occurrence relative frequency of the structural plane of the two groups of rocks.

S_{xoy} is the projected area of the node on the structural plane projected onto the *xoy* plane.

Thus, the exposed area of rock mass structural plane is calculated. For convenience, the structural plane can be replaced by an equivalent circle with equal area. The radius is expressed in

$$S = \pi r^2. \tag{11}$$

The equivalent trace length of the two groups of rock mass structural planes in this paper can be characterized by the equivalent radius obtained by equation (11). The results are shown in Figure 11.

2.4.5. Statistics of Structural Plane Information of Rock Mass. Based on the theory of mathematical statistics, according to the point cloud data of S8 rock slope, the probability distribution types and statistical parameters of geometric parameters such as the occurrence of rock mass structural plane calculated above are counted, as shown in Table 2.

3. Numerical Simulation Analysis

In this paper, RS2 elastic-plastic finite element software is used for numerical simulation analysis. An important function of RS2 is to calculate the safety factor of slope stability based on the finite element strength reduction method. By using the Hoek-Brown strength criterion, the system can automatically reduce the strength and obtain the safety factor of the slope. In this software, the constitutive model of rock mass includes the generalized Hoek-Brown model, Mohr-Coulomb model, and Cam-Clay model. At the same time, based on the statistical model, users can input relevant joint parameters according to the actual situation when building the slope model, and the system will automatically generate the joint fracture network.

3.1. Establishment of Model and Selection of Parameters. In order to obtain the relevant mechanical parameters of rock slope and establish a complete geomechanical model, samples were taken from the site and divided into 6 groups with 2 samples in each group. The samples of each group were subjected to 0, 20, 40, 60, 80, and 100 times of freeze-thaw cycle, respectively, and physical and mechanical tests were

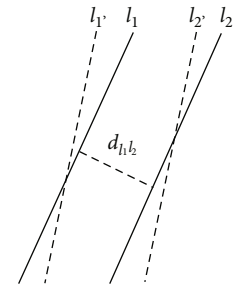

Figure 9: Plots of the 7same group of structural surface space distance by calculating.

carried out. Finally, the parameters shown in Table 3 are counted.

We intercepted a section line on the west slope of the mining area to automatically generate the section map of the west slope, import it into RS2 software, and generate the model boundary. The structural plane of rock mass is based on the generalized Hoek-Brown criterion, and the joint is a constitutive model based on Barton-Bandis criterion. According to the previous research, the slope is mainly affected by two sets of joint surfaces. The above physical and mechanical parameters were input into RS2 software, and the three node triangular element was used to generate the finite element grid. The model contained 17207 nodes and 29427 elements. We considered the actual boundary conditions on site and get the final result, as shown in Figure 12. Finally, five monitoring points were arranged for subsequent research.

3.2. Numerical Simulation Results

3.2.1. Analysis of Maximum Principal Stress and Maximum Shear Strain of Slope Model. According to the definition of principal stress, under the same external force, the principal stress increases with the increase of buried depth. In order to study the variation of the maximum principal stress under different times of freeze-thaw cycle, the cloud chart of the maximum principal stress is obtained as shown in Figure 13. It can be found from the figure that the maximum principal stress at the bottom of the slope model is greater than that in other areas, while the top is the smallest. At the same time, the value range of the maximum principal

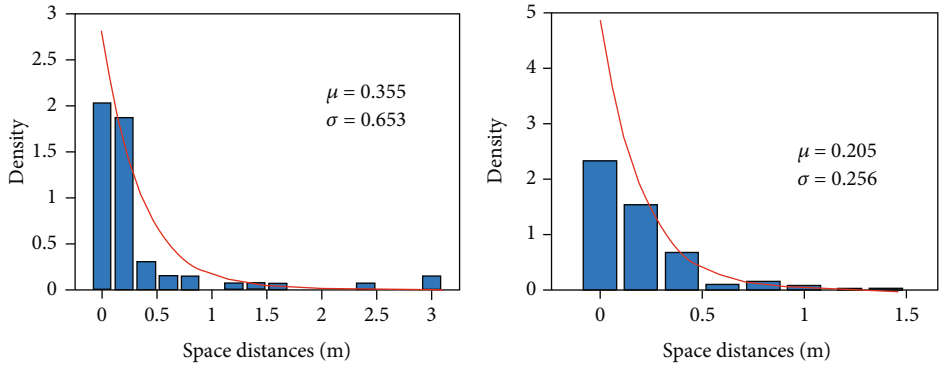

Figure 10: Histogram of space distance distribution of two groups of the rock mass structure plane.

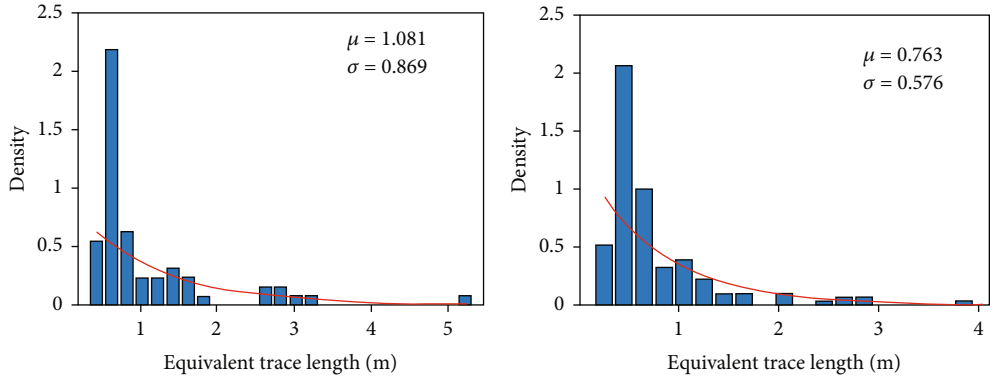

Figure 11: Histogram of equivalent trace length distribution of two groups of rock mass structure plane.

Table 2: Mathematical statistical information of rock mass structural planes.

Parameters	Distribution Type	Statistical parameters	Structure plane	Value
Tendency (°)	Empirical probability	Mean	Plane 1	261.000
			Plane 2	309.000
		Standard deviation	Plane 1	61.942
			Plane 2	103.558
Dip angle (°)	Empirical probability	Mean	Plane 1	75.000
			Plane 2	77.000
		Standard deviation	Plane 1	9.266
			Plane 2	10.173
Space distances (m)	Negative exponential distribution	Mean	Plane 1	0.355
			Plane 2	0.205
		Standard deviation	Plane 1	0.653
			Plane 2	0.256
Equivalent trace length (m)	Negative exponential distribution	Mean	Plane 1	1.081
			Plane 2	0.763
		Standard deviation	Plane 1	0.869
			Plane 2	0.576

stress does not change with the increase of the times of the freeze-thaw cycle and generally shows a slight upward trend, but it is between -0.75 MPa and 14.25 MPa. This shows that the increase of times of freeze-thaw cycle has little effect on the maximum principal stress of the slope.

In order to reflect the influence of different times of the freeze-thaw cycle on slope failure and instability, the cloud chart of corresponding maximum shear strain is obtained by numerical simulation, as shown in Figure 14. It can be seen from the figure that the safety factor decreases with

Table 3: Basic mechanical and physical parameters of freeze-thaw-treated granite samples.

Sample number	Length × width (mm × mm)	Mass (kg)	Density (g/cm^3)	Peak strength (MPa)	Elasticity modulus (MPa)	P-wave velocity (m/s)	S-wave velocity (m/s)
y0-1	100.07 × 49.46	541.4	2.863	172.38	58.65	4302	3577
y0-2	100.01 × 49.62	540.5	2.796	182.45	60.08	4412	3456
y20-1	99.58 × 49.30	543.1	2.859	168.73	56.31	4131	3391
y20-2	100.01 × 50.21	540.2	2.729	167.24	55.46	4265	3325
y40-1	99.85 × 50.05	542.6	2.763	163.98	52.78	4012	3101
y40-2	100.12 × 49.63	544.9	2.815	158.35	53.44	4000	3210
y60-1	100.22 × 49.85	547.5	2.800	158.78	50.89	3906	2984
y60-2	100.06 × 49.19	544.6	2.865	155.66	49.65	3894	3015
y80-1	99.90 × 49.88	548.9	2.813	152.39	47.36	3826	2883
y80-2	100.11 × 49.76	543.5	2.793	149.23	45.23	3856	2913
y100-1	100.12 × 49.29	547.2	2.866	146.65	42.94	3690	2664
y100-2	100.08 × 49.34	546.6	2.858	142.33	43.89	3546	2703

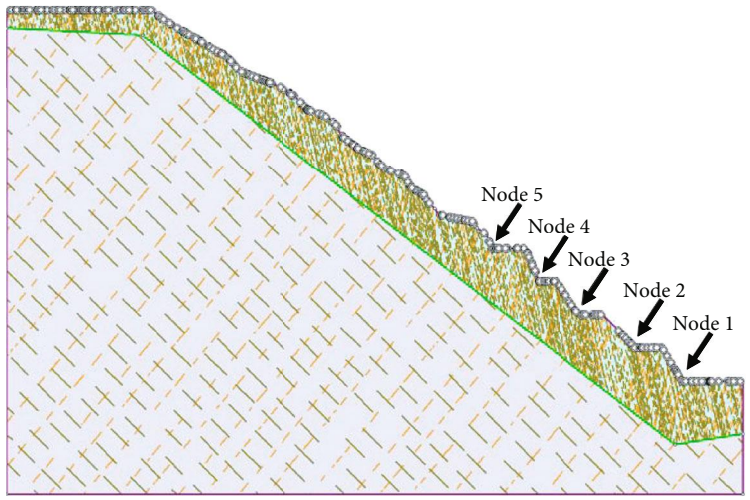

Figure 12: Contour map of Beizhan iron mine and slope calculation model.

the increasing times of the freeze-thaw cycle. At the same time, the maximum shear strain reflects the relative deformation of slope failure. The figure also shows that the relative deformation of failure gradually increases with the increase of the times of the freeze-thaw cycle. Because this paper studies the rock slope, it will not form a complete sliding zone like the soil slope. However, local rock mass spalling and instability failure will occur within the freeze-thaw shear area of the slope. The results show that the times of the freeze-thaw cycle has a great impact on the strength and stability of slope rock mass. The more times of the freeze-thaw cycle, the more serious the deterioration of internal performance of rock mass and the lower the stability of slope.

3.2.2. Analysis of Total Displacement of Slope Model. Figure 15 shows the change of total displacement nephogram of slope rock mass under different times of the freeze-thaw cycle. It can also be found from the figure that the safety factor decreases gradually with the increase of the times of the freeze-thaw cycle. At the same time, due to the self-weight of the overlying rock mass and mechanical excavation, the total displacement reaches the maximum in the first two steps.

According to the numerical simulation results, the strength reduction factor decreases with the increasing times of the freeze-thaw cycle. In order to further reflect the relationship between the strength reduction factor and the total displacement of the slope, the curve shown in Figure 16 is drawn. It can be clearly seen from the figure that under the same times of the freeze-thaw cycle, the initial increase of the maximum total displacement of the slope is not obvious, and then with the continuous increase of the strength reduction factor, the maximum total displacement changes abruptly and increases significantly. This shows that the slope is obviously damaged when the strength reduction

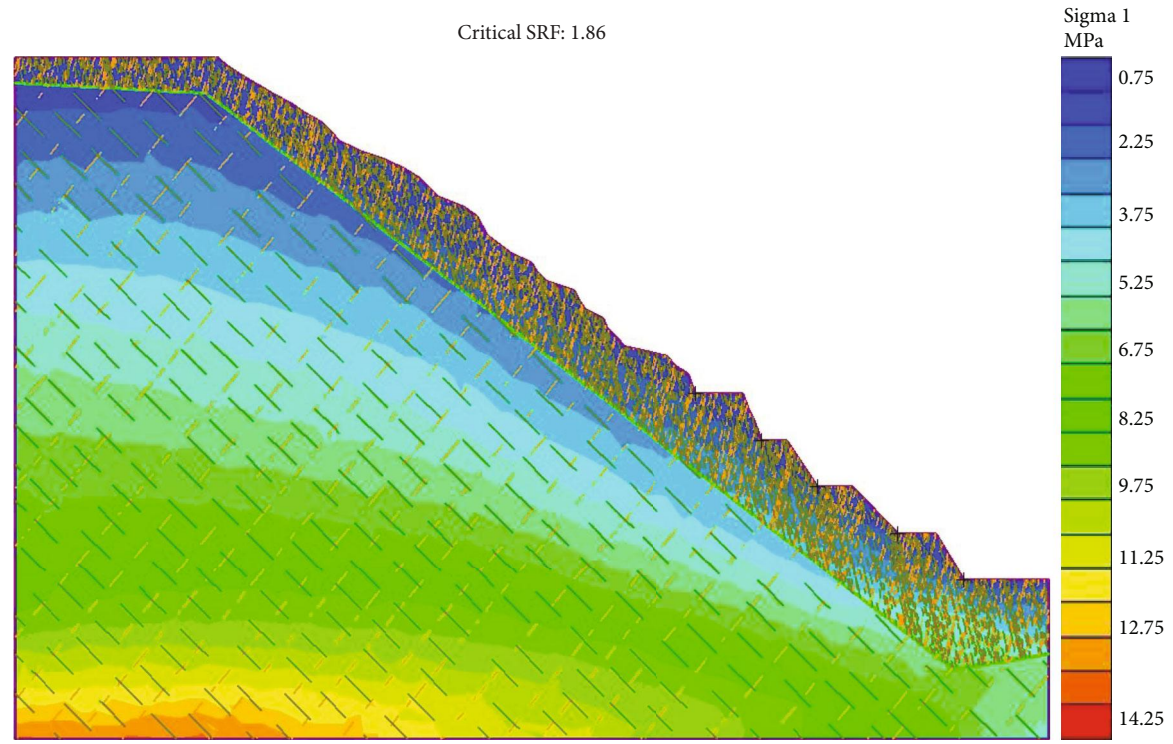

(a) Cloud chart of maximum principal stress for 0 times of the freeze-thaw cycle

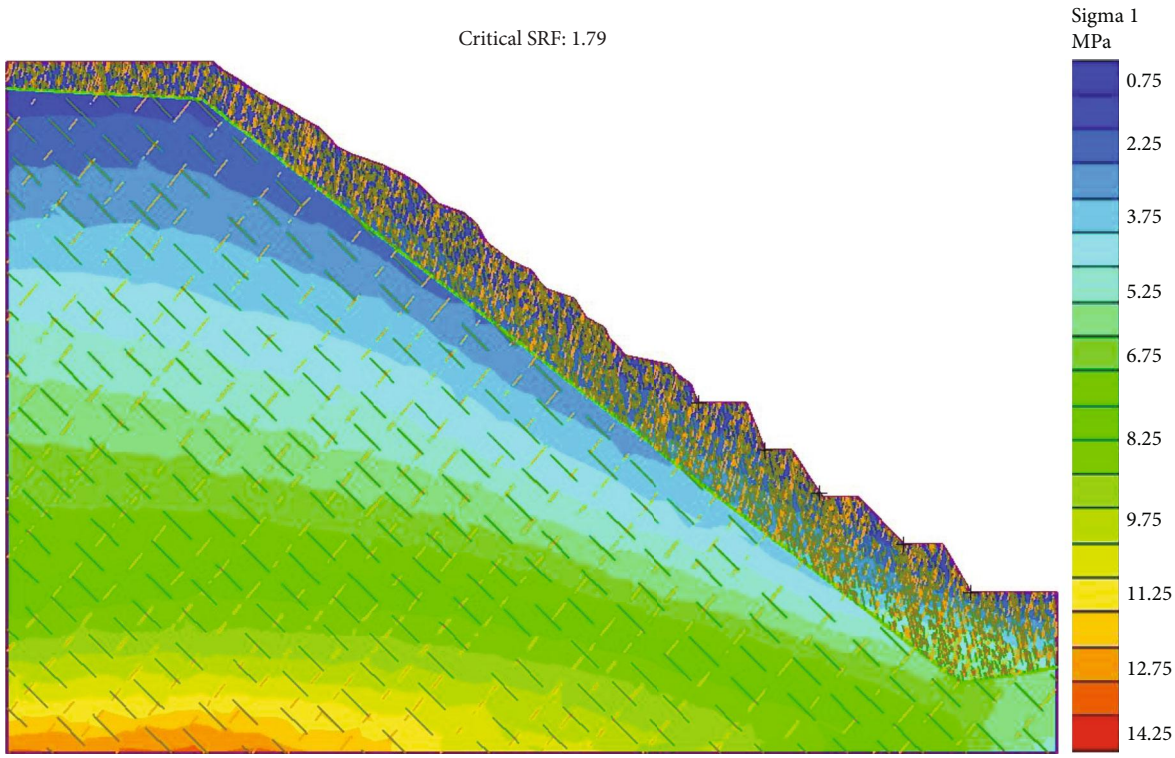

(b) Cloud chart of minimum principal stress for 20 times of the freeze-thaw cycle

Figure 13: Continued.

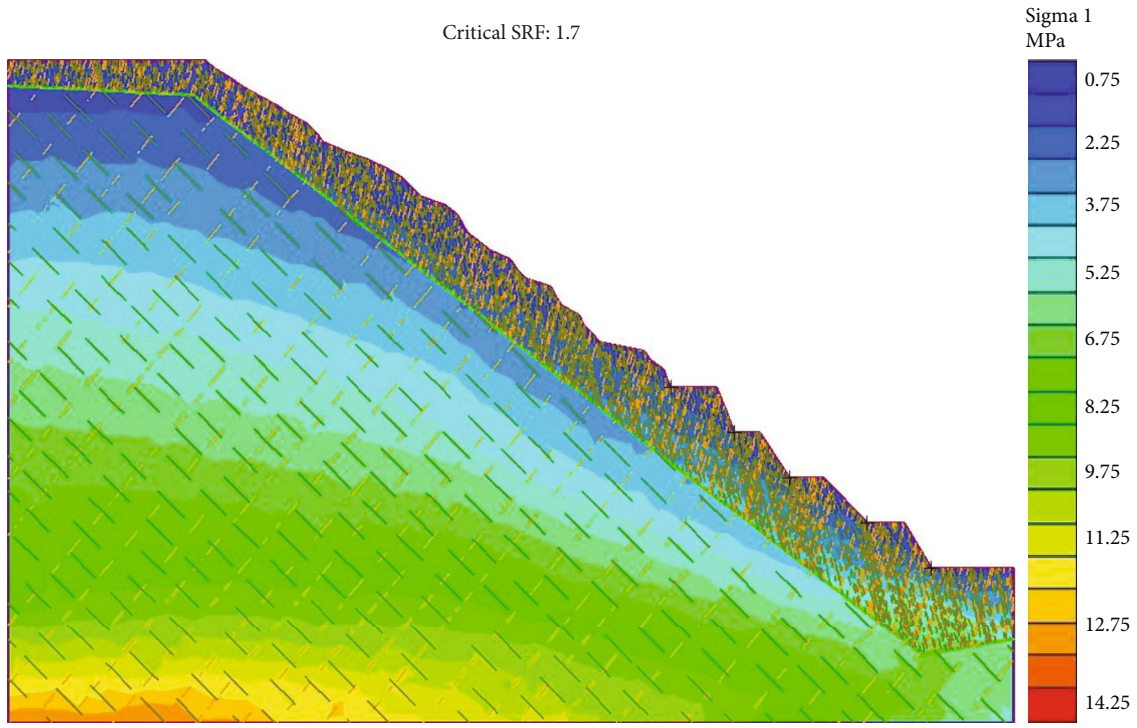

(c) Cloud chart of maximum principal stress for 40 times of the freeze-thaw cycle

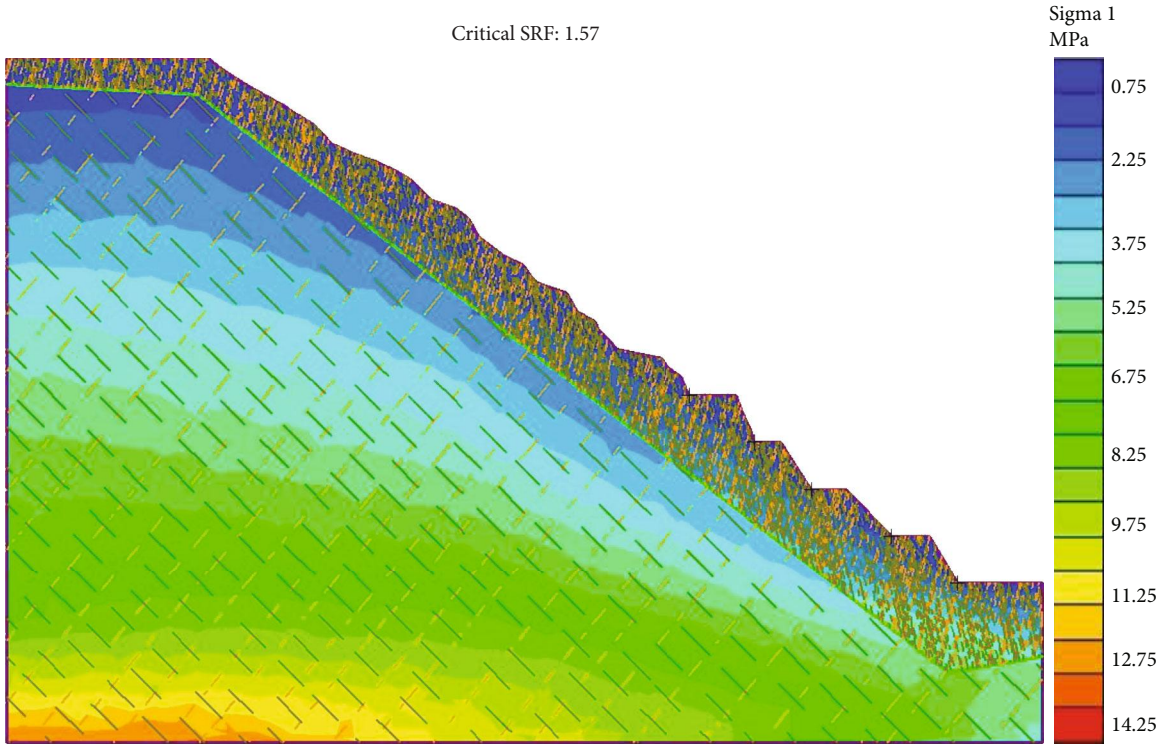

(d) Cloud chart of maximum principal stress for 60 times of the freeze-thaw cycle

Figure 13: Continued.

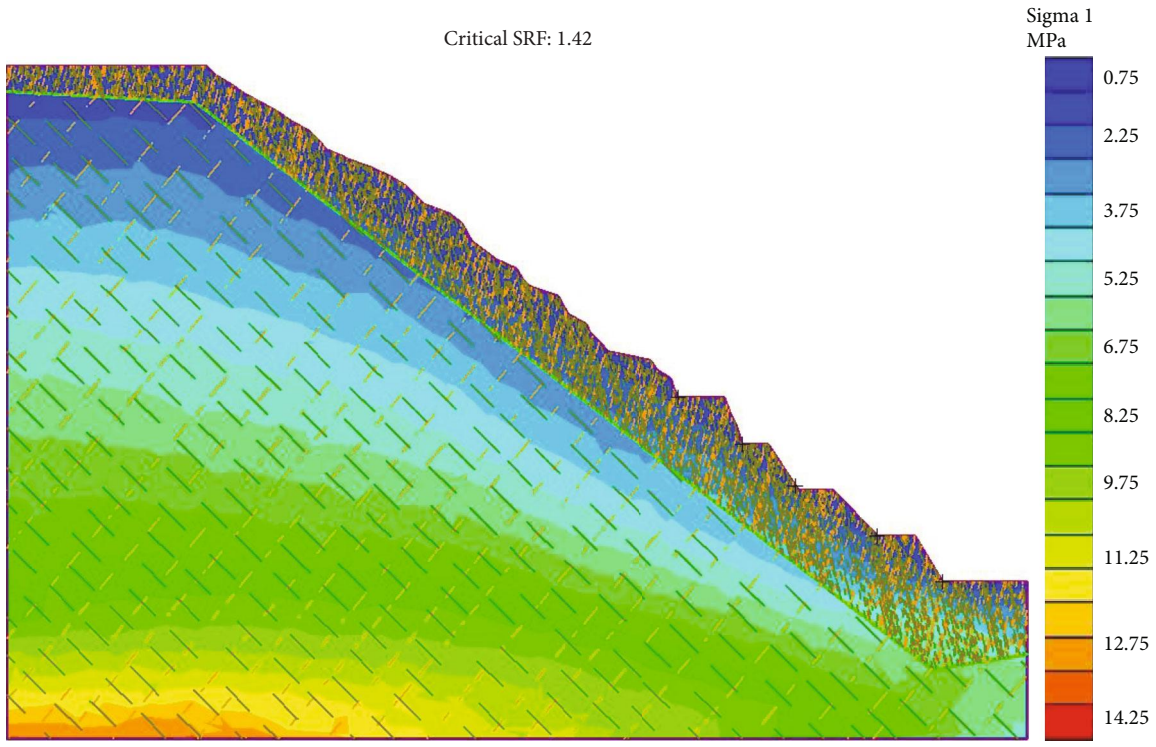

(e) Cloud chart of maximum principal stress for 80 times of the freeze-thaw cycle

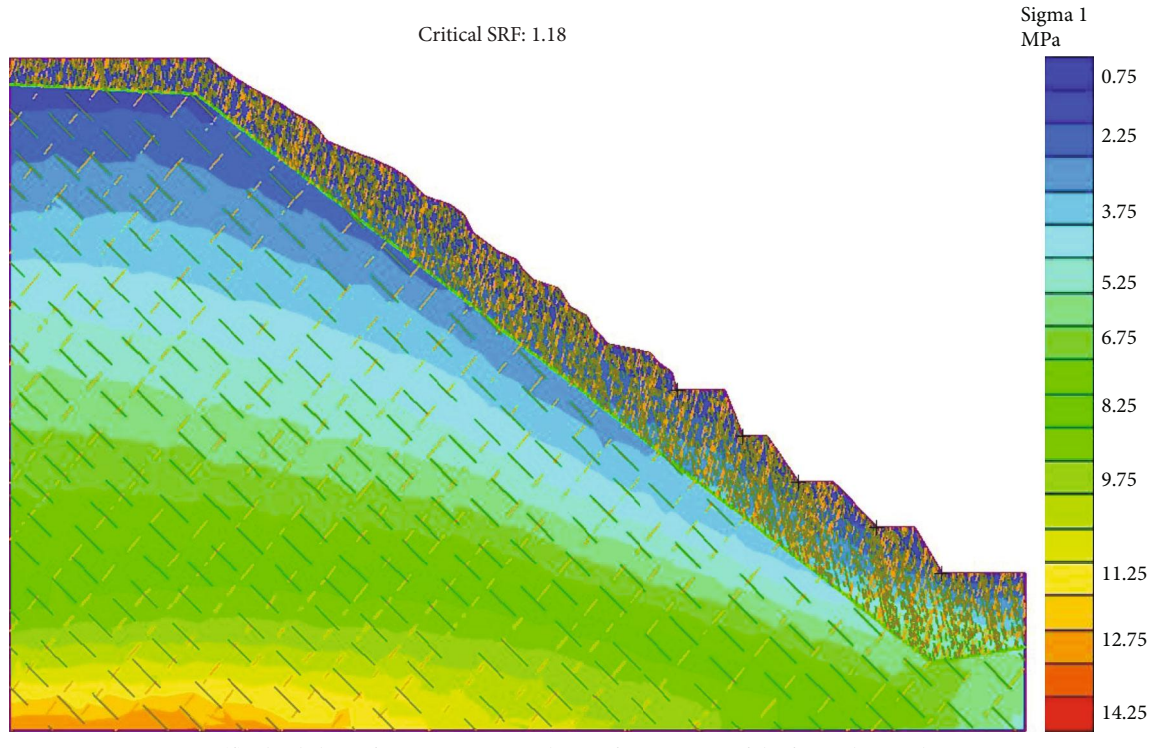

(f) Cloud chart of maximum principal stress for 100 times of the freeze-thaw cycle

Figure 13: Cloud chart of maximum and minimum principal stress for different times of the freeze-thaw cycle.

factor reaches this value. When the times of the freeze-thaw cycle increases, the strength reduction factor decreases gradually, and the decreasing range is larger and larger. It shows that the freeze-thaw cycle has a great weakening effect on the mechanical properties of slope rock mass.

3.2.3. Analysis of Yield Elements and Yield Joints of Slope Model. The number of yield elements, yield joints, and their distribution can well show the specific failure degree and failure area of rock. According to the previous test results, the physical and mechanical properties of slope rock mass deteriorate due

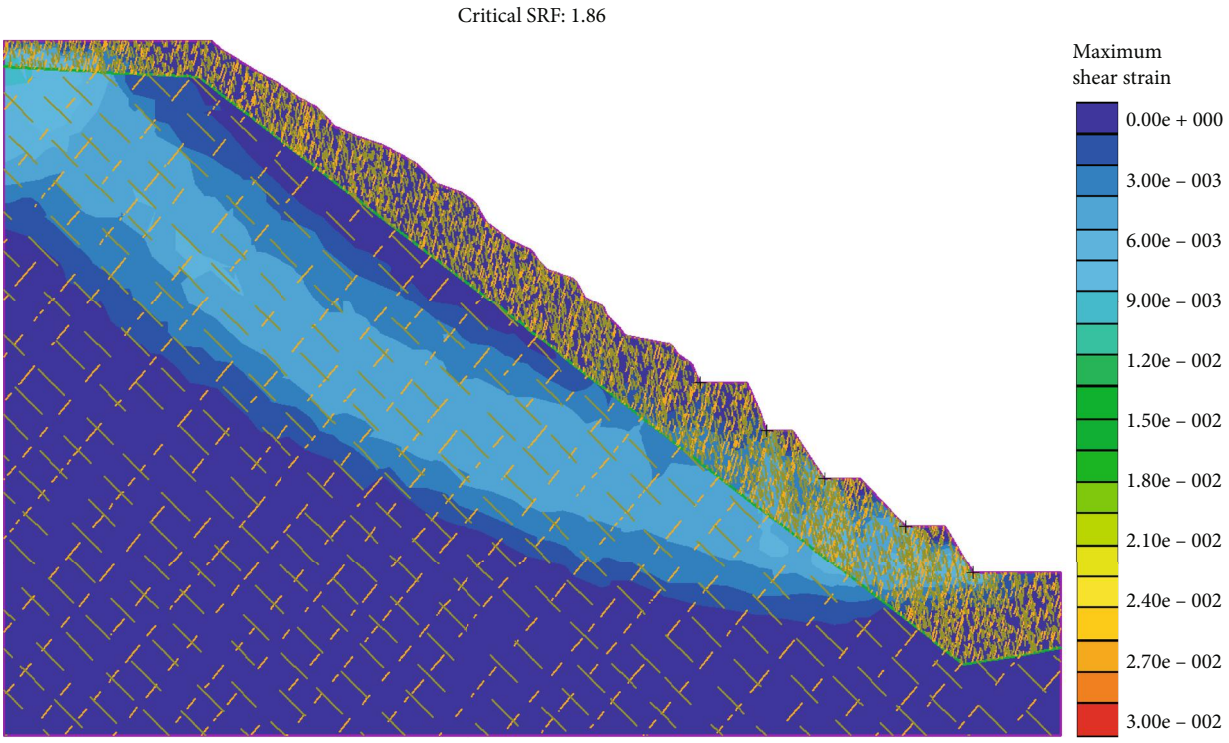

(a) Cloud chart of maximum shear strain for 0 times of the freeze-thaw cycle

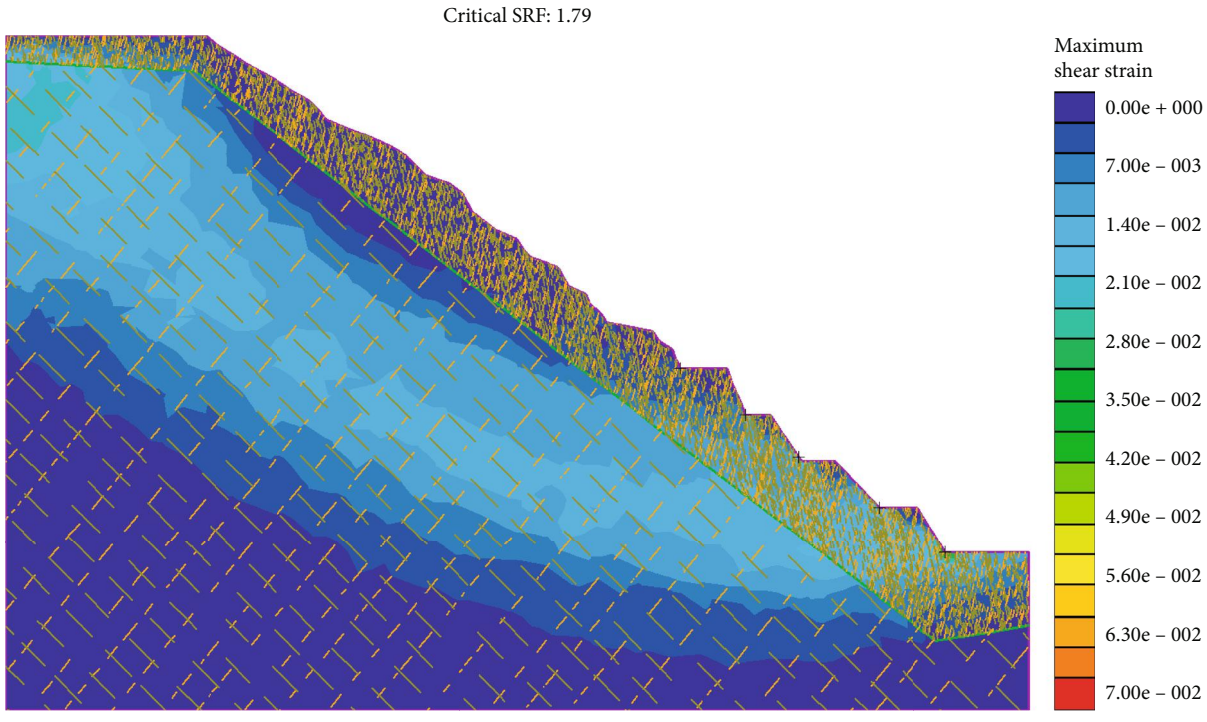

(b) Cloud chart of maximum shear strain for 20 times of the freeze-thaw cycle

Figure 14: Continued.

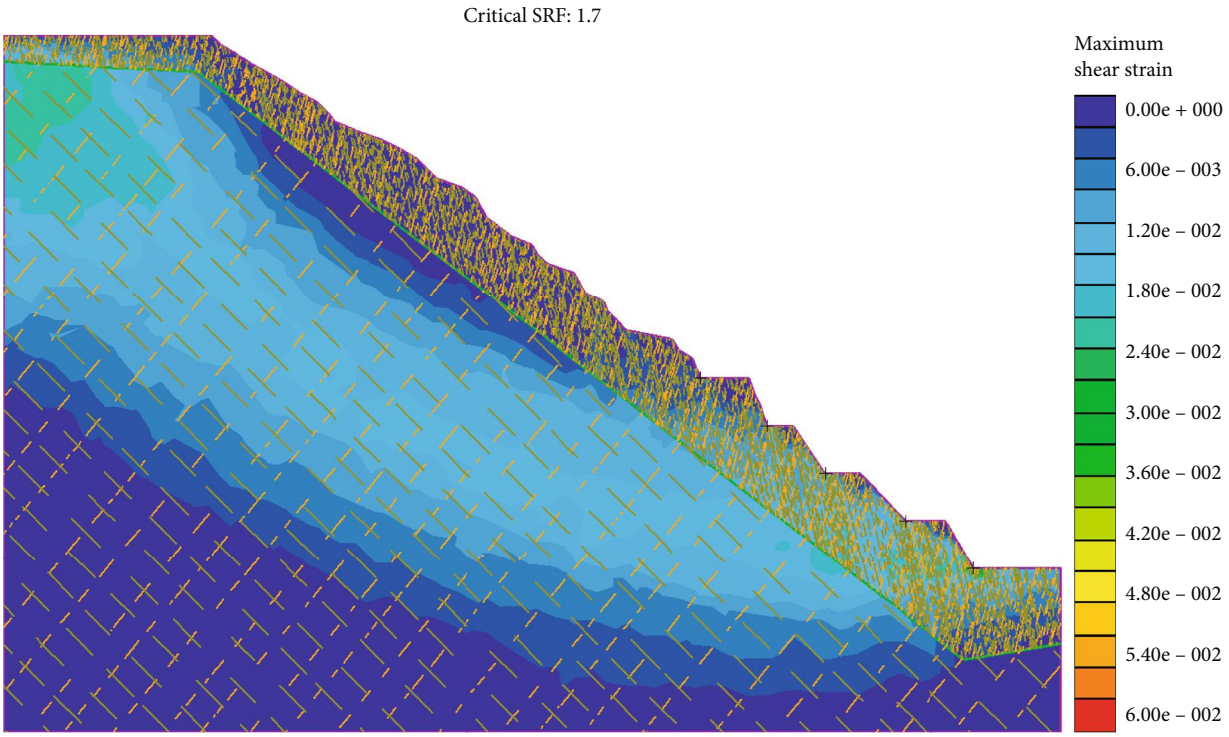

(c) Cloud chart of maximum shear strain for 40 times of the freeze-thaw cycle

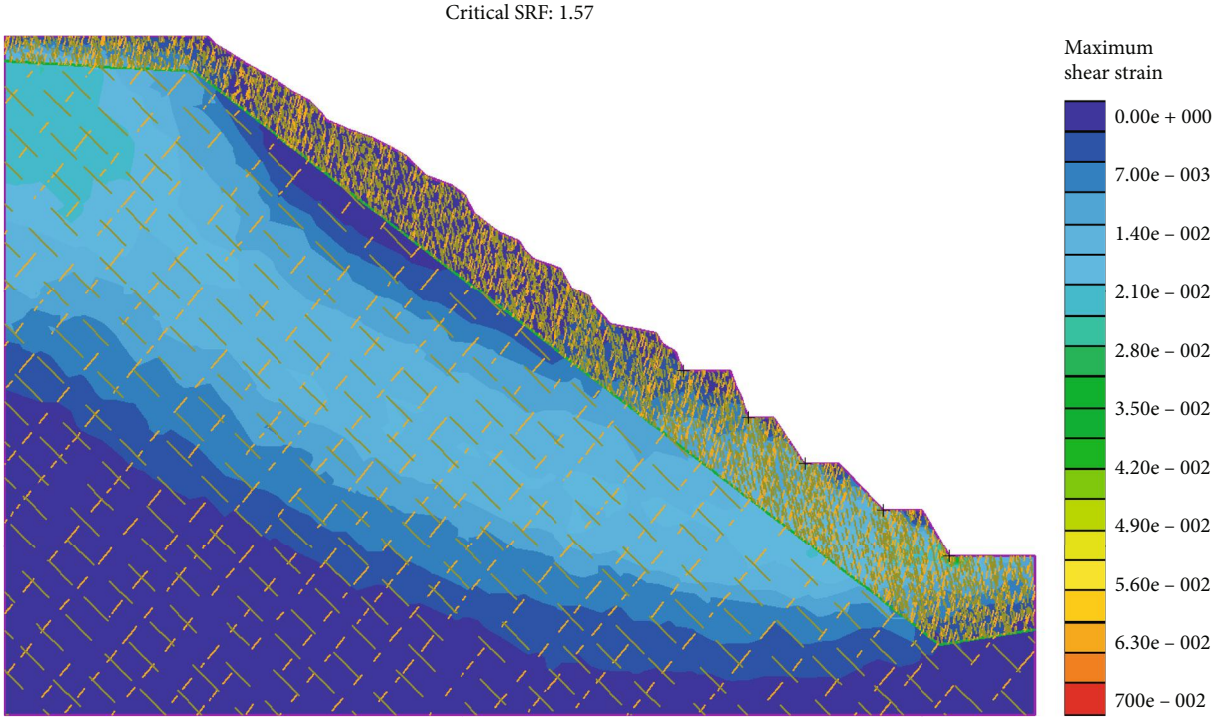

(d) Cloud chart of maximum shear strain for 60 times of the freeze-thaw cycle

Figure 14: Continued.

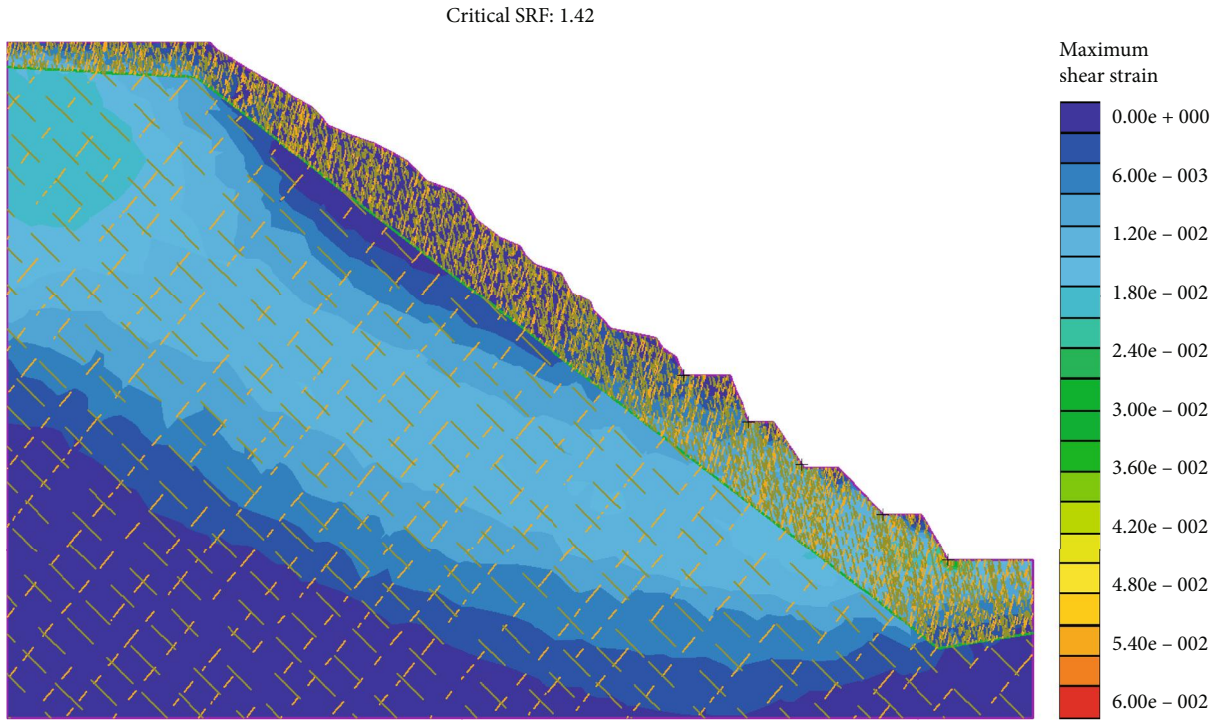

(e) Cloud chart of maximum shear strain for 80 times of the freeze-thaw cycle

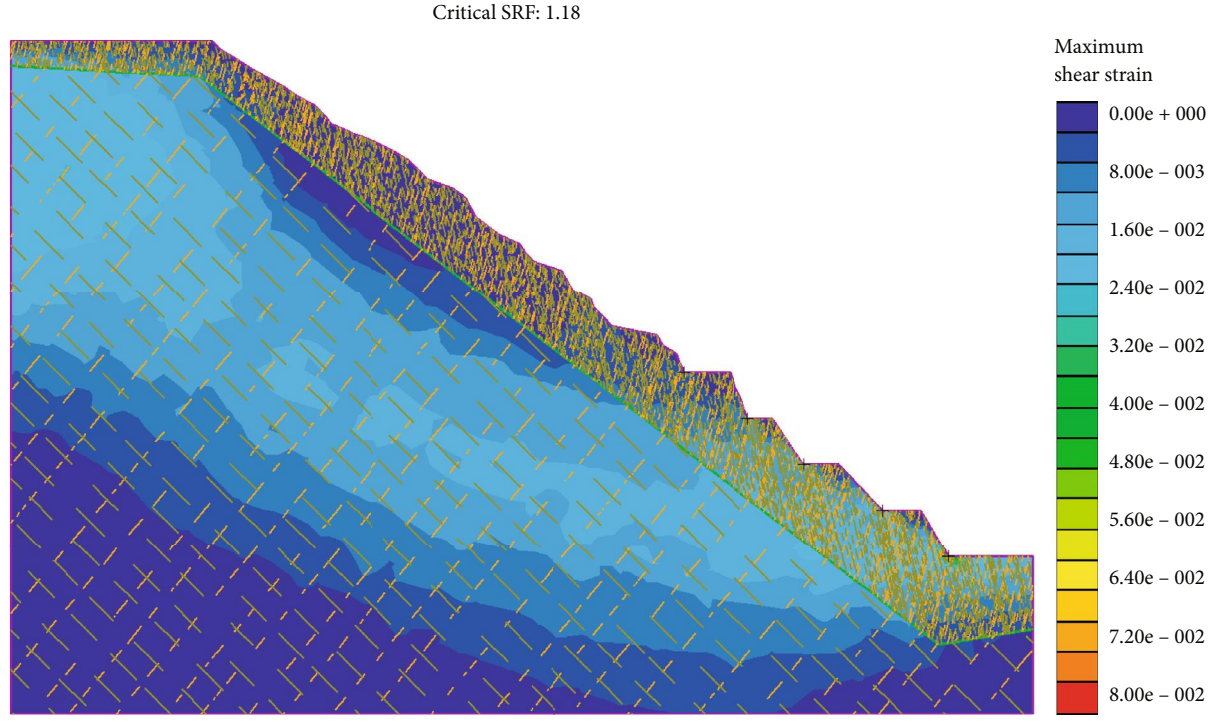

(f) Cloud chart of maximum shear strain for 100 times of the freeze-thaw cycle

Figure 14: Cloud chart of maximum shear strain for different times of the freeze-thaw cycle.

to freeze-thaw damage, and the strength of rock mass decreases. From the numerical simulation results, it can be found that with the increase of the times of the freeze-thaw cycle, the yield elements of the slope are increasing, and their distribution is spreading from the weathered steps above to the steps below. The distribution of yield joints is becoming more and more dense, and they are mainly distributed on the slope surface like the yield elements. In

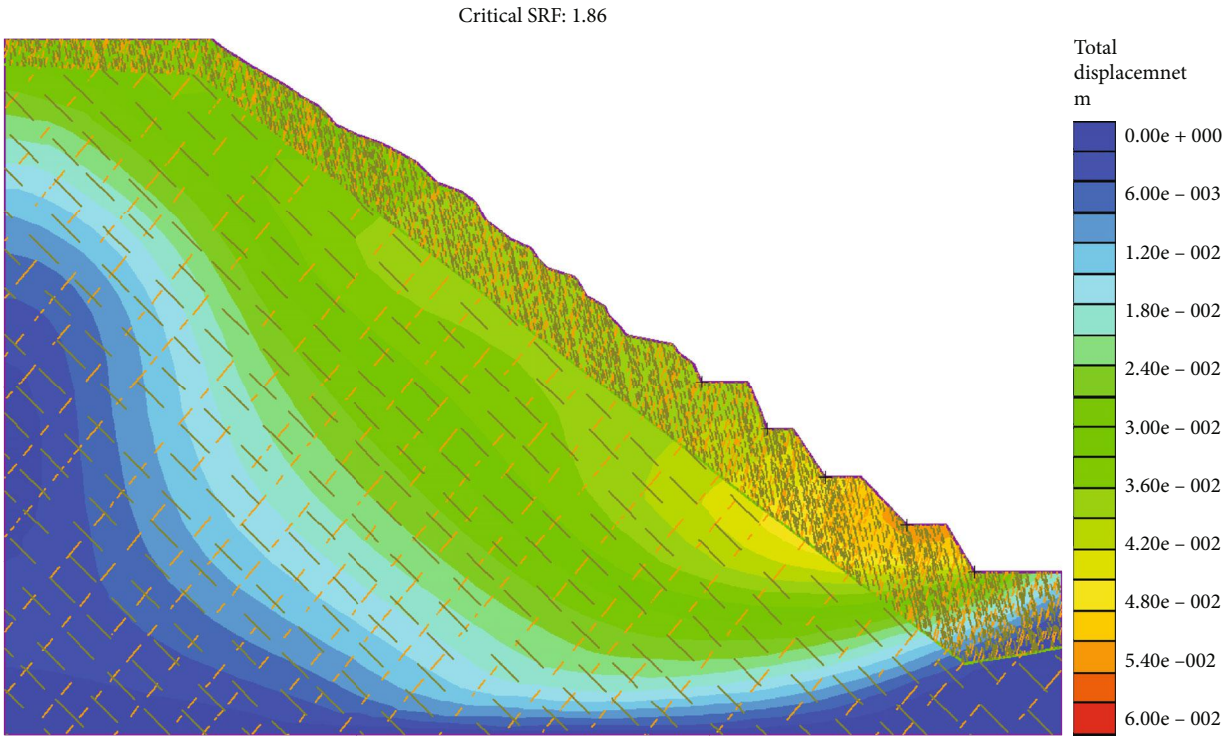

(a) Cloud chart of total displacement for 0 times of the freeze-thaw cycle

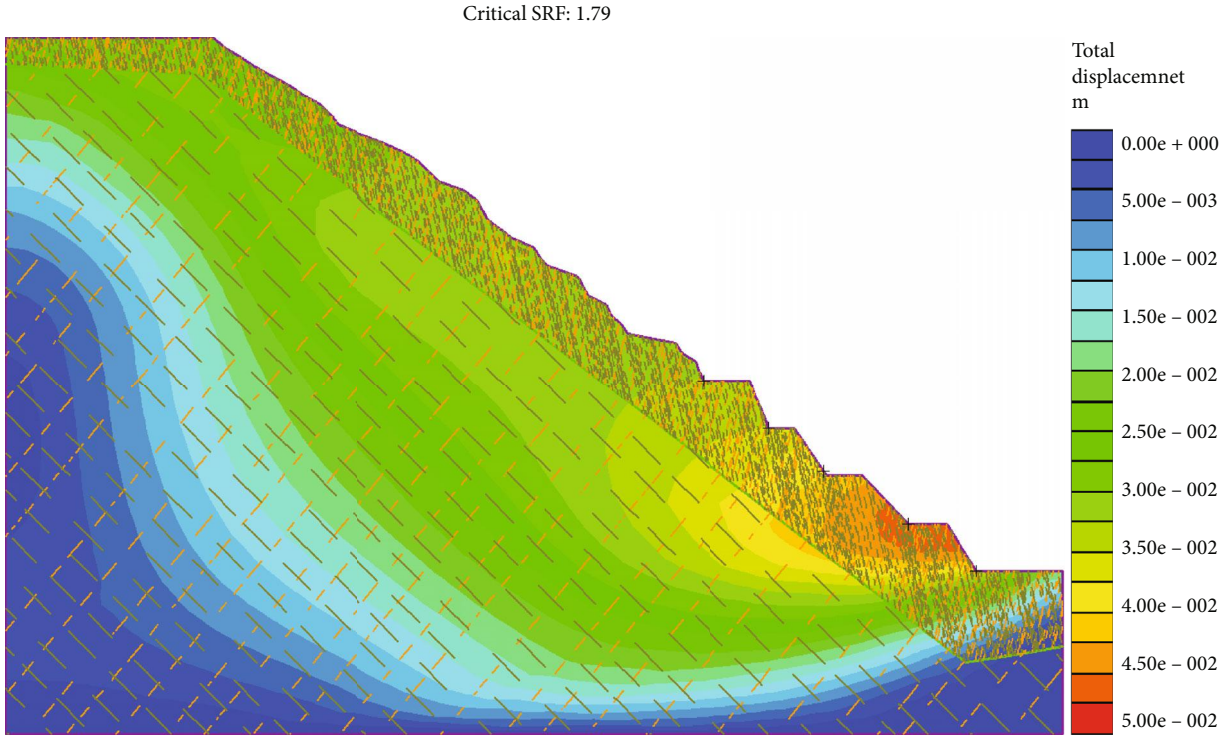

(b) Cloud chart of total displacement for 20 times of the freeze-thaw cycle

Figure 15: Continued.

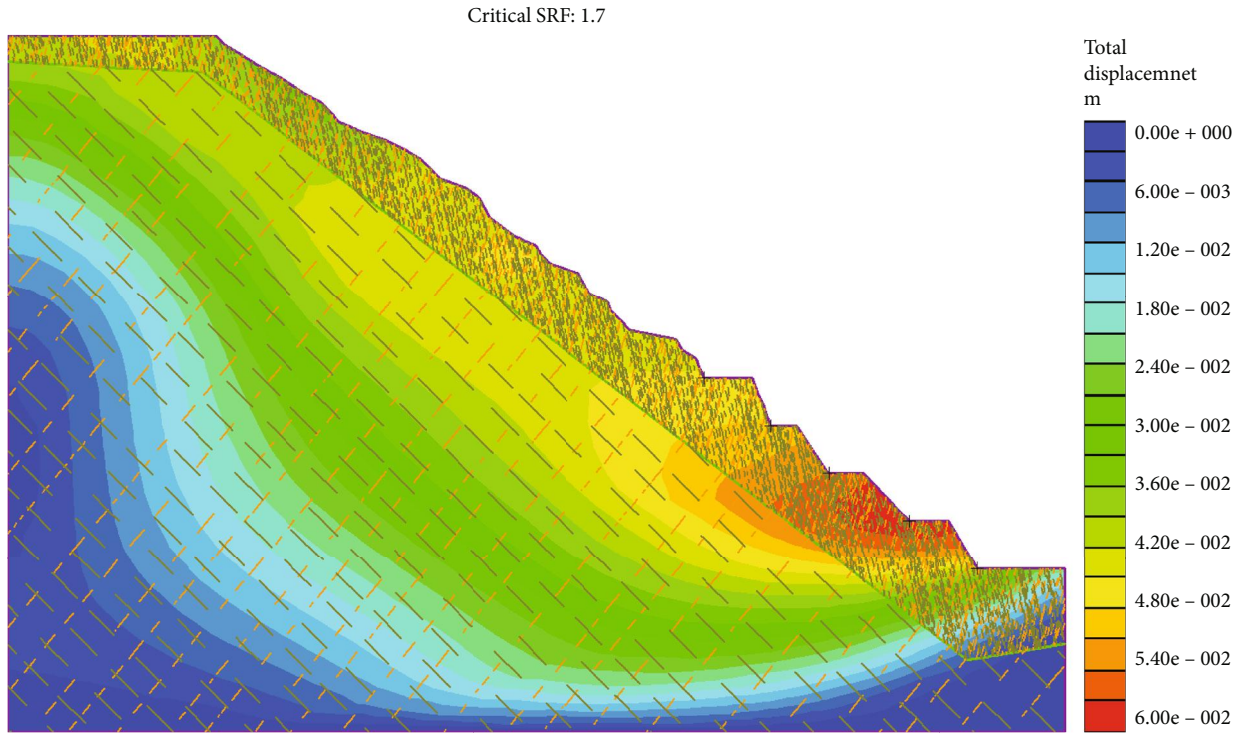

(c) Cloud chart of total displacement for 40 times of the freeze-thaw cycle

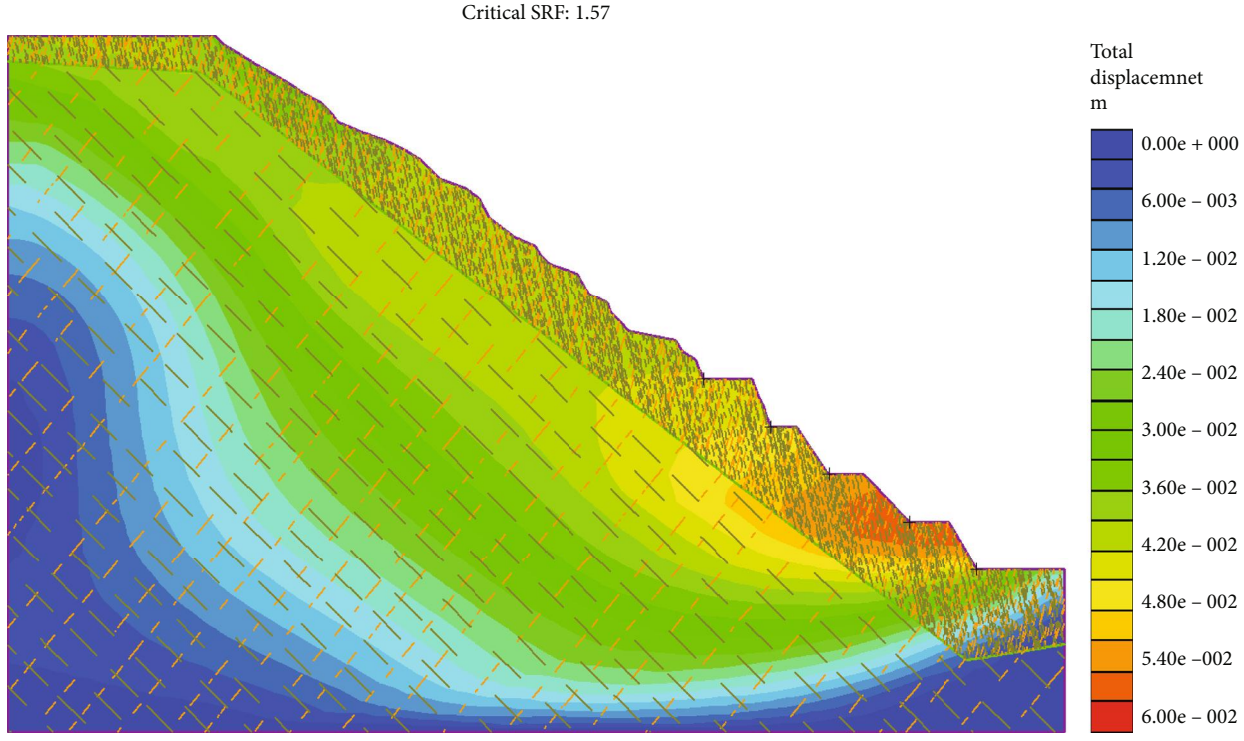

(d) Cloud chart of total displacement for 60 times of the freeze-thaw cycle

Figure 15: Continued.

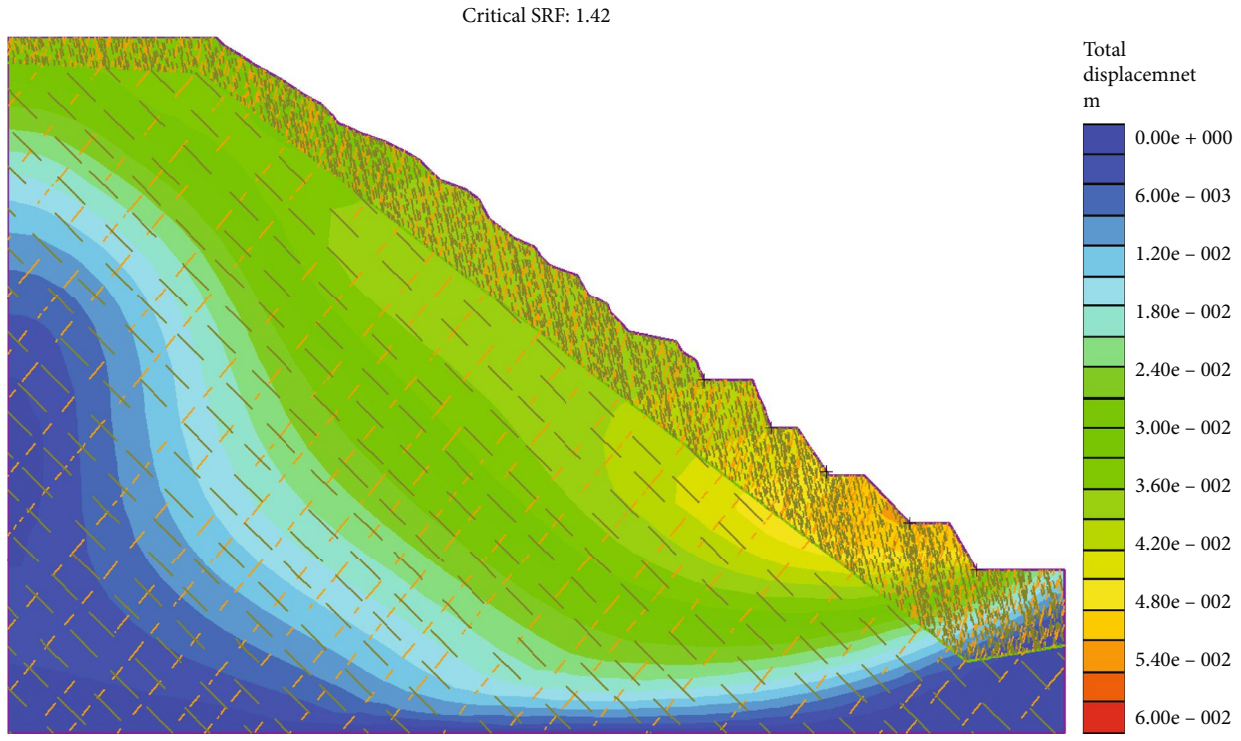

(e) Cloud chart of total displacement for 80 times of the freeze-thaw cycle

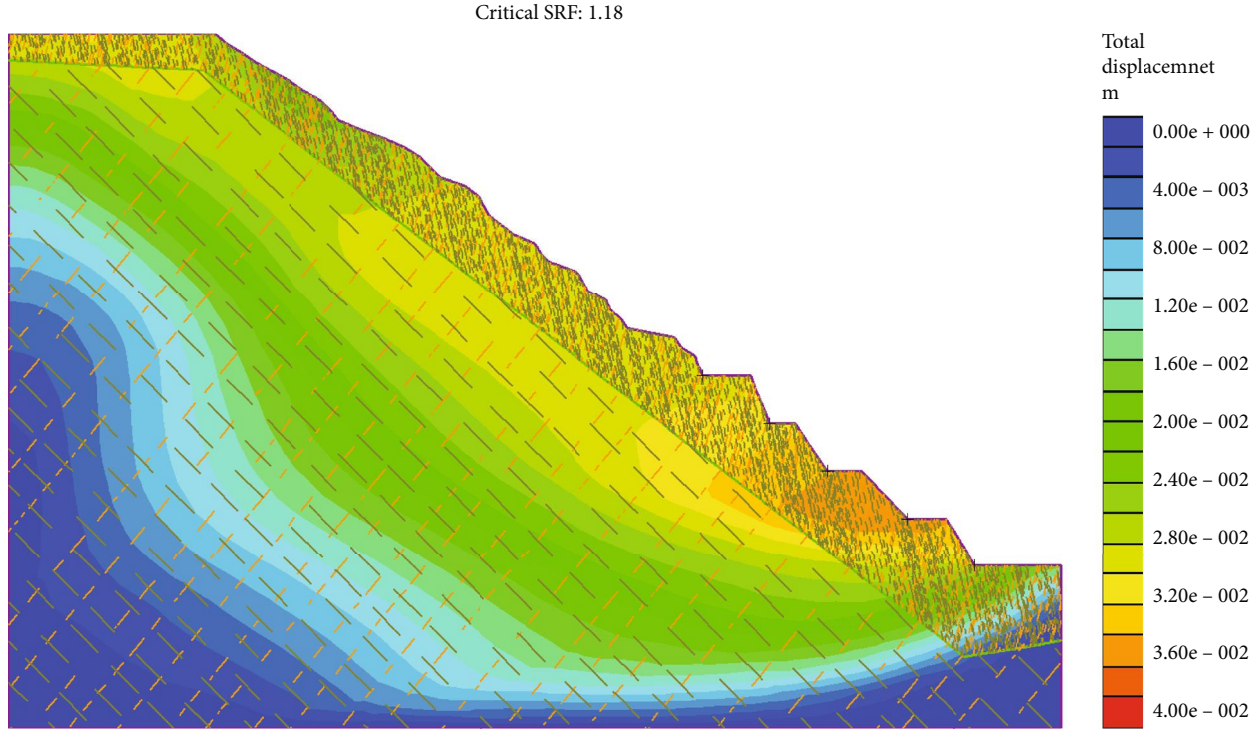

(f) Cloud chart of total displacement for 100 times of the freeze-thaw cycle

Figure 15: Cloud chart of total displacement for different times of the freeze-thaw cycle.

order to clearly reflect the changes of the number of yield elements and yield joints, the curves of the number of yield elements and yield joints of the slope with the times of the freeze-thaw cycle are drawn, as shown in Figure 17. They all increase gradually with the increase of the times of the freeze-thaw cycle, and the increasing rate increases first and then decreases.

3.2.4. Analysis of Horizontal Displacement and Strength Reduction Times of Nodes. Figure 12 shows the positions of

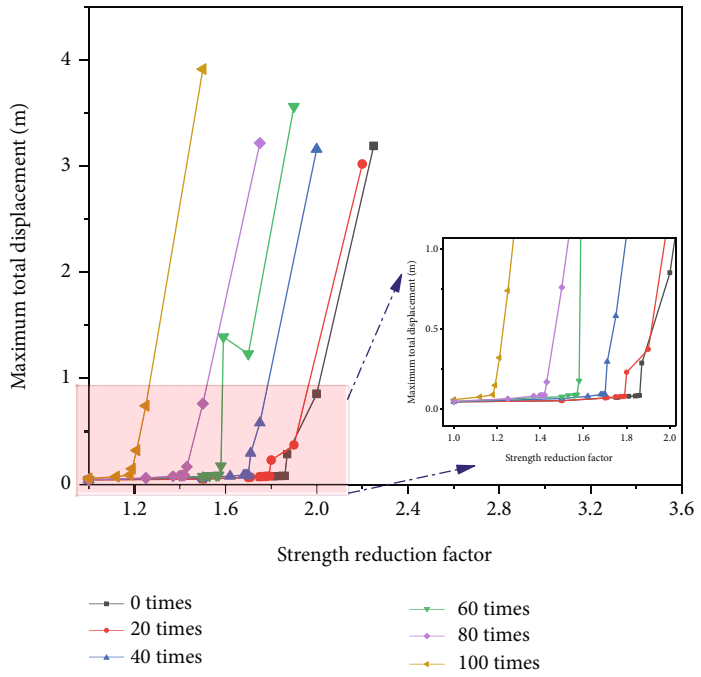

Figure 16: Relationship between strength reduction factor and maximum total displacement of slope under different times of the freeze-thaw cycle.

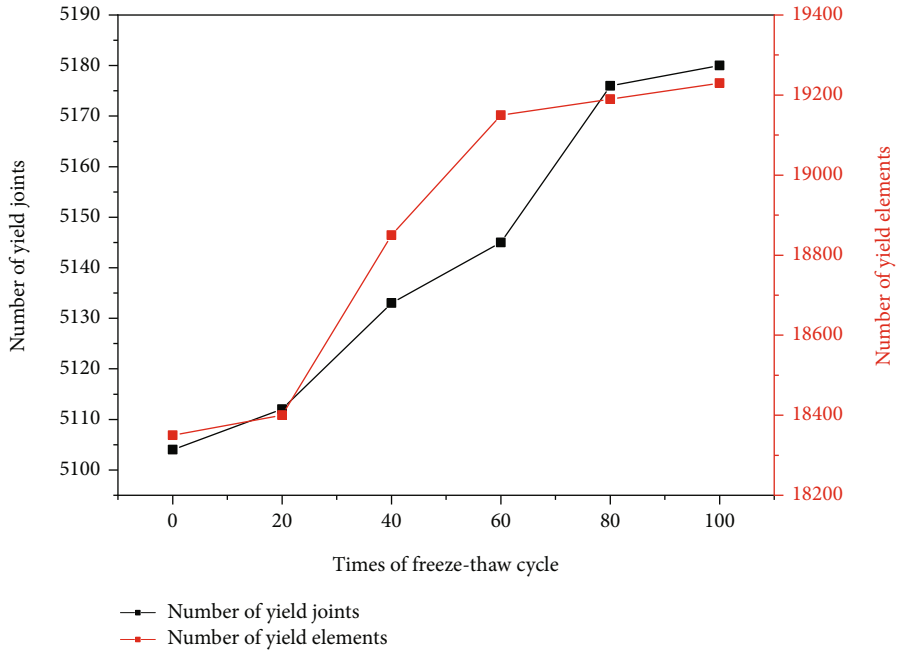

Figure 17: Number of yield elements and yield joints of slope surface.

the five selected nodes in the slope model. By analyzing the relationship between the horizontal displacement and the reduction times of each node under different times of the freeze-thaw cycle, we can further understand the instability and failure of the slope. It can be seen from Figure 18 that the horizontal displacement of the node changes slightly at the beginning, and then, the displacement changes abruptly, indicating that the slope has undergone obvious instability and failure. From node 5 to node 1, the height of the node decreases, and the horizontal displacement of the node also decreases gradually. In addition, the total displacement change of each node and the number of stages corresponding to the mutation decrease gradually with the increase of the times of the freeze-thaw cycle. This result shows that the failure occurs gradually in advance and the slope stability becomes worse.

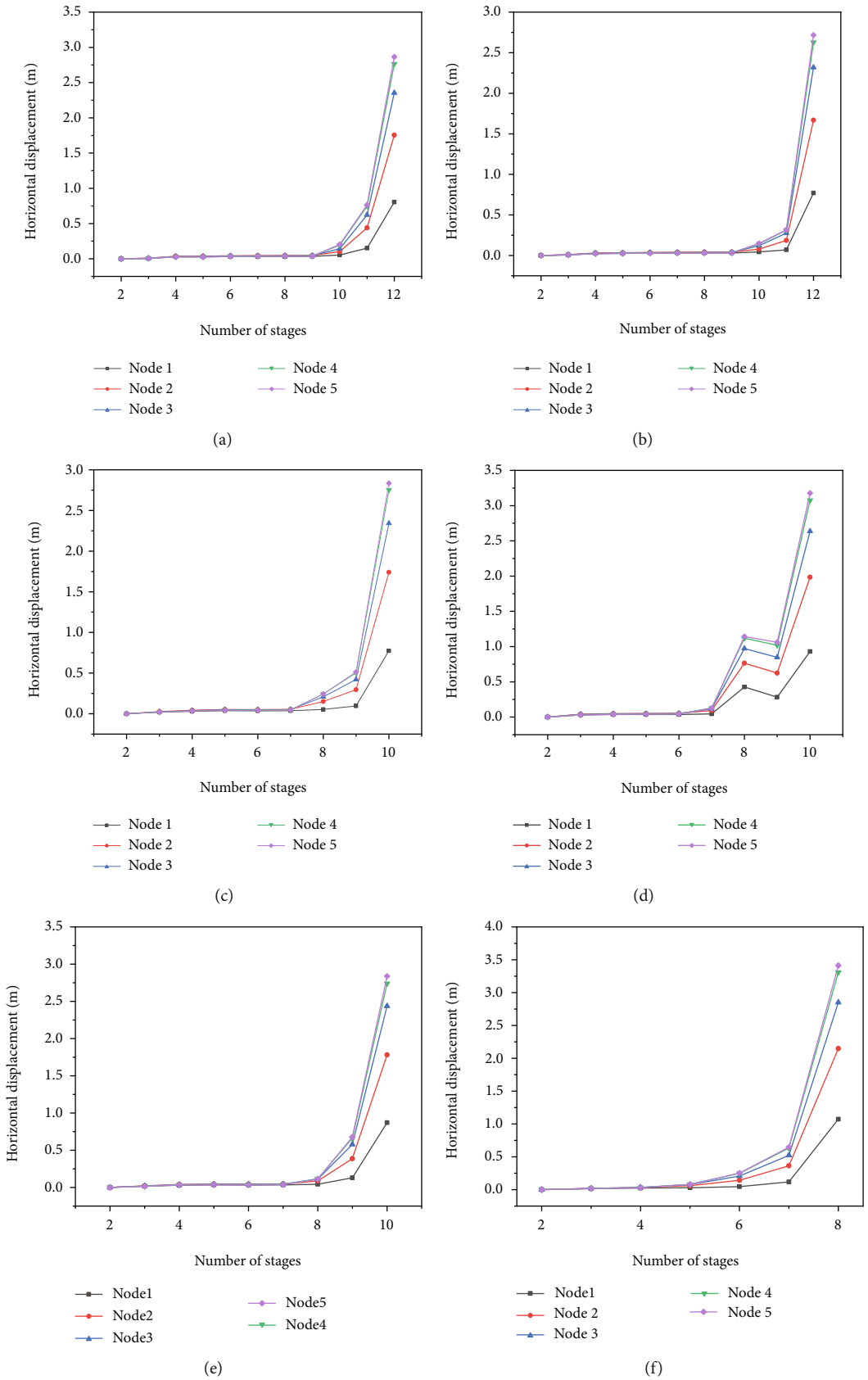

Figure 18: Horizontal displacement curve of each point under different times of the freeze-thaw cycle ((a–f) The times of the freeze-thaw cycle are 0, 20, 40, 60, 80, and 100, respectively).

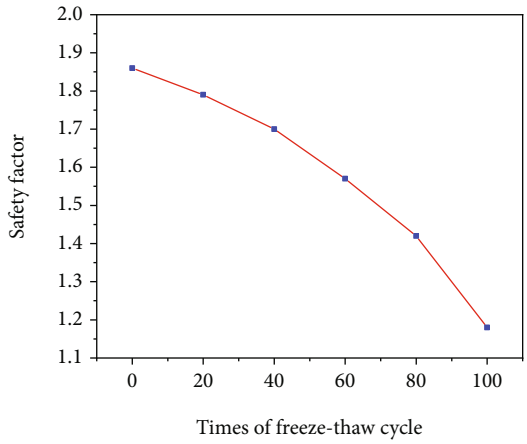

Figure 19: Relationship between safety factor and times of the freeze-thaw cycle.

3.2.5. Analysis of Safety Factor of Slope Model. According to the above analysis, when the times of the freeze-thaw cycle are 0, 20, 40, 60, 80, and 100, the safety factors of the slope are 1.86, 1.79, 1.7, 1.57, 1.42, and 1.18, respectively, and the safety factors are getting smaller and smaller. At the same time, it is found that the reduction ranges of the safety factor are 3.76%, 5.03%, 7.65%, 9.55%, and 16.9%, respectively. The gradually increasing reduction range further shows that the more freeze-thaw cycle, the worse the slope stability. This law can also be found from the trend of the curve in Figure 19. This is because the pore water in the rock mass freezes to form frost heaving force, and the volume expansion leads to the further development of joint fissures. With the increase of the freeze-thaw cycle, the strength of rock slope decreases gradually. Freeze-thaw fatigue damage reduces the physical and mechanical properties of rock, and rock and joints are more prone to yield instability. Therefore, we can understand the freeze-thaw mechanism of rock slope as the cumulative process of rock freeze-thaw damage.

4. Conclusions

In this paper, the influence of the freeze-thaw cycle on the slope stability of an open pit mine is studied with the help of 3D laser scanning technology and RS2 finite element software. The following three conclusions are obtained:

(1) For the point cloud data obtained by 3D laser scanning, firstly, the 3D difference method is used for grid processing. After selecting the discrimination index, all nodes are scanned for flatness detection. After the data is simplified, the improved image segmentation algorithm is used to complete the regional division of the structural plane, and the reasonable flatness detection threshold, regional growth threshold, and area threshold are selected to complete the intelligent recognition of rock mass structural plane

(2) The geometric parameters and other information of rock mass discontinuity are extracted, the plane equation of rock mass discontinuity is fitted by the least square method, and the dip angle of rock mass discontinuity is calculated. The structural plane is divided by *K*-means cluster analysis method based on occurrence information, and the spacing and equivalent trace length of structural plane are calculated. The calculation results are basically consistent with the actual investigation of the mining area

(3) According to the mechanical parameters obtained from the freeze-thaw cyclic test and the distribution of joint surfaces measured by 3D laser scanning technology, the slope mechanical model is established. The finite element strength reduction method is used to numerically simulate and analyze the slope structural plane, and the safety factor of the slope under different times of the freeze-thaw cycle is calculated. The results show that with the increase of the freeze-thaw cycle, the principal stress, volume strain, and displacement gradually increase. The number of yield elements and yield joints increases gradually, the safety factor decreases continuously, and the stability of the slope becomes worse, which shows that the rocks in high-altitude mining areas are in a freeze-thaw cycle all year round. The freeze-thaw fatigue damage degrades the physical and mechanical properties of rocks, and the rocks and joints are more prone to yield instability

Data Availability

The experimental data used to support the findings of this study are included within the article.

Conflicts of Interest

The authors declare no conflict of interest.

Authors' Contributions

Juzhou Li performed experiments and data analysis. Changhong Li and Guoqing Li did the methodology and conceptualization. Yongyue Hu and Xuefeng Yi did the visualization and data curation and acquired resources. Yu Wang did the supervision, funding acquisition, and project administration;

Acknowledgments

This study was supported by the National Natural Science Foundation of China (52174069), Beijing Natural Science Foundation (8202033), and National Key Technologies Research & Development Program (2018YFC0808402).

References

[1] F. Gu and H. Xie, "Status and development trend of 3D laser scanning technology in the mining field," in *Proceedings Of The 2013 The International Conference On Remote Sensing, Environment And Transportation Engineering (Rsete 2013)*, vol. 31, pp. 407–410, Nanjing, China, 2013.

[2] Y. G. Qin, Z. Q. Luo, W. Wang, and K. H. Zheng, "Cavity 3D Laser Scanning Point Cloud Data Processing Technology," *Journal of Northeastern University (Natural Science)*, vol. 37, no. 11, pp. 1635–1639, 2016.

[3] Y. Wang, X. Yi, J. Han, and Y. Xia, "Acoustic emission and computed tomography investigation on fatigue failure of fissure-contained hollow-cylinder granite: cavity diameter effect," *Fatigue & Fracture of Engineering Materials & Structures*, vol. 45, no. 8, pp. 2243–2260, 2022.

[4] Z. G. Tao, Q. Geng, C. Zhu et al., "The mechanical mechanisms of large-scale toppling failure for counter-inclined rock slopes," *Journal of Geophysics and Engineering*, vol. 16, no. 3, pp. 541–558, 2019.

[5] Q. Wang, S. Xu, M. He, B. Jiang, H. Wei, and Y. Wang, "Dynamic mechanical characteristics and application of constant resistance energy-absorbing supporting material," *International Journal of Mining Science and Technology*, vol. 32, no. 3, pp. 447–458, 2022.

[6] Y. Wang, J. Z. Li, C. Zhu, and T. Mao, "Fatigue failure identification using deformation and energy rate for hole-fissure contained granite under freeze–thaw and variable-frequency–variable-amplitude cyclic loads," *Fatigue & Fracture of Engineering Materials & Structures*, vol. 45, no. 3, pp. 834–851, 2022.

[7] F. Tonon and J. T. Kottenstette, *Laser and photogrammetric methods for rock face characterization*, American Rock Mechanics Association, 2007.

[8] M. Lato, M. S. Diederichs, D. J. Hutchinson, and R. Harrap, "Optimization of LiDAR scanning and processing for automated structural evaluation of discontinuities in rockmasses," *International Journal of Rock Mechanics and Mining Sciences*, vol. 46, no. 1, pp. 194–199, 2009.

[9] M. Vöge, M. J. Lato, and M. S. Diederichs, "Automated rockmass discontinuity mapping from 3-dimensional surface data," *Engineering Geology*, vol. 164, pp. 155–162, 2013.

[10] R. Fanti, G. Gigli, L. Lombardi, D. Tapete, and P. Canuti, "Terrestrial laser scanning for rockfall stability analysis in the cultural heritage site of Pitigliano (Italy)," *Landslides*, vol. 10, no. 4, pp. 409–420, 2013.

[11] W. Kociuba, W. Kubisz, and P. Zagórski, "Use of terrestrial laser scanning (TLS) for monitoring and modelling of geomorphic processes and phenomena at a small and medium spatial scale in Polar environment (Scott River – Spitsbergen)," *Geomorphology*, vol. 212, pp. 84–96, 2014.

[12] A. M. Ferrero, G. Forlani, R. Roncella, and H. I. Voyat, "Advanced geostructural survey methods applied to rock mass characterization," *Rock Mechanics and Rock Engineering*, vol. 42, no. 4, pp. 631–665, 2009.

[13] G. Umili, A. Ferrero, and H. H. Einstein, "A new method for automatic discontinuity traces sampling on rock mass 3D model," *Computational Geosciences*, vol. 51, pp. 182–192, 2013.

[14] S. Chen, M. L. Walske, and I. J. Davies, "Rapid mapping and analysing rock mass discontinuities with 3D terrestrial laser scanning in the underground excavation," *International Journal of Rock Mechanics and Mining Sciences*, vol. 110, pp. 28–35, 2018.

[15] Y. Z. Wang, W. L. Tu, and H. Li, "Fragmentation calculation method for blast muck piles in open–pit copper mines based on three-dimensional laser point cloud data," *International Journal of Applied Earth Observations and Geoinformation*, vol. 100, article 102338, 2021.

[16] R. A. Kromer, A. Abellán, D. J. Hutchinson et al., "Automated terrestrial laser scanning with near-real-time change detection – monitoring of the Séchilienne landslide," *Earth Surface Dynamics*, vol. 5, no. 2, pp. 293–310, 2017.

[17] J. Ma, H. M. Tang, X. L. Hu, R. Yong, H. Xia, and Y. J. Song, "Application of 3D laser scanning technology to landslide physical model test," *Rock and Soil Mechanics*, vol. 35, no. 5, pp. 1495–1505, 2014.

[18] Y. Wang, J. Han, Y. Xia, and D. Long, "New insights into the fracture evolution and instability warning predication for fissure-contained hollow-cylinder granite with different hole diameter under multi-stage cyclic loads," *Theoretical and Applied Fracture Mechanics*, vol. 119, article 103363, 2022.

[19] L. C. Pereira and M. S. Lana, "Stress–strain analysis of buckling failure in phyllite slopes," *Geotechnical & Geological Engineering*, vol. 31, no. 1, pp. 297–314, 2013.

[20] W. Liu, "Experimental and numerical study of rock stratum movement characteristics in longwall mining," *Shock and Vibration*, vol. 2019, Article ID 5041536, 15 pages, 2019.

[21] C. H. C. Silva and M. S. Lana, "Numerical modeling of buckling failure in a mine slope," *Rem: Revista Escola de Minas*, vol. 67, no. 1, pp. 81–86, 2014.

[22] A. T. Arslan, B. Kahraman, M. K. Özfırat, T. Frühwirt, K. Yıldızdağ, and H. Köse, "A parametric study using numerical modelling to assess the stability of marble quarries," *Procedia Engineering*, vol. 191, pp. 646–655, 2017.

[23] K. Adach-Pawelus, "Application of seismic monitoring and numerical modelling in the assessment of possibility of seismic event occurrence in the vicinity of ore remnant," *IOP Conference Series–Earth and Environmental Science*, vol. 221, article 012095, 2019.

[24] Y. Wang, Z. Y. Song, T. Q. Mao, and C. Zhu, "Macro–meso fracture and instability behaviors of hollow-cylinder granite containing fissures subjected to freeze–thaw–fatigue loads," *Rock Mechanics and Rock Engineering*, vol. 55, no. 7, pp. 4051–4071, 2022.

Hindawi
Geofluids
Volume 2022, Article ID 3644147, 12 pages
https://doi.org/10.1155/2022/3644147

Research Article

Analysis of Surrounding Rock Pressure of Deep Buried Tunnel considering the Influence of Seepage

Qingchen Yao,[1] **Yukun Ma**,[2] **Zongyang Xiao**,[1] **Zudi Zhang**,[1] **Yaxin Lu**,[3] **and Chenyang Liu**[4]

[1]*Key Laboratory of Transportation Tunnel Engineering, Ministry of Education, Southwest Jiaotong University, Chengdu 610000, China*
[2]*Research Center of Geotechnical and Structural Engineering, Shandong University, Jinan 250061, China*
[3]*Key Laboratory of Transportation Tunnel Engineering, Southwest Petroleum University, Chengdu 610000, China*
[4]*College of Construction and Engineering, Jilin University, Changchun 130000, China*

Correspondence should be addressed to Qingchen Yao; yqc534149384@my.swjtu.edu.cn
and Chenyang Liu; chenyangl19@mails.jlu.edu.cn

Received 11 March 2022; Revised 6 May 2022; Accepted 10 May 2022; Published 20 July 2022

Academic Editor: Long Yan

This paper takes the surrounding rock of deep tunnel as the research object and considers the action mechanism under the influence of seepage. Based on the Mohr-Coulomb criterion, the stress mechanism of surrounding rock of deep buried tunnel is analyzed by a convergence constraint method. Based on the elastic-plastic solution, the nonlinear elastic-plastic solution of the interaction between surrounding rock and lining structure considering the effect of seepage force is proposed, and the radius of surrounding rock plastic zone is obtained. The relationship between surrounding rock stress and displacement, radial deformation of lining, and support reaction force was observed. At the same time, considering the effects of seepage, strain softening, and intermediate principal stress, the surrounding rock is divided into a plastic residual zone, plastic softening zone, and elastic zone, and the stress distribution expressions of the plastic zone and each zone of surrounding rock of circular tunnel are derived. The results show that with the change of nonuniform permeability coefficient, the seepage shows anisotropy in different directions, and the closer to the horizontal or vertical direction, the more obvious the influence of nonuniform permeability coefficient on pore water pressure distribution. Seepage and material softening have different effects on the distribution of surrounding rock stress field and the size of plastic zone. Material softening is more unfavorable to the stability of surrounding rock than seepage. The intermediate principal stress coefficient has a significant impact on the tangential stress and plastic zone of surrounding rock. When the intermediate principal stress effect is not considered, the calculation results are relatively conservative and cannot give full play to the strength of surrounding rock effectively. The research conclusion can provide a theoretical reference for studying the stability of surrounding rock in tunnel excavation under water-bearing rock.

1. Introduction

With the rapid development of economy, domestic infrastructure construction is in full swing, and all kinds of transportation are gradually expanding to remote mountain areas. As one of the key points of traffic construction, tunnel can give full play to the characteristics of high rock compressive strength when crossing mountainous areas, so it has been widely used [1–4]. However, the change of stress and displacement of tunnel surrounding rock caused by the coupling of seepage field and stress field after tunnel excavation and the interaction between surrounding rock and lining are unavoidable problems in current tunnel construction. During tunnel excavation under water-rich conditions [5–7], the tunnel is mainly affected by water in two aspects. One is that the existence of water reduces the mechanical

parameters of rock mass and changes the strength of rock mass. On the other hand, the tunnel excavation leads to the redistribution of surrounding rock seepage field and changes the pore water pressure. The coupling between the two fields of the stress field and seepage field is the key reason for aggravating formation deformation. Therefore, considering the influence of seepage, the research on the stress and stress distribution of surrounding rock of deep tunnel has become a hot spot in academic and engineering circles.

On the stress and displacement of tunnel surrounding rock, some scholars mainly use elastic-plastic constitutive to analyze such problems. The main research methods include theoretical analysis method [6–15] and numerical simulation method [16–20]. In terms of theoretical analytical method, Liu et al. [6] substituted the Hoek-Brown criterion into the equilibrium differential equation considering the influence of seepage volume force to solve it. By solving the transcendental equation, the numerical solution of stress around the tunnel in the plastic zone and the numerical solution of rock mass stress in the elastic zone are obtained; Liu et al. [7] applied the seepage force to the stress field in the form of volume force without considering the lining and obtained the analytical expressions of elastic displacement and stress and then applied the Mohr-Coulomb yield criterion to obtain the analytical expressions of plastic stress and plastic radius; Lee and Pietyuszczak [8] used a simplified numerical method to calculate the stress and displacement distribution of circular caverns in Mohr-Coulomb and Hoek-Brown surrounding rock media considering strain softening. In terms of numerical simulation, Dou et al. [16] set the surrounding rock and lining as elastic-plastic materials and gave the calculation method of safety factor of tunnel surrounding rock, primary support, and secondary lining by using the method of limit analysis; Wu et al. [17] used the analysis program based on the rock elastic-plastic stress seepage damage coupling model, used the coupling model to inverse the damage parameters according to the field monitoring displacement, and then analyzed the distribution law of the tunnel surrounding rock stress field, seepage field, damage field, and stress characteristics of lining structure. On the other hand, there are many achievements in the research on the interaction between displacement and lining [21]. Based on Drucker-Prager yield criterion, Wang et al. [21] deduced the elastic-plastic analytical solution of the interaction between surrounding rock and lining structure under the influence of seepage effect and expounded the application of the above analytical results in determining the load of lining structure; Wu et al. [22] used the Mohr-Coulomb yield criterion and bilinear constitutive model to put forward the analytical expression of elastic-plastic solution of interaction system between surrounding rock and lining in deep buried circular roadway under generalized load; Zhu et al. [23] analyzed and studied the bearing water pressure of railway tunnel composite lining by the finite element method with the help of a load structure model.

In recent years, many scholars have studied on the basis of the classical elastic-plastic solution of the tunnel and deduced the tunnel elastic-plastic solution considering the influence of the seepage field. In Reference [7], by simplifying the deep buried circular tunnel and solving it by using the Mohr-Coulomb strength criterion, the analytical solution of surrounding rock stress considering seepage field is obtained, and the influence of seepage field on surrounding rock stress is discussed. In Reference [24], based on the study of reference [7], the stress adjustment coefficient is introduced to obtain the elastic-plastic analytical solution of deep buried circular permeable tunnel considering the influence of in situ stress redistribution. In Reference [24], the theoretical solution of the stability of roadway surrounding rock is derived by using the theory of elastic-plastic damage mechanics. By summarizing four rock strength criteria including the Mohr-Coulomb criterion and Hoek-Brown criterion, literature [25] obtains the unified form of the surrounding rock yield equation under plane strain. On this basis, the unified solutions of surrounding rock stress field and displacement field under seepage are derived. Reference [6] improved the elastoplastic stress solution of surrounding rock derived based on Hoek-Brown criterion so that it does not contain integral term. It can be seen that most scholars choose the Mohr-Coulomb criterion [24] and Hoek-Brown criterion [26] without considering the intermediate principal stress in the elastic-plastic calculation and analysis of surrounding rock, resulting in conservative calculation results. In the past, isotropic calculation was mostly used in the calculation of the seepage field; that is, the permeability coefficients in all directions were equal. This is different from the engineering practice. Only by mastering the distribution law of surrounding rock seepage field after tunnel excavation can we analyze the influence of seepage on surrounding rock stress and plastic zone.

On the basis of previous studies, based on the unified strength theory criterion and considering the effects of strain softening, seepage, and intermediate principal stress, this paper divides the tunnel surrounding rock considering the influence of seepage into plastic residual zone, plastic softening zone, and elastic zone, deduces the analytical expressions of stress and half diameter of each zone of surrounding rock, and considers the differences of permeability coefficients in horizontal and vertical directions. By defining the nonuniform permeability coefficient, its influence on the distribution law of pore water pressure in all directions of surrounding rock is analyzed. Finally, an example is given to analyze the effects of surrounding rock softening, seepage, and intermediate principal stress coefficient on the tangential stress and plastic zone radius of the tunnel. The research results can provide reference for further study on the stability of surrounding rock in tunnel excavation under water-bearing rock.

2. Analysis of Surrounding Rock Pressure and Displacement considering Seepage

2.1. Basic Assumptions and Mechanical Models. After the tunnel is excavated in water-rich mountain area, the surrounding rock and lining structure near the tunnel will be

affected by seepage force. According to the basic theory of seepage mechanics, the seepage water pressure after tunnel excavation and seepage stability is calculated as the boundary condition for the analysis of the interaction between surrounding rock and lining structure under the influence of equivalent seepage effect. In order to facilitate the subsequent calculation, the following assumptions and simplifications are made of the characteristics of seepage in high head mountain tunnel and the theory of plastic mechanics:

(1) The tunnel is deeply buried and the excavation surface is circular

(2) The surrounding rock is isotropic, homogeneous, and continuous ideal elastic-plastic medium

(3) Lateral pressure coefficient of rock around tunnel is 1, and the tunnel bears equal pressure in all directions

(4) Groundwater is incompressible, and obey the seepage law under a steady state

(5) Because of the axial length of the tunnel, the value of the transverse dimension is very large, ignoring the influence of both ends of the tunnel; the tunnel is simplified as a plane strain problem

Based on the above assumptions, the analysis model of tunnel surrounding rock and lining seepage field is determined as shown in Figure 1 (the circular area from inside to outside in the figure is lining and surrounding rock, respectively; the circle with a distance of R from the center of the tunnel is the far-field seepage boundary, and its stable seepage head is H (corresponding water pressure is p_{w0})). The inner diameter of tunnel lining is r_0, and the outer diameter is r_1. In addition, the permeability coefficients of surrounding rock and lining are k_r and k_l, respectively.

2.2. Analysis of Steady Seepage Field. The seepage flow Q at each position of surrounding rock and lining has the following relationship with seepage water pressure:

$$Q = \frac{2k\pi r dp_w}{\gamma_w dr}, \tag{1}$$

where k is the permeability coefficient of surrounding rock or lining at the calculated section; r is the radius of any surrounding rock or lining circular section with the tunnel center as the center; γ_w is the gravity of water; and p_w is the seepage water pressure.

The boundary conditions of equation (1) include the following: on the inner and outer diameter of tunnel lining, when $r = r_0$, the seepage water pressure $p_w = 0$; when $r = r_1$, seepage water pressure $p_w = p_{w1}$. At the far-field seepage stability radius ($r = R$), the seepage water pressure $p_w = p_{w0}$. The continuity condition is as follows: assuming that the seepage flow at a radius section of surrounding rock is Q_r and the seepage flow at a radius section of lining is Q_1, considering that the tunnel lining and surrounding rock

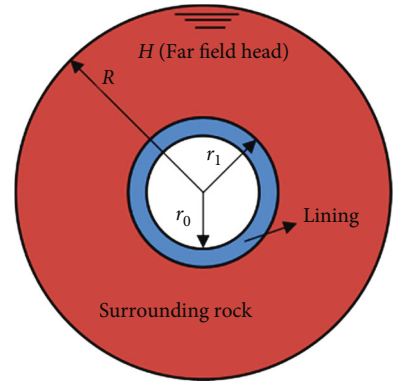

Figure 1: Tunnel seepage model.

are in a stable seepage field, the seepage flow at the junction of surrounding rock and lining is continuous; that is, when $r = r_1$, $Q_r = Q_1$.

By solving equation (1) with boundary conditions and continuity conditions, the expression of seepage water pressure p_w at any radius of lining and surrounding rock can be obtained:

$$P_w \begin{cases} P_{w0} = \dfrac{kr\ \ln(r/r_0)}{k1\ln(R/r_1) + kr\ln(r_1/r0)}, & r_0 \leqslant r \leqslant r,_1 \\ P_{w0} = \dfrac{kr\ \ln(r_1/r_0) + k1\ln(r/r_1)}{k1\ln(R/r_1) + kr\ln(r_1/r0)}, & r_1 \leqslant r \leqslant R. \end{cases} \tag{2}$$

Equation (2) is the seepage water pressure state after the tunnel seepage is in a stable state.

2.3. Theoretical Analysis of Stress and Displacement. The initial equilibrium of surrounding rock is disturbed by tunnel excavation. Due to the change of seepage state and in situ stress, the stress state around the tunnel will also change. Some surrounding rock will undergo nonlinear plastic deformation, not just elastic deformation. Displacement and stress of rock around tunnel such deep buried tunnel are suitable to be analyzed by elastic-plastic constitutive law.

2.3.1. Elastoplastic Mechanical Analysis Model. Based on the assumption, the elastic-plastic analysis model of tunnel surrounding rock is made, as shown in Figure 2. The inner diameter and outer diameter of tunnel lining are r_0 and r_1, respectively. The seepage water pressure at the far-field stable seepage is p_{w0}, the support reaction force of lining on surrounding rock after lining is applied is p_1, and the surrounding rock pressure uniformly distributed around the tunnel is q. Under the combined action of surrounding rock pressure, seepage water pressure, and support reaction force, the surrounding rock adjacent to the tunnel produces plastic deformation. The outer radius of the plastic zone is R_p, and the surrounding rock outside the plastic zone is still elastic. Take the rock mass element at any point a on the

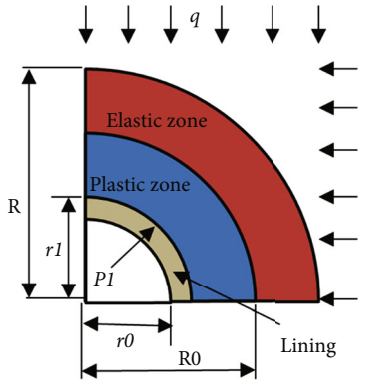

Figure 2: Elastoplastic analysis model.

surrounding rock in Figure 2 for stress analysis. The stress balance equation of point A is

$$\frac{d\sigma_r}{dr} + \frac{\sigma_r - \sigma_\theta}{r} - \beta\frac{dp_w}{dr} = 0, \tag{3}$$

where r is the distance from point A to the center of the tunnel; p_w is the seepage water pressure; and β refers to the reduction coefficient of seepage water pressure caused by fluid stress coupling during construction, and its value is related to the porosity of the material. For concrete, the value is generally 2/31, and for rock close to failure, the value is close to 1. If there is no special description in this paper, the value is 5/6 according to the actual project; σ_r is the circumferential effective stress, and σ_θ takes the tensile stress as positive and the compressive stress as negative. The stresses not specified below refer to the effective stress.

2.3.2. Stress Analysis of Surrounding Rock

(1) Analysis of the plastic zone of surrounding rock

Under the joint action of surrounding rock pressure, seepage water pressure, and support reaction force, part of the surrounding rock enters the plastic state, which is in the annular area between the lining and the radius R_p. After yielding, the rock mass in this area meets the Mohr-Coulomb criterion, that is:

$$\sigma_\theta^p = \frac{1+\sin\varphi}{1-\sin\varphi}\sigma_r^p + \frac{2c\cos\varphi}{1-\sin\varphi}, \tag{4}$$

where σ_θ^p and σ_r^p are the radial effective stress and circumferential effective stress of the plastic zone element, respectively; c is the cohesion of rock mass; and φ is the friction angle in the rock body.

Substituting equations (2) and (4) into the equilibrium equation (3), the first-order nonlinear differential equation is obtained and solved with reference to [8].

$$\sigma_\theta^p = \frac{1+\sin\varphi}{1-\sin\varphi}(B-p_1)\left(\frac{r}{r_1}\right)^{2\sin\varphi/(1-\sin\varphi)} - \frac{B(1+\sin\varphi)}{1-\sin\varphi} + \frac{2\cos\varphi}{1-\sin\varphi}. \tag{5}$$

(2) Elastic zone analysis of surrounding rock

It is assumed that the radius at the junction of the plastic zone and elastic zone of surrounding rock is R_p, and the radial stress of rock mass at this location is σ_{RP}. The elastic zone of surrounding rock of deep buried tunnel is regarded as a thick walled cylinder, and the earth pressure q and internal stress in the elastic zone can be expressed by Kirsch formula stress state of the elastic zone under σ_{RP}:

$$\sigma_r^E = \frac{R_p^2}{r^2}\sigma_{RP} + \frac{-q}{2}\left[(1+\lambda)\left(1-\frac{R_p^2}{r^2}\right) + (1-\lambda)\left(1-\frac{4R_p^2}{r^2}+\frac{3R_P^4}{r^4}\right)\cos 2\theta\right], \tag{6}$$

$$\sigma_\theta^E = -\frac{R_p^2}{r^2}\sigma_{RP} + \frac{-q}{2}\left[(1+\lambda)\left(1+\frac{R_p^2}{r^2}\right) + (1-\lambda)\left(1+\frac{3R_P^4}{r^4}\right)\cos 2\theta\right]. \tag{7}$$

In formulas (13)–(14), σ_r^E and σ_θ^E are the total radial stress and total circumferential stress of surrounding rock in the elastic zone, respectively; q is the surrounding rock pressure; λ is the lateral pressure coefficient; and θ is the angle between the calculated point and the tunnel center line and the vertical direction.

In this paper, the stresses under various equal pressure conditions are considered, so the lateral pressure coefficient λ takes 1. At the same time, considering the influence of seepage water pressure, it can be simplified as follows:

$$\sigma_r^E = -q\left(1-\frac{R_p^2}{r^2}\right) + \frac{R_p^2}{r^2}\sigma_{RP} + \beta p_w, \tag{8}$$

$$\sigma_\theta^E = -q\left(1+\frac{R_p^2}{r^2}\right) - \frac{R_p^2}{r^2}\sigma_{RP} + \beta p_w. \tag{9}$$

(3) Analysis of the plastic radius of surrounding rock

According to the stress continuity condition of surrounding rock at the elastic-plastic boundary ($r = R_p$),

on the elastic-plastic boundary of surrounding rock, there are

$$\sigma_r^P + \sigma_\theta^P = \sigma_r^E + \sigma_\theta^E. \tag{10}$$

According to the calculation and simplification in Reference [14], the following can be obtained:

$$p_1 = B + \left(\frac{r_1}{R_p}\right)^{2\sin\varphi/(1-\sin\varphi)} (1-\sin\varphi) \cdot \left(q + \frac{c\cos\varphi}{1-\sin\varphi} + \frac{B}{1-\sin\varphi}\right), \tag{11}$$

$$R_p = \frac{r_1}{[(p_1 - B)/(q(1-\sin\varphi) + c\cos\varphi + B)]^{(91-\sin\varphi)/2\sin\varphi}}. \tag{12}$$

The relationship between support reaction force and surrounding rock plastic radius under different rock mass parameters and seepage conditions can be obtained from equations (11) and (12).

(4) Displacement analysis of surrounding rock

After the tunn5el is excavated and lined, the initial in situ stress and seepage field of surrounding rock will change, resulting in displacement and deformation of rock mass. The displacement of surrounding rock is divided into elastic zone displacement and plastic zone displacement.

In the elastic zone of surrounding rock, according to the theory of elasticity, the displacement of rock mass is

$$\begin{cases} u_e = \dfrac{1-\mu^2}{E_s} r\left(\Delta\sigma_\theta - \dfrac{\mu}{1-\mu}\Delta\sigma_r\right), & r_1 \leqslant r \leqslant R_p, \\ u_p = \dfrac{1-\mu^2 R_p^2}{E_s r}\left(\Delta\sigma_0 - \dfrac{\mu}{1-\mu}\Delta\sigma_r\right), & R_p \leqslant r \leqslant R. \end{cases} \tag{13}$$

3. Analysis of Surrounding Rock Pressure and Displacement considering Softening

3.1. Mechanical Model. In order to qualitatively study the stress distribution of surrounding rock of circular tunnel under seepage, the following assumptions are made for the practical problems: (1) the calculation process is considered as the plane strain problem under axisymmetry, (2) the water-bearing surrounding rock is regarded as a two-phase medium satisfying Darcy's law, and (3) for the convenience of coupling calculation, the compressive stress is positive and the tensile stress is negative.

Figure 3 shows the mechanical model of tunnel surrounding rock. According to the stress-strain state of surrounding rock, the tunnel surrounding rock is divided into three areas, namely elastic area, plastic softening area, and plastic residual area. The surrounding rock in the elastic area is in a complete state. When the surrounding rock stress

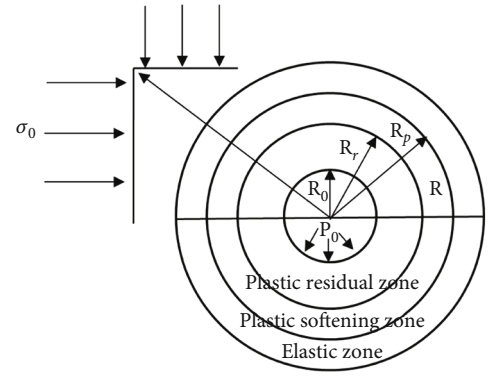

Figure 3: Mechanical model of tunnel surrounding rock.

exceeds the strength limit of rock mass, the surrounding rock is in a plastic softening state. With the gradual increase in deformation, the strength of rock mass decreases gradually. Finally, the residual strength is reached. At this time, the surrounding rock enters the plastic residual area. See formulas (1) and (2) for the values of corresponding mechanical parameters. The excavation radius of the tunnel is R_0 (m), the distance from the center of the tunnel to the outer boundary of the plastic residual zone is R_r (m), and the distance from the center of the tunnel to the outer boundary of the plastic softening zone is R_p (m). The water pressure of the stable seepage field outside the radius R (m) is the same as the water pressure P_i (Pa) outside the original seepage field, and R can be obtained from borehole test [27]. The tunnel support force is P_0 (Pa), the initial in situ stress is σ_0 (Pa), and the side pressure coefficient λ is 1; that is, the horizontal in situ stress is equal to the vertical in situ stress.

3.2. Strain Softening Model. The strain softening of surrounding rock shows the opening and penetration of microcracks and the weakening of surrounding rock properties under stress. Macroscopically, it can be considered that the cohesion and internal friction angle of surrounding rock have changed, and the mechanical parameters of surrounding rock, cohesion c (Pa) and internal friction angle, have changed φ (°), respectively, η piecewise function:

$$c(\eta) = \begin{cases} c^p(\eta = 0), \\ c^p - (c^p - c^r)\dfrac{\eta}{\eta *}(0 < \eta < \eta *), \\ c^r(\eta \geq \eta *), \end{cases} \tag{14}$$

$$\varphi(\eta) = \begin{cases} \varphi^p(\eta = 0), \\ \varphi^p - (\varphi^p - \varphi^r)\dfrac{\eta}{\eta *}(0 < \eta < \eta *), \\ \varphi^r(\eta \geq \eta *). \end{cases} \tag{15}$$

where c^p and φ^p are the peak mechanical parameters of surrounding rock; c^r and φ^r are the residual mechanical parameter of surrounding rock; $\eta *$ is the plastic softening parameter, whose value is equal to the plastic shear strain. According to Reference [28], when $\eta = 0$, the surrounding

rock is in the prepeak elastic stage. At this time, the c value of surrounding rock and the peak value φ is taken as the parameter. When $0 < \eta < \eta*$, the surrounding rock is in the plastic softening stage. With the η increase in the value, the c value and the φ value decrease gradually. When $\eta > \eta*$, the surrounding rock is in the plastic residual stage. At this time, the c value of surrounding rock and the φ value takes the residual parameter. The calculation formula obtained in Reference [29] is as follows:

$$\eta* = \left(\sigma_1^p - \sigma_1^r\right)\left(\frac{1}{E} + \frac{1}{M}\right)\left(1 + K_\psi\right), \tag{16}$$

$$K\psi = \frac{1 + \sin\psi}{1 - \sin\psi}, \tag{17}$$

where ψ is rock expansion angle (°); E is the elastic modulus of surrounding rock (Pa); and M is the slope of softening curve (Pa). Since there is little difference between the unloading slope and loading slope of the rock stress-strain curve, it is assumed that they are the same here.

3.3. Unified Strength Theory. The unified strength theory has many expressions. For rock materials, the internal friction angle of rock is used φ and rock cohesion c is expressed as follows:

When $\sigma_2 \leqslant ((\sigma_1 + \sigma_3)/2) - (\sigma_1 - \sigma_3/2)\sin\varphi$:

$$F = \sigma_1(1 - \sin\varphi) - \sigma_3'(1 + \sin\varphi) = 2C\cos\varphi, \tag{18}$$

$$\sigma_3' = \frac{b\sigma_2 + \sigma_3}{1 + b}. \tag{19}$$

When $\sigma_2 \geqslant ((\sigma_1 + \sigma_3)/2) - ((\sigma_1 - \sigma_3)/2)\sin\varphi$:

$$F' = \sigma_1'(1 - \sin\varphi) - \sigma_3(1 + \sin\varphi) = 2C\cos\varphi \tag{20}$$

$$\sigma_1' = \frac{\sigma_1 + b\sigma_2}{1 + b}, \tag{21}$$

where σ_1, σ_2, and σ_3 are the maximum principal stress, intermediate principal stress, and minimum principal stress, respectively; b is the influence degree of intermediate principal shear stress and normal stress on its action surface on material failure, and its value range is $[0, 1]$.

3.4. Seepage Field Calculation. In the axisymmetric plane stable seepage field, considering that the rock mass has different permeability coefficients in the horizontal and vertical directions, Darcy's law in the two directions is expressed as

$$\begin{cases} V_x = -k_x\dfrac{\partial h}{\partial x}, \\ V_y = -k_y\dfrac{\partial h}{\partial y}, \end{cases} \tag{22}$$

where V is the seepage flow velocity (m/d); h is seepage potential (m); and k_x and k_y are permeability coefficient in horizontal and vertical directions (m/d).

The continuity equation of incompressible water flow in rock mass is

$$\frac{\partial V_x}{\partial x} + \frac{\partial V_y}{\partial y} = 0. \tag{23}$$

Pore water pressure is $P_w = h \cdot \gamma_w$, and γ_w is the gravity of water (N/m^3). It is defined that the ratio of permeability coefficient in horizontal and vertical directions is uneven permeability coefficient ν, namely $k_x = \nu k_y$. When $\nu = 1$, the rock mass is isotropic.

The axisymmetric plane stable seepage differential equation is obtained by combining formulas (9) and (10) and expressed in the cylindrical coordinate system:

$$\frac{\partial^2 P_w(r)}{dr^2}\left(\nu\cos^2\beta + \sin^2\beta\right) + \frac{1}{r}\frac{dP_w(r)}{dr}\left(\nu\sin^2\beta + \cos^2\beta\right) = 0, \tag{24}$$

where β is the included angle between r and the horizontal coordinate axis $\delta = (\nu\cos^2\beta + \sin^2\beta)/(\nu\sin^2\beta + \cos^2\beta)$, so that the above formula becomes

$$\frac{\partial^2 P_2(r)}{dr^2} + \frac{1}{\delta r}\frac{dP_w(r)}{dr} = 0. \tag{25}$$

When $\nu = 1$, the above formula becomes an axisymmetric plane stable seepage field of isotropic rock mass. According to the boundary conditions $P_{w(r=R_0)} = 0$, $P_{w(r=R)} = P_i$, the distribution law of pore water pressure along the radius of tunnel surrounding rock is obtained as follows:

$$\begin{cases} P_{\omega(r)} = P_i\dfrac{\ln(r/R_0)}{\ln(R/R_0)} \quad (\nu = 1\,;\, R_0 \leqslant r \leqslant R), \\ P_{w(r)} = P_i\left(\dfrac{r^{(\delta-1)/\delta} - R_0^{(\delta-1)/\delta}}{R^{(\delta-1)/\delta} - R_0^{(\delta-1)/\delta}}\right) \quad (\nu \neq 1\,;\, R_0 \leqslant r \leqslant R). \end{cases} \tag{26}$$

4. Analysis of Surrounding Rock Pressure and Displacement considering Seepage and Softening

Because the surrounding rock of seepage tunnel is affected by internal water pressure, external water pressure, and in situ stress, under different working conditions, the first principal stress of surrounding rock may be either radial stress or tangential stress. When the tunnel is in construction or operation and the initial in situ stress is greater than the water pressure in the tunnel, if the initial in situ stress is greater than the water pressure in the tunnel or the tunnel is in construction, it is $\sigma_0 > P_0$; there are $\sigma_\theta > \sigma_r$ established. Because the research object of this paper is the deep buried diversion tunnel during the construction period, without considering the influence of internal water pressure, the first

principal stress is tangential stress. For the plane strain problem, the intermediate principal stress is

$$s_2 = \frac{m}{2}(s_1 + s_3), \tag{27}$$

where m is the intermediate principal stress parameter, and for rock materials, $m = 1$.

4.1. Plastic Residual Zone. The equilibrium equation considering seepage is

$$\frac{d\sigma_r}{dr} + \frac{\sigma_r - \sigma_\theta}{r} + \alpha\frac{dP_{w(r)}}{dr} = 0, \tag{28}$$

where α is the action area coefficient of seepage water pressure. For the sake of safety, it is generally taken when studying the failure and stability of rock mass $\alpha = 1$ [21].

Since the maximum principal stress at the junction of plastic residual zone and plastic softening zone ($r = R_r$) is σ_{r1}, since the maximum principal stress under this working condition is tangential stress, that is, the stress boundary condition on the outer boundary of plastic residual area ($r = R_r$) is $\sigma_\theta^{pr} = \sigma_1^r$; the expression of radius Rr of the plastic residual area under this working condition is obtained:

$$R_r = R_0\left[\frac{\sigma_1^r - A_1B - A_2}{A_1(P_0 - B)}\right]^{1/(A_1-1)}. \tag{29}$$

4.2. Plastic Softening Zone. The plastic softening zone also meets the strength criterion of the previous formula and the equilibrium equation of equation (28). The solution process of the stress equation is similar to that of the plastic residual zone. The stress expression of the plastic softening zone can be obtained through the stress boundary condition $\sigma_\theta^{ps} = \sigma_1^p$ on the inner boundary of the plastic softening zone ($r = R_r$):

$$R_p = R_r\left(\frac{\sigma_1^p - A_2 - A_1B)}{\sigma_1^r - A_2 - A_1B}\right)^{1/A_1}. \tag{30}$$

4.3. Elastic Zone. It is assumed that the radial stress σ_r^{gp} is caused by in situ stress on the contact surface between the plastic softening zone of surrounding rock and the elastic zone, and the elastic zone of surrounding rock can be regarded as the initial in situ stress at infinity σ_0. With radial compressive stress on the elastic-plastic contact surface for thick-walled cylinder under the combined action of σ_{rp} and seepage water pressure, the expression of stress in the elastic zone is

$$\begin{cases} \sigma_\theta^c = \sigma_0\left(1 + \dfrac{R_p^2}{r^2}\right) - \sigma_r^{gp}\dfrac{R_p^2}{r^2} + \alpha P_w, \\ \sigma_r^e = \sigma_0\left(1 - \dfrac{R_p^2}{r^2}\right) + \sigma_r^{gp}\dfrac{R_p^2}{r^2} + \alpha P_w. \end{cases} \tag{31}$$

From the sum of tangential stress and radial stress, which is continuous at the elastic-plastic interface of surrounding rock ($r = R_r$), it can be obtained that the peak stress completely caused by in situ stress without seepage is

$$\sigma_\theta^{gp} = \sigma_1^{gp} = \frac{2\sigma_0 A_1 + A_2}{1 + A_1}, \tag{32}$$

$$\sigma_r^{gp} = \sigma_3^{gp} = \frac{2\sigma_0 - \Lambda_2}{1 + A_1} \tag{33}$$

The stress expression of surrounding rock considering seepage and softening effect expressed by softening parameters and related rock parameters can be obtained.

5. Example Analysis

A tunnel in Yunnan is a separated tunnel. The starting and ending piles of the right line are K22+ 455-k22 + 711, with a length of 2256 m, and the starting and ending piles of the left line are zk22+ 437-zk24 + 680, with a length of 2243 m. It is a long highway tunnel. The maximum design speed of the whole tunnel is 100 km/h, the net width of the tunnel is limited to 14.5 m, and the net height is 5 m. The tunnel type is downhill tunnel, with the right longitudinal slope gradient of -2.5% and the right longitudinal slope gradient of -2.5%. The center line distance is 22 m-30 m, with a total length of 4499 m. The inlet section adopts biased end wall and end wall portal, the outlet section adopts open hole portal, and the lighting mode adopts photoelectric lighting. The ventilation mode is mechanical ventilation, and the mechanical parameters of tunnel surrounding rock are shown in Table 1. The construction site of tunnel entrance is shown in Figure 4.

5.1. Effect of Nonuniform Permeability Coefficient on Pore Water Pressure Distribution. It can be seen from the previous discussion that there are many factors affecting the distribution of pore water pressure in surrounding rock. The nonuniform permeability coefficient is analyzed below ν having influence on pore water pressure distribution in different directions of surrounding rock. Figure 5 shows different ν. The horizontal axis is the ratio of the distance r from the point to the center of the tunnel and the influence radius R of the external water pressure of the original seepage field. It can be seen from Figure 5 that the uneven permeability coefficient has an impact on the pore water pressure distribution in different directions. Figure 5(a) shows that when the external water pressure is constant, with the increase in uneven permeability coefficient, the growth rate of pore water pressure along the 0° direction (horizontal direction) gradually slows down and finally tends to the external water pressure. The variation trend of pore water pressure along the 30° direction is similar to that in the 0° direction (Figure 5(b)), but different ν. The difference of growth rate under value is not as obvious as the latter; Figures 5(c) and 5(d) show that the change trend of pore water pressure in the 60° direction is the same as that in the 90° direction (vertical direction), and the growth rate of pore

Table 1: Mechanical parameters of surrounding rock of the example project.

Mechanical parameters	Value	Mechanical parameters	Value
Elastic modulus E (Gpa)	7.8	Crustal stress σ_0	22
Strength attenuation modulus M (GPa)	7.8	External water pressure P_i	6
Peak internal friction angle φ^p (°)	35	Density ρ (g·cm^{-3})	2.6
Residual internal friction angle φ^r (°)	30	Poisson's ratio μ	0.25
Peak cohesion C^p (MPa)	1.5	Dilatancy angle ψ (°)	10
Residual cohesion C^r (MPa)	0.9	Critical plastic softening coefficient η^*	0.007

Figure 4: Construction site drawing of tunnel entrance.

water pressure gradually accelerates with the increase in uneven permeability coefficient, which is different in the 90° direction ν. The difference of growth rate under the value is more obvious than that in the 60° direction. This shows that with ν the change of value, the seepage shows anisotropy in different directions, and the closer to the horizontal or vertical direction, the more vulnerable the pore water pressure distribution is to the influence of uneven permeability coefficient. Specifically, when $\nu < 1$, the closer to the horizontal direction, the faster the change speed of pore water pressure. When $\nu > 1$, the closer to the vertical direction, the faster the pore water pressure changes. This shows that when $\nu < 1$, that is, when the permeability coefficient in the horizontal direction is less than that in the vertical direction, the reduction range of pore water pressure in the horizontal direction is much less than that in the vertical direction in the surrounding rock deep away from the tunnel free face. Because the boundary condition of hydraulic force at the tunnel free face is a certain value, therefore, the calculation results show that the hydraulic gradient increases sharply in the horizontal direction near the free face.

5.2. Influence of Seepage on Different Zoning Ranges and Stress Distribution of Surrounding Rock. In order to reveal the effects of strain softening and seepage on the stress and plastic zone radius of surrounding rock, it is compared with the elastic-plastic solutions of the following three cases: no strain softening, no seepage, and neither softening nor seepage. In order to simplify the calculation, the attenuation of rock material parameters in the softening zone is regarded as a linear change.

When the intermediate principal stress coefficient $b = 0$, the unified strength criterion degenerates to the Mohr-Coulomb strength criterion. The relationship curve between P_0 and plastic zone radius R_p in 4 cases is calculated, as shown in Figure 6. It can be seen from Figure 6 that P_0 has a significant impact on the radius R_p of the surrounding rock plastic zone. When B is constant, with the increase in P_0, the radius R_p of the plastic zone gradually decreases until there is no plastic zone (because the excavation radius $P_0 = 2$ m, $R_p < 2$ m indicates that the plastic zone does not exist). When $P_0 = 4$ MPa, the R_p corresponding to the four cases is 27.2%, 15.5%, 19.7%, and 12.8% lower than that corresponding to $P_0 = 2$ MPa. When $P_0 = 10$ MPa, the R_p corresponding to the four cases is only 10.5%, 6.3%, 8.9%, and 5.2% lower than that when $P_0 = 8$ MPa, indicating that the support force can reduce the plastic zone of surrounding rock within a certain range, and the smaller the support force, the more significant the impact. When considering seepage and softening, the obtained R_p is greater than that when only a single factor is considered or neither is considered. Therefore, during tunnel construction, the rock mass should be reinforced by grouting treatment to reduce the softening degree and permeability coefficient of surrounding rock, reduce the range of plastic zone of surrounding rock and improve the stability of surrounding rock. The calculated R_p only considering softening is greater than that only considering seepage, and R_p in both cases is greater than that calculated without considering both, indicating that both seepage and material softening will affect the stability of surrounding rock, which should not be ignored in calculation, and material softening is more unfavorable to the stability of surrounding rock than seepage.

Figure 7 shows the distribution of tangential stress of surrounding rock under 4 conditions when $P_0 = 2$ MPa and $b = 0$, and the first principal stress generally controls the surrounding rock. Under this working condition, the tangential stress is the first principal stress, so only the influence of various parameters on tangential stress is analyzed. It can be seen from Figure 7 that near the free face of the tunnel, the tangential stress value considering material softening is less than that without considering material softening. This is because the mechanical parameters of surrounding rock in the plastic zone deteriorate, resulting in the decline of the bearing capacity of surrounding rock and the transmission of stress to the depth of surrounding rock, resulting in the continuous expansion of the plastic zone. At the same time, the tangential stress distribution of surrounding rock considering the influence of seepage field and not considering the influence of seepage field is basically the same near the

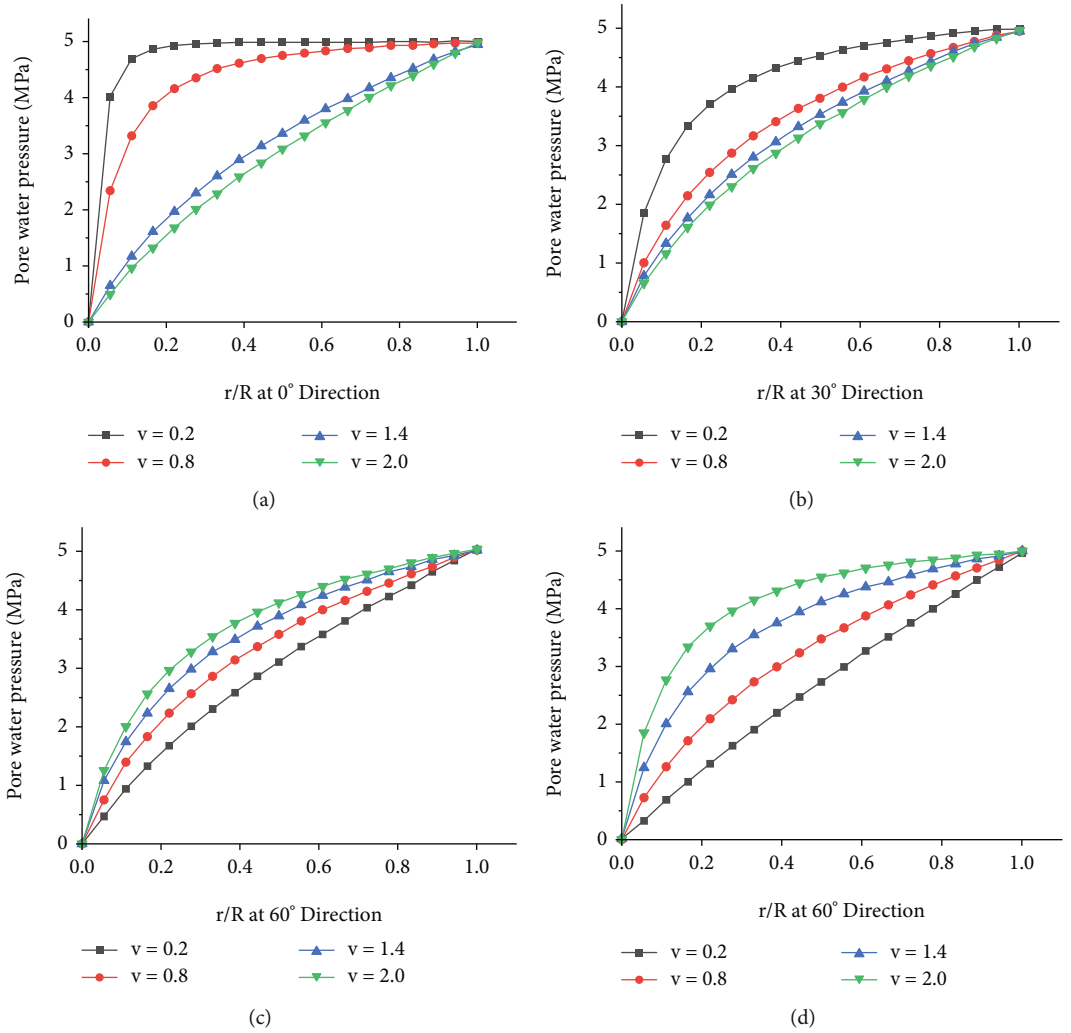

Figure 5: Different v pore water pressure distribution of surrounding rock in different directions under the condition of value.

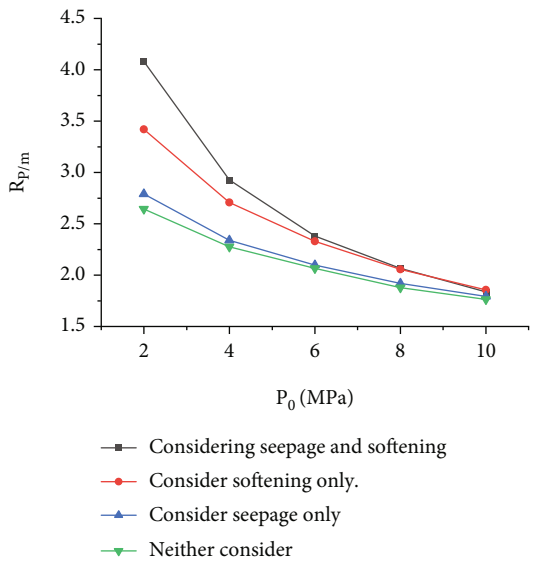

Figure 6: Relationship curve between P_0 and R_p in 4 cases ($b = 0$).

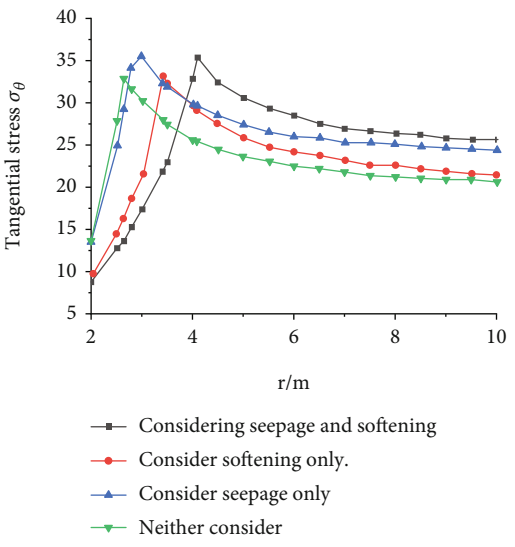

Figure 7: Tangential stress distribution of surrounding rock in 4 cases ($P_0 = 2$ MPa, $b = 0$).

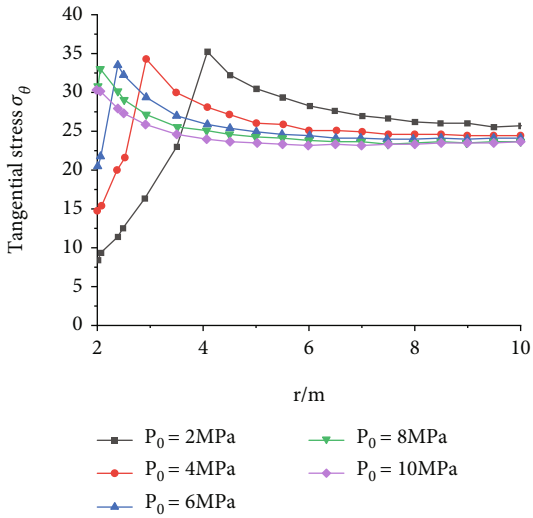

Figure 8: Tangential stress distribution of surrounding rock corresponding to different P_0 (considering seepage and softening, $B = 0$).

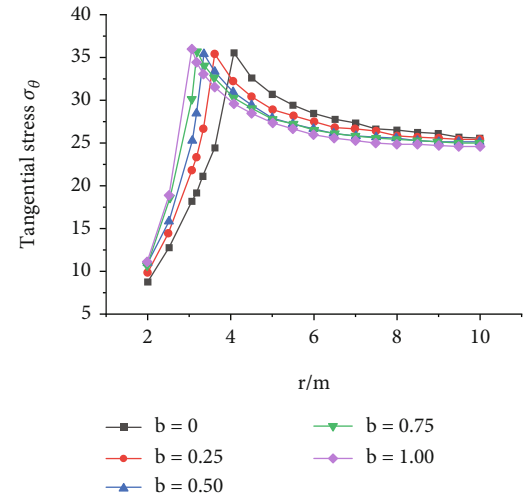

Figure 9: Tangential stress distribution of surrounding rock corresponding to different b values ($P_0 = 2$ MPa).

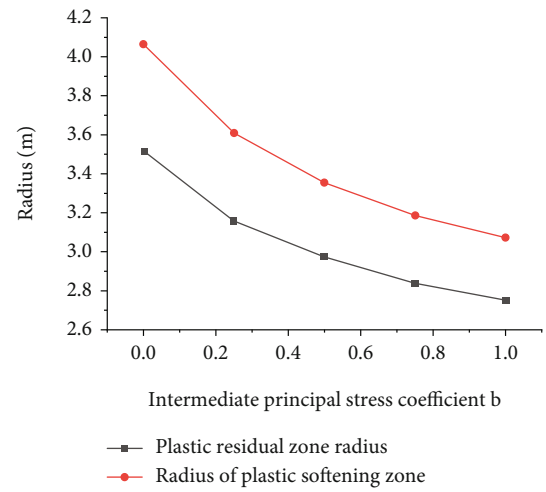

Figure 10: Radius of the plastic zone corresponding to different b values.

free face, but near the depth, the tangential stress of surrounding rock considering the influence of seepage field is gradually greater than that without considering the effect of seepage field. This is because when the seepage field is not considered, the support reaction acting on the tunnel wall is considered surface force, and its action range is limited. The seepage pressure is actually a volume force acting on any point of the stress field.

Figure 8 shows the tangential stress distribution of surrounding rock corresponding to different P_0 when $b = 0$ considering seepage and softening conditions, and the radius of plastic zone is shown in Figure 6. It can be seen from Figure 8 that with the increase in P_0, the tangential stress of surrounding rock near the free face gradually increases. P_0 increases from 2 MPa to 10 MPa, the tangential stress at the inner wall of the tunnel increases from 8.6 MPa to 30.4 MPa, an increase in 2.5 times, while the peak tangential stress decreases from 35 MPa to 30.6 MPa, a decrease in 14.4%.

5.3. Influence of Intermediate Principal Stress Coefficient on Different Zoning Ranges and Stress Distribution of Surrounding Rock. Based on the unified strength theory criterion, the elastic-plastic analytical solution of tunnel surrounding rock is obtained by comprehensively considering the influence of seepage field and surrounding rock strain softening. It is known that this series of solutions can be transformed into known solutions by changing the intermediate principal stress coefficient b. For example, when b is equal to 0, 0.25, 0.50, 0.75, and 1.00, respectively, this solution can be transformed into a special solution satisfying Mohr-Coulomb, double shear strength criterion, and other strength criteria. By changing the intermediate principal stress coefficient b, the influence of the intermediate principal stress on the tangential stress of surrounding rock under seepage and softening effect is analyzed. Figure 9 shows the tangential stress distribution of surrounding rock corresponding to different b values when $P_0 = 2$ MPa, and Figure 10 shows the radius of the plastic zone corresponding to different b values. It can be seen from Figures 9 and 10 that b value has a significant impact on the tangential stress of surrounding rock and the range of plastic zone. With the increase in b value, the radius of plastic zone gradually decreases, while the tangential stress of surrounding rock near the free face gradually increases. When considering the intermediate principal stress effect ($b = 0.25$, 0.50, 0.75, and 1.00), the peak tangential stress of surrounding rock increases by 0.2%, 0.8%, 0.9%, and 1.8%, respectively, compared with that without considering the intermediate principal stress effect ($b = 0$), and the radius of the plastic zone decreases by 10.8%, 17.2%, 21.3%, and 24.2%, respectively, which shows that compared with considering the intermediate principal stress effect, without considering the effect of intermediate principal stress, the calculation results are

relatively conservative and cannot give full play to the strength of surrounding rock effectively.

6. Conclusions

(1) In order to study the interaction between surrounding rock and lining of deep buried tunnel considering the influence of seepage, based on Mohr Coulomb criterion, the interaction between surrounding rock and lining of deep buried tunnel is analyzed by convergence constraint method. Based on the elastic-plastic solution, the nonlinear elastic-plastic solution of the interaction between surrounding rock and lining structure considering the effect of seepage force is proposed, and the radius of surrounding rock plastic zone is obtained The relationship between surrounding rock stress and displacement, radial deformation of lining and support reaction force. At the same time, the seepage, strain softening and intermediate principal stress of surrounding rock are analyzed as parameters, and the calculation results are combined with the properties of surrounding rock. The surrounding rock is divided into plastic residual area, plastic softening area, and elastic area. The stress distribution expression of plastic area and surrounding rock in each area of circular tunnel is deduced

(2) The radial displacement around the tunnel is mainly related to the nonlinear deformation of surrounding rock lining. After the tunnel is excavated and lined, under the action of surrounding rock earth pressure and seepage water pressure, the surrounding rock and lining deform, and the support reaction provided by the lining gradually increases. The two coordinate deformation, making the tunnel tend to be stable. The final radial displacement around the tunnel depends on the convergence curve of surrounding rock and the support characteristic curve

(3) Define the coefficient of nonuniform permeability ν to quantitatively analyze the influence of two-way unequal permeability coefficient on pore water pressure distribution in all directions of surrounding rock: with ν with the change of value, the seepage shows anisotropy in different directions. When $\nu < 1$, the closer to the horizontal direction, the faster the change speed of pore water pressure. When $\nu > 1$, the closer to the vertical direction, the faster the pore water pressure changes

(4) Through the comparison of numerical examples, seepage and material softening have varying degrees of influence on the distribution of surrounding rock stress field and the size of plastic zone: due to the deterioration of surrounding rock mechanical parameters, the tangential stress when considering softening is smaller than when not considering softening, and the radius of plastic zone is larger. At the same time, The softening characteristic of the studied material has a greater influence on the stability of surrounding rock than that of seepage

(5) The intermediate principal stress coefficient b has a significant impact on the tangential stress of surrounding rock and the range of plastic zone. With the increase in b value, the radius of the plastic zone decreases gradually, while the tangential stress of surrounding rock near the free face increases gradually. In the calculation example in this paper, when $b = 1$, the peak tangential stress of surrounding rock increases by 1.8% compared with $B = 0$, and the radius of plastic zone decreases by 25%, which shows that compared with considering the intermediate principal stress effect, the calculation results are relatively conservative without considering the intermediate principal stress effect and cannot give full play to the strength of surrounding rock effectively

Data Availability

The experimental data used to support the findings of this study are included within the article.

Conflicts of Interest

The authors declare that there is no conflict of interest regarding the publication of this paper.

References

[1] J. Zou, K. Chen, and Q. Pan, "An improved numerical approach in surrounding rock incorporating rockbolt effectiveness and seepage force," *Acta Geotechnica*, vol. 13, no. 3, pp. 707–727, 2018.

[2] Q. Xu, J. T. Chen, and M. Xiao, "Analysis of unsteady seepage field and surrounding rock stability of underground cavern excavation," *Tunnelling and Underground Space Technology*, vol. 97, article 103239, 2020.

[3] Y. F. Xu, Z. Z. Shen, and C. X. Shao, "Seepage stability analysis for surrounding rock mass of diversion tunnel by FEM," *Advanced Materials Research*, vol. 787, pp. 622–625, 2013.

[4] S. Zhang and L. Ming, "Fluid-solid coupling numerical simulation of temperature field of roadway surrounding rock in water-bearing formation," in *2010 3rd International Conference on Computer Science and Information Technology*, pp. 440–442, Information Technology. IEEE, Chengdu, China, 2010.

[5] S. Nan, Q. Gao, and Z. Liu, "Numerical simulation of fluid-solid coupling in surrounding rock and parameter optimization for filling mining," *Procedia Engineering*, vol. 26, pp. 1639–1647, 2011.

[6] C. Y. Liu, Y. Wang, X. M. Hu, Y. L. Han, X. P. Zhang, and L. Z. du, "Application of GA-BP neural network optimized by Grey Verhulst model around settlement prediction of foundation pit," *Geofluids*, vol. 2021, Article ID 5595277, 16 pages, 2021.

[7] C. Liu, L. Du, X. Zhang, Y. Wang, X. Hu, and Y. Han, "A new rock brittleness evaluation method based on the complete stress-strain curve," *Lithosphere*, vol. 2021, article 4029886, no. Special 4, 2021.

[8] Y. K. Lee and S. Pietyuszczak, "A new numerical procedure for elasto-plastic analysis of a circular opening excavated in a strain-softening rock mass," *Tunnelling and Underground Space Technology*, vol. 23, no. 5, pp. 588–599, 2008.

[9] G. Li, Y. Hu, and T. Sm, "Analysis of deformation control mechanism of prestressed anchor on jointed soft rock in large cross-section tunnel," *Bulletin of Engineering Geology and the Environment*, vol. 80, no. 12, pp. 9089–9103, 2021.

[10] N. K. Samadhiya, M. N. Viladkar, and M. A. Al-Obaydi, "Numerical implementation of anisotropic continuum model for rock masses," *International Journal of Geomechanics*, vol. 8, no. 2, pp. 157–161, 2008.

[11] L. R. Alejano, E. Alonso, A. Rodríguez-Dono, and G. Fernández-Manín, "Application of the convergence-confinement method to tunnels in rock masses exhibiting Hoek–Brown strain-softening behavior," *International Journal of Rock Mechanics and Mining Sciences*, vol. 47, no. 1, pp. 150–160, 2010.

[12] H. Liang, W. Lin, D. Xuaning, H. Wen, X. Yuan, and W. Zhang, "Similarity quantification of soil parametric data and sites using confidence ellipses," *Geoscience Frontiers*, vol. 13, article 101280, 2022.

[13] Z. Dou, Y. M. Liu, X. Y. Zhang et al., "Influence of layer transition zone on rainfall-induced instability of multilayered slope," *Lithosphere*, vol. 2021, no. Special 4, article 2277284, 2021.

[14] S. K. Sharan, "Analytical solutions for stresses and displacements around a circular opening in a generalized Hoek-Brown rock," *International Journal of Rock Mechanics & Mining Sciences*, vol. 45, no. 1, pp. 78–85, 2008.

[15] D. Chen, H. Chen, W. Zhang, J. Lou, and B. Shan, "An analytical solution of equivalent elastic modulus considering confining stress and its variables sensitivity analysis for fractured rock masses," *Journal of Rock Mechanics and Geotechnical Engineering*, vol. 14, 2021.

[16] Z. Dou, S. X. Tang, X. Y. Zhang et al., "Influence of shear displacement on fluid flow and solute transport in a 3D rough fracture," *Lithosphere*, vol. 2021, no. Special 4, article 1569736, 2021.

[17] Z. J. Wu, Z. Y. Wang, L. F. Fan, L. Weng, and Q. S. Liu, "Micro-failure process and failure mechanism of brittle rock under uniaxial compression using continuous real-time wave velocity measurement," *Journal of Central South University*, vol. 28, no. 2, pp. 556–571, 2021.

[18] Y. Q. Su, F. Q. Gong, S. Luo, and Z. X. Liu, "Experimental study on energy storage and dissipation characteristics of granite under two-dimensional compression with constant confining pressure," *Journal of Central South University*, vol. 28, no. 3, pp. 848–865, 2021.

[19] Q. Wang, M. C. He, S. C. Li et al., "Comparative study of model tests on automatically formed roadway and gob-side entry driving in deep coal mines," *International Journal of Mining Science and Technology*, vol. 31, no. 4, pp. 591–601, 2021.

[20] Z. Yi, H. Chuan, and W. Bo, "Research on deformation control technology for tunnels in soft rocks and meizoseismic area based on supporting parameters optimization," *Rock and Soil Mechanics*, vol. 34, no. 4, p. 1147, 2013.

[21] Y. Wang, H. N. Yang, J. Q. Han, and C. Zhu, "Effect of rock bridge length on fracture and damage modelling in granite containing hole and fissures under cyclic uniaxial increasing-amplitude decreasing-frequency (CUIADF) loads," *International Journal of Fatigue*, vol. 158, article 106741, 2022.

[22] W. Shunchuan, P. Danguang, and G. Yongtao, "Analytic solution for rock-liner interaction of deep circular tunnel," *Engineering Mechanics*, vol. 28, no. 3, p. 136, 2011.

[23] C. Zhu, M. Karakus, M. C. He et al., "Volumetric deformation and damage evolution of Tibet interbedded skarn under multistage constant-amplitude-cyclic loading," *International Journal of Rock Mechanics and Mining Sciences*, vol. 152, article 105066, 2022.

[24] L. Chengxue, Y. Linde, and L. Peng, "Elastoplastic solution of deep buried circular permeable tunnel considering stress redistribution," *Engineering Mechanics*, vol. 26, no. 2, pp. 16–20, 2009.

[25] X. Li, Q. Li, Y. Hu et al., "Study on three-dimensional dynamic stability of open-pit high slope under blasting vibration," *Lithosphere*, vol. 2021, no. Special 4, article 6426550, p. 17, 2022.

[26] Y. Ma, J. Yang, L. Li, and Y. Li, "Analysis on ultimate water pressure and treatment measures of tunnels operating in water rich areas based on water hazard investigation," *Alexandria Engineering Journal*, vol. 61, no. 8, pp. 6581–6589, 2022.

[27] P. Zhang, D. F. Zhang, Y. Yang et al., "A case study on integrated modeling of spatial information of a complex geological body," *Lithosphere*, vol. 2022, no. Special 10, article 2918401, 2022.

[28] C. Zhu, M. C. He, X. H. Zhang, Z. G. Tao, Q. Yin, and L. F. Li, "Nonlinear mechanical model of constant resistance and large deformation bolt and influence parameters analysis of constant resistance behavior," *Rock and Soil Mechanics*, vol. 42, no. 7, pp. 1911–1924, 2021.

[29] L. R. Alejano, E. Alonso, A. Rodriguez-Dono, and G. Fernandez-Manin, "Application of the convergence-confinement method to tunnels in rock masses exhibiting Hoek-Brown strain-softening behaviour," *International Journal of Rock Mechanics & Mining Sciences*, vol. 47, no. 1, pp. 150–160, 2010.

Hindawi
Geofluids
Volume 2022, Article ID 3831652, 22 pages
https://doi.org/10.1155/2022/3831652

Research Article

Quantitative Attribution Analysis of the Spatial Differentiation of Gully Erosion in the Black Soil Region of Northeast China

Ranghu Wang,[1,2] **Nan Wang**,[1] **Yingchao Fan**,[3] **Huan Sun**,[1] **Hanpei Fu**,[3] **and Jiuchun Yang**[2]

[1]*Institute of Loess Plateau, Shanxi University, Taiyuan 030006, China*
[2]*Northeast Institute of Geography and Agroecology, Chinese Academy of Sciences, Changchun 130102, China*
[3]*College of Environment & Resource Science, Shanxi University, Taiyuan 03000, China*

Correspondence should be addressed to Jiuchun Yang; yangjiuchun@iga.ac.cn

Received 8 April 2022; Revised 7 June 2022; Accepted 13 June 2022; Published 20 July 2022

Academic Editor: Long Yan

Gully erosion is the major soil erosion type in the black soil region of Northeast China. However, studies on multifactor synthesis at a large scale and on the driving mechanism of spatial differentiation are still relatively lacking for gully erosion in this region. In this study, the simulation of gully erosion and its quantitative attribution analysis have been conducted in the Sancha River catchment in Northeast China, based on high-resolution satellite imagery mapping and the geodetector method. A total of 18 indicators in 6 categories, including topography, climate and weather, soil properties, lithology, land use, have been taken into consideration. The influence of each influencing factor and its interactive influence on gully erosion were quantitatively evaluated. The results showed that at the large catchment scale, the submeter images had a strong capacity for the recognition of a permanent gully and obtained satisfactory results. According to the results of the geodetector, lithology and soil type are the main factors that affect the spatial differentiation of gully erosion in the Sancha River basin, because their interpretation power for gully density and gully intensity was close to 10%. The lithology belonged to gray–white matter rhyolite, spherulite rhyolite, and crystal clastic tuff, with the highest gully density and intensity. The interpretation power of the secondary factors, including rainfall erosivity, watershed area, elevation, soil erodibility, land use pattern, slope, and distance from the river, amounted to more than 1%. The interactions among most driving factors showed nonlinear enhancement. The influence of the interaction between lithology and soil type appeared to be the largest. In particular, the lithology of different soil types accounted for 28.7% and 32.5% of the gully density and gully intensity. The interaction of factors had a stronger influence on the spatial differentiation of gully erosion than any single factor.

1. Introduction

Gully erosion is the formation and subsequent expansion of erosional channels in the soil as a result of concentrated water flow [1]. Runoff water through the catchment area removes soil from the channels and accumulates in the narrow channels. After several iterations, a gully of considerable depth will appear. Hence, gully erosion is one of the most effective drivers of sediment removal and runoff from highland areas to valley floors [2]. Gully erosion was, is, and will continue to be one of the world's most important environmental problems, especially in semiarid and arid areas, where soils are suffering from severe gully erosion [3]. For instance, Iran, located in Western Asia, is suffering from serious soil erosion, with approximately 2-2.5 billion tons of soil being lost every year, accounting for approximately 50% of the country's land area. Gully initiation and development is a natural process that greatly impacts agricultural activities and environmental quality as it promotes land degradation, desertification, and ecosystem disruption [2].

In the last 100 years, with the expansion of the agricultural land area, the black soil in Northeast China has

suffered serious soil erosion, becoming one of the largest soil erosion regions in China [4]. Several studies have proposed that gully erosion is the major soil erosion type in this region [5, 6]. According to the findings of the first national water conservancy survey, there are nearly 300,000 gullies in the black soil region of Northeast China, causing a loss of cultivated land of approximately $4.83 \times 105\,hm^2$, and 3.62×10^9 kg of grain is lost annually due to the development of eroded gullies [7]. Due to the unique geographical environment, such as the long, gentle slopesm and large catchment area, the gully erosion process of the black soil region in Northeast China is obviously different from that of other areas. Gully erosion has mostly occurred on sloping farmland [8]. Ephemeral gullies and gullies are usually formed, which are characterized by a short length and small area. Mapping gullies in a wide range of temporal and spatial scales and identifying the formation mechanism and influencing factors are the key issues for soil conservation and land management in Northeast China.

The conventional ground-based measurement methods, such as methods that utilize tape [9], microtopographic profilers [10], total stations [11], pins [12], and differential GPS [13], are time-consuming and labor-intensive when seeking high accuracy in field surveys. The ground-based monitoring methods are typically applicable at a small scale and for short-term monitoring [13, 14]. Unmanned aerial vehicles (UAV) with the photogrammetric technique of structure from motion (SFM) allow a higher level of detail and insights into the process of gully erosion [15, 16]. However, the flexible and promising method provides the user with limited continuous space coverage. At larger temporal and spatial scales, visual analysis or object-oriented analysis of high-resolution satellite remote sensing images have been used to quantify the temporal changes in various gully planar morphological parameters [17–19]. Of particular importance is the continuous mapping of gullies over large areas covering large regions. In recent years, many studies have used high-resolution satellite images to identify and extract the distribution of large-scale gullies and then to study the spatial distribution and dynamic changes in gullies. From 2010 to 2012, the National Administration of Surveying, Mapping and Geographic Information (NASG) conducted the first special census of gully erosion in the black soil region of Northeast China [20]. The survey was mainly based on the method of visual interpretation and field verification, making full use of high-resolution satellite images, airborne sensors, and ground data to obtain information on gullies. According to the field survey, the width of many gullies in the black soil region of Northeast China is less than 5 m. However, when the spatial resolution of satellite images is higher than 5 m, these gullies will be ignored, resulting in an increase in mapping errors. At this time, high spatial–temporal-resolution remote sensing images provide new possibilities for studying large-scale gully erosion [19, 21, 22].

At present, researchers in China and elsewhere are carrying out relevant research on the influencing factors of gully erosion [23–26]. According to previous studies, the distribution of gullies is related to topography, soil, climate, precipitation, vegetation, land use, and human activities, etc. [1, 27]. With the rapid development of computer science, most studies use correlation, regression analysis, or machine learning models to identify the importance of gully erosion factors in order to assess gully erosion sensitivity [2, 3, 28–30]. However, these statistical methods cannot directly quantify the influence of the driving factors [31]. In addition, there is still a lack of studies that comprehensively compare factors and combinations of variables. Do these influencing factors operate independently or by interacting? The emergence of geodetectors provides new ideas and means to solve the above problems. A geodetector is a new tool for geographic research that can effectively analyze spatial differentiation in geographic phenomena and the factors that influence them [32]. It can not only quantitatively determine the dominant factors but can quantify the influence of two interacting explanatory variables on a specific target variable. Thus far, geodetectors have been used to analyze the driving forces and mechanisms of soil erosion [33, 34].

It is still a major challenge to monitor and map the spatial differentiation of gully erosion at a large scale and quantitatively evaluate its driving mechanism in the black soil region of Northeast China. Thus, the purpose of this work is to (1) use the submeter satellite remote sensing image to perform the large-scale spatial mapping of gully erosion in the Sancha River basin located in the south of the typical black soil region of Northeast China by visual interpretation and field validation and (2) perform a quantitative attribution analysis of the spatial differentiation mechanism of gully erosion based on geodetection.

2. Materials and Methods

2.1. Study Area. Soil degradation caused by gully erosion has become an important problem of ecological restoration in the black soil region of Northeast China. The Sancha River basin, located in the south of Northeast China (Figure 1(a)) and covering 163.83 km^2, is a typical black soil region and suffers serious soil and water loss. This study area (Figures 1(b) and 1(c)), situated in the hilly area between the Changbai Mountains and Songliao Plain, has a mid-temperate continental monsoon climate with an annual temperature of 5.3°C; the highest average monthly temperature is 23.3°C and the lowest average monthly temperature is 16.3°C, and the soil types include black soil, meadow soil, albic soil, and dark brown soil. The annual precipitation ranges from 550 to 600 mm. The Sancha River basin has a mosaic of land cover comprising 66.2% farmland, 26.4% forest, 2.0% grassland, 2.9% water area, and 2.5% road and housing construction area. The land use type of this area is mainly slope farmland; the slope length of the slope farmland is mostly in the range of 300~500 m, where the main crops are soybean and corn. Due to the comprehensive influence of topographic factors, climatic factors, soil properties, land use types, and lithology, gully erosion is widely distributed in this area and has most occurred on the sloping farmland. Due to the substantial terrain undulation and long-term human activities, this region has little vegetation coverage and suffers from severe soil erosion by water. In particular, high-intensity reclamation and unreasonable

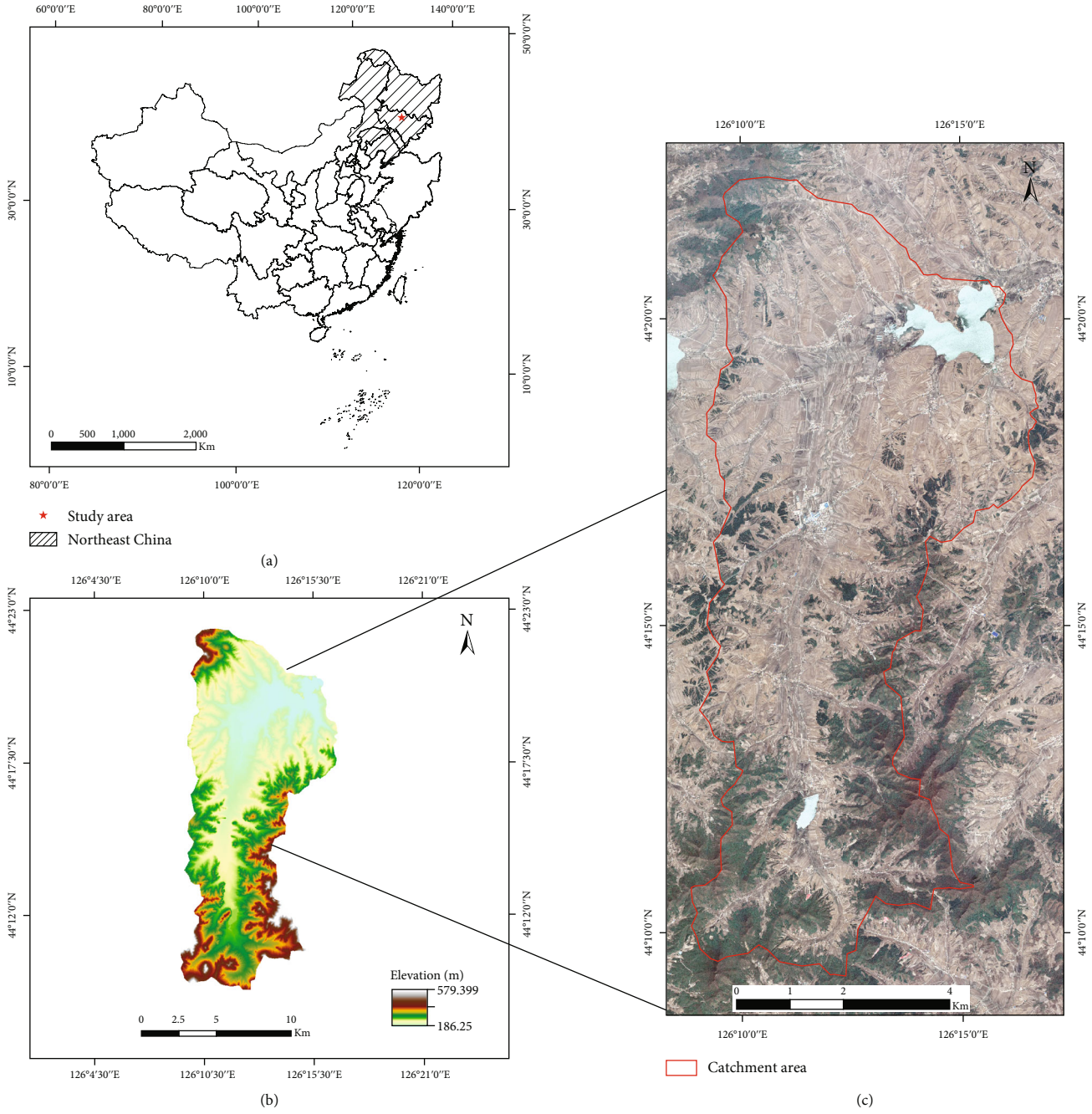

Figure 1: (a) The study area located in Northeast China. (b) DEM of the study area. (c) Pleiades-1B satellite image including the Sancha River catchment (27 April 2018).

land use have become important factors accelerating soil erosion in this region in the past 50 years.

2.2. Data Sources and Processing. To map gully erosion, Pleiades-1B images with a resolution of 0.5 m, collected from Google Earth, were drawn into a polygon according to the gully erosion area. The Pleiadia-1B image taken on 27 April 2018 shows a panchromatic band and four multi-spectral bands (blue, green, red, and near-infrared) (Figure 1(c)). The data provider has made geometric, radiometric, and atmospheric corrections to the data.

Gully erosion is a threshold-dependent process under the influence of a number of effective factors [35]. On the basis of referring to the relevant literature and considering the availability of data and the actual situation of the Sancha River basin, we finally selected 18 influencing factors. Elevation affects the types of vegetation in a region. Therefore, many researchers believe that altitude plays a crucial role in the study of gully erosion [36]. Slope shape and slope position can also cause the spatial differentiation of gully erosion. Slope aspect affects humidity, temperature conditions, and vegetation growth by affecting solar radiation.

Slope degree is an important basic parameter to describe surface morphology and an important analysis factor in soil and water conservation. Slope length can control surface runoff velocity. The runoff and sediment yield increase with the increase in slope length. Plane curvature is an indicator of the turning of the ground, and sectional curvature can reflect the degree of terrain complexity. Runoff will be affected by slope shape [28], and plane curvature and sectional curvature become important indexes affecting gully erosion. The surface runoff and the resulting soil loss can be determined by the unit catchment area. It is the main factor causing the spatial differentiation of gully erosion. The topographic wetness index (TWI) is commonly employed as a proxy for the potential for surface and subsurface water accumulation due to runoff and lateral transmissivity [37]. TWI is considered to be an important factor affecting the development of gullies. Rainfall erosivity is positively correlated with soil and water loss, which can reflect the effect of rainfall on the triggering factors of gully erosion. The rate and pattern of gully development are largely controlled by soil type. Soil erodibility is influenced by the soil's physical properties [38], which have an important impact on soil erosion and sediment yield. Lithological features are related to geomorphologic features and land surface characteristics [39]. The lithology of the geologic parent material influences the development of gullies [40]. In addition, unreasonable land use has become an important factor accelerating gully erosion in this region in the past 50 years. The distance from the river is directly related to runoff in the catchment area, so the distance from the river will affect gully erosion. Distance from the residential area and distance from the road represent the influence of human factors on gully erosion. Excessive utilization of land resources will promote land degradation and have a profound impact on gully erosion [41].

The above factors were identified and divided into 6 categories: (1) topography factors, (2) climate and weather factors, (3) soil properties, (4) lithology, (5) land use, and (6) other factors (Figure 2). Table 1 provides a more detailed overview of each variable. Topography factors, including elevation, slope shape, slope aspect, slope position, slope degree, slope length, plane curvature, sectional curvature, catchment area, and topographic wetness index, were mainly obtained by calculation or analysis in ArcGIS on the basis of a DEM of 5 m pixel size with a scale of 1 : 10,000. Climate and weather factors were represented by rainfall erosivity. Soil properties and lithology were represented by soil type, soil erodibility, and lithology. The soil type distribution map was provided by the Chinese Academy of Sciences. The lithology was obtained through 1 : 50,000 geological maps, provided by the Jilin Provincial Geological Database. Detailed algorithms and data on rainfall erosivity and soil erodibility are available from a previous study [42]. The land use data were derived from submeter-level images and ground data, as an important result of geographical condition monitoring. The other factors, including the distances from residential areas, rivers, and roads, were generated by using the buffer tool in ArcGIS. The other high-resolution satellite/aerial images, including Landsat8 (2013), Planet Labs (2014), Alos (2009), ZY3 (2013), Pleiades-1A (2013), Digital Mapping Camera (DMC, 2010), and Unmanned Air Vehicle (UAV, 2015), were provided by the Jilin Province Geomatics Center and the Chinese Academy of Sciences. The digital elevation model (DEM), land use, road, water, and residential sites were also provided by the Jilin Province Geomatics Center.

2.3. Methods

2.3.1. Gully Erosion Mapping Based on High-Resolution Satellite Imagery. The distribution information on gully erosion in the study area was mainly obtained through visual interpretation (Table 2), combined with field investigation and verification, to judge the gully from the image and then obtain its data, including linear data and area data. The distribution of gully erosion was analyzed in terms of gully density and gully intensity. As the main indicator for assessing gully erosion, gully density within the study area was defined as the total gully length per area of the whole study area. The distribution of gully density was estimated by using the line density tool in ArcGIS. The density was calculated as the ratio of the total length of the gully within the circular kernel (50 m search radius) and the total area of the circular kernel. Gully intensity refers to the total length of gully erosion per unit area, reflecting the degree of fragmentation of the surface and the degree of soil erosion.

According to the field validation result, the gully data were modified. The omitted and committed gullies were included and excluded, respectively. Then, the final gully distribution data were obtained. The gully density distribution was estimated by using the Focal Statistics tool in ArcGIS. The specific steps were as follows: a fishnet polygon containing cells of 50 m × 50 m was created, and then, the total length per area of each cell was calculated and a value was assigned to the corresponding cell; (2) the polygon was converted into a grid with a 5 m pixel size; and (3) focal Statistics was applied to calculate the average value of each input cell within a rectangular neighborhood of 100 m × 100 m; thus, the distribution map of gully density was obtained. Similarly, gully intensity was calculated by using the measurement of total gully area per area.

2.3.2. Geodetector Method. The geodetector method was established by Wang et al. and has been used extensively, mainly in factor detection, risk detection, interactive detection, and ecological detection. For more details about the geographical detector model, please see [43]. Briefly, the process is as follows:

(1) The factor detector uses the q value to assess the impact of risk factors on the spatial pattern of gully erosion. A higher q value means that the risk factor has a stronger contribution to the spatial differentiation of gully erosion. It uses F-tests to compare whether the accumulated variance of each subregion is significantly different from the variance of the entire study region

$$q = 1 - \frac{\sum_{h=1}^{L} N h \sigma_h^2}{N \sigma^2}, \quad (1)$$

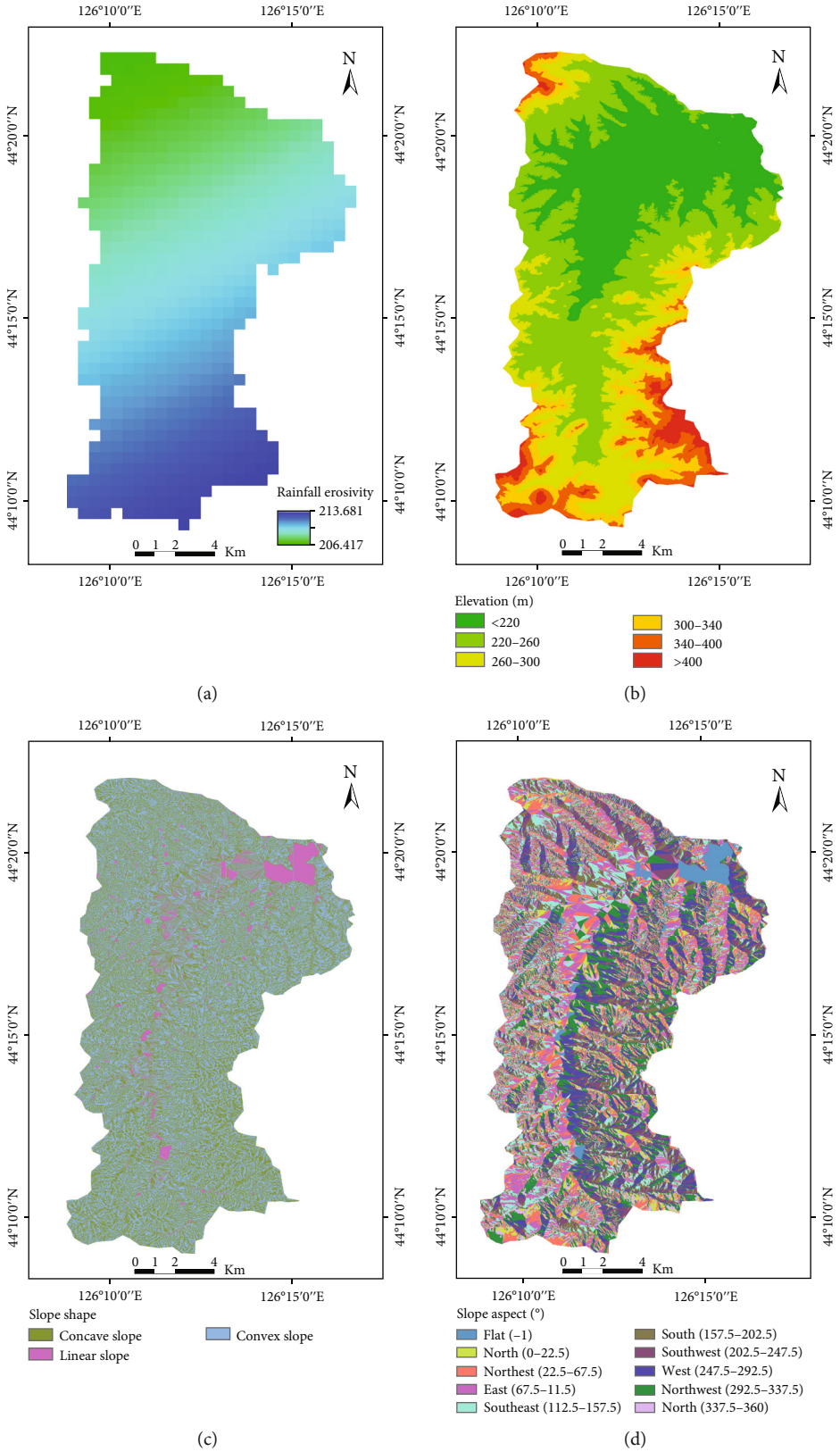

Figure 2: Continued.

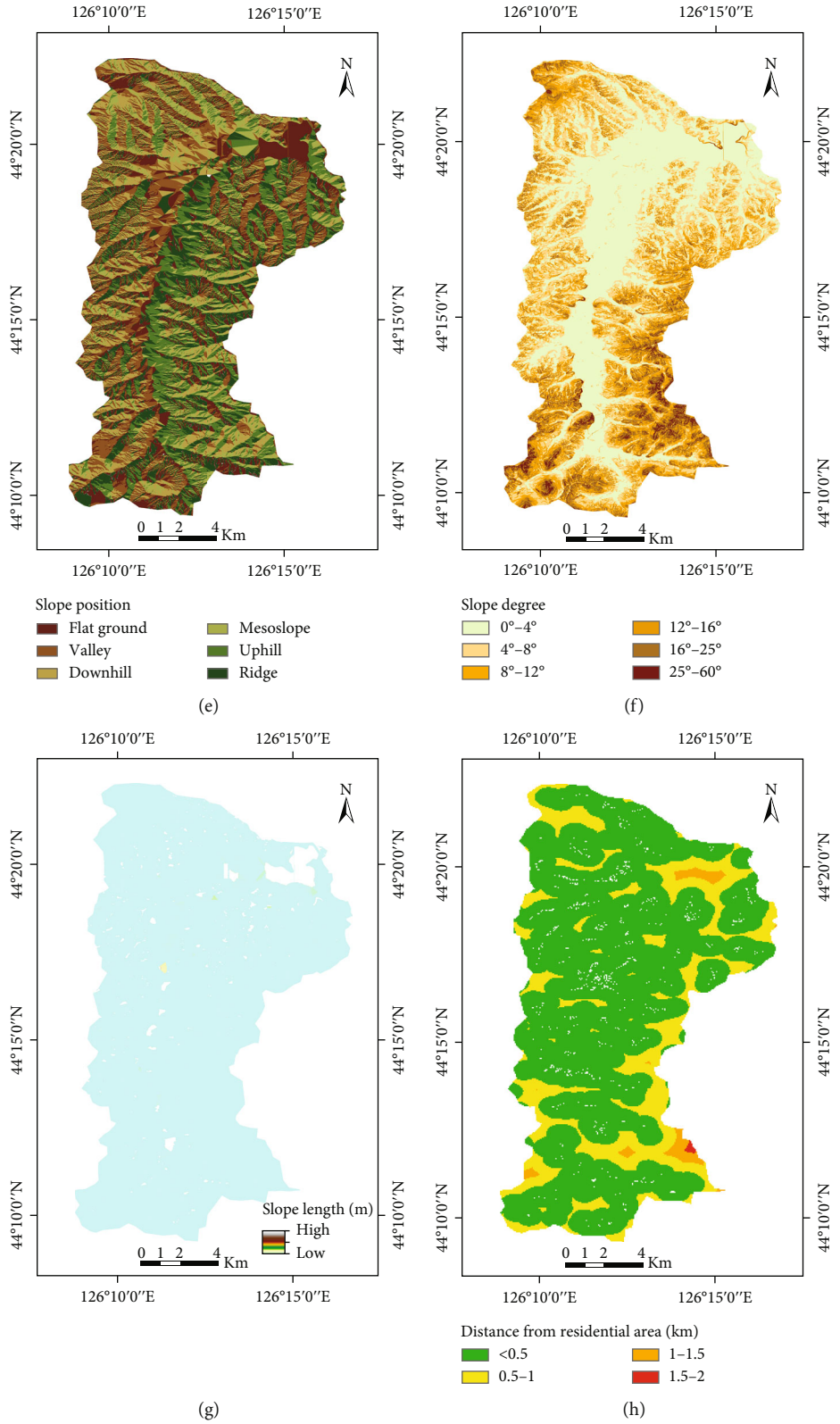

Figure 2: Continued.

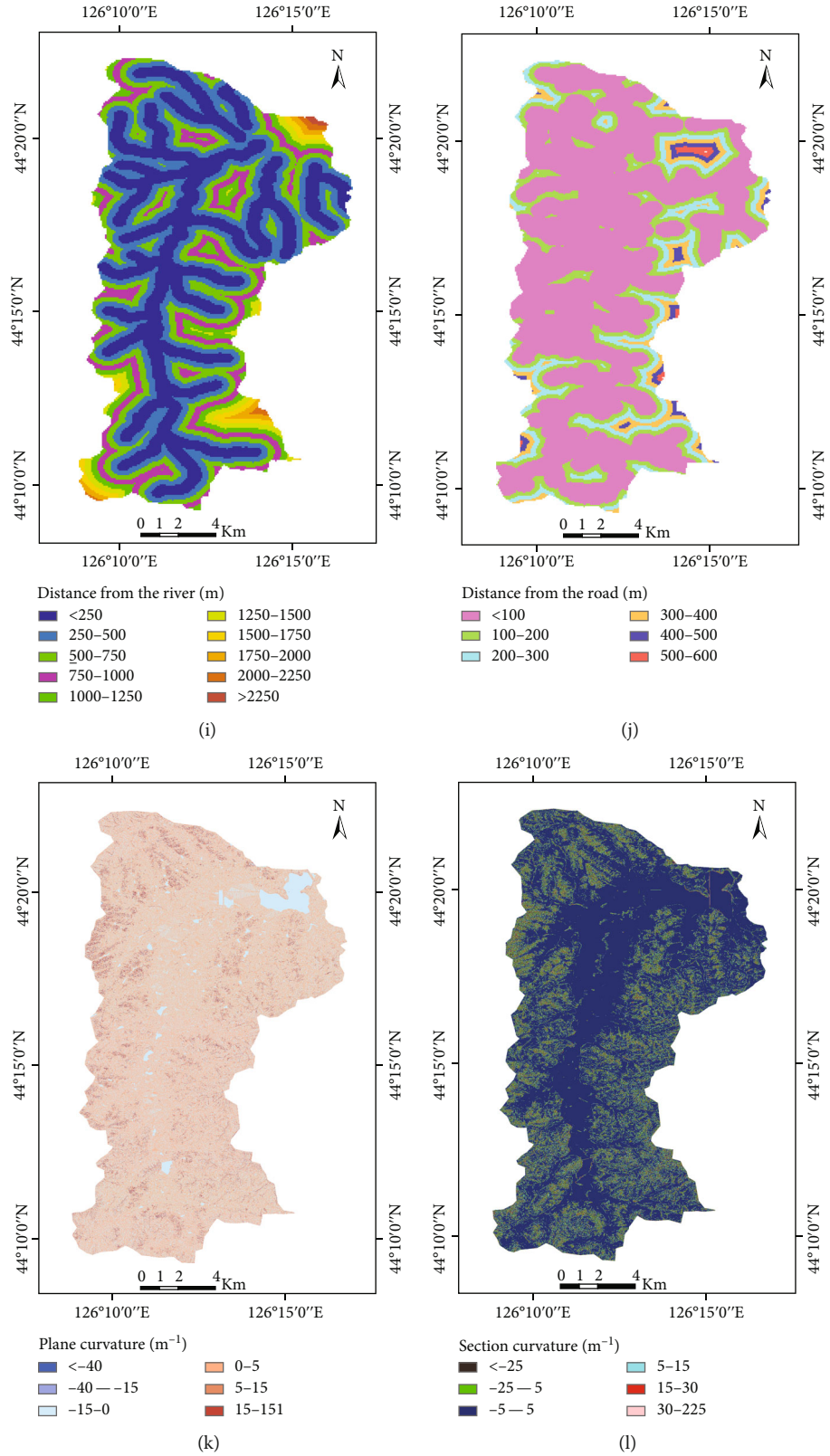

Figure 2: Continued.

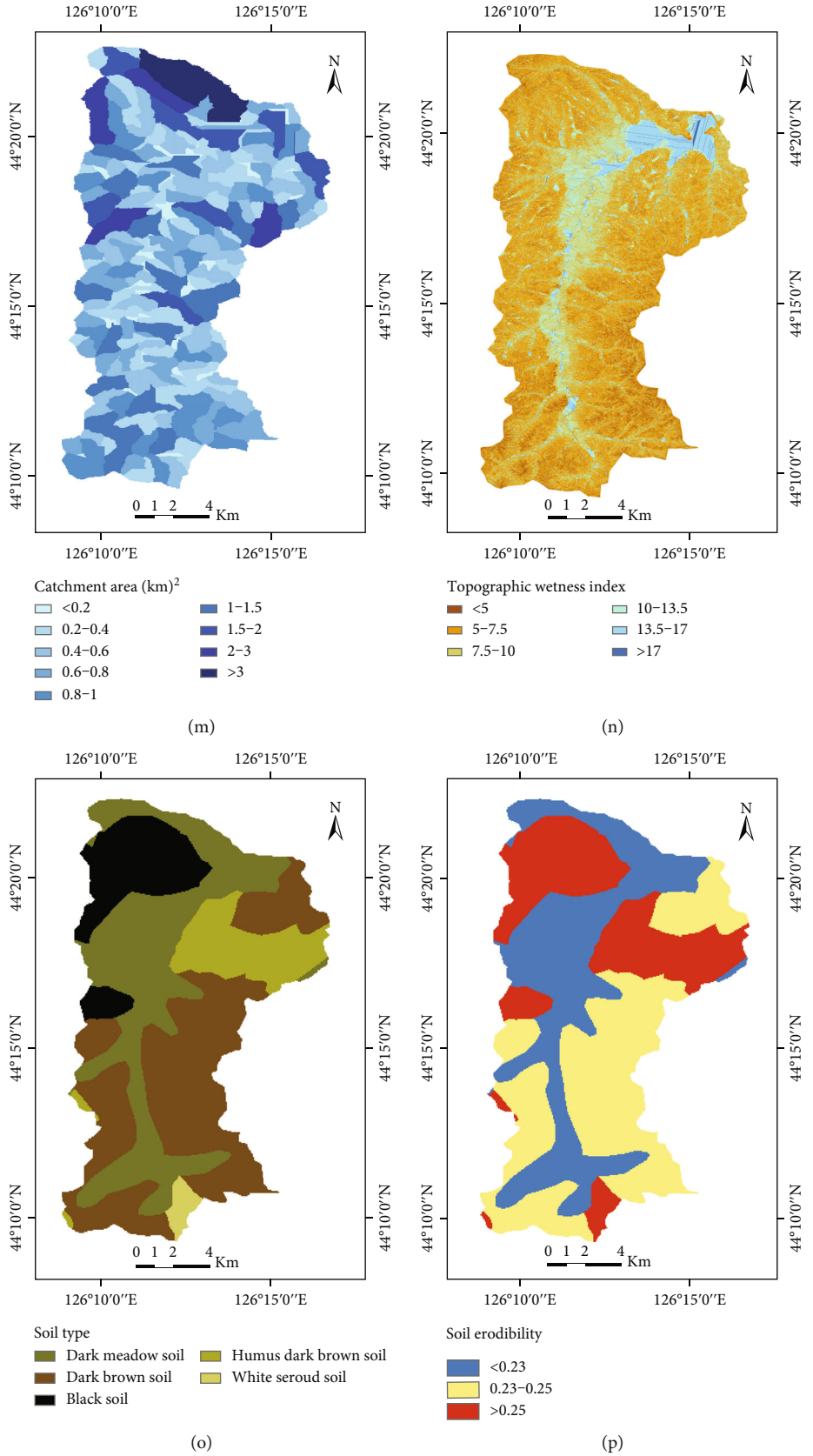

Figure 2: Continued.

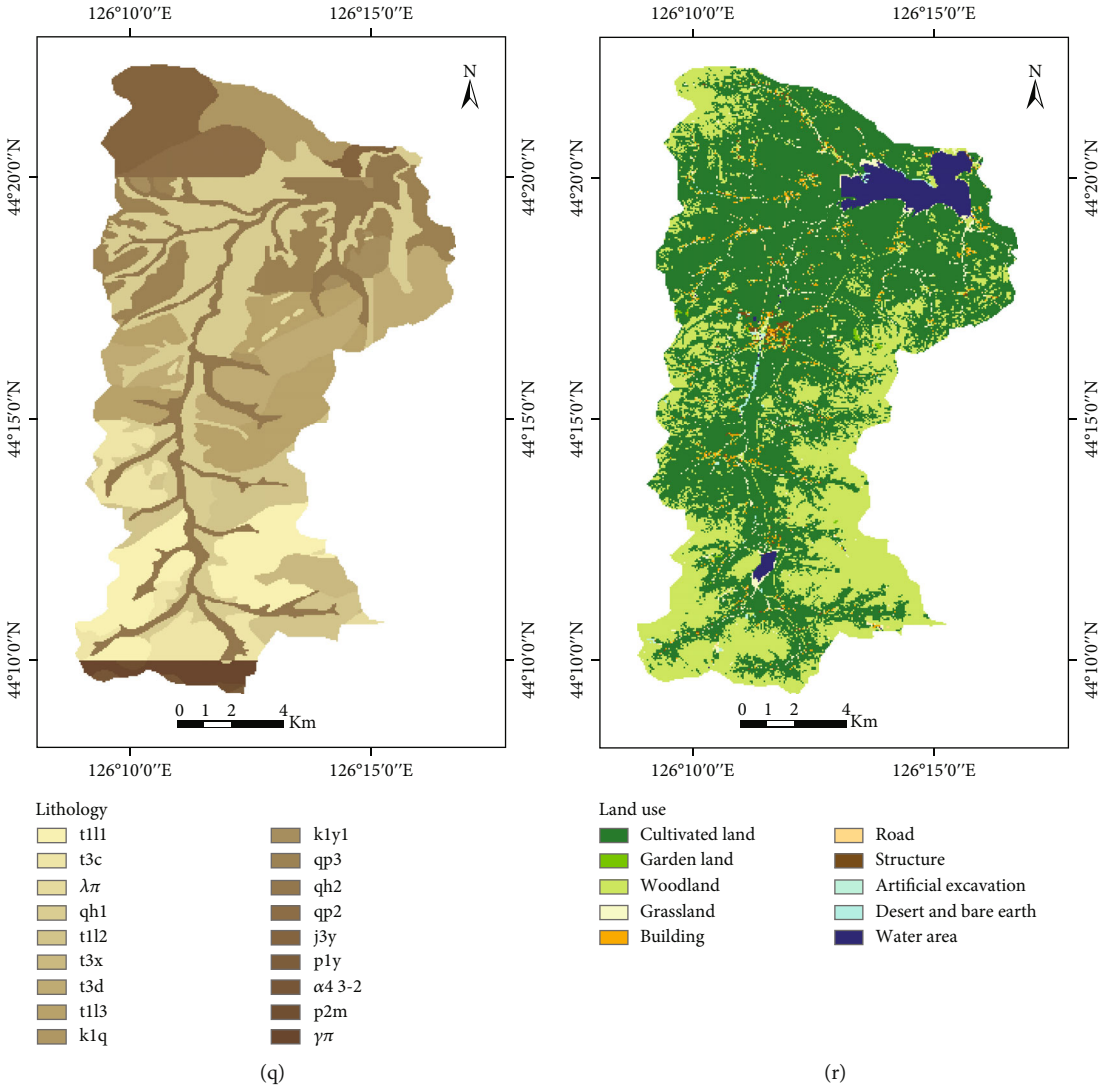

FIGURE 2: Influencing factors on gully erosion ((a) rainfall erosivity, (b) elevation, (c) slope shape, (d) slope aspect, (e) slope position, (f) slope degree, (g) slope length, (h) distance from residential area, (i) distance from the river, (j) distance from the road, (k) plane curvature, (l) sectional curvature, (m) catchment area, (n) topographic wetness index, (o) soil type, (p) soil erodibility, (q) lithology, and (r) land use).

where $h = 1, \cdots, L$ is the layer of independent variable X, N_h and N are the number of sample units in layer h and the total region, respectively, and ${\sigma_h}^2$ and σ^2 are the variance in the h layer and the variance in the region. The q value lies in [0, 1]. If factor X completely controls the soil erosion, the q value equals 1; if the factor X is completely unrelated to Y, the q value equals 0

(2) The interaction detector compares the comprehensive contributions of two separate risk factors to the spatial differentiation of gully erosion, as well as their independent contributions. By doing so, it assesses whether the two risk factors weaken or reinforce each other, or whether they independently affect the spatial differentiation of gullies (Table 3)

(3) Risk area detection can evaluate the differences in different driving factors in different areas of the study area and can be used to identify the distribution of gully erosion in different areas, which can be tested by t statistics

(4) The ecological detector evaluates whether the two risk factors are significantly different in the distribution and development of gully erosion. It also uses F-tests to compare the variance calculated in a subregion attributed to one risk factor with the variance attributed to another risk factor

Discretization is aimed at transforming continuous data into discrete data. Compared with continuous data, discrete data are easier to understand, use, and explain and are closer to a knowledge-level representation [44]. Data discretization is the process whereby continuous data are divided into several intervals with selected cut points, where each interval is mapped to a qualitative symbol. A cut point is a value from

Table 1: Information on factors affecting gully erosion.

	Factors	Date type	Scale/resolution
Climate and weather factors	Rainfall erosivity (X_1)	Raster	500 m
Topography factors	Elevation (X_2)	Raster	5 m
	Slope shape (X_3)		
	Slope aspect (X_4)		
	Slope position (X_5)		
	Slope degree (X_6)		
	Slope length (X_7)		
	Plane curvature (X_{11})		
	Sectional curvature (X_{12})		
	Catchment area (X_{13})		
	Topographic wetness index (X_{14})		
Soil properties	Soil type (X_{15})	Feature	1 : 1,000,000
	Soil erodibility ($X_{16}16$)	Raster	500 m
Lithology	Lithology (X_{17})	Feature	1 : 50000
Land use	Land use (X_{18})	Feature	1 : 10000
Other factors	Distance from residential area (X_8)	Raster	10 m
	Distance from the river (X_9)		
	Distance from the road (X_{10})		

Table 2: Interpretation signs on Pleiades images.

Location	Pleiades images	Ground photos
126.137°E 44.213°N		
126.261°E 44.301°N		

the adjacent continuous data that divides them into two intervals. In actual applications, researchers always discretize continuous data with user-defined discretization and select the cut points according to their experience [45]. In this study, soil erodibility and distance from the residential area are divided into 4 grades. Soil type and slope shape are divided into 5 grades. Slope position, slope length, elevation, plane curvature, section curvature, distance from the road, and terrain wetness index are divided into 6 grades. Rainfall erosivity is divided into 8 grades. Regarding slope aspect, the catchment area is divided into 9 grades. Land use and distance from rivers are divided into 10 grades. Lithology is divided into 18 grades. In the process of division, while the soil type, slope shape, slope aspect, and land use are divided

Table 3: Types of interaction between two covariates.

Criterion	Interaction
$q(X_1 \cap X_2) < \mathrm{Min}(q(X_1), q(X_2))$	Weakened, nonlinear
$\mathrm{Min}(q(X_1), q(X_2)) < q(X_1 \cap X_2) < \mathrm{Max}(q(X_1), q(X_2))$	Weakened, single factor nonlinear
$q(X_1 \cap X_2) > \mathrm{Max}(q(X_1), q(X_2))$	Enhanced, double factors
$q(X_1 \cap X_2) = q(X_1) + q(X_2)$	Independent
$q(X_1 \cap X_2) > q(X_1) + q(X_2)$	Enhanced, nonlinear

by a fixed cut point, the other factors are divided by the natural breaks (NB) method. The Fishnet tool in ArcGIS was used to extract the raster data to points. The sampling interval was set to 74 m. A total of 29876 points were extracted and used as the operating data for the geodetector.

3. Results

3.1. Analysis of the Spatial Variation in Gully Erosion. Remote sensing data need to be verified by a field investigation to ensure the accuracy of gully erosion mapping and correct errors. In the field validation work, 20 gullies were observed and recorded at the Jilin Continuous Operation Reference Station (JLORS), installed with Trimble equipment. The indoor study showed that 18 gullies were captured correctly, while a roadside gully was omitted and another field path was mistaken for an ephemeral gully (Table 4). Nevertheless, the overall accuracy of gully interpretation reached 90%, and the very-high-resolution (submeter) satellite image showed a strong capacity for the detection of various gully types.

Based on the high-resolution images, gullies were extracted by visual interpretation and field investigation (Figure 3). There were 611 gullies in 2018, with a total area of 128.31 km and 0.86 km^2. According to the distribution map of gully density and intensity in 2018, it could be seen that the area with higher gully density was concentrated in the northeast. The overall distribution was more uniform, and the highest density reached 10.55 km/km^2. The distribution area of gully intensity was concentrated in the northeast and south, with less in the north, and the highest reached 158457 m^2/km^2. The areas with high gully density and intensity in the study area were all in the northeast, which may have been due to the high soil erodibility in the northeast, where soil is more prone to erosion. The gully density of the whole area was 505.98 m/km^2 and the average gully intensity was 3412.29 m^2/km^2.

3.2. Geodetector-Based Quantitative Attribution Analysis of Gully Erosion

3.2.1. Significance Analysis of Factors Affecting Gully Erosion. The spatial differentiation of gully density and intensity in 2018 was attributed to the geodetector mode, and the detection results are shown in Table 5. The ability of different factors to explain the spatial distribution of gully density and intensity was as follows: gully density: lithology (X_{17}) > soil type (X_{15}) > rainfall erosivity (X_1) > elevation (X_2) > soil erodibility (X_{16}) > land use (X_{18}) > slope degree (X_6) > distance from the river (X_9) > topographic wetness index (X_{14}) > catchment area (X_{13}) > distance from residential area (X_8) > distance from the road (X_{10}) > slope shape (X_3) > slope aspect (X_4) > slope length (X_7) > slope position (X_5) > plane curvature (X_{11}) > section curvature (X_{12}). Gully intensity: lithology (X_{17}) > soil type (X_{15}) > rainfall erosivity (X_1) > elevation (X_2) > soil erodibility (X_{16}) > catchment area (X_{13}) > slope degree (X_6) > land use (X_{18}) > distance from river (X_9) > topographic wetness index (X_{14}) > slope direction (X_4) > slope shape (X_3) > distance from road (X_{10}) > slope position (X_5) > distance from residential area (X_8) > slope length (X_7) > plane curvature (X_{11}) > sectional curvature (X_{12}). It can be seen that different factors have different explanatory power with regard to gully density and intensity, indicating that lithology and soil type are the main factors affecting gully erosion distribution. Among them, the explanatory power of lithology and soil type is the highest, the explanatory power of erosion density is 12.9% and 9.9%, respectively, and the explanatory power of erosion intensity is 12.7% and 11.1%, respectively, which is the main influencing factor. The explanatory power of rainfall erosivity, catchment area, elevation, soil erodibility, land use, slope, and distance from the road for gully density and intensity is more than 1%; thus, they are secondary influencing factors. The explanatory power of the terrain wetness index, settlement distance, distance from the road, slope aspect, slope length, slope position, slope shape, plane curvature, and profile curvature is less than 1%, and their influence is low.

3.2.2. Analysis of Interactions between Factors Affecting Gully Erosion. When most of the factors interact, their explanatory power of each one is enhanced. The main conclusion is that the explanatory power of the interaction between two factors is higher than that of a single factor. Among them, the dominant factors represented by lithology are more obvious. The following table considers the interactions among dominant factors in the spatial distribution of gully density and intensity (Tables 6 and 7).

The following describes the interaction relationship between the dominant factors in the spatial distribution of gully density: $X_{17} \cap X_{15}(0.287) > X_{17} \cap X_{16}(0.229) > X_{17} \cap X_{13}(0.224) > X_{17} \cap X_1(0.217) > X_{17} \cap X_2(0.214) > X_{17} \cap X_{18}(0.211) > X_{17} \cap X_{10}(0.188) > X_{17} \cap X_9(0.1722) > X_{17} \cap X_6(0.1715) > X_{17} \cap X_4(0.1542) > X_{17} \cap X_8(0.1538) > X_{17} \cap X_{14}(0.150) > X_{17} \cap X_5(0.145) > X_{17} \cap X_{12}(0.1364) > X_{17} \cap X_7(0.1356) > X_{17} \cap X_{11}(0.134) > X_{17} \cap X_3(0.131)$. The following describes the interactive relationship between the dominant factors in the spatial distribution of gully intensity: $X_{17} \cap X_{15}(0.325) > X_{17} \cap X_{16}(0.249) > X_{17} \cap X_{13}(0.241) > X_{17} \cap X_1(0.203) > X_{17} \cap X_2(0.185) > X_{17} \cap X_{18}(0.178) > X_{17} \cap X_{10}(0.161) > X_{17} \cap X_9(0.156) > X_{17} \cap X_6(0.152) > X_{17} \cap X_4(0.151) > X_{17} \cap X_5(0.146) > X_{17} \cap X_8(0.139) > X_{17} \cap X_{14}(0.138) X_{17} \cap X_{12}(0.131) > X_{17} \cap X_{11}(0.1303) > X_{17} \cap X_7(0.1297) > X_{17} \cap X_3(0.128)$.

The results show that the role of the dominant factors in the spatial distribution of gully density and intensity is roughly

Table 4: Examples of validation results.

Location	Pleiades images	Ground photos	Validation results
126.155°E 44.264°N			√
126.149°E 44.357°N			√
126.134°E 44.217°N			×

the same. There is a nonlinear, enhanced relationship between lithology as the dominant factor and most other factors. Regarding the spatial distribution of gully intensity, only two pairs of factors are independent: the interaction between slope and lithology, slope length, and lithology.

3.2.3. Ecological Detection and Analysis of Factors. Ecological exploration can reflect whether there is a significant difference in the influence of various driving factors on the development of gully erosion. If there is a significant difference between the two factors, we mark it as "Y." If there is no significant difference, it is marked "N." Among the rainfall factors, there is no significant relationship between rainfall and topography and land use; there is only an interaction with soil and lithology. Among the topographic factors, most of them are significantly related to soil, lithology, and land use, but not to rainfall erosion. Among soil and lithologic factors, all factors are significantly related to other factors, among which lithology is particularly prominent. There is a significant relationship between land use and most topographic factors, but not with rainfall, soil, and lithology factors.

3.2.4. Identification of High-Risk Areas of Gully Erosion. According to the risk detection in the geodetector mode, we can obtain the distribution characteristics of gullies and the high-risk areas of gullies. Moreover, we can further judge whether there are significant differences in the amount of erosion between different levels of influencing factors (Table 8). Among them, rainfall erosivity, elevation, slope shape, slope aspect, slope position, slope length, slope, residential distance, distance from river, distance from road, catchment area, terrain wetness index, soil type, soil erodibility, lithology, and land use display significant differences among different levels. Among the rainfall factors, the average value of gully density and intensity is the highest when the rainfall erosivity is between 210 and 211. Among the topographic factors, when the elevation is 220-260 m and the slope is 4-8°, the average value of gully density and intensity is the highest, indicating that the risk of gully erosion is higher on flat land. The lithology belongs to gray–white matter rhyolite, spherulite rhyolite, and crystal clastic tuff, with the highest gully density and intensity.

According to risk detection, on the whole, the soil and lithology are the main factors affecting the distribution of

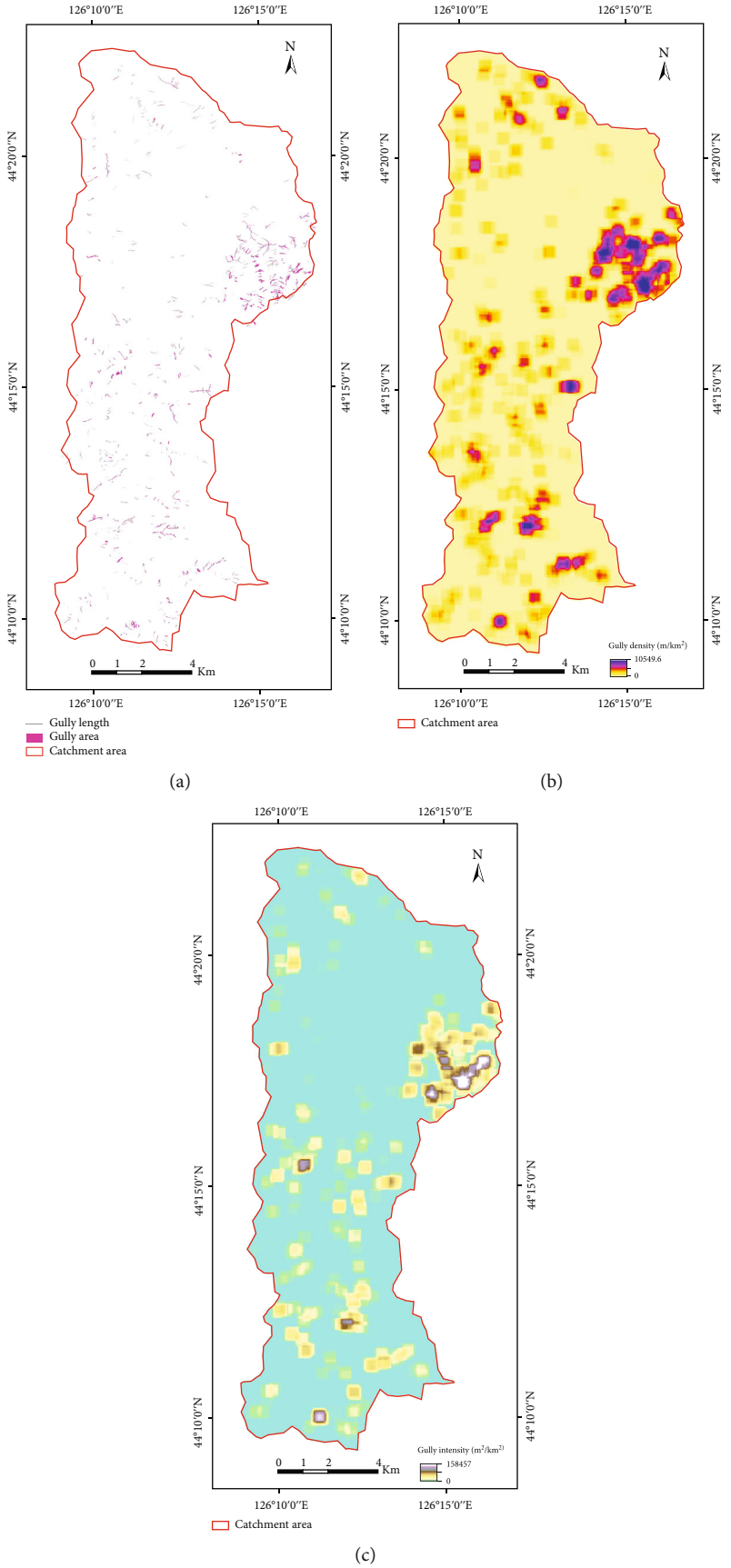

FIGURE 3: The distribution map of (a) gullies, (b) gully density, and (c) gully intensity in the study area.

Table 5: The q values of influencing factors in gully density and intensity.

Influencing factor	X_1	X_2	X_3	X_4	X_5	X_6	X_7	X_8	X_9	X_{10}	X_{11}	X_{12}	X_{13}	X_{14}	X_{15}	X_{16}	X_{17}	X_{18}
Gully density	0.078194	0.067757	0.007711	0.007429	0.003410	0.038331	0.006036	0.009934	0.024270	0.009250	0.000888	0.000735	0.016067	0.017062	0.099009	0.047805	0.128744	0.044721
Gully intensity	0.071288	0.040110	0.004432	0.005618	0.003861	0.024671	0.003204	0.003509	0.012329	0.004022	0.000706	0.000629	0.024898	0.010067	0.110813	0.035174	0.127037	0.016478

Table 6: The dominant interactions between two covariates in gully density.

Interaction	Two-factor q value	The sum of the q values of two factors	Result	Explanation
$X_{17} \cap X_1$	0.217	$>0.207 = X_{17} \cap X_1$	$C > A + B$	Nonlinear enhanced
$X_{17} \cap X_2$	0.214	$>0.197 = X_{17} \cap X_2$	$C > A + B$	Nonlinear enhanced
$X_{17} \cap X_3$	0.131	$>0.129 = X_{17} \cap X_3$	$C > A + B$	Nonlinear enhanced
$X_{17} \cap X_4$	0.154	$>0.136 = X_{17} \cap X_4$	$C > A + B$	Nonlinear enhanced
$X_{17} \cap X_5$	0.145	$>0.132 = X_{17} \cap X_5$	$C > A + B$	Nonlinear enhanced
$X_{17} \cap X_6$	0.172	$>0.167 = X_{17} \cap X_6$	$C > A + B$	Nonlinear enhanced
$X_{17} \cap X_7$	0.136	$>0.134 = X_{17} \cap X_7$	$C > A + B$	Nonlinear enhanced
$X_{17} \cap X_8$	0.154	$>0.139 = X_{17} \cap X_8$	$C > A + B$	Nonlinear enhanced
$X_{17} \cap X_9$	0.172	$>0.153 = X_{17} \cap X_9$	$C > A + B$	Nonlinear enhanced
$X_{17} \cap X_{10}$	0.188	$>0.138 = X_{17} \cap X_{10}$	$C > A + B$	Nonlinear enhanced
$X_{17} \cap X_{11}$	0.134	$>0.130 = X_{17} \cap X_{12}$	$C > A + B$	Nonlinear enhanced
$X_{17} \cap X_{12}$	0.136	$>0.129 = X_{17} \cap X_{12}$	$C > A + B$	Nonlinear enhanced
$X_{17} \cap X_{13}$	0.224	$>0.203 = X_{17} \cap X_{13}$	$C > A + B$	Nonlinear enhanced
$X_{17} \cap X_{14}$	0.150	$>0.146 = X_{17} \cap X_{14}$	$C > A + B$	Nonlinear enhanced
$X_{17} \cap X_{15}$	0.287	$>0.228 = X_{17} \cap X_{15}$	$C > A + B$	Nonlinear enhanced
$X_{17} \cap X_{16}$	0.229	$>0.177 = X_{17} \cap X_{16}$	$C > A + B$	Nonlinear enhanced
$X_{17} \cap X_{18}$	0.211	$>0.173 = X_{17} \cap X_{18}$	$C > A + B$	Nonlinear enhanced

Table 7: The dominant interactions between two covariates in gully intensity.

Interaction	Two-factor q value	The sum of the q values of two factors	Result	Explanation
$X_{17} \cap X_1$	0.203	$>0.198 = X_{17} \cap X_1$	$C > A + B$	Nonlinear enhanced
$X_{17} \cap X_2$	0.185	$>0.167 = X_{17} \cap X_2$	$C > A + B$	Nonlinear enhanced
$X_{17} \cap X_3$	0.128	$>0.127 = X_{17} \cap X_3$	$C > A + B$	Nonlinear enhanced
$X_{17} \cap X_4$	0.151	$>0.133 = X_{17} \cap X_4$	$C > A + B$	Nonlinear enhanced
$X_{17} \cap X_5$	0.146	$>0.131 = X_{17} \cap X_5$	$C > A + B$	Nonlinear enhanced
$X_{17} \cap X_6$	0.152	$= 0.152 = X_{17} \cap X_6$	$C = A + B$	Independent of each other
$X_{17} \cap X_7$	0.130	$= 0.130 = X_{17} \cap X_7$	$C = A + B$	Independent of each other
$X_{17} \cap X_8$	0.139	$>0.131 = X_{17} \cap X_8$	$C > A + B$	Nonlinear enhanced
$X_{17} \cap X_9$	0.156	$>0.139 = X_{17} \cap X_9$	$C > A + B$	Nonlinear enhanced
$X_{17} \cap X_{10}$	0.161	$>0.131 = X_{17} \cap X_{10}$	$C > A + B$	Nonlinear enhanced
$X_{17} \cap X_{11}$	0.130	$>0.128 = X_{17} \cap X_{11}$	$C > A + B$	Nonlinear enhanced
$X_{17} \cap X_{12}$	0.131	$>0.128 = X_{17} \cap X_{12}$	$C > A + B$	Nonlinear enhanced
$X_{17} \cap X_{13}$	0.241	$>0.202 = X_{17} \cap X_{13}$	$C > A + B$	Nonlinear enhanced
$X_{17} \cap X_{14}$	0.138	$>0.137 = X_{17} \cap X_{14}$	$C > A + B$	Nonlinear enhanced
$X_{17} \cap X_{15}$	0.325	$>0.238 = X_{17} \cap X_{15}$	$C > A + B$	Nonlinear enhanced
$X_{17} \cap X_{16}$	0.249	$>0.162 = X_{17} \cap X_{16}$	$C > A + B$	Nonlinear enhanced
$X_{17} \cap X_{18}$	0.178	$>0.144 = X_{17} \cap X_{18}$	$C > A + B$	Nonlinear enhanced

gullies. Regarding land use types, the main influence on the distribution of gully erosion is cultivated land. This may be due to the shortage of woodland caused by residential farming, which further leads to soil erosion. Thus, it can be seen that returning farmland to forests may slow down the development trend of gullies and improve the erosion conditions.

4. Discussion

4.1. Assessment of Gully Erosion Mapping Based on High-Resolution Satellite Imagery. With improvements in image resolution, the ground area represented by a single pixel becomes smaller and smaller, and the same gully is more

Table 8: High-risk areas of gully erosion and its mean value.

Factors	High-risk area of gully density	Average gully density (m/km^2)	High-risk area of gully intensity	Average gully intensity (m^2/km^2)
Rainfall erosivity	210-211	1281.461	210-211	11752.866
Elevation	220-260 m	1197.326	220-260 m	7991.692
Slope shape	Convex slope	856.4095653	Convex slope	5781.986
Slope direction	West slope	948.096	West slope	6605.746
Slope position	Midslope	932.913	Midslope	6706.873
Slope degree	4-8°	1218.920	4-8°	8326.412
Slope length	0-150 m	834.017	0-150 m	5588.848
Residential distance	<0.5	879.799	<0.5	5806.133
Distance from the river	250 m-500 m	955.356	250 m-500 m	6701.476
Distance from the road	100 m-200 m	906.231	200 m-300 m	6452.205
Plane curvature	0-5	857.684	0-5	5802.145
Sectional curvature	-25–-5	880.640	5-15	5990.171
Catchment area	2-3 km^2	1223.724	2-3 km^2	10554.147
Topographic wetness index	5-7.5	939.908	5-7.5	6449.666
Soil type	Humus dark brown soil	1923.932	Humus dark brown soil	17149.954
Soil erodibility	0.27-0.29	1250.745	0.27-0.29	9139.993
Lithology	Gray–white matter rhyolite, globular rhyolite, crystal clastic tuff	3542.989	Gray–white matter rhyolite, globular rhyolite, crystal clastic tuff	22833.733
Land use	Cultivated land	1027.192	Cultivated land	6656.717

likely to appear as pure pixels in the image, while the contour characteristics and internal details of the gullies become clearer. In the opposite case, it will appear in the form of mixed pixels, and the contour features of gully erosion will become more blurred. As shown in Figure 4, the number of pixels constituting the same area of gully erosion increases in the order of "15 m-Landsat8, 3 m-Planet Labs, 2.5 m-Alos, 2 m-ZY3, 0.7 m-Pleiades, 0.5 m-DMC, and 0.04 m-UAV." The number of mixed pixels decreases gradually, and the outline of the gully erosion becomes clearer. Especially for the ramified gully system, when the image resolution increases from 2.5 m, the contour of the gully becomes increasingly recognizable, and the land plots between the gullies can also be distinguished. The ridge planting direction of the land plots between the gully can even be seen in the Pleiades image.

To alleviate the influence of the imaging time and the spectral resolution of different remote sensing images on the analysis results, the resampled Pleiades image was analyzed. As shown in Figure 5, the permanent gully and ephemeral gully on the sloping farmland are visible in the 0.7 m Pleiades image. According to the actual measurement, the average width of the permanent gully marked by the red circle on the drawing is 2.3 m, and the average width of the ephemeral gully is 0.32 m. The contour of the gully is clear, and the ephemeral gully is very easy to identify. However, with the decrease in resolution, the ephemeral gully and permanent gully begin to become blurred. When the resolution is less than 1.5 m, the ephemeral gully becomes difficult to identify. When the resolution is 3 m, the ephemeral gully is "submerged" in the mixed pixels and cannot be identified in the image. Although there is still a gully on the 3 m resolution image, its contour and shape cannot be recognized, and the recognizable length of the trench becomes smaller.

An improvement in the remote sensing image resolution will not only make the image contour characteristics of the gully more obvious but also make its internal structure characteristics clearer. On the scale of 1 : 1000, the internal features of submeter images have little visual difference. However, the opinion that the higher the spatial resolution of remote sensing image, the better remains to be discussed. This is because the improvement in resolution will also bring more noise, which greatly increases the likelihood of obtaining different objects with the same spectral characteristics or the same object with different spectra. The spectral characteristics of the gully mainly depend on the vegetation or soil on its surface, while the spectral values of vegetation or bare soil in the gully are usually consistent with other vegetation or bare soil in the surroundings. The field path is usually easy to misjudge as an ephemeral gully because the spectral and geometric features between them are relatively similar. The improvement in resolution not only

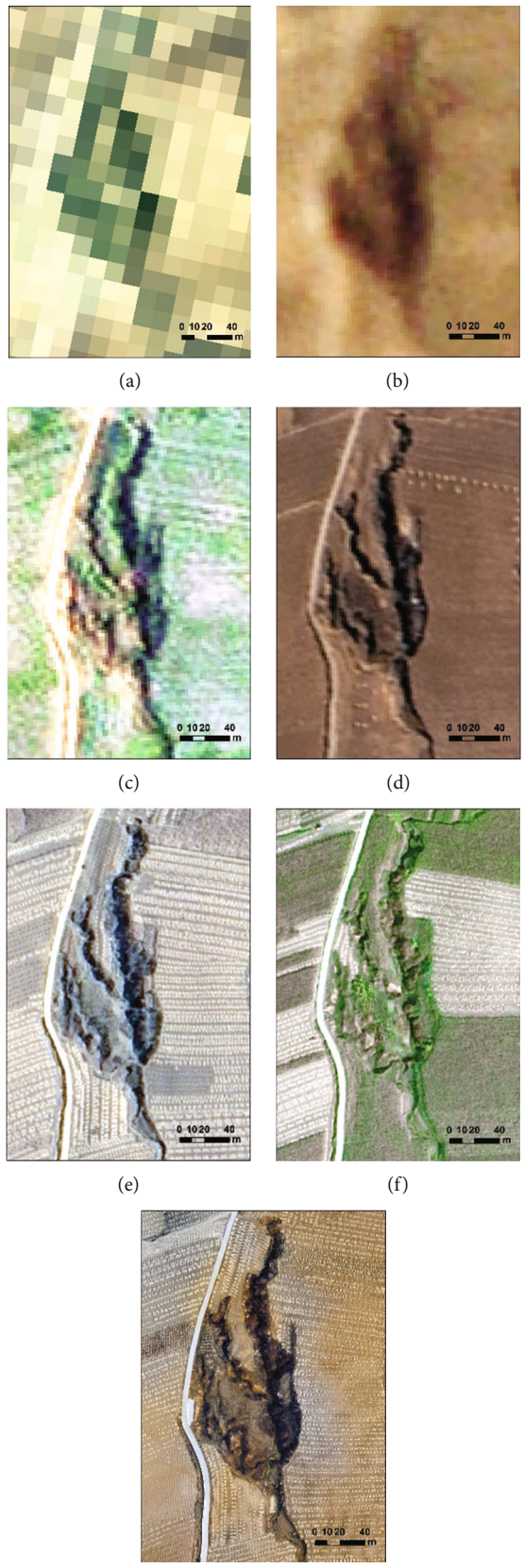

(a) (b) (c) (d) (e) (f) (g)

Figure 4: Image characteristics of branch gully on different images ((a) 15 m-Landsat8, (b) 3 m-Planet Labs, (c) 2.5 m-Alos, (d) 2 m-ZY3, (e) 0.7 m-Pleiades, (f) 0.5 m-DMC, and (g) 0.04 m-UAV).

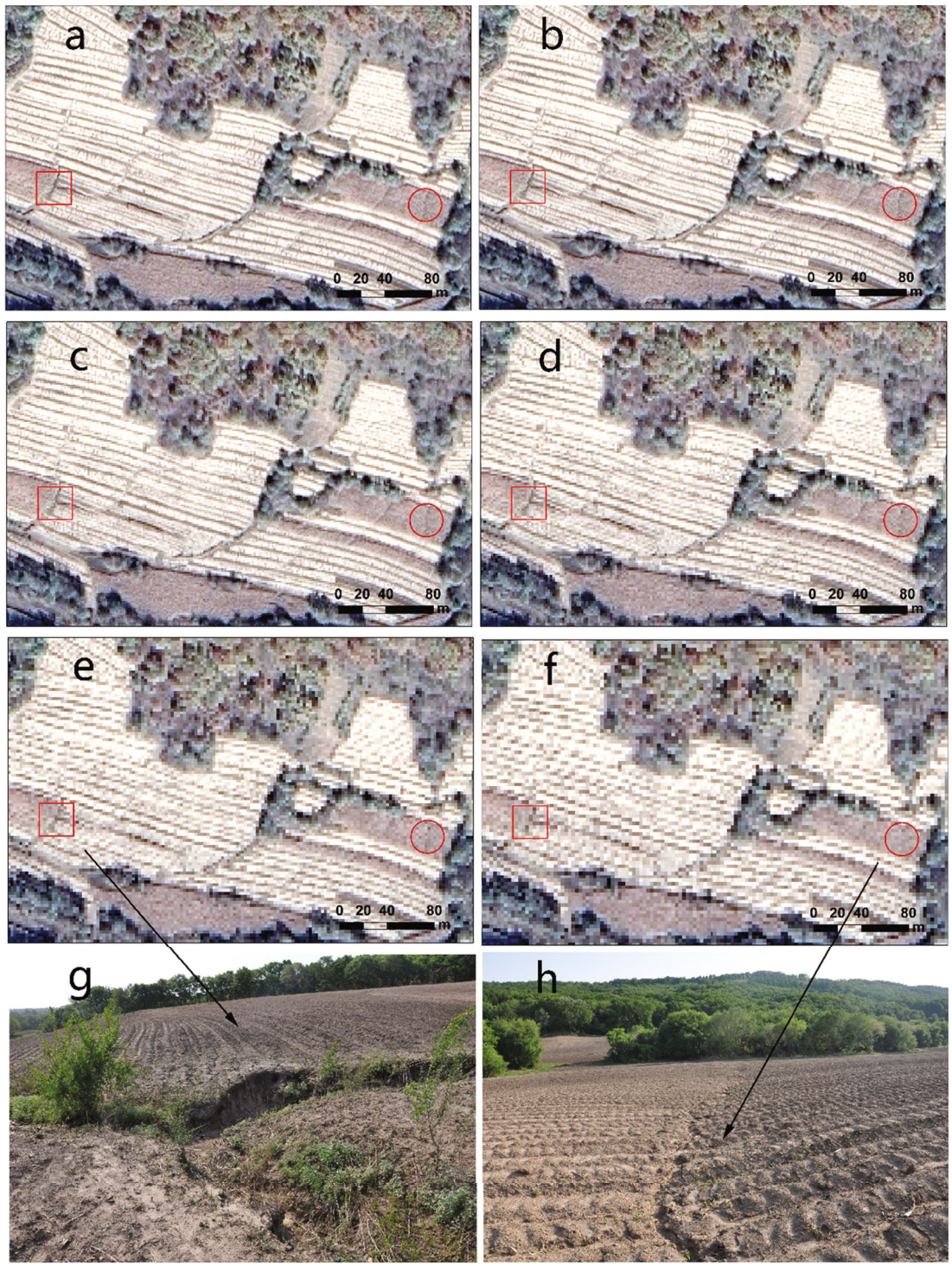

Figure 5: Image characteristics of the permanent gully and ephemeral gully on Pleiades images with different resolutions ((a) 0.7 m, (b) 1 m, (c) 1.5 m, (d) 2 m, (e) 2.5 m, (f) 3 M, and (g, h) photos of the gullies at ground).

improves the ability to identify the ephemeral gully but also improves the ability to find the field path, which is more likely to increase the possibility of misjudging the field path as an ephemeral gully, interfering with the interpretation of the gully. Therefore, the improvement in image resolution will increase the interference noise in remote sensing identification and impede the information extraction of the gully.

4.2. Analysis of Controlling Factors of Gully Erosion. In this study, the geodetector-based quantitative attribution results showed that lithology, soil type, rainfall erosivity, catchment area, elevation, soil erodibility, land use, slope degree, and distance from the river have a strong influence on the development of gully erosion. Other factors, such as TWI, slope shape, slope aspect, slope position, slope length, distance from

the residential area, distance from the road, plane curvature, and section curvature, cannot sufficiently explain the changes and development of gully erosion. However, the interaction of these factors with lithology, soil type, and land use shows a stronger influence on the development of gully erosion.

The formation and expansion of gullies is commonly influenced by particular soil characteristics and behavior. The most relevant properties are likely soil texture characteristics (e.g., percentage of sand, silt, and clay) and soil organic carbon content [46]. Moreover, the underlying lithology can play an important role in determining the occurrence and dimensions of gullies [47]. In this study, soil and lithology played a more important role. The explanatory power of lithology with regard to the spatial distribution of gullies was more than 10%. When the lithology belonged to gray–white matter rhyolite, globular rhyolite, and crystal clastic tuff, the gully erosion risk reached the highest level. The explanatory power of soil type regarding gully density was close to 10%, and the explanatory power for gully intensity was more than 10%, indicating that this is the dominant factor. When the soil type was humus dark brown soil, the risk of gully erosion was the greatest.

Topographic variables play a key role in the prediction of both gully initiation and expansion. The present results showed that elevation, slope, and catchment area have a significant influence on the occurrence of gully erosion. These findings are similar to those of previous studies in the black soil region [5, 48]. Climate and weather conditions, and especially rainfall, are key drivers of gully erosion. According to the results of the geodetector model, it can be seen that the impact of rainfall erosivity on the distribution of gully erosion is obvious, showing a trend of first increasing, then decreasing, and then increasing. However, due to the lack of meteorological stations in the basin, rainfall erosivity is obtained by interpolating the surrounding meteorological stations' data, which would increase the uncertainty of the results. Land cover/use can influence gully initiation through its effect on runoff production [49]. In this study, the type of land use had a significant effect on the distribution of gully erosion, and its explanatory power with regard to gully density and intensity was 4.47% and 1.65%, respectively. Among them, cultivated land has the greatest impact, which may be due to the frequent human activities on cultivated land. This result is consistent with some previous studies [50, 51]. For example, the results of Ali Azareh et al.'s study in 2019 showed that slope aspect, lithology, and land use were identified as the most important factors affecting gully sensitivity in Iran by using a maximum entropy model [3]. However, this contradicts our findings. We believe that the reason for the difference may be that the geographical environment and hydrological conditions of the study area were not fully considered in the selection of impact factors. The slope degree of sloping farmland in the black soil region in Northeast China is mostly 3°-10°. As a result, slope has no significant influence on gully erosion in Northeast China. Lithology and land use are the main factors affecting the distribution of gully erosion, which is consistent with our results.

According to the results of the geodetector, the interaction of most factors showed nonlinear enhancement, which indicated that a gully is more likely to occur under the combined action of various factors. The most influential interaction groups were lithology with other factors, especially lithology in different soil types. In particular, the lithology of different soil types accounted for 28.7% and 32.5% of gully density and gully intensity, which also reflects the dominant role of lithology and soil. The interaction of lithology and land use also had a significant effect on gully erosion, which demonstrates the importance of returning cropland to forest in the process of gully erosion control in Northeast China. The results show that the interaction between lithology and soil, topography, rainfall, and land use factors can significantly improve the explanatory power in terms of gully erosion development, and the interactive q values are more than 10%. Only two pairs of factors are independent: (1) slope and lithology and (2) slope length and lithology.

The geodetector revealed the single and paired driving factors affecting the spatial differentiation of gully erosion in Northeast China and enriched the research content on gully erosion in this area. The results show that the interaction effect of soil type, land use type, and lithology is stronger than that of a single factor. This shows that the prevention and control of gullies should not only start from the main risk factors but also from the perspective of the whole. However, there are still some shortcomings. Interaction analysis based on a geodetector can only evaluate the interaction of two factors—it cannot analyze the interaction of more than two factors.

5. Conclusion

The present work represents a contribution to the multifactor synthesis for gully erosion at a large watershed scale. The Sancha River basin, a typical area in the black soil region of Northeast China, was taken as the study area. A high-resolution satellite image was used to obtain the spatial distribution of the gullies by visual image interpretation with field verification. We analyzed the dominant factors affecting the spatial distribution of gully erosion and the degree of interaction between any two of these factors using the geodetector method, and we identified areas at high risk of gully erosion between strata of each factor. The following conclusions were obtained:

(1) At the large catchment scale, the submeter images show a strong capacity for the recognition of permanent gullies and obtained satisfactory results

(2) According to the results of the geodetector, lithology and soil type are the main factors that affect the spatial differentiation of gully erosion in the Sancha River basin. The interpretation power of gully density and gully intensity is close to 10%, and the explanatory power of gully erosion occurrence is greater. As rainfall erosivity, watershed area, elevation, soil erodibility, land use pattern, slope, and distance from the river accounted for more than 1% of gully density and gully intensity, they were identified as secondary factors

(3) The interaction detection results of the geodetector show that there is a nonlinear enhancement relationship between lithology and most factors. In particular, the lithology of different soil types accounted for 28.7% and 32.5% of gully density and gully intensity. The results show that the interaction between lithology and soil, topography, rainfall, and land use factors can significantly improve the explanatory power of gully erosion development, and the interactive q values reached more than 10%. The results show that the interaction of several factors has a stronger influence on the spatial differentiation of gully erosion than a single factor. The prevention and control of gullies should not only start from the main risk factors but also from the perspective of the whole

(4) The lithology belongs to gray–white matter rhyolite, spherulite rhyolite, and crystal clastic tuff, with the highest gully density and intensity

Data Availability

The data are available and explained in this article; readers can access the data supporting the conclusions of this study.

Conflicts of Interest

The authors declare no conflicts of interest.

Acknowledgments

We thank our partners who provided assistance during the research process and the team for their great support. This research was supported by the Natural Science Foundation of Jilin Province (No. 20200201040JC), the National Natural Science Foundation of China (Nos. 42171380 and 41801350), the Natural Science Foundation for Youth of Shanxi Province (No. 201901D211119), and the Scientific and Technological Innovation Programs of Higher Education Institutions in Shanxi (No. 2020L0042).

References

[1] J. Poesen, J. Nachtergaele, G. Verstraeten, and C. Valentin, "Gully erosion and environmental change: importance and research needs," *Catena*, vol. 50, no. 2-4, pp. 91–133, 2003.

[2] A. Gayen, H. R. Pourghasemi, S. Saha, S. Keesstra, and S. Bai, "Gully erosion susceptibility assessment and management of hazard-prone areas in India using different machine learning algorithms," *Science of The Total Environment*, vol. 668, pp. 124–138, 2019.

[3] A. Azareh, O. Rahmati, E. Rafiei-Sardooi et al., "Modelling gully-erosion susceptibility in a semi-arid region, Iran: investigation of applicability of certainty factor and maximum entropy models," *Science of The Total Environment*, vol. 655, pp. 684–696, 2019.

[4] B. Liu, B. Yan, B. Shen, Z. Wang, and X. Wei, "Current status and comprehensive control strategies of soil erosion for cultivated land in the northeastern black soil area of China," *Science of Soil and Water Conservation*, vol. 6, no. 1, pp. 1–8, 2008.

[5] G. Hu, Y. Wu, B. Liu, Z. Yu, Z. You, and Y. Zhang, "Short-term gully retreat rates over rolling hill areas in black soil of Northeast China," *Catena*, vol. 71, no. 2, pp. 321–329, 2007.

[6] S. Zhang, F. Li, T. Li et al., "Remote sensing monitoring of gullies on a regional scale: a case study of Kebai region in Heilongjiang Province, China," *Chinese Geographical Science*, vol. 25, no. 5, pp. 602–611, 2015.

[7] Q. Wei, W. Qin, C. Zuo, J. Fan, X. Xu, and J. Xu, "Control measures for gully erosion in black soil areas of Northeast China," *China Water Resources*, vol. 20, pp. 37–41, 2014.

[8] J. C. Yang, S. Zhang, L. Chang, F. Li, T. Li, and Y. Gao, "Gully erosion regionalization of black soil area in northeastern China," *Chinese Geographical Science*, vol. 27, no. 1, pp. 78–87, 2017.

[9] L. Vandekerckhove, J. Poesen, D. Oostwoud Wijdenes, and G. Gyssels, "Short-term bank gully retreat rates in Mediterranean environments," *Catena*, vol. 44, no. 2, pp. 133–161, 2001.

[10] J. Casali, J. Loizu, M. A. Campo, L. M. De Santisteban, and J. Álvarez-Mozos, "Accuracy of methods for field assessment of rill and ephemeral gully erosion," *Catena*, vol. 67, no. 2, pp. 128–138, 2006.

[11] C. Castillo, R. Pérez, M. R. James, J. N. Quinton, E. V. Taguas, and J. A. Gómez, "Comparing the accuracy of several field methods for measuring gully erosion," *Soil Science Society of America Journal*, vol. 76, no. 4, pp. 1319–1332, 2012.

[12] I. Ionita, "Gully development in the Moldavian Plateau of Romania," *Catena*, vol. 68, no. 2-3, pp. 133–140, 2006.

[13] Y. Wu and H. Cheng, "Monitoring of gully erosion on the Loess Plateau of China using a global positioning system," *Catena*, vol. 63, no. 2-3, pp. 154–166, 2005.

[14] Y. Wu, Q. Zheng, Y. Zhang, B. Liu, H. Cheng, and Y. Wang, "Development of gullies and sediment production in the black soil region of northeastern China," *Geomorphology*, vol. 101, no. 4, pp. 683–691, 2008.

[15] C. Gong, S. Lei, Z. Bian, Y. Liu, Z. Zhang, and W. Cheng, "Analysis of the development of an erosion gully in an open-pit coal mine dump during a winter freeze-thaw cycle by using low-cost UAVs," *Remote Sensing*, vol. 11, no. 11, p. 1356, 2019.

[16] C. Stöcker, A. Eltner, and P. Karrasch, "Measuring gullies by synergetic application of UAV and close range photogrammetry — a case study from Andalusia, Spain," *Catena*, vol. 132, pp. 1–11, 2015.

[17] Y. Yan, S. Yue, and S. Zhang, "Application of corona and spot imagery on erosion gully research in typical black soil regions of Northeast China," *Resources Science*, vol. 27, no. 8, pp. 650–656, 2006.

[18] Q. Xu, P. Kou, C. Wang et al., "Evaluation of gully head retreat and fill rates based on high-resolution satellite images in the loess region of China," *Environmental Earth Sciences*, vol. 78, no. 15, p. 465, 2019.

[19] R. B. V. Shruthi, N. Kerle, V. Jetten, L. Abdellah, and I. Machmach, "Quantifying temporal changes in gully erosion areas with object oriented analysis," *Catena*, vol. 128, pp. 262–277, 2015.

[20] N. Morueta-Holmea, K. Engemann, P. Sandoval-Acuña, J. D. Jonas, R. M. Segnitz, and J.-C. Svenning, "Reply to Feeley and Rehm: land-use intensification increases risk of species

losses from climate change," *Proceedings of the National Academy of Sciences of the United States of America*, vol. 112, no. 45, article E6085, 2015.

[21] Y. Ma, P. Yan, G. Wang et al., "Preliminary results of gully erosion by remote sensing monitoring in Weiliantan, Gonghe basin, Qinghai Province," *Research of Soil and Water Conservation*, vol. 16, pp. 1–5, 2009.

[22] Z. Li and J. Balcom, "Estimating gully development rates in hilly loess region of western Shanxi province based on QuickBird images," *Transactions of the Chinese Society of Agricultural Engineering*, vol. 28, pp. 141–148, 2012.

[23] Y. Wen, T. Kasielke, H. Li, H. Zepp, and B. Zhang, "A case-study on history and rates of gully erosion in Northeast China," *Land Degradation & Development*, vol. 32, no. 15, pp. 4254–4266, 2021.

[24] B. Wang, Z. Zhang, X. Wang, X. Zhao, L. Yi, and S. Hu, "Object-based mapping of gullies using optical images: a case study in the black soil region, Northeast of China," *Remote Sensing*, vol. 12, no. 3, p. 487, 2020.

[25] J. Xu, H. Li, X. B. Liu et al., "Gully erosion induced by snowmelt in Northeast China: a case study," *Sustainability*, vol. 11, no. 7, p. 2088, 2019.

[26] Y. Dong, Y. Wu, W. Qin, Q. Guo, Z. Yin, and X. Duan, "The gully erosion rates in the black soil region of northeastern China: induced by different processes and indicated by different indexes," *Catena*, vol. 182, article 104146, 2019.

[27] M. Vanmaercke, J. Poesen, B. van Mele et al., "How fast do gully headcuts retreat?," *Earth-Science Reviews*, vol. 154, pp. 336–355, 2016.

[28] X. Lei, W. Chen, M. Avand et al., "GIS-based machine learning algorithms for gully erosion susceptibility mapping in a semi-arid region of Iran," *Remote Sensing*, vol. 12, no. 5, article 2478, 2020.

[29] D. Tien Bui, A. Shirzadi, H. Shahabi et al., "A novel ensemble artificial intelligence approach for gully erosion mapping in a semi-arid watershed (Iran)," *Sensors*, vol. 19, no. 11, article 2444, 2019.

[30] V.-H. Nhu, S. Janizadeh, M. Avand et al., "Gis-based gully erosion susceptibility mapping: a comparison of computational ensemble data mining models," *Applied Sciences*, vol. 10, no. 6, article 2039, 2020.

[31] H. Wang, J. Gao, and W. Hou, "Quantitative attribution analysis of soil erosion in different geomorphological types in karst areas: based on the geodetector method," *Journal of Geographical Sciences*, vol. 29, no. 2, pp. 271–286, 2019.

[32] J. Han, Y. Liu, and Y. Zhang, "Sand stabilization effect of feldspathic sandstone during the fallow period in Mu Us Sandy Land," *Journal of Geographical Sciences*, vol. 25, no. 4, pp. 428–436, 2015.

[33] X. Yuan, J. Han, Y. Shao, Y. Li, and Y. Wang, "Geodetection analysis of the driving forces and mechanisms of erosion in the hilly-gully region of northern Shaanxi Province," *Journal of Geographical Sciences*, vol. 29, no. 5, pp. 779–790, 2019.

[34] Y. Zhao, L. Liu, S. Kang, Y. Ao, L. Han, and C. Ma, "Quantitative analysis of factors influencing spatial distribution of soil erosion based on geo-detector model under diverse geomorphological types," *Land*, vol. 10, no. 6, p. 604, 2021.

[35] O. Rahmati, N. Tahmasebipour, A. Haghizadeh, H. R. Pourghasemi, and B. Feizizadeh, "Evaluating the influence of geo-environmental factors on gully erosion in a semi-arid region of Iran: an integrated framework," *Science of The Total Environment*, vol. 579, pp. 913–927, 2017.

[36] A. Arabameri, W. Chen, L. Lombardo, T. Blaschke, and D. Tien Bui, "Hybrid computational intelligence models for improvement gully erosion assessment," *Remote Sensing*, vol. 12, no. 1, p. 140, 2020.

[37] T. Grabs, J. Seibert, K. Bishop, and H. Laudon, "Modeling spatial patterns of saturated areas: a comparison of the topographic wetness index and a dynamic distributed model," *Journal of Hydrology*, vol. 373, no. 1-2, pp. 15–23, 2009.

[38] K. Auerswald, P. Fiener, W. Martin, and D. Elhaus, "Use and misuse of the K factor equation in soil erosion modeling: an alternative equation for determining USLE nomograph soil erodibility values," *Catena*, vol. 118, pp. 220–225, 2014.

[39] C. F. Lee, J. Li, Z. W. Xu, and F. C. Dai, "Assessment of landslide susceptibility on the natural terrain of Lantau Island, Hong Kong," *Environmental Geology*, vol. 40, no. 3, pp. 381–391, 2001.

[40] V. Agnesi, S. Angileri, C. Cappadonia, C. Conoscenti, and E. Rotigliano, "Multiparametric GIS analysis to assess gully erosion susceptibility: a test in southern Sicily, Italy," *Landform Analysis*, vol. 7, pp. 15–20, 2011.

[41] J. Lesschen, K. Kok, P. H. Verburg, and L. H. Cammeraat, "Identification of vulnerable areas for gully erosion under different scenarios of land abandonment in Southeast Spain," *Catena*, vol. 71, no. 1, pp. 110–121, 2007.

[42] R. Wang, S. Zhang, J. Yang et al., "Integrated use of GCM, RS, and GIS for the assessment of hillslope and gully erosion in the Mushi River sub-catchment, Northeast China," *Sustainability*, vol. 8, no. 4, p. 317, 2016.

[43] J. F. Wang, X. H. Li, G. Christakos et al., "Geographical detectors-based health risk assessment and its application in the neural tube defects study of the Heshun region, China," *International Journal of Geographical Information Science*, vol. 24, no. 1, pp. 107–127, 2010.

[44] H. Liu, F. Hussain, C. L. Tan, and M. Dash, "Discretization: an enabling technique," *Data Mining and Knowledge Discovery*, vol. 6, no. 4, pp. 393–423, 2002.

[45] Y. Liao, J. Wang, Y. Guo, and X. Zheng, "Risk assessment of human neural tube defects using a Bayesian belief network," *Stochastic Environmental Research and Risk Assessment*, vol. 24, no. 1, pp. 93–100, 2010.

[46] P. Panagos, K. Meusburger, C. Ballabio, P. Borrelli, and C. Alewell, "Soil erodibility in Europe: a high-resolution dataset based on LUCAS," *Science of the Total Environment*, vol. 479-480, pp. 189–200, 2014.

[47] L. Hopp and J. J. McDonnell, "Connectivity at the hillslope scale: identifying interactions between storm size, bedrock permeability, slope angle and soil depth," *Journal of Hydrology*, vol. 376, no. 3-4, pp. 378–391, 2009.

[48] R. Wang, S. Zhang, L. Pu et al., "Gully erosion mapping and monitoring at multiple scales based on multi-source remote sensing data of the Sancha River catchment, Northeast China," *ISPRS International Journal of Geo-Information*, vol. 5, no. 11, p. 200, 2016.

[49] D. Torri and J. Poesen, "A review of topographic threshold conditions for gully head development in different environments," *Earth-Science Reviews*, vol. 130, pp. 73–85, 2014.

[50] M. Li, T. Li, L. Zhu, M. E. Meadows, W. Zhu, and S. Zhang, "Effect of land use change on gully erosion density in the black soil region of Northeast China from 1965 to 2015: a case study of the Kedong County," *Frontiers in Environmental Science*, vol. 9, 2021.

[51] C. Valentin, J. Poesen, and Y. Li, "Gully erosion: impacts, factors and control," *Catena*, vol. 63, no. 2-3, pp. 132–153, 2005.

Hindawi
Geofluids
Volume 2022, Article ID 6546372, 17 pages
https://doi.org/10.1155/2022/6546372

Research Article

Stability Evaluation of Massive Landslides Using Ensembled Analysis of Time-Series InSAR and Numerical Simulation along the Yellow River, Northwestern of China

Chengcheng Tian,[1,2] Hao Tian ,[1,2] Chunyang Li,[1,2] and Feifei Chen[1,2]

[1]*Qinghai Survey Institute of Hydrogeology and Engineering & Environmental Geology, Xining, 810000 Qinghai, China*
[2]*Qinghai Provincial Key Laboratory of Hydrogeology and Geothermal Geology, Xining, 810000 Qinghai, China*

Correspondence should be addressed to Hao Tian; tianhao13897660096@163.com

Received 16 March 2022; Accepted 26 April 2022; Published 21 May 2022

Academic Editor: Long Yan

Loess landslides are a major geological disaster in the southeastern Qinghai Province, causing huge economic losses and casualties. The particularity of loess determines the disaster initiation mechanism, disaster mode, genetic mechanism, and complexity of the evolution process. This paper studies the deformation and stability analysis of the Quwajiasa large-scale multislip loess landslide in the Yellow River Basin from the perspective of field investigation, Interferometric Synthetic Aperture Radar (InSAR) monitoring, and numerical simulation. This study determines the deformation characteristics and genetic mechanism of the landslide through on-site field investigation, then quantitatively evaluates the overall deformation of the landslide using InSAR monitoring, locates the strong deformation area, and finally determines the control relationship between the two sliding surfaces on the landslide deformation using FLAC3D numerical simulation, obtaining the stability coefficient of the two sliding surfaces. The landslide is divided into seven engineering geological zones. The deformation history of the landslide is studied using InSAR technology. Results show that the landslide can be divided into significant deformation areas and no significant deformation areas. Two strong deformation areas are found. The FLAC3D numerical simulation results show that the deformation and stability of the right side of landslide are controlled by sliding surface 1, and the deformation and stability of the left side are controlled by sliding surface 2. The landslide is in an unstable state overall. The research done in this paper proposes a basis for the treatment of the Quwajiasa landslide.

1. Introduction

During the Quaternary, ossification created large amounts of aeolian sediments, which form yellowish, carbonate-bearing, quartz-rich, silt-dominated strata called loess [1]. Loess is widely distributed in Asia, Europe, North America, and South America [2]. In China, loess is concentrated in the Loess Plateau. The loess area is 630,000 square kilometers and accounts for 6.63% of the land area. Due to its high porosity, strong water sensitivity, and joint and fracture development, loess collapse, landslides, and ground fissures are common in loess areas [3]. The stability of slopes and natural slopes has always attracted the attention of scholars [4]. According to statistics, 1/3 of all landslides occur in the loess area. Loess landslides are commonly accompanied by a series of major disasters in the affected areas, including traffic interruption, river blockage, destruction of farmland, factories and mines, and even burial of livestock, people, and villages [5]. Rainfall commonly induces landslide instability, and loess landslides are no exception [6], but the specific properties of loess determine the disaster mechanism, disaster formation mode, genetic mechanisms, and evolution process of loess disasters, which are significantly different from those in other regions and other rock and soil mass. Technologies and methods used on other soil and rock masses do not apply to loess deposits.

Landslide surface deformation is the most intuitive indicator of landslide stability and has been a hot research topic

[7–11].Geological hazards have always been the focuses of scholars, which have been studied with different methods [12, 13]. Interferometric Synthetic Aperture Radar (InSAR) can provide a large-range of microdeformation information as well as long-term sequence of slow surface deformation and is widely used in landslide research [9, 14, 15]. In recent years, numerous scholars have carried out a series of studies on loess landslides using InSAR technology. Liu et al. studied the deformation history and failure mechanisms of small-scale loess landslides in the Heifangtai loess terrace in Gansu Province using multisource synthetic aperture radar (SAR) data [16], which provides a good precursor for the detection of small-scale loess landslides. Cao et al. used field investigation, optical remote sensing interpretation, and Interferometric Synthetic Aperture Radar (InSAR) to estimate the source material quality in xulonggou (xlg) debris flow in China [17], demonstrating the superiority of the multisource method formed by the combination of InSAR and other methods to solve practical problems. Bayer et al. used InSAR to record the deformation history of four dormant deep landslides reactivated by the excavation of a double track tunnel in the northern Apennine mountains of Italy [18]. Takada et al. studied the spatiotemporal behavior of a large-scale landslide in Onnebetsu-dake mountain, Japan, using InSAR technology [19].

With the development of information technology, numerical analysis has become an important means of analyzing slopes. Since Bowson and Rothf et al. used the strength reduction method to compile FLAC to calculate the safety factor of a slope, a large number of documents and results from numerical simulation analysis of slopes have emerged, which have been widely applied to loess landslides. Wang et al. used the finite element software platform FLAC3D for secondary development and proposed a strength reduction method considering rheological properties [20]. Mu et al. used FLAC3D software to simulate the formation mechanism of a surface landslide under different slope angles within the Shendong mining area and provided a scientific basis for the effective prevention and control of geological disasters through the stability analysis of a goaf collapse slope in a loess gully region [21]. Wang et al. used FLAC3D to analyze the influence of groundwater on FoS of a dump slope and found the engineering solution [22]. He et al. used FLAC three-dimensional numerical simulation to evaluate the treatment effect of compaction pile composite foundation and further demonstrated the feasibility of compaction pile composite foundation in a collapsible loess area [23]. Wang et al. used FLAC3D to build an anchoring model for a loess vertical slope and found that the modified pile unit was suitable for simulating the loess slope reinforced by anchor [24]. The application of FLAC3D numerical simulation is well developed, and the stability analysis of loess landslide has always been an important step in the process of landslide. Therefore, the stability analysis of loess landslide using FLAC3D is a very good method for analyzing loess landslides.

Therefore, in this study, we studied the deformation and stability of loess landslides with multiple sliding surfaces in the Yellow River Basin using field investigation, InSAR monitoring, and numerical simulation. Firstly, a qualitative evaluation of the Quwajiasa landslide is carried out by field investigation, and engineering geological zoning is carried out. Then, the deformation history of the landslide is studied using the small baseline subset (SBAS) time series method. The strong deformation area and the weak deformation area are identified, and the abnormal deformation area is found. The results are compared with field survey results for verification. Finally, the stability coefficient of the landslide is obtained using FLAC3D numerical simulation, which provides the basis for the treatment of the Quwajiasa landslide. This paper is aimed at solving the problem of deformation analysis and stability evaluation of multisliding loess landslides in the Yellow River Basin using InSAR, numerical simulation, and traditional field investigation. The method and results presented in this study provide a good case for the study of complex large loess landslides.

2. Geological Setting

As shown in Figure 1, the study area is located in Lajia Town, Maqin County, Qinghai Province (the coordinates are 100°37′55″-100°38′59″E, 34°40′07″-34°40′52″N). The study area is located on the South Bank of the Yellow River, and the landform is valley plain composed of class II and VII terraces of the Yellow River. Quwajiasa landslide is located in an erosion area where the Yellow River is strongly incised. The valley in the study area forms a canyon with high and steep slopes composed of Neogene mudstone on both sides. The top is covered with pebbles and loess like the soil accumulated in the high terrace of the Quaternary Yellow River. Quaternary alluvial proluvial silt, pebbles, broken stone soil, and silty clay are also distributed in the area. The study area is located in the southeastern Lajia basin. Due to the extrusion of adjacent tectonic units and the influence of later tectonic movement, the NW-SE Maqin-Maqu fault is visible. The iron fault (F1) developed on the north side of the Quwajiasa landslide is a branch fault of the Maqin fault, which is a compressive torsional reverse fault with an attitude of 297° ∠67° – 10°∠76°, and the width of the fault fracture zone is 10–30 m. The study area has a typical plateau continental climate. Due to the invasion of humid airflow in the southwest and southeast, the climate is semihumid to alpine. Precipitation is small and uneven, evaporation is large, and the multiyear average temperature in the area is -0.1°C. The average annual precipitation is 420–560 mm, the maximum daily rainfall is 40.6 mm, and the maximum hourly rainfall is 21.0 mm. The seismic peak acceleration in the study area is 0.15 g, and the basic seismic intensity is VII.

Weak layered mudstone is exposed in the study area, with a thickness of 0.05–0.1 m, inclined to the northeast at an inclination of 5°–12°. The groundwater in the study area is divided into two types: clastic rock pore fissure water and loose rock pore water. As shown in Figure 2, based on the landform characteristics and the relationship between deformation and failure, the landslide is divided into 7 engineering geological zones. The Quwajiasa landslide trends NE-SW, with the main sliding direction of 298°–307°. The landslide is 700–900 m long and 2500 m wide, the height

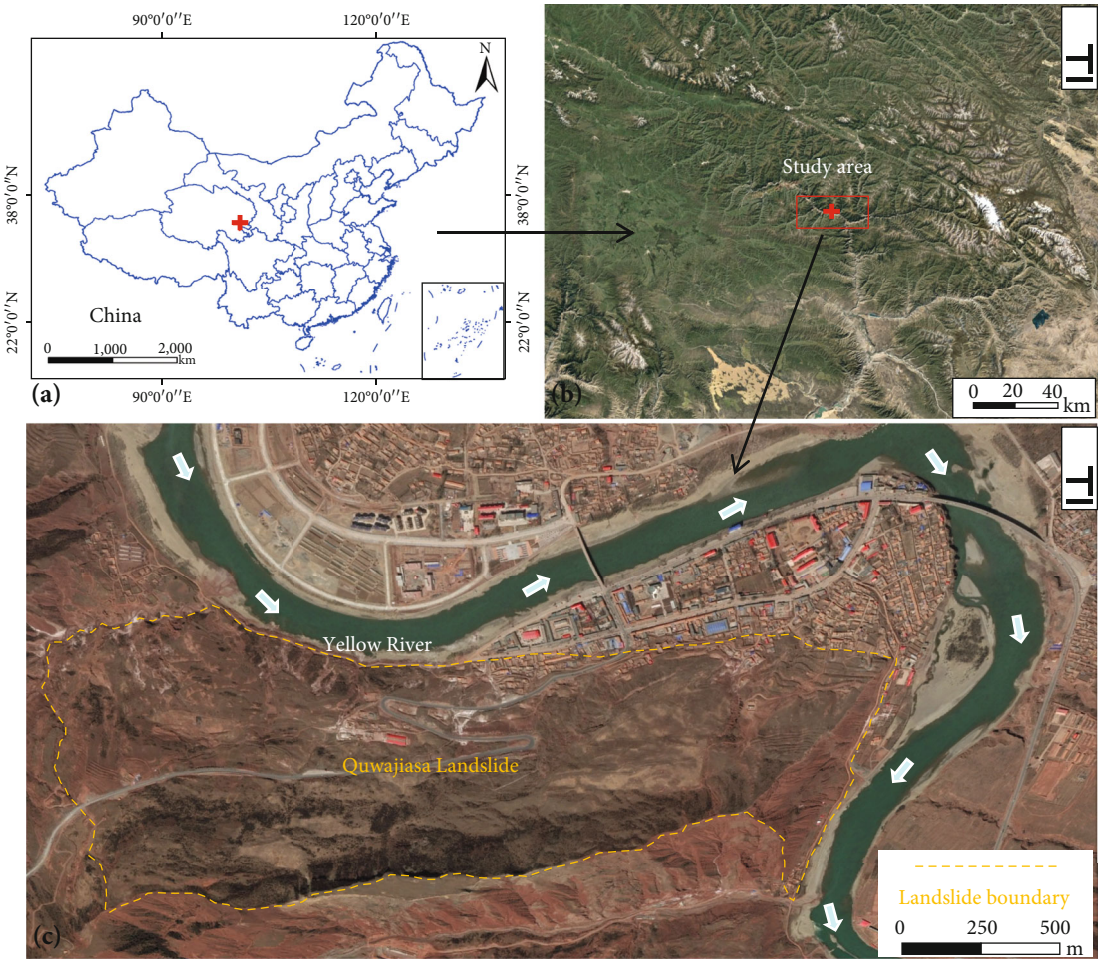

Figure 1: Location and topography of the study area.

difference between the front and rear edges ranges from 185 to 300 m, the slope is 25°–36°, and the total volume can reach 1.67×10^8 m^3, making this a giant ancient landslide. The main failure mode of the Quwajiasa landslide is traction tension failure. The front slope is seriously deformed, forming large-scale shallow surface sliding failure with a continuous armchair shaped steep wall. The surface soil is seriously damaged and disintegrated. The central platform forms a multilevel parallel downward dislocation with well-developed tension fractures with a fracture width of 20–30 cm and downward dislocation of 0.3–2 m. A series of vertical cracks are developed along the rear part of the slope. The antislide pile beside the highway is deformed and damaged, the joint between the antislide pile and the sheet wall is sheared, deformed, and cracked, and the front of the pile is cracked and deformed and tilts out of the slope.

3. Data and Methods

3.1. Small Baseline Subset Interferometric Synthetic Aperture Radar (SBAS-InSAR). In this study, the Small Baseline Subsets Interferometric Synthetic Aperture Radar (SBAS-InSAR) method is adopted. Its basic principle is to first register images within a scene to the main image and then filter and unwrap the obtained interferogram by setting the temporal and spatial baseline threshold. Coherence information is used to select highly coherent pixels in the unwrapping results. Then, after removing the elevation error phase and atmospheric delay phase in the difference map, the average deformation rate is obtained using singular value decomposition. Finally, the law of slow deformation of the surface with time is obtained. This method is suitable for mountainous areas with fewer buildings and fewer permanent scattering points.

This study uses Sentinel-1A satellite image data for SBAS-InSAR analysis. The Sentinel-1A satellite is a radar satellite launched by the European Space Agency in April 2014 with a cycle of 12 days. Satellite image data since October 2014 can be obtained on the official ESA website. The data coverage and monitoring scope are shown in Figure 3. The satellite has four imaging modes, EW, SM, IW, and wave. The SM mode and IW mode adopt the latest top imaging technology, which can address the scaling effect during wide range imaging and enhance imaging radiance. Sentinel-1 is equipped with a new generation C-band synthetic aperture radar system, which has a shorter wavelength than L-band. The main parameters of data image are shown in Table 1.

Figure 2: (a) Engineering geological zones of landslide. (b) Intermediate crack. (c) Deformation of antislide pile. (d) The deformation of the path. (e) Central scarp. (f) Landslide trailing edge.

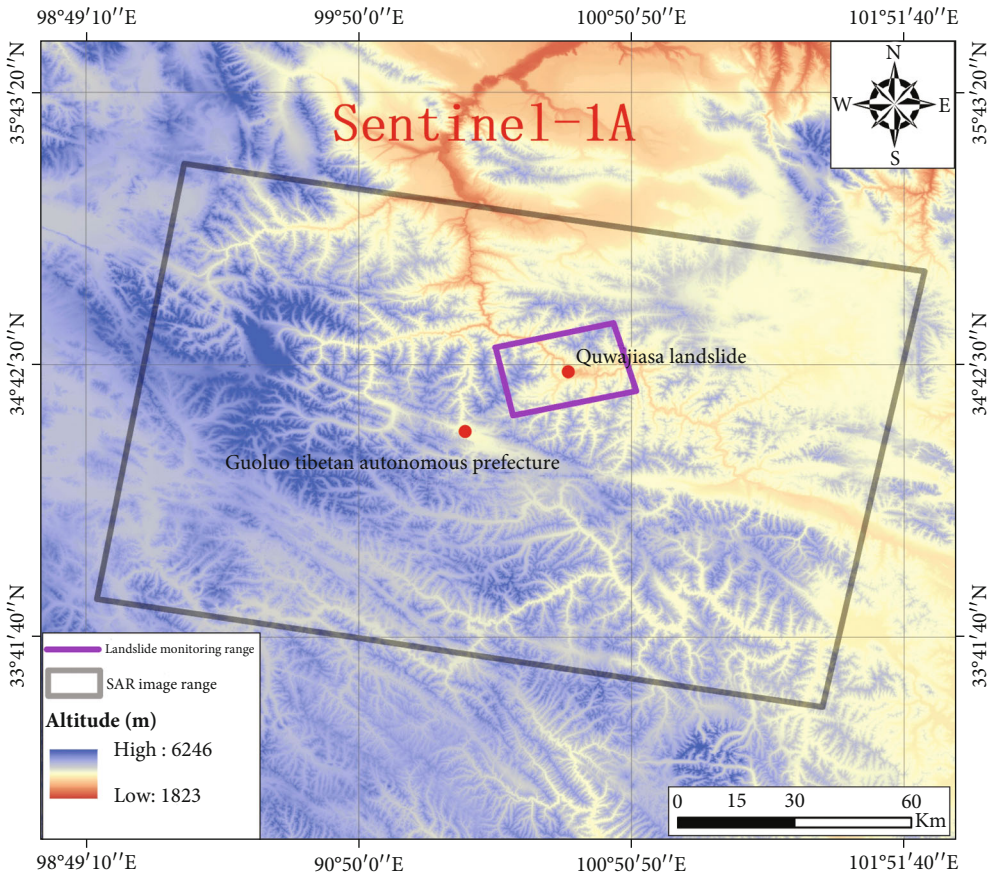

Figure 3: Data coverage and monitoring scope.

Table 1: Main parameters of data image.

Index	Flight platform	Flight direction	Imaging mode	Polarization mode	Resolving power	Wavelength	Coverage period
Parameter information	Sentinel-1A	Orbit lowering	IW	VV	5 m × 20 m	5.63 cm	2017.3.25-2020.6.25

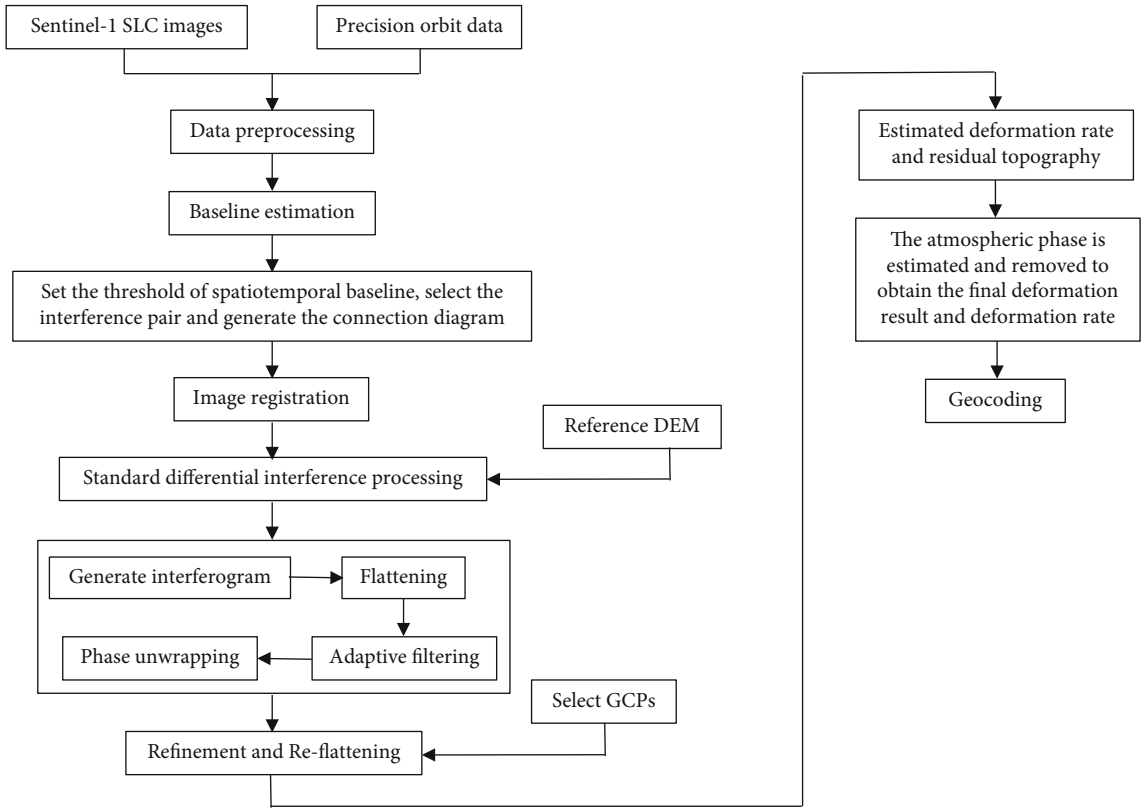

Figure 4: Data processing flow.

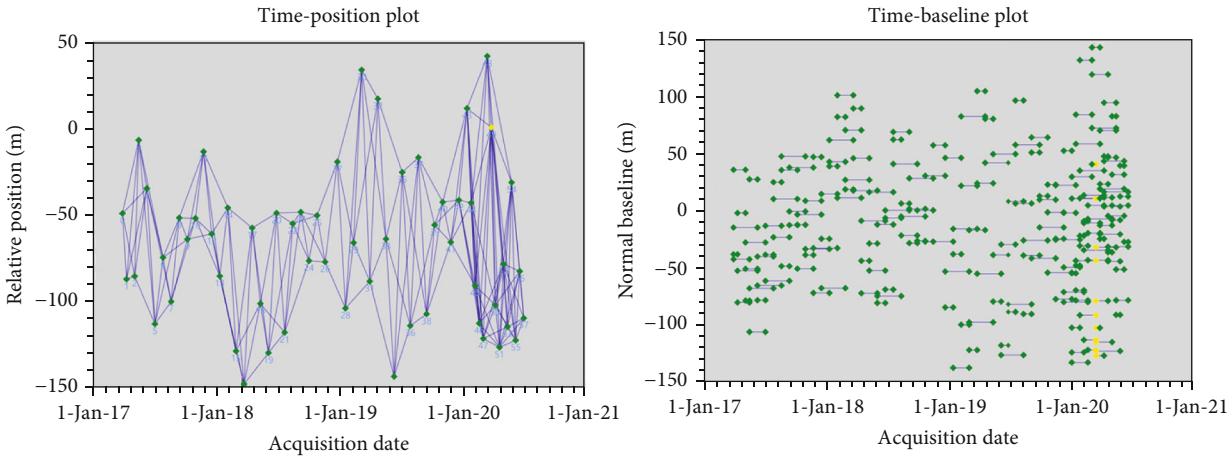

Figure 5: Spatial baseline (a) and temporal baseline (b).

This study uses the SBAS module in ENVI SARscape software to process the SAR data. As shown in Figure 4, SBAS technology primarily includes the generation of connection diagrams (the parameter settings of spatial baseline and temporal baseline are shown in Figure 5), the generation of interferograms, flattening interferograms, adaptive

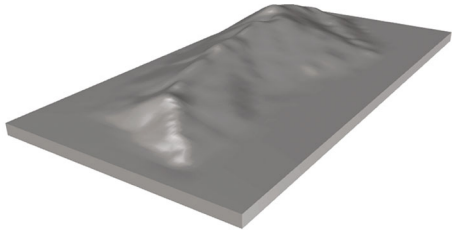

Figure 6: 3D calculation model diagram.

filtering, phase unwrapping, orbit refining and reflattening, phase to deformation, and geocoding.

3.2. Numerical Simulation

3.2.1. Establishment of the Calculation Model. Midas is a finite element analysis software for structural design, which is divided into four categories: architecture, bridge, geotechnical, and simulation. This study primarily uses the Midas geotechnical module. In this modeling, the Midas software is used to establish the landslide model. As shown in Figure 6, the calculation range is 361 m high in the Z direction, the X axis runs along the front edge of the slope, the model length is 3930 m, the vertical slope outward is the Y axis, the model width is 2037 m, the model bottom elevation is 0 m, and the elevation of the highest point at the rear edge of the model is 361 m. As shown in Figure 7, according to the engineering geological profile in the area, there are two potential sliding surfaces, deep sliding surface 1 and deep sliding surface 2. The gravelly soil, silty clay, and clay on the upper part of the sliding surface are combined and classified as overburden. The parameters are determined by a combination of test results, empirical data, and inverse analysis [4, 25].

3.2.2. Selection of Calculation Parameters. The parameters of interest are bulk modulus K and shear modulus G [26]. As shown in Formula (1), the bulk modulus K and shear modulus G are converted by Poisson's ratio and elastic modulus. The selection of other rock and soil parameters is shown in Tables 2 and 3.

$$K = \frac{E_0}{3(1-2\mu)} \quad G = \frac{E_0}{2(1+\mu)}. \tag{1}$$

3.2.3. Computing Method. The Mohr Coulomb (M-C) constitutive model is adopted in this calculation, and the strength reduction method is used to determine the stability coefficient of the specified sliding surface of the slope. The safety factor of slope stability in the strength reduction method is defined as the degree of shear strength reduction of the rock and soil mass when the slope reaches the critical failure state. The safety factor is defined as the ratio of the actual shear strength of the rock and soil mass to the reduced shear strength at critical failure. The key point of the strength reduction method is the formula:

$$\begin{aligned} C_F &= C/F, \\ \varphi_F &= \tan^{-1}((\tan\varphi)/F). \end{aligned} \tag{2}$$

To adjust the strength index C and φ, then the slope stability numerical analysis is carried out. By continuously increasing the reduction coefficient and repeatedly calculating until it reaches critical failure, the reduction coefficient obtained at this time is the safety factor F.

3.3. Combination Methodology. The first part of this study is the field investigation, which primarily determines the engineering geological conditions of the Quwajiasa landslide. Based on the landform and relationship between deformation and failure, the landslide is divided into zones, and the failure mode of landslide is analyzed. In addition, a detailed investigation was conducted inside the landslide to determine the local deformation and location of the landslide, such as shallow surface sliding, scarp, soil disintegration, tension cracks, and small landslide. Then, the whole deformation rate of the Quwajiasa landslide mass is obtained via InSAR interpretation, and the areas with significant deformation and no significant deformation were identified. For the strong deformation region, the time series deformation cumulative curve of feature points is extracted, and its deformation characteristics are analyzed. Finally, using FLAC3D numerical simulation, the stability coefficient of the landslide is determined using the strength reduction method, the stability coefficients of the two sliding surfaces are calculated, and the deformation law of the landslide is analyzed. The joint use of the three methods allows for comparison and confirmation of the field investigation and InSAR monitoring results, and InSAR monitoring results and FLAC3D simulation results ensure the accuracy of the calculation. Compare the local deformation of the landslide and small landslide in the field investigation with the position of strong deformation area monitored by InSAR as well as recheck the InSAR monitoring results with the field investigation. Then, the deformation monitored using InSAR is compared with the FLAC3D simulation results to determine the control relationship between the two deep sliding surfaces and the landslide deformation.

4. Results

4.1. InSAR Monitoring Results and Deformation Analysis

4.1.1. Overall Deformation Monitoring Results of Landslide. As shown in Figure 8, InSAR interpretation results show that the maximum surface deformation rate of the Quwajiasa landslide mass (black solid line range) can reach -70 mm/y, and the overall deformation rate is -70–7 mm/y. There are clear deformation signs from area I to area V overall, and there are no significant deformation signs in areas VI and VII. The slope deformation within the red dotted line is the strongest (areas A and B). The deformation rate is -70 −-35 mm/y. The significant deformation area in area A is 0.1 km^2, and the significant deformation area in area B is 0.33 km^2. As shown in Figure 8, the black arrow is the possible sliding direction of the deformation area. In the case of a landslide disaster, local village roads are under direct threat (according to the radar side imaging characteristics, the positive value of the rate represents that the azimuth of surface

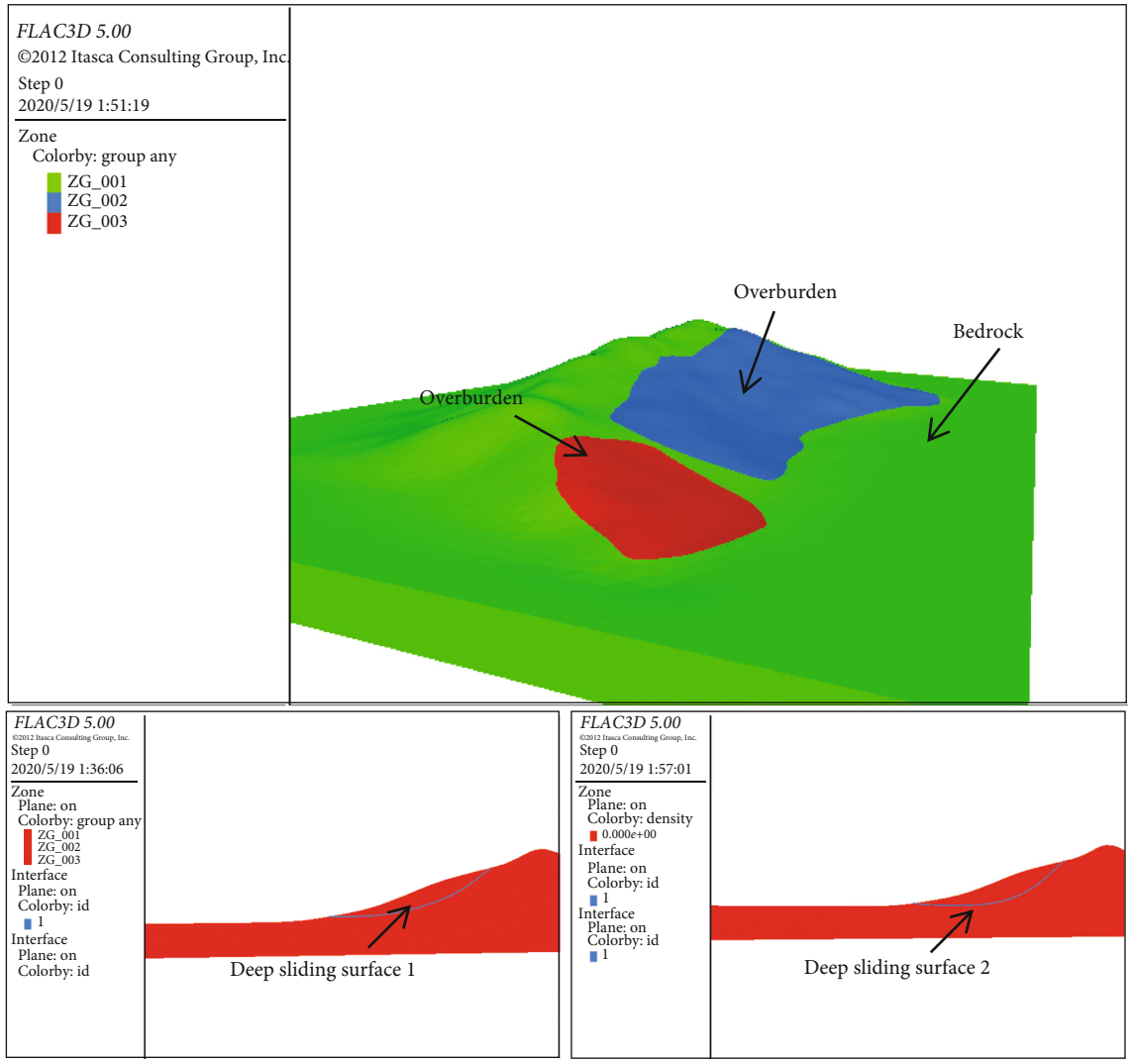

Figure 7: FLAC calculation model diagram.

Table 2: Model parameter value table.

Rock and soil type	Bulk density (natural) γ (KN/m^3)	Cohesion (natural) (c/KPa)	Internal friction angle (natural) (φ/°)	Bulk modulus (K/pa)	Shear modulus (G/pa)
Overburden	19.9	19.9	17.9	4.6×10^8	2.3×10^8
Mudstone	21	690	35.2	8.1×10^9	6×10^9

Table 3: Parameter value of sliding surface.

Slip surface type	Cohesion (natural) (c/KPa)	Internal friction (natural) angle (φ/°)	Normal stiffness (KS/pa)	Tangential stiffness (KN/pa)
Deep sliding surface 1	23.5	19.8	4.6×108	2.3×108
Deep sliding surface 2	32.5	25.1	6.6×108	4.3×108

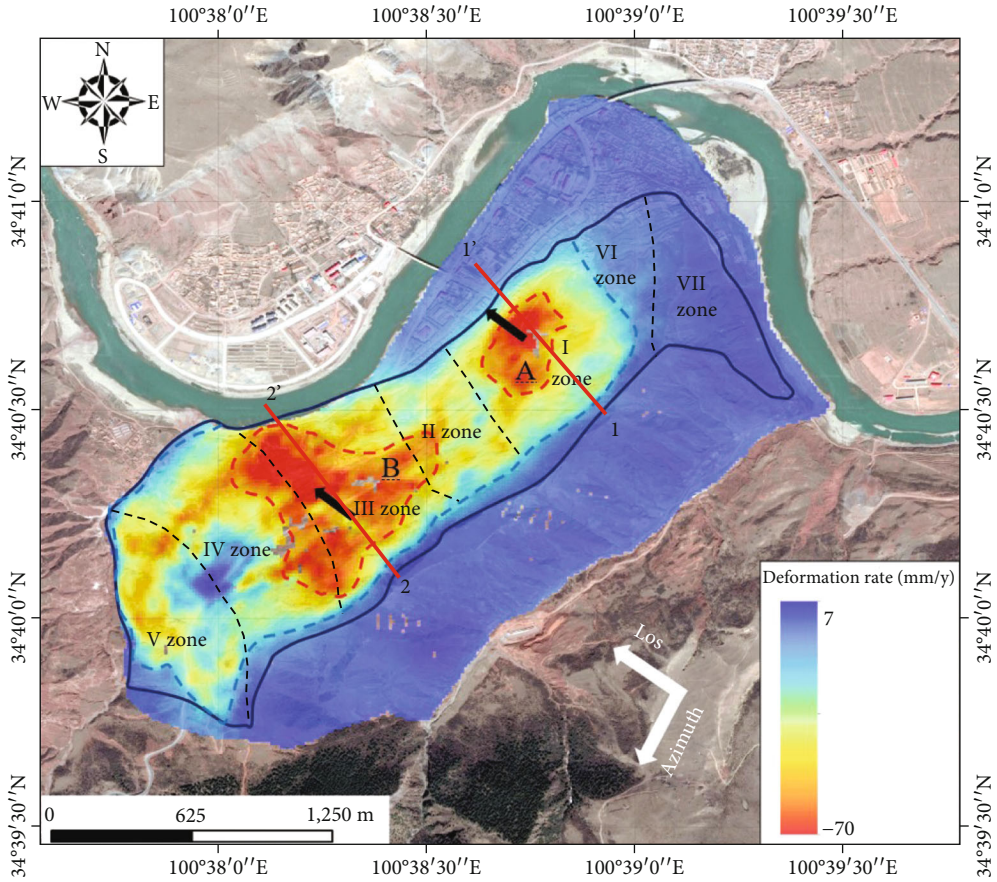

Figure 8: The annual average rate of deformation of the Quwajiasa landslide.

movement is close to the satellite shooting azimuth, and the negative value represents that the azimuth of surface movement is far away from the satellite shooting azimuth; there are no clear deformation signs in other areas outside the blue dotted line, and the slope surface is relatively stable in this time period).

4.1.2. Deformation Analysis of the Strong Deformation Zone. The overall deformation rate of zone I is -70–-7 mm/y. Using InSAR technology, the surface deformation information of I area in different years is extracted. The deformation rate of 1-1′ section in I area is shown in Figure 9. During the monitoring period from March 2017 to June 2020, the fluctuation of the deformation rate curve of section I in 2018 was the strongest, indicating that significant deformation occurred on the slope surface during this period. During the monitoring period from January to June in 2020, the change in the section deformation rate curve in zone I was relatively stable compared to previous years, and the deformation rate magnitude was small, indicating that the deformation of the slope body in zone I was weak in this period. The deformation rate curves of 2017 and 2019 are consistent, and the deformation magnitude is less than that of 2018 as well as greater than that from January to June 2020.

The slope in zone III is in a state of strong deformation, and the maximum deformation rate can reach -70 mm/y, which is the area with the widest distribution of strong deformation and largest deformation rate. Using InSAR technology, the section deformation rate in different years was extracted for zone III. The 2-2′ deformation rate profile of zone III is shown in Figure 9. The interruption of the profile deformation rate curve indicates that there is a decoherence in the slope body during InSAR monitoring, and no deformation information is available. During the monitoring period of 2017, the deformation rate of the middle of the landslide was the largest, followed by the deformation of the leading edge, and the deformation rate reached a maximum value of -60 mm/y near the ZK22 borehole location. During the monitoring period in 2018 and 2019, the deformation rate in the middle was the largest, and the deformation rate near the ZK23 drilling position reached a maximum value of -58 mm/y and -62 mm/y, respectively. During the monitoring period from January to June 2020, the maximum deformation rate reached -42 mm/y.

There is a strong deformation zone A in the middle and front of zone I, and the deformation rate of zone A is -70 –-35 mm/y, indicating moderate to strong deformation in zone I. The slope in zone A (within the range enclosed by the red circle) has a maximum line-of-sight deformation rate of -70 mm/y. The area is 0.1 km^2, and the average slope is 41°. According to the radar side imaging characteristics, the slope in area A is roughly interpreted to be moving to

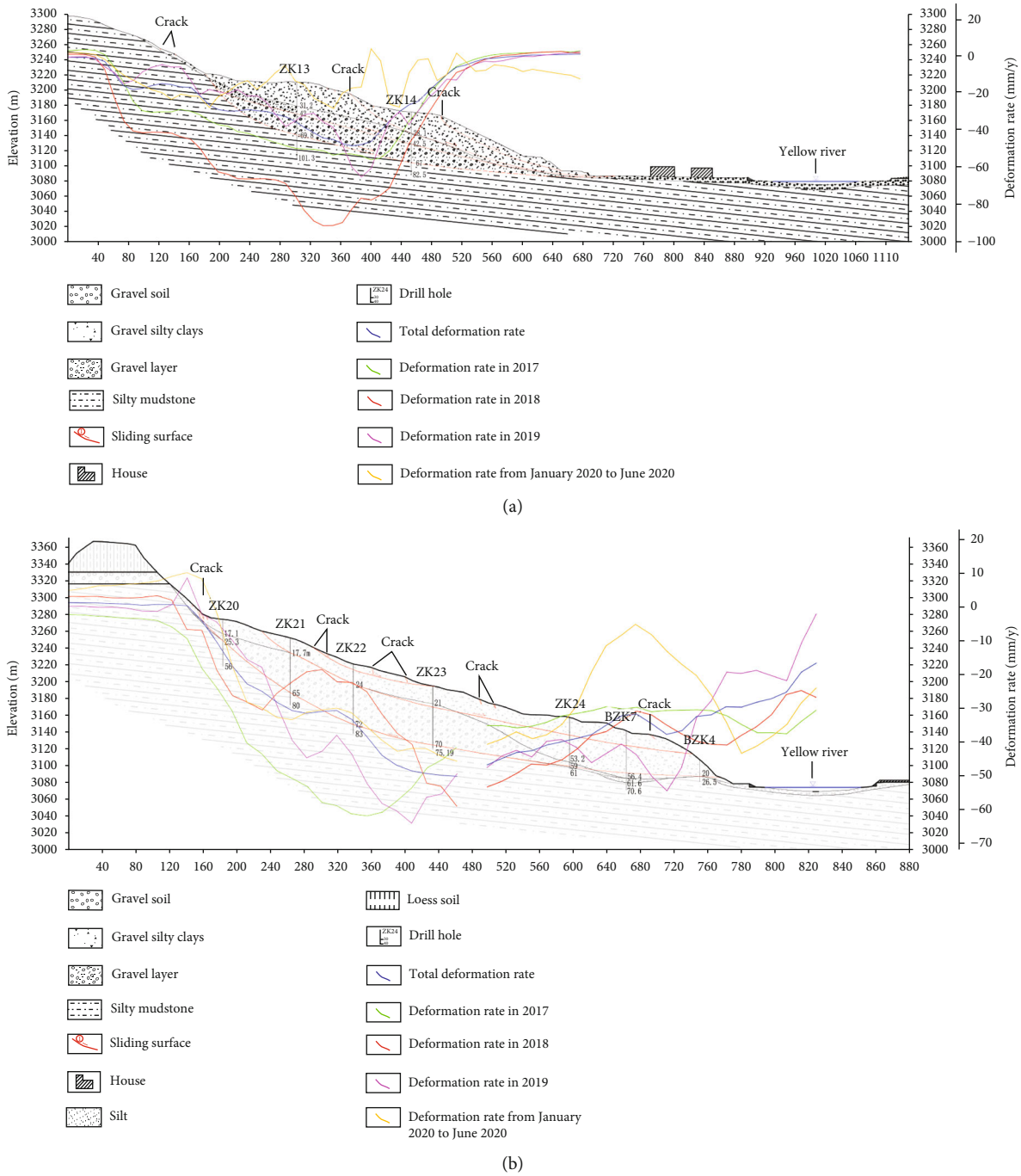

FIGURE 9: (a) 1-1′ InSAR deformation profile. (b) 2-2′ InSAR deformation profile.

the northwest, as shown by the black arrow in Figure 10. As shown in Figure 10, in order to analyze the time-series change characteristics of the strong deformation area in area A, three feature points of the trailing edge P1, middle P2, and leading edge P3 were extracted, and their deformation accumulation curves were drawn. The timing diagram shows that during the monitoring time from 20170325 to 20191216, the cumulative deformation value of point P3 is the largest (190 mm), the cumulative deformation value of point P2 is the second largest (180 mm), and the cumulative deformation value of point P1 is the smallest. In terms of deformation trend, the deformation of the leading edge of the slope in area A > the deformation of the middle part > the deformation of the trailing edge and the deformation characteristics are similar to the local traction sliding deformation.

The strong deformation zone B spans zone II, zone III, and zone IV. The maximum line-of-sight deformation rate of zone B can reach -70 mm/y. The area of this deformation zone is 0.43 km^2, the altitude distribution ranges from 3085

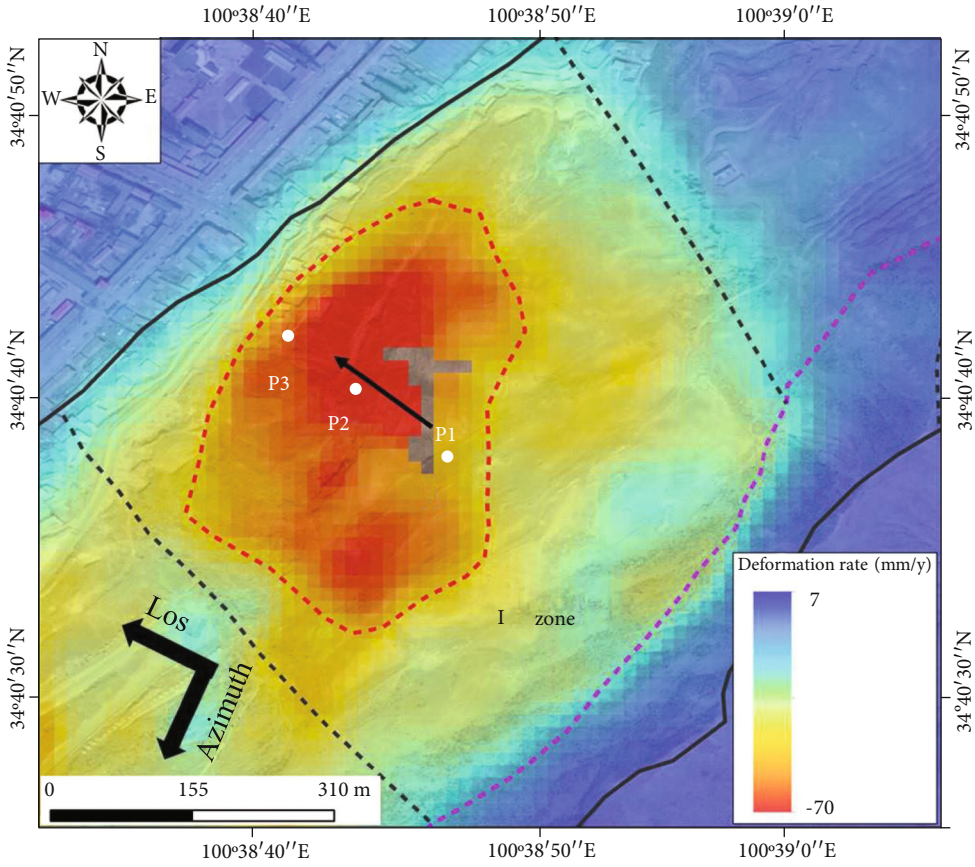

(a)

(a)

Figure 10: Continued.

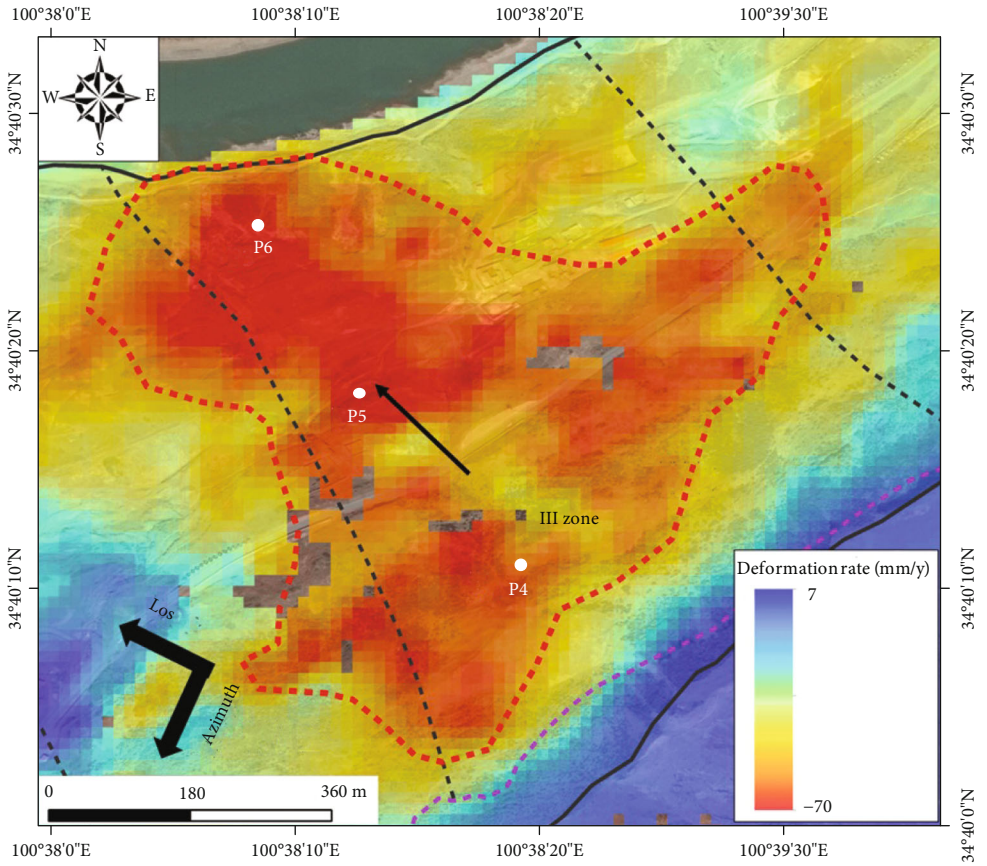

(b)

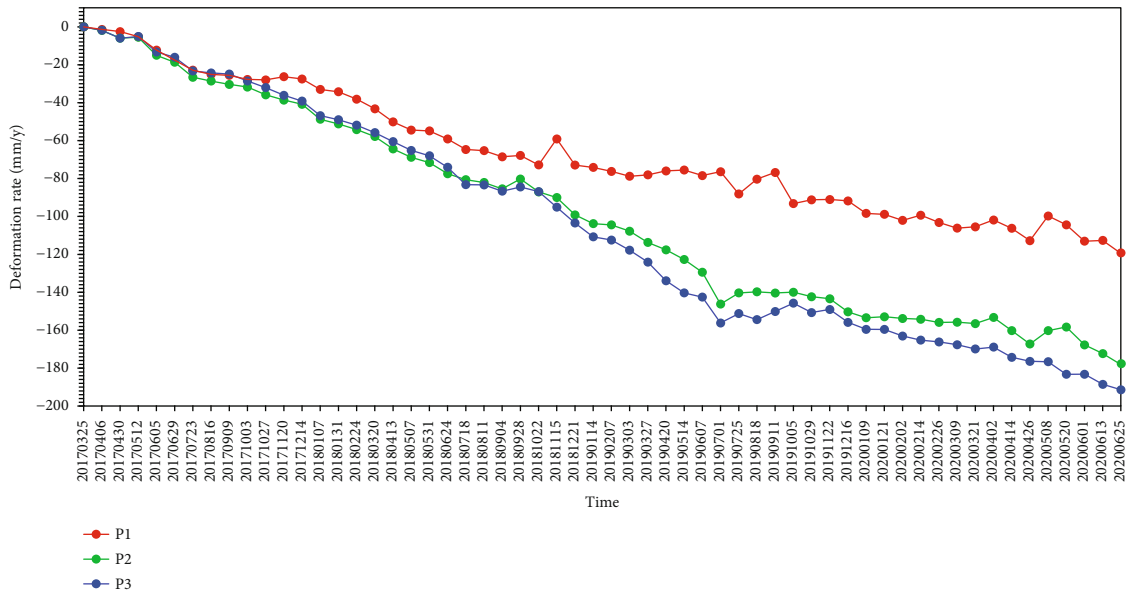

(c)

Figure 10: Continued.

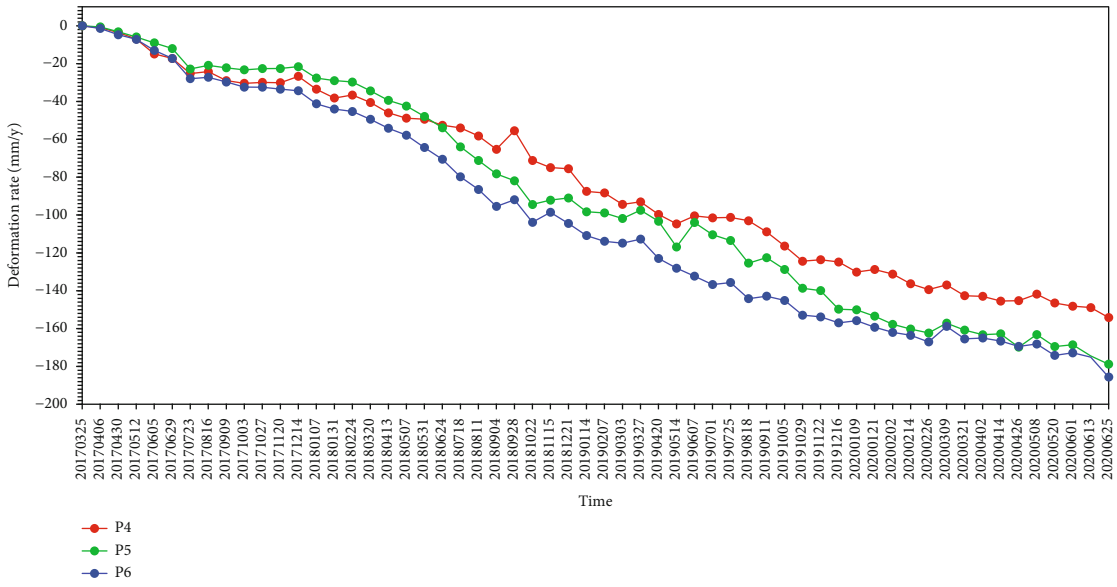

(d)

Figure 10: (a) The average annual deformation rate distribution of strong deformation zone A (2017.3-2020.6). (b) The average annual deformation rate distribution of strong deformation zone B (2017.3-2020.6). (c) Time series deformation diagram of characteristic point A in strong deformation zone. (d) Time series deformation diagram of characteristic point B in strong deformation zone.

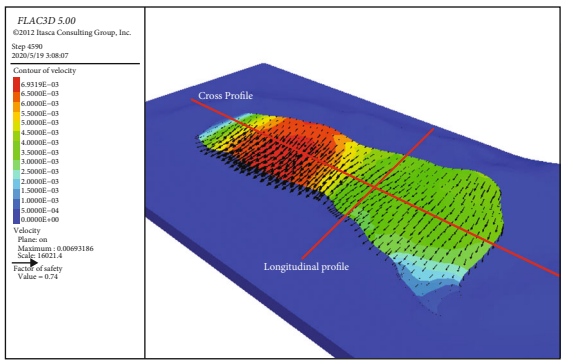

(a)

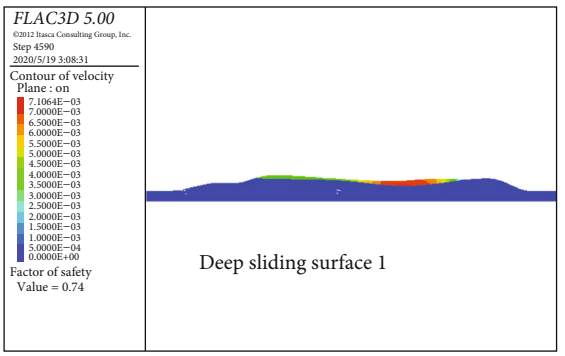

(b)

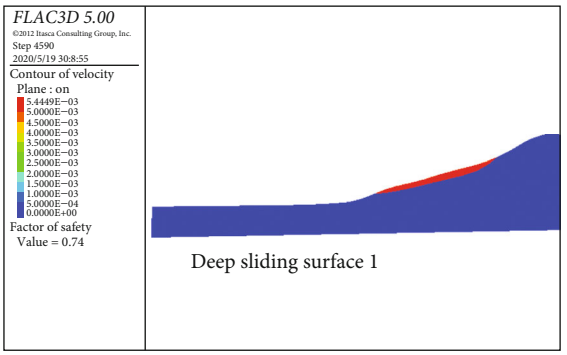

(c)

Figure 11: (a) Stability calculation results of deep sliding surface 1 (I-IV) under seismic conditions. (b) Stability calculation results of deep sliding surface 1 (I-IV) under seismic conditions (crossprofile). (c) Stability calculation results of deep sliding surface 1 (I-IV) under seismic conditions (longitudinal profile).

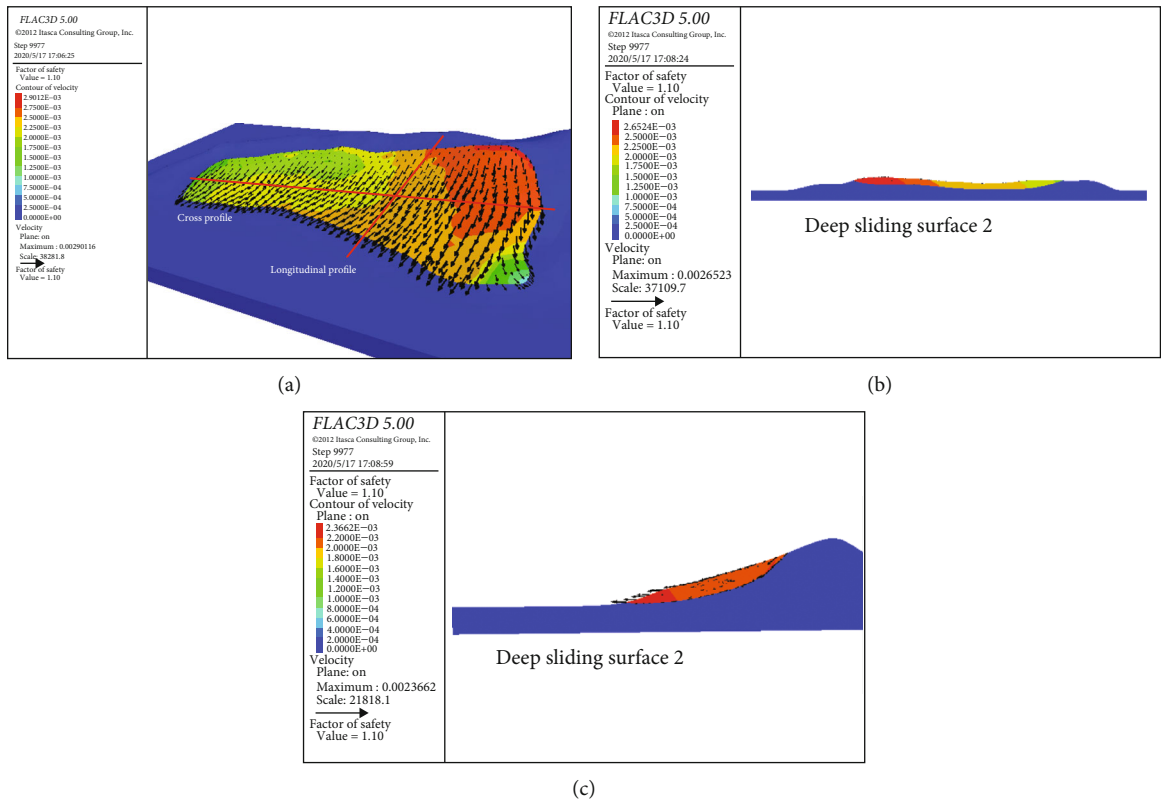

Figure 12: (a) Stability calculation results of deep sliding surface 2 (I-IV) under seismic conditions. (b) Stability calculation results of deep sliding surface 2 (I-IV) under seismic conditions (crossprofile). (c) Stability calculation results of deep sliding surface 2 (I-IV) under seismic conditions (longitudinal profile).

to 3325 m, and the height difference is 240 m. The slope inclination is 18°–25°, the leading edge is steeper, the middle is gentler, and the trailing edge is steeper. Artificially excavated roads along the leading edge and middle as well as human engineering activities are clearly visible. According to the radar side imaging characteristics, the slope in area A is roughly interpreted to be moving to the northwest, as shown by the black arrow in Figure 10. As shown in Figure 10, in order to analyze the time-series change characteristics of the slope in area B, three characteristic points on the trailing edge P4, middle P5, and leading edge P6 were extracted, and the cumulative deformation curve was drawn, as shown in Figure 10. The time series diagram shows that during the monitoring time from 20170325 to 20200625, the cumulative deformation variables of each feature point are different but have a similar trend. The cumulative deformation of point P6 is the largest (185 mm); the cumulative deformation of point P5 is the second largest (178 mm); the cumulative deformation of point P4 is the smallest (154 mm). Clearly visible deformation features are visible across the overall slope. The cumulative deformation of the three feature points continued to increase from March 2017 to June 2020, among which the deformation of P6 feature point increased the fastest. The increase rate of P4 feature point deformation was slower than that of P5. Comprehensive analysis shows that the overall deformation characteristics of the slope in area B are similar to the local traction sliding deformation.

4.2. Numerical Simulation Results. A seismic acceleration of 0.15 g in the horizontal direction is added to the model. On this basis, the strength reduction method is used to determine the slope stability coefficient. Results show that the stability coefficient of the deep sliding surface 1 of the slope (areas I-IV) is 0.74, and the stability coefficient of deep sliding surface 2 is 1.10 for the overall deformation. Under seismic conditions, the deep sliding surface 1 of the slope is in an unstable state, and the deep sliding surface 2 is stable.

As shown in Figure 11, results of sliding surface 1 show that the maximum displacement of the landslide appears on the right side of the landslide. In general, the high value area of displacement is also primarily concentrated on the right side of the landslide. The displacement distribution in the main sliding direction (X direction) is generally consistent with the overall displacement distribution, and the displacement in the Y direction and Z direction is small. Displacement of the leading edge on the right side of the landslide is large, indicating that the leading edge on the right side of the landslide has undergone significant deformation.

As shown in Figure 12, results of sliding surface 2 show that the maximum displacement of the landslide appears on the left side of the landslide. In general, the high value area of displacement is also primarily concentrated on the left side of the landslide. The displacement distribution in the main sliding direction (X direction) is generally consistent with the overall displacement distribution, and the displacement in the Y and Z directions is small. The displacement of the

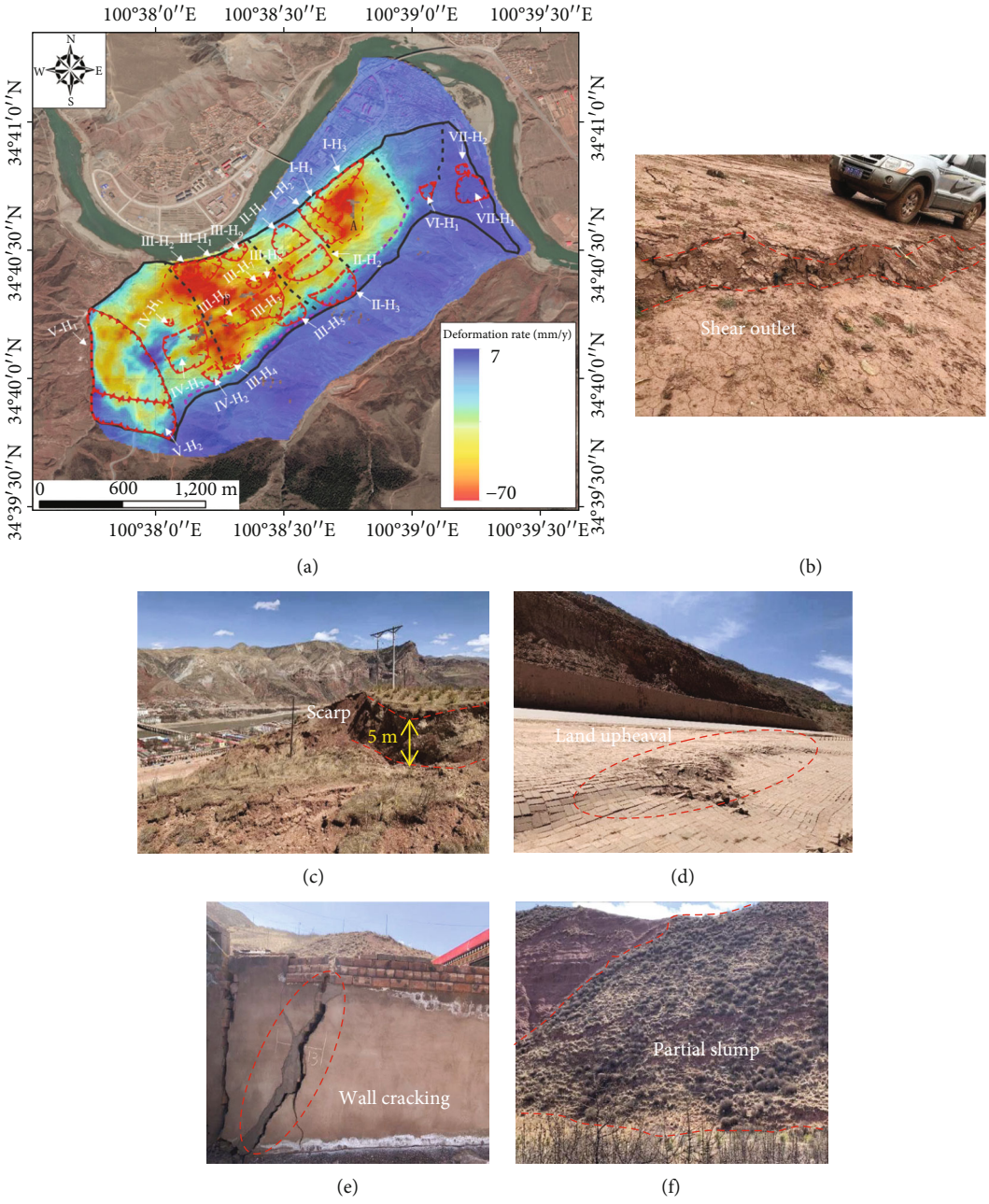

FIGURE 13: (a) Comparison and verification diagram of InSAR interpretation and field survey. (b) Front shear outlet. (c) Front steep wall. (d) Ground uplift of the viewing platform. (e) Building deformation. (f) Partial slump.

left trailing edge of the landslide is large, indicating that the left trailing edge of the landslide has undergone significant deformation and gradually decreases to the leading edge of the landslide.

5. Discussion

From the InSAR results, the deformation characteristics of zone I in different years from March 2017 to June 2020 are as follows: central deformation > leading edge deformation > trailing edge deformation. For the total deformation, the fluctuation of deformation rate in the middle is the largest, and the maximum value of deformation variable can reach -55 mm/y. The leading edge shape variable is the second largest, and the trailing edge shape variable is the smallest. The slope in zone I shows traction sliding deformation overall. According to the field investigation results, the highway excavation slope and local residents' slope cutting and building houses in area I form free surfaces of varying heights, which provides space for shear deformation of the landslide. Local sliding failure occurred on the inner side of the highway in area I. A free surface I formed again at the rear edge of the small landslide, and the tension deformation of the top platform at the rear edge begins to occur under traction

deformation due to the weight of the landslide. The overall performance is also traction sliding deformation [27], which is consistent with the InSAR monitoring results.

From the change trend of the InSAR curve in zone III, the deformation rate characteristics of the general section are as follows: the deformation rate of the middle part is the largest, the deformation rate of the leading edge is the second largest and gradually weakens as the slide slows down, and the deformation rate of the trailing edge is the smallest. Comprehensive analysis shows that the slope in zone III is traction sliding deformation overall. According to the field investigation results, the erosion of the Yellow River on the bank slope forms a good front shear outlet [28], and human engineering excavation provides the spatial conditions for deformation of the landslide. After a free surface is formed again at the rear edge of the small landslide, tension deformation of the platform at the top of the rear edge begins to occur under traction deformation due to the weight of the landslide. The shallow surface of the front edge of this area is significantly slippery, and the slope surface disintegrates. Zone III belongs to the traction failure mode, which is consistent with InSAR monitoring results.

Using InSAR technology to monitor the Quwajiasa landslide, the surface of the slope body in areas I ~ V shows clear deformation signs, and the deformation rate is between -70 and -7 mm/y [29]. There are 2 strong deformation areas (A ~ B areas) and a total of 23 small landslides, and the overall distribution of landslides is shown in Figure 13. The 20 surveyed landslides are all within the significant deformation area monitored by InSAR, and the deformation rate of the remaining 3 landslides (VI-H_1, VII-H_1, VII-H_2) is -7 −7 mm/y. Compared with the overall landslide mass, there is no clear deformation signal, and the slope mass is relatively stable. Strong deformation zone A is located in the middle and front of zone I, and the middle and trailing edges of landslides I-H_1 to I-H_3 are all located in zone A, indicating that the deformation of the trailing edge of the landslides at I-H_1 to I-H_3 is greater than the deformation of the leading edge. The deformation range of area A continues to expand upward to 4018 m above sea level along the trailing edge of 3 landslides I-H_1 ~ I-H_3. The strong deformation area B has a wider distribution range, and the deformation area extends from 4016 m above sea level to 4025 m above sea level. Seven landslides H_1-III-H_4 ad III-H_6-III-H_8 are located in the strong deformation area of B area; the other 10 landslides (II-H_1-II-H_3, III-H_5, III-H_9, IV-H_1-IV-H_3, V-H_1-V-H_2) are not within the strong deformation zones A or B; although, they still show clearly deformation signals. The deformation rates of these 10 landslides are less than those of A and B zones.

Comparing the monitoring results of InSAR with the results of numerical simulation, the numerical simulation results for sliding surface 1 show that the high value area of landslide displacement is concentrated on the right side of the landslide, which is the same as the location of strong deformation area A from the InSAR monitoring results, and the range of high value area of displacement is roughly the same as that of strong deformation area A. The numerical simulation results for slip surface 2 show that the high value area of landslide displacement is concentrated on the left side of the landslide, which is the same as the location of strong deformation area B from the InSAR monitoring results, and the range of high value area of displacement is roughly the same as that of strong deformation area B. However, there is no strong deformation area on the left side of the landslide in the numerical simulation results for sliding surface 1, and there is no strong deformation area on the right side of the landslide in the numerical simulation results for sliding surface 2. To summarize, the deformation and stability of the right side of the Quwajiasa landslide are controlled by sliding surface 1, and the deformation and stability of the left side are controlled by sliding surface 2 [30]. Numerical simulation results show that the high displacement area of the landslide is concentrated on the left and right sides of the landslide, which is the same as the strong deformation areas A and B from the InSAR data. The main controlling factors of strong deformation area A are the construction of provincial road excavation slopes and local slope cutting and house construction by residents, forming free surfaces with different heights. The main controlling factor of strong deformation area B is undercutting of the Yellow River, which makes the front edge of the area free, providing better conditions for landslide cutting [21].

6. Conclusions

The main purpose of this paper is to study the deformation and stability analysis of a multislip surface large-scale loess landslide in the Yellow River Basin from the perspective of field investigation, InSAR monitoring, and numerical simulation. First, a field investigation was conducted to determine the lithology and structure of the study area as well as carry out engineering geological zoning according to the deformation and failure characteristics of the landslide. Through InSAR monitoring and analysis of the deformation history of the landslide, the strong, weak, and abnormal deformation areas were identified and compared with the field investigation results. Finally, the overall stability of the landslide was evaluated through numerical simulation. The primary conclusions of this study are as follows:

(1) The landslide is divided into seven engineering geological zones, of which zones I to V have clear deformation signs overall, and zones VI and VII show no significant deformation

(2) InSAR monitoring results show that strong deformation area A is located in area I, and area B spans areas II, III, and IV, which shows local traction sliding deformation

(3) Numerical simulation results show that the deep sliding surface 1 of the landslide is in an unstable state, and the deep sliding surface 2 is in a stable state. By comparing the deformation characteristics of numerical simulation with field investigation and InSAR results, it is found that the deformation and stability of zone I are primarily controlled by deep sliding surface 1, and the deformation and stability

of zones II, III, and IV are primarily controlled by the deep sliding surface 2

(4) In this study, a deformation analysis and stability evaluation of a large-scale loess landslide with multiple slip surfaces in the Yellow River Basin were conducted using InSAR, numerical simulation, and traditional field investigation. The treatment process should focus on the strong deformation areas A and B. The results are useful for disaster prevention and reduction of loess disasters in the Yellow River Basin

Data Availability

The data are available and explained in this article; readers can access the data supporting the conclusions of this study.

Disclosure

I would like to declare on behalf of my co-authors that the work described is original research and has not been previously published.

Conflicts of Interest

The authors declare no conflict of interest.

Authors' Contributions

The manuscript is approved by all authors for publication.

Acknowledgments

The author thanks the project supported by the Department of Natural Resources of Qinghai Province. We thank the editor and anonymous reviewers for improving the original manuscript.

References

[1] J. Peng, S. Wang, Q. Wang et al., "Distribution and genetic types of loess landslides in China," *Journal of Asian Earth Sciences*, vol. 170, pp. 329–350, 2019.

[2] M. Pécsi, "Loess is not just the accumulation of dust," *Quaternary International*, vol. 7, pp. 1–21, 1990.

[3] J. Zhuang, J. Peng, G. Wang, I. Javed, Y. Wang, and W. Li, "Distribution and characteristics of landslide in Loess Plateau: a case study in Shaanxi province," *Engineering Geology*, vol. 236, pp. 89–96, 2018.

[4] X. S. Li, Q. H. Li, Y. J. Hu et al., "Study on three-dimensional dynamic stability of open-pit high slope under blasting vibration," *Lithosphere*, vol. 2021, no. Special 4, article 6426550, 2022.

[5] J. Zhuang, J. Peng, X. Zhu, W. Li, P. Ma, and T. Liu, "Spatial distribution and susceptibility zoning of geohazards along the Silk Road, Xian-Lanzhou," *Environmental Earth Sciences*, vol. 75, no. 8, article 711, 2016.

[6] Z. Dou, Y. M. Liu, X. Y. Zhang et al., "Influence of layer transition zone on rainfall-induced instability of multilayered slope," *Lithosphere*, vol. 2021, no. Special 4, article 2277284, 2021.

[7] C. Meisina, F. Zucca, D. Fossati, M. Ceriani, and J. Allievi, "Ground deformation monitoring by using the Permanent Scatterers Technique: the example of the Oltrepo Pavese (Lombardia, Italy)," *Engineering Geology*, vol. 88, no. 3-4, pp. 240–259, 2006.

[8] M. Necsoiu, R. N. McGinnis, and D. M. Hooper, "New insights on the Salmon Falls Creek Canyon landslide complex based on geomorphological analysis and multitemporal satellite InSAR techniques," *Landslides*, vol. 11, no. 6, pp. 1141–1153, 2014.

[9] J. Wasowski and F. Bovenga, "Investigating landslides and unstable slopes with satellite multi temporal interferometry: current issues and future perspectives," *Engineering Geology*, vol. 174, pp. 103–138, 2014.

[10] Y. Zhang, X. Meng, G. Chen, L. Qiao, R. Zeng, and J. Chang, "Detection of geohazards in the Bailong River Basin using synthetic aperture radar interferometry," *Landslides*, vol. 13, no. 5, pp. 1273–1284, 2016.

[11] E. Intrieri, F. Raspini, A. Fumagalli et al., "The Maoxian landslide as seen from space: detecting precursors of failure with Sentinel-1 data," *Landslides*, vol. 15, no. 1, pp. 123–133, 2018.

[12] M.-Z. Gao, B.-G. Yang, J. Xie et al., "The mechanism of microwave rock breaking and its potential application to rock-breaking technology in drilling," *Petroleum Science*, 2022.

[13] C. Zhu, M. Karakus, M. C. He et al., "Volumetric deformation and damage evolution of Tibet interbedded skarn under multistage constant-amplitude-cyclic loading," *International Journal of Rock Mechanics and Mining Sciences*, vol. 152, article 105066, 2022.

[14] Y. Zhang, X. Meng, C. Jordan, A. Novellino, T. Dijkstra, and G. Chen, "Investigating slow-moving landslides in the Zhouqu region of China using InSAR time series," *Landslides*, vol. 15, no. 7, pp. 1299–1315, 2018.

[15] K. Zhu, P. Xu, C. Cao, L. Zheng, Y. Liu, and X. Dong, "Preliminary identification of geological hazards from Songpinggou to Feihong in Mao County along the Minjiang River using SBAS-InSAR technique integrated multiple spatial analysis methods," *Sustainability*, vol. 13, no. 3, p. 1017, 2021.

[16] X. Liu, C. Zhao, Q. Zhang, Z. Lu, and F. Dai, "Investigating the Deformation History and Failure Mechanism of HEIFANGTAI Loess Landslide, China with Multi-Source SAR Data," in *In Proceedings of the IEEE International Geoscience and Remote Sensing Symposium (IGARSS)*, Yokohama, Japan, 2019.

[17] C. Cao, W. Zhang, J. P. Chen, B. Shan, S. Y. Song, and J. W. Zhan, "Quantitative estimation of debris flow source materials by integrating multi- source data: a case study," *Engineering Geology*, vol. 291, article 106222, 2021.

[18] B. Bayer, A. Simoni, D. Schmidt, and L. Bertello, "Using advanced InSAR techniques to monitor landslide deformations induced by tunneling in the Northern Apennines, Italy," *Engineering Geology*, vol. 226, pp. 20–32, 2017.

[19] Y. Takada and G. Motono, "Spatiotemporal behavior of a large-scale landslide at Mt. Onnebetsu-dake, Japan, detected by three L-band SAR satellites," *Earth Planets and Space*, vol. 72, no. 1, 2020.

[20] L. Wang, S. Wang, G. Li, and L. Wang, "Construction of 3D creep model of landslide slip-surface soil and secondary development based on FLAC3D," *Advances in Civil Engineering*, vol. 2020, 15 pages, 2020.

[21] X. Q. Yuan, Z. Duan, and F. S. Zhao, "The Formation Mechanism of River Erosion-Induced Loess Landslide," *IOP Conference Series: Earth and Environmental Science*, vol. 186, 2018.

[22] Z. Wang, B. Liu, Y. Han, J. Wang, B. Yao, and P. Zhang, "Stability of inner dump slope and analytical solution based on circular failure: illustrated with a case study," *Computers and Geotechnics*, vol. 117, article 103241, 2020.

[23] Y. He, H. Zhang, B. Liu, and Y. Wu, "Research on FLAC 3D numerical simulation of working mechanism of compaction pile composite foundation," *Applied Mechanics and Materials*, vol. 204-208, pp. 220–223, 2012.

[24] W.-c. Wang, S.-r. Sun, J.-h. Wei, Y.-x. Yu, W. He, and J.-l. Song, "Numerical experimental study on optimum design of anchorage system for Xiashu loess slope," *Journal of Central South University*, vol. 28, no. 9, pp. 2843–2856, 2021.

[25] P. Zhang, D. Zhang, Y. Yang et al., "A case study on Integrated modeling of spatial information of a complex geological body," *Lithosphere*, vol. 2022, no. Special 10, article 2918401, 2022.

[26] D. Chen, H. Chen, W. Zhang, J. Lou, and B. Shan, "An analytical solution of equivalent elastic modulus considering confining stress and its variables sensitivity analysis for fractured rock masses," *Journal of Rock Mechanics and Geotechnical Engineering*, 2021.

[27] D. Peng, Q. Xu, F. Liu et al., "Distribution and failure modes of the landslides in Heitai terrace, China," *Engineering Geology*, vol. 236, pp. 97–110, 2018.

[28] H. Deng, L. Z. Wu, R. Q. Huang, X. G. Guo, and Q. He, "Formation of the Siwanli ancient landslide in the Dadu River, China," *Landslides*, vol. 14, no. 1, pp. 385–394, 2017.

[29] Q. Meng, W. Li, F. Raspini et al., "Time-series analysis of the evolution of large-scale loess landslides using InSAR and UAV photogrammetry techniques: a case study in Hongheyan, Gansu Province, Northwest China," *Landslides*, vol. 18, no. 1, pp. 251–265, 2021.

[30] Z.-j. Meng, P.-h. Ma, and J.-b. Peng, "Characteristics of loess landslides triggered by different factors in the Chinese loess plateau," *Journal of Mountain Science*, vol. 18, no. 12, pp. 3218–3229, 2021.

Hindawi
Geofluids
Volume 2022, Article ID 6235044, 16 pages
https://doi.org/10.1155/2022/6235044

Research Article

Study on Characteristics of the Water-Sediment Two-Phase Flow in Fractures Based on Numerical Simulation

Lili Cao,[1] Chuan Wu,[1] Hanhua Xu,[2,3] Hao Yu,[4] Ming Li,[4] Yu Han,[4] and Zhanqing Chen[4]

[1]*School of Medical Information and Engineering, Xuzhou Medical University, Xuzhou, Jiangsu 221004, China*
[2]*Kunming Prospecting Design Institute of China Nonferrous Metals Industry Co., Ltd., Kunming, Yunnan 650051, China*
[3]*State Key Laboratory for Geomechanics and Deep Underground Engineering, China University of Mining and Technology, Xuzhou, Jiangsu 221116, China*
[4]*School of Earth Science, China University of Geosciences, Wuhan, Hubei 430074, China*

Correspondence should be addressed to Chuan Wu; wwcent@163.com

Received 2 March 2022; Accepted 28 March 2022; Published 6 May 2022

Academic Editor: Long Yan

The instability of water-sediment flow in fractures can easily induce water-sediment disasters. Therefore, it is of great significance for the prevention and control of water-sediment inrush to study the water-sediment two-phase flow in fractures. Based on the water-sediment two-phase flow theory, a model of the water-sediment two-phase flow system was established. The Ansys Fluent software was used to study the characteristics of the water-sediment two-phase flow in smooth and rough fractures. The spatial-temporal evolution laws of the water-sediment two-phase flow were studied; the results indicated that they did not change with time in the smooth fractured flow fields, while changing continuously with time in the rough fractured flow fields and in a dynamic steady state. The research results can provide references for the water-sediment two-phase flow in fractures and rock mass.

1. Introduction

Water and sand inrush is one of the main disasters in the mining of shallow coal seams in Western China [1]. Fractures or small faults often connect the water-rich layer with unbalanced sand bodies due to weathering [2, 3]. Then, under the action of gravity, the water-sediment mixture will submerge the equipment underground and even cause casualties. Water-sediment two-phase flow is one of the important incentives of water-sediment inrush disasters [4]. Therefore, it is of great significance to study the water-sediment two-phase flow in fractures to ensure the safe and efficient production of mines [5, 6].

Scholars have carried out numerous researches on water-sediment two-phase mixture seepage characteristics and their influencing factors [7, 8]. Liu et al. analyzed the variation laws of permeability parameters of rock-fractured rock mass fracture roughness, sand particle size, and sediment concentration [9]. Yang et al. revealed the influence of sediment-water interactions on movement characteristics and rheological characteristics of water-sediment mixture [10]. Qi and Bo studied the failure mechanism and evolution characteristics of water-sediment inrush disasters caused by the instability of the filling medium of karst caves [11]. Yang et al. conducted a nonlinear flow experiment on the fracture network and revealed the mechanism of water inrush in fractures [12]. Zhang et al. analyzed the influence of the aeolian sand's particle size distribution, void ratio, and initial mass on the flow characteristics [13]. Xu et al. simulated the process of water-sediment inrush in the goaf and proposed the prevention and control techniques [14]. However, due to the limitation of test conditions, there were still some shortcomings in the study of the flow characteristics of the water-sand mixture by experimental means. For example, it was difficult to find the test equipment that met the requirements of high performance when the water-sand

mixture needed to be transported at a stable flow rate. In addition, it was difficult to describe the vortex structure efficiently and accurately using the existing experimental means, which made it difficult to conduct a more in-depth study on the flow field of water-sediment two-phase flow.

Considering the complex geological conditions of undergrounding mining [15, 16], some scholars have used the finite element analysis and discrete element method to reveal the whole process of water-sediment two-phase flow and have achieved remarkable results [17]. Du et al. used the FORTRAN programming language for numerical calculation and determined the main factors affecting the characteristic parameters of water-sediment two-phase mixture seepage in fractured rock mass [18]. Pu analyzed the laws of water-sediment two-phase flow in fractures using the lattice Boltzmann method. They also simulated the water-sand inrush by numerical simulation and analyzed the impacts of particle size and fracture width on the water-sand inrush velocity [19]. Guo et al. simulated the whole process of water-sand inrush process during the mining of the working face by using the self-developed simulation test system [20]. Lei et al. used the PFC3D to simulate the development process of overburden fissures and the water hydraulic of Paleogene aquifers [21]. In summary, scholars have conducted studies on the characteristics of water-sediment two-phase seepage in fractures using experimental methods, but there are still some deficiencies. The research only focuses on the seepage of a single fluid and rarely involves the liquid-solid two-phase movement in fractures. There are few studies on seepage of the particle phase and continuous phase simultaneously in fractures. Meanwhile, there is currently no universally accepted standard for the description of fracture surface morphology [2, 22].

In this paper, Ansys Fluent 17.0 will be used to simulate water-sediment two-phase flow in fractures with smooth and rough surfaces. Firstly, the mechanical model and numerical model of the water-sediment two-phase flow will be established. Then, different turbulence simulation methods will be used to calculate the flow field of the continuous phase. The calculated results will be compared with the experimental results, and a preferable method will be selected for fractures with rough and complex surfaces. Finally, the dispersed phase particles will be injected into the flow field of the continuous phase in dynamic equilibrium, and the coupling calculation will be performed. The calculated results will be compared with the experimental results to further study the influence factors of the water-sediment seepage field. The research results are aimed at providing a theoretical foundation for the mechanism of water-sediment inrush during coal mining.

2. The Mechanical Model of Water-Sediment Two-Phase Flow in Fractures

2.1. The Model Hypothesis and Selection of Water-Sediment Flow in Fractures. The following assumptions were made during the numerical simulation of water-sediment flow in fractures [23, 24]. (I) Water is incompressible. That is, the density of water was a constant. (II) Sand particles were spheres with the same particle sizes. (III) The rigid entities were spherical sand particle units and would not obtain obvious damage. (IV) The water-sediment mixture flowed into fractures from the flow guide transition plate with a larger aperture. The transition was smooth at the inlet of the fracture, and the flow velocity was uniform on the cross-section of the inlet of the fracture. (V) The disperse phase sand particle velocity was the same with that of the continuous-phase fluid at the inlet of the fracture. (VI) When sand particles escaped from the exit of the fracture, the tracking would be stopped. (VII) The physical quantity did not change along the X_3 direction, and the flow was taken as a two-dimensional flow.

The model of water-sediment flow in fractures was composed of the continuous-phase model and the discrete-phase model. The Reynolds averaging method and the large eddy simulation method were used to simulate the turbulent flow for the continuous phase [25]. According to different methods of stress treatment, the Reynolds averaging model could be divided into the eddy viscosity model and Reynolds stress model [26]. The former is to introduce the turbulent viscosity to treat the Reynolds stress instead of treating the stress directly. The Reynolds stress is expressed by a function of the turbulent viscosity. The commonly used eddy viscosity models in engineering include the Spalart-Allmaras model, k-ε model, and k-ω model. In this paper, the selected turbulence models include the RNG k-ε model in the k-ε model, Realizable k-ε model, and SST k-ω model in the k-ω model. In the Reynolds stress model (RSM), the equations of the Reynolds stress are established directly. The isotropic viscosity hypotheses can be avoided. Meanwhile, the influences of fluid rotation, streamline bending, and sharp change in the strain rate will be considered. Compared with the eddy viscosity models, RSM is more suitable for accurate prediction of complex flows. The Stress-Omega RSM was adopted in this paper. The Stress-Omega model of the wall-modeled large eddy simulation (WMLES) was used for the mathematical model of subgrid-scale stress [27].

It is necessary to simulate the rotation and translation of sand particles in the study of water-sediment flow in fractures. In this paper, the random orbit model was used to simulate the particle diffusion caused by the turbulent motion of the continuous phase. Meanwhile, based on the distinct element method and the program BALL proposed by Cundall and Strack [28], the Hertzian-Dashpot model and the Rolling Friction model were used to simulate the normal contact and the tangential contact force among particles, respectively.

2.2. Computational Domain of the Water-Sediment Flow in Fractures. The computational domain Ω was a set of particles surrounded by two fracture surfaces, the inlet section and the outlet section. The set of particles was time varying. That is, water and sand entered continuously from the inlet section and flowed out from the outlet section, and the control volume was constant. The computational domains of the smooth fractures and the rough fractures were descried as follows.

2.2.1. The Computational Domain of the Smooth Fractures. As shown in Figure 1, water and sand flowed into the area

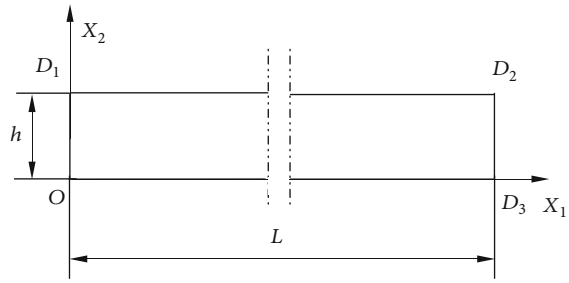

Figure 1: The computational domain of the smooth fracture.

formed by two parallel smooth fracture surfaces. The distance between the two fracture surfaces is h, and the length of the fracture is L. The projection of the upper and lower fracture surfaces on the OX_1X_2 section is a straight line. The boundary of the computational domain is the inlet section $\overline{OD_1}$, the upper fracture section $\overline{D_1D_2}$, the outlet section $\overline{D_2D_3}$, and the lower fracture surface $\overline{D_3O}$.

2.2.2. The Computational Domain of the Rough Fractures. As shown in Figure 2, water and sand flowed in the area formed by two anastomotic fracture surfaces. The curve of the upper and lower fracture surfaces on the cross-section OX_1X_2 is a broken line which divides the surface into 50 equal broken line segments marked by FL_i^u and FL_i^d, $i = 1, 2, 3, \cdots 50$. The computational domain Ω is formed by the inlet section $\overline{OC_1}$, the upper fracture surface $\bigcup_{i=1}^{50} FL_i^u$, the outlet section $\overline{C_2C_3}$, and the lower fracture section $\bigcup_{i=1}^{50} FL_i^d$.

2.3. Boundary Conditions and the Initial Conditions. The boundary and initial conditions needed to be specified to solve the equations for the water-sediment two-phase flow fields. The boundary and initial conditions of the continuous phase and the discrete phase were given, respectively.

2.3.1. Boundary Conditions of the Continuous Phase. The inlet boundary was set as the velocity inlet. The four-level seepage velocity was used in the experiment. The hydraulic diameter was twice the aperture of the fracture inlet. The turbulence intensity could be obtained by the following equation:

$$I = 0.16\left(R_{eD_H}\right)^{-1/8}, \quad (1)$$

where R_{eD_H} is the Reynolds number with the hydraulic diameter of D_H. The outlet boundary was set as the pressure outlet. The outlet connected with the air, so the outlet pressure was the standard atmospheric pressure of 1. The wall boundary was set as a no-slip wall boundary. The gravity direction was along the negative direction of X_2.

2.3.2. Boundary Conditions of the Dispersed Phase. The discrete-phase sand particle velocity was the same as the continuous-phase fluid velocity at the inlet of the fracture. The volume concentration of sand particles was set to 4.06%. The outlet of the fracture was set as the escape boundary of the discrete phase, where the tracing would stop. The sand particles and the wall boundary were set as the rebound boundary. The values of the initial boundary conditions were fixed and did not change with time.

2.4. Numerical Calculation Methods and Parameter Settings. The grid division is a key step in the numerical calculation by using the finite volume method. Its quality directly affects the accuracy of the numerical calculation results. In this paper, the structured grids were used, because the boundary of the smooth fracture model was relatively regular. The grid nodes were evenly distributed at the inlet to make the sand particles evenly distributed along the X_2 direction. The Stress-Omega RSM was used in this paper. y^+ was the dimensionless distance between the first layer of grid nodes and the wall, which was approximately 1. Therefore, the fine grids were arranged in the near-wall region. After calculation, it was necessary to check whether y^+ could meet the requirements.

In order to ensure the accuracy of the calculation results, the grid independence test was carried out. The size of the initial grid in the boundary layer was 0.005 mm, and the global grid size was 0.08 mm. After the grid independence test, the size of the grid in the boundary layer was 0.003 mm, and the global grid size was 0.02 mm. Through calculation, it was found that both grids could satisfy that y^+ was less than 1. The inlet pressure difference of two grids was less than 1%. The velocity difference was less than 0.3% on the cross-section of $X_1 = 20$ mm, indicating that the initial grids could meet the requirements of the calculation accuracy. In view of the calculation accuracy and efficiency, the initial grids were selected for calculation. Figure 3 shows the grid division.

The hybrid grid was used, due to sharp bending of the wall of the rough fracture model. Multilayer structured grids were set in the boundary layer, and the remaining computational domain was unstructured quadrilateral grids. The y^+ was tested, and the grid independence test was conducted. The total number of grids was about 145,000, as shown in Figure 4. The grids in the boundary layer are shown in Figure 5.

After the grid division of the computational domain, it was necessary to discretize the governing equations and definite conditions (boundary conditions and initial conditions) in the space domain and the time domain. The Least Squares Cell-Based method was used. The pressure interpolation method was the pressure staggering option (PRESTO). The momentum conservation equation, the equation for the turbulence kinetic energy k, and the equation for the specific dissipation rate ω adopted the third-order MUSCL scheme to reduce the numerical diffusion. The Reynolds stress equation used the QUICK discrete scheme (the quadrilateral grids used the QUICK discrete scheme, and other grids used the second-order discrete scheme). The second-order implicit time integration scheme was used to solve the continuous-phase equations, and the Runge-Kutta method was used to calculate the discrete-phase equations.

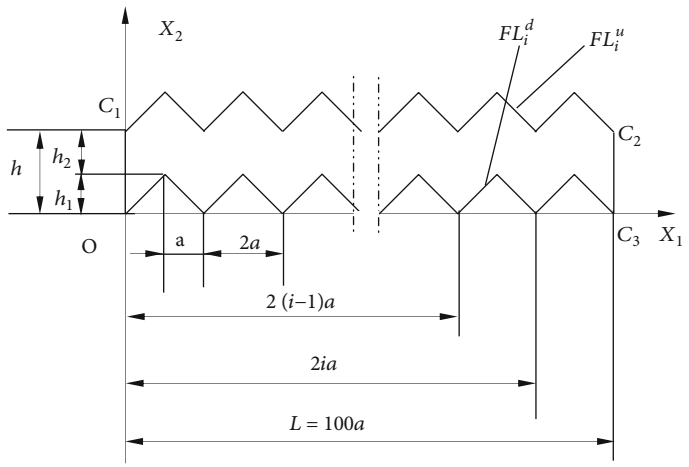

Figure 2: The computational domain of the rough fracture.

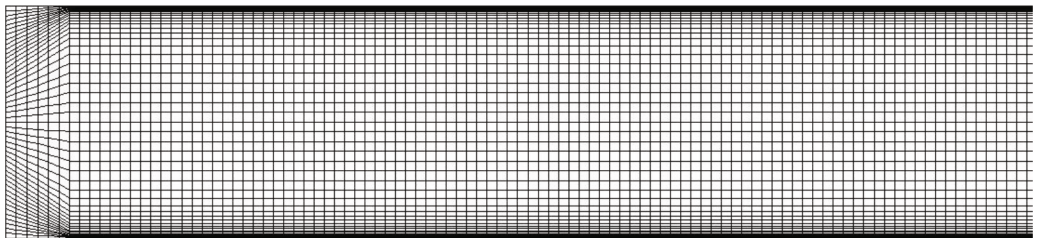

Figure 3: The grid of the smooth fracture.

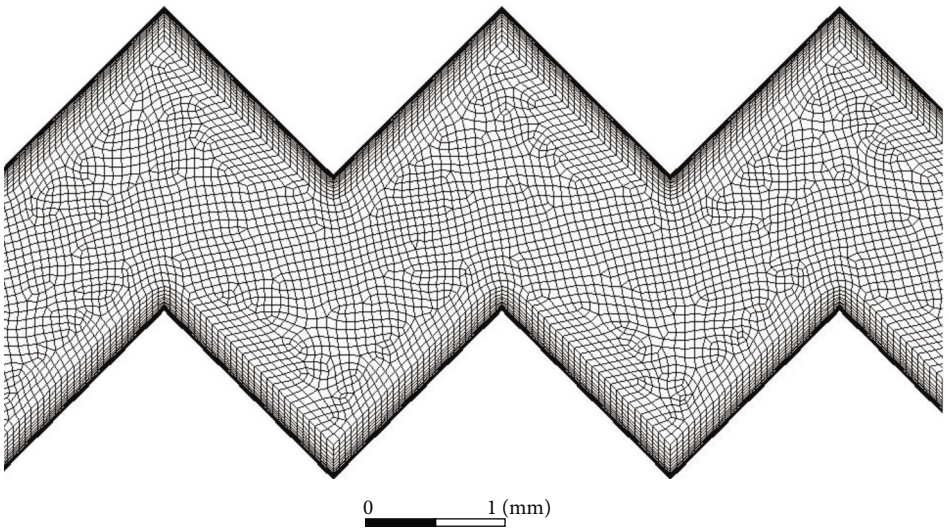

Figure 4: Grids of the rough fracture.

Table 1 shows the material properties. Table 2 shows the interaction parameters of sand particles and the wall. Table 3 shows the parameters among sand particles.

The pressure-based solver was used for calculation. The pressure-velocity coupling PSIO (pressure implicit with splitting of operator) algorithm was used. The interphase coupling calculation method was used, and interactions between the continuous phase and the discrete phase were considered. After adjustment, the time step was set as 10^{-5} s. The tracking time step of the sand particles was one percent of the continuous-phase calculation time step. The velocity and inlet pressure changes were monitored during the calculation process. Parallel computing was used to enhance the calculation speed.

2.5. The Experimental Scheme. In this paper, some water-sediment seepage experimental data were from the results of Zhanqing Chen's Research Group, State Key Laboratory for Geomechanics and Deep Underground Engineering, China University of Mining and Technology. Restricted by

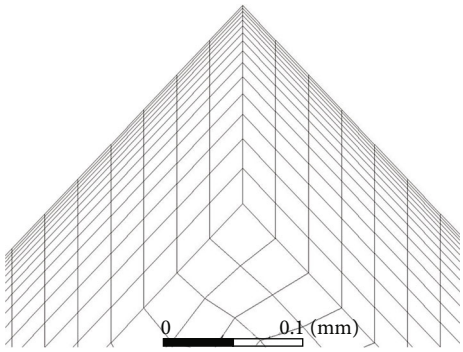

Figure 5: Grids in the boundary layer of the rough fracture.

Table 1: Material properties [29].

	Water	Sand particles
Density (kg·m^{-3})	998.2	2650
Dynamic viscosity (kg·m^{-1}·s^{-1})	1.003×10^{-3}	/
Elastic modulus (GPa)	/	55.9
Poisson's ratio	/	0.13
Particle size (mm)	/	0.04

Table 2: Interaction parameters between the sand particles and the wall.

Properties	Between sand particles and wall
Friction factor	0.45
Normal recovery factor	0.2
Tangential recovery factor	0.9

Table 3: Interaction parameters among sand particles [29].

Properties	Among sand particles
Coefficient of static friction	0.3
Coefficient of sliding friction	0.2
Coefficient of restitution	0.05

the test conditions, only the water-sediment two-phase flow in regular and rough fractures was studied without the test of water-sediment two-phase flow in smooth fractures.

Numerical simulation is a necessary supplement and extension of experimental research and theoretical analysis. It can simulate complex flow problems and obtain the data that is difficult to obtain in experiments [30]. In this paper, the numerical simulation was used to study the characteristics of the water-sediment two-phase flow in fractures.

To better describe the flows in fractures, it was necessary to compare the simulation results and the experimental data of the unidirectional flow in fractures before performing the simulation of two-phase flow in fractures. In this paper, several different turbulence simulation calculation methods were used to calculate the continuous-phase flow fields, and the calculation results were compared with the experimental results. Based on the comparison results, the appropriate turbulence simulation method was chosen.

The Ansys Fluent was used to simulate the water-sediment two-phase flow in the smooth and rough fractures. The geometric description of the fracture surface was given before the simulation. Then, the grid division was performed in the computational domain. The experimental parameters were given. The sand density ρ_p was 2650 kg/m^3, the sand particle size D_p was 0.04 mm, and the volume concentration Φ of the sand particles was 4.06%. On this basis, the numerical model was established. Finally, the inlet velocities of the fractures were set as 0.349 m/s, 0.532 m/s, 0.697 m/s, and 0.869 m/s. Then, the program was debugged.

After the simulation, the spatial-temporal evolution laws and influence factors of the water-sediment two-phase flow were analyzed according to the simulation results.

3. Results of the Numerical Simulation

3.1. Selection of the Turbulence Model. According to the assumptions made in Section 2.1, the physical quantities did not change in the width direction during the simulation. However, the fracture specimens used in the experiment had certain widths, which would affect the fluid flow. Thus, it was necessary to clarify the influence of the fracture width before choosing the turbulence model. The relationship between the absolute values of the pressure gradient between the real experiment considering the width and the numerical model without considering the width was expressed by the following equation:

$$G_p = 2.01 G_p', \tag{2}$$

where G_p is the absolute value of the pressure gradient in the experiment. G_p' is the absolute value of the pressure gradient in the numerical model. Equation (3) could be used to get the value of α, that is, 2.01 [31].

$$a = \frac{1}{\left[1 - (h/D)(192/\pi^2)\sum_{n=1}^{\infty} \tanh((2n-1)\pi D/2h)/(2n-1)^5\right]}, \tag{3}$$

where h is the fracture aperture and D is the fracture width. Equation (2) could be obtained by substituting D of 70 mm and h of 1.8 mm into Equation (3). Equation (2) was used as a two-dimensional model G_p' of a rough fracture to approximately get the equation of the three-dimensional model.

Figure 6 shows the change curves of the absolute value of the pressure gradient G_p in the continuous-phase flow in rough fractures in different turbulence models. There was linear loss and partial loss during the seepage test, so the value of G_p was larger than the actual value. Similarly, the value of G_p by the numerical simulation was less than the measured value. As shown in Figure 6, the values of G_p obtained by the RNG k-ε model and Realizable k-ε model

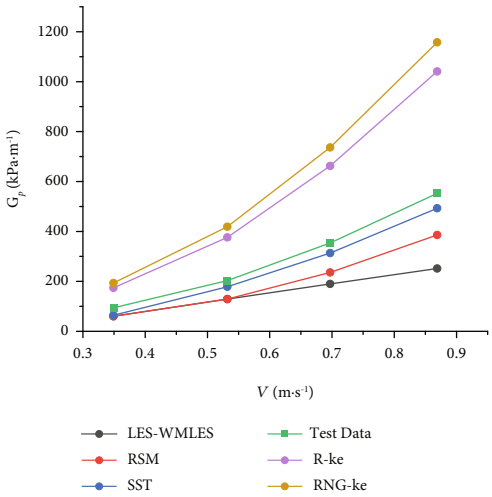

Figure 6: Comparison of simulation and test results.

were much larger than the measured values, while the values of G_p obtained by using the Shear-Stress Transport (SST) k-ω model, Stress-Omega RSM, and LES were less than the measured values. It could be seen that the measured G_p value changed nonlinearly with the seepage velocity, which was consistent with the change tendencies of simulation results obtained by the SST k-ω model and Stress-Omega RSM. The value of G_p obtained by LES showed an approximately linear relationship with the seepage velocity. Therefore, the SST k-ω model and Stress-Omega RSM could better simulate the pressure loss of the flow in rough fractures. In order to determine the optimal turbulence model, it was necessary to further analyze the structures of their flow fields.

LES could directly calculate the turbulent motion larger than the grid scale through instantaneous Navier-Stokes equations, which could predict the formation and distribution of large-scale eddy currents. In this paper, LES, Stress-Omega RSM, and SST k-ω model were used to simulate the water-sediment flow in rough fractures with the fracture inlet velocity of 0.869 m/s. The vortex structure obtained by LES was used as a reference to compare with the results of the other two models. Figures 7 and 8 show the streamline diagrams obtained by the three simulation methods when $t = 0.06$ s and $t = 0.1$ s, respectively. In Figure 7, when $t = 0.06$ s, the streamline diagrams were basically the same obtained by RSM and LES. Specifically, two kinds of vortices were formed at the concave corner of the fracture. One was a three-vortex structure composed of one large and two small vortices, and the large vortex was located downstream of the small vortex. The other was a double-vortex structure composed of one large and one small vortex. The small vortex was located at the bottom of the concave corner of the fracture. However, the form of the vertex obtained by the SST k-ω model was single and was composed of a large vortex and a small vortex at the bottom of the concave corner of the fracture.

In Figures 7 and 8, the streamline diagrams are different, showing the randomness of the two forms of vortices along the flow direction, while the streamline diagrams obtained by the SST k-ω model were nearly the same when $t = 0.06$ s and $t = 0.1$ s, which could not reflect the evolution of the vortex over time. In summary, Stress-Omega RSM could accurately calculate the pressure loss and simulate the structure of the flow field in the rough fractures, so it was chosen to simulate the continuous-phase flow in fractures.

3.2. Simulation Results of the Water-Sediment Two-Phase Flow in Smooth Fractures. Figure 9 shows the change curve of the average pressure at the inlet of the fracture with time when the inlet velocity was 0.869 m/s. The interval from $t = 0$ to $t = 0.015$ s was the continuous-phase flow field pressure curve, and the interval from $t = 0.015$ s to $t = 0.5$ s was the water-sediment two-phase flow field pressure curve after the sand particles were injected.

In Figure 9, the average pressure at the inlet of the fracture increased gradually after the injection of sand particles. With the continuous increase of injected sand particles, it increased to the extreme value and then began to reduce and finally showed small amplitude oscillations within a certain range. It could be seen that the sand particles significantly decreased the average pressure at the inlet. Figure 10 shows the pressure gradient absolute value-velocity curve, and an approximately linear relationship existed.

In Figure 11, with the inlet velocity of 0.869 m/s, the distributions of velocities, turbulence energy, and pressure on the cross-section of $X_2 = 0.9$ mm (midline position) could be observed when $t = 0.17$ s, 0.22 s, and 0.27 s. In Figures 11(a) and 11(b), in the interval of $X_1 \leq 30$ mm, the flow velocity and turbulent kinetic energy changed continuously along $X_2 = 0.9$ mm. In the interval of $X_1 \geq 30$ mm, they remained stable, indicating that the flow was fully developed. In Figure 11(c), the pressure was approximately linearly distributed along $X_2 = 0.9$. The velocities, turbulent kinetic energy, and pressure curves were basically consistent at different times on the cross-section of $X_2 = 0.9$ mm, indicating that they did not change over time on this section.

Figure 12 shows the distributions of velocities, turbulent kinetic energy, and pressure at different times on the cross-section of $X_1 = 40$ mm. In Figures 13(a) and 13(b), the velocity and turbulent kinetic energy curves basically coincide on the cross-section of $X_1 = 40$ mm, indicating that they were stable and did not change over time. In Figure 14(c), the pressure on the cross-section of $X_1 = 40$ mm changed with time in a small change amplitude.

Based on the above analysis, the physical quantities did not change along the flow direction in the interval of $X_1 \geq 25$ mm. Therefore, the interval of $0 \leq X_1 \leq 40$ mm was chosen to analyze the particle distribution and discrete-phase momentum source term distribution.

Figure 13 shows the sand distribution in the interval of $0\text{ mm} \leq X_1 \leq 40$ mm, which was divided into two segments. It could be found that there was a layer of particles with lower velocities on the lower wall of the fracture, and there were no particles on the upper wall. It was indicated that particles were deflected downward due to the action of gravity, and a small part of particles was deposited on the lower wall of the fracture.

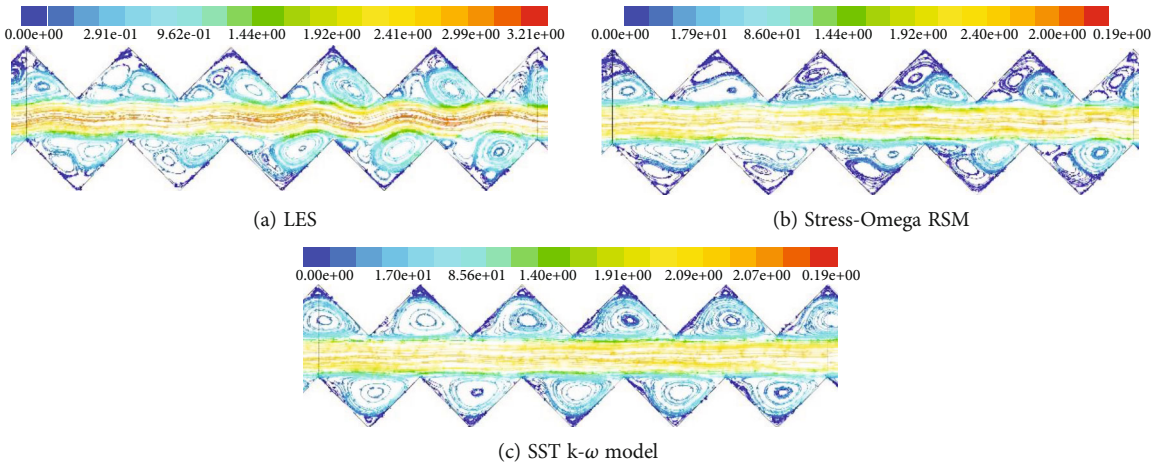

(a) LES (b) Stress-Omega RSM

(c) SST k-ω model

Figure 7: Streamline diagrams when $t = 0.06$ s.

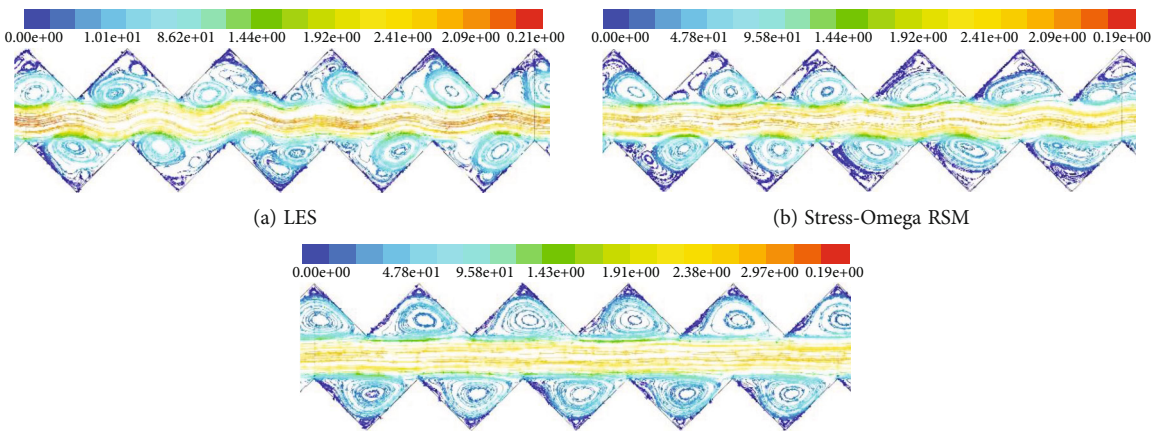

(a) LES (b) Stress-Omega RSM

(c) SST k-ω model

Figure 8: Streamline diagrams when $t = 0.1$ s.

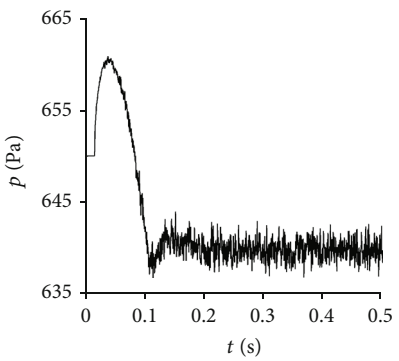

Figure 9: Average pressure-time curve at the inlet of the fracture.

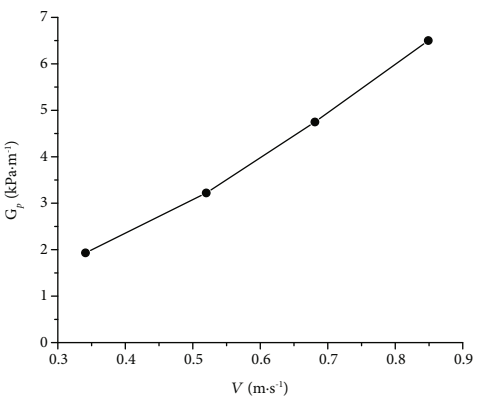

Figure 10: The pressure gradient absolute value-velocity curve.

Figure 14 shows the distribution of momentum source terms in the discrete-phase model in the fracture interval of $0\,\text{mm} \le X_1 \le 40\,\text{mm}$. In Figure 14(a), the absolute value of the momentum source term in the X_1 direction component was relatively large at the inlet segment, and the direction was along the negative direction of X_1. It was indicated that the force of the continuous-phase fluid on particles was opposite to the flow direction at the inlet segment of the fracture. In the interval of $X_1 \ge 40\,\text{mm}$, the flow was fully developed, and the momentum source terms in the X_1 direction component were evenly distributed along the X_2 direction. In Figure 14(b), the absolute value of the momentum source term in the X_2 direction component was relatively

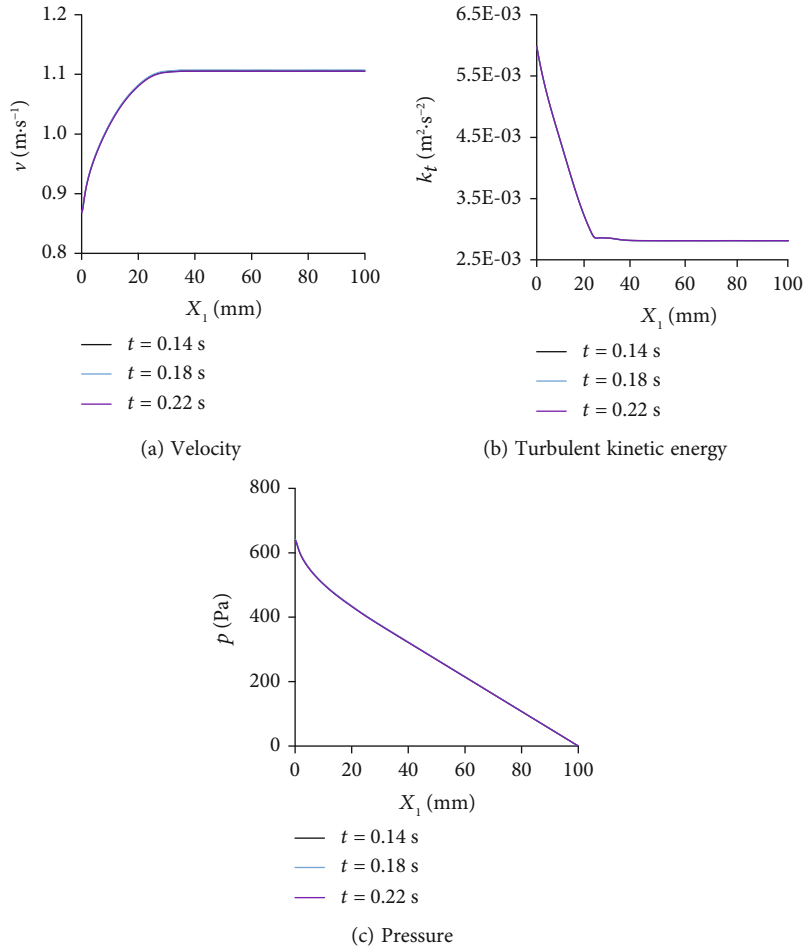

Figure 11: Distribution of physical quantities on the cross-section of $X_2 = 0.9$ mm.

large in the inlet segment. It was positive at the upper part of $X_2 = 0.9$ mm and was negative at the lower part.

3.3. Simulation Results of the Water-Sediment Two-Phase Flow in Rough Fractures

3.3.1. Comparison of Numerical Simulation Results and Test Results. Figure 15 shows the comparison between the simulated results and the experimental results of the pressure gradient absolute value-seepage velocity curves. Figure 15(a) shows the comparison result of the single phase flow, and Figure 15(b) shows the comparison result of the water-sediment two-phase flow.

In Figure 15(a), the pressure gradient absolute value-seepage velocity curve of the single phase in fractures obtained by the numerical simulation is basically consistent with that in the experiment, showing a nonlinear relationship. The numerical simulation result was smaller than the experimental result, and the relative error was between 30.1% and 33.4%. This is because Equation (2) describes the relationship between the pressure gradient absolute value of the three-dimensional model of the smooth fracture and the pressure gradient absolute value of the two-dimensional model. The flow was laminar, while in this paper, the flow was turbulent through rough fractures [32]. It is worth noting that the relative errors between the numerical simulation results and the experimental results were relatively close at different flow rates.

In Figure 15(b), the absolute value of the pressure gradient-seepage velocity of the water-sediment two-phase flow in fractures obtained by the numerical simulation is basically consistent with the curve obtained by the experiment, showing a nonlinear relationship. The numerical simulation result was smaller than the experimental result, and the relative error was between 18.5% and approximately 46.7%. This is because Equation (2) describes the relationship between the absolute value of the pressure gradient in the three-dimensional model of the smooth fracture in laminar flow and that in the two-dimensional model. The flow was a single-phase laminar flow, while this paper focuses on the two-phase turbulence in rough fractures. It should be noted that the absolute error of the numerical simulation results and the test results were relatively close at different flow velocities, and the relative error decreased with the increase of the flow velocity [33].

3.3.2. Change Laws of Physical Quantities in Flow Fields with Time. Figure 16 gives the change curve of the average pressure at the inlet with time, when the inlet velocity was 0.869 m/s. It was the pressure curve of the continuous-

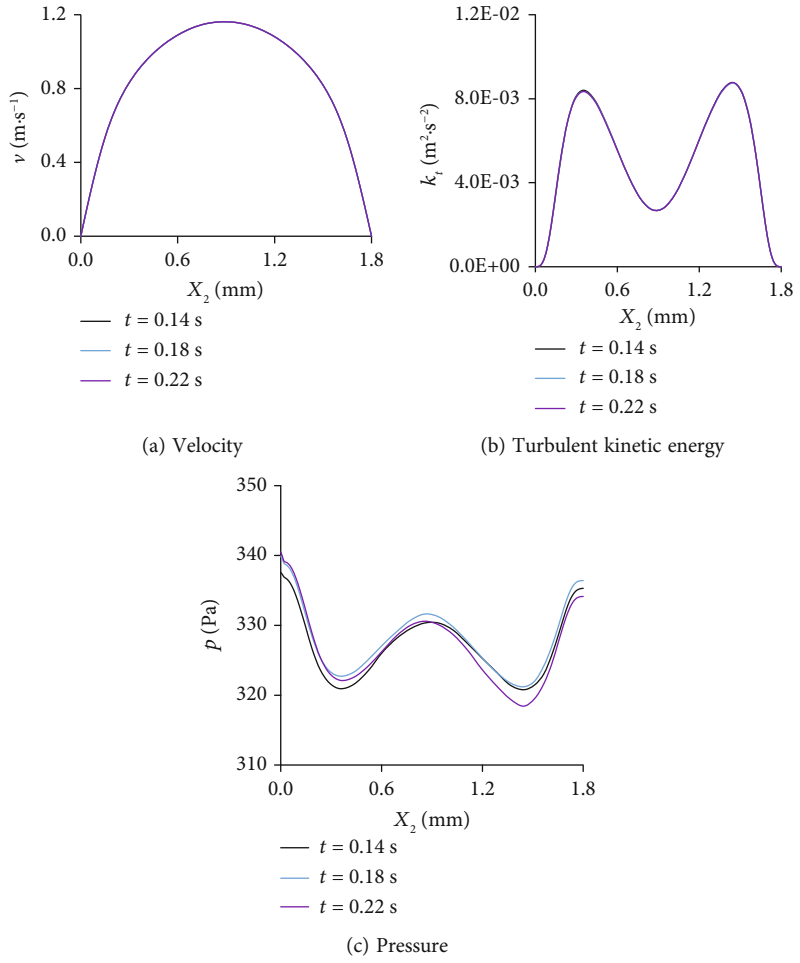

Figure 12: Distribution of physical quantities on the cross-section of $X_1 = 40$ mm.

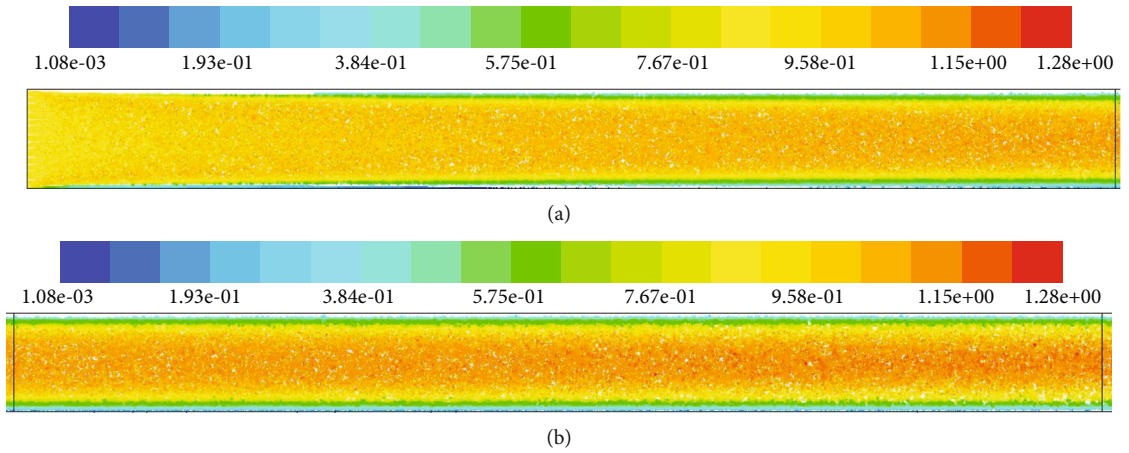

Figure 13: Distributions of sand particles: (a) 0 mm $\le X_1 \le$ 20 mm fracture segment; (b) 20 mm $\le X_1 \le$ 40 mm fracture segment.

phase flow field during the time interval $0 \le t \le 0.12$ s, and it was the pressure curve of the water-sediment two-phase flow field during the interval $0.12 \le t \le 0.20$ s.

In Figure 16, the inlet pressure of the fracture fluctuated violently around 20 kPa, without an obvious decreasing trend. The average value of adjacent peaks and valleys basically reached dynamic stability. This indicated that sand particles had no significant effects on the inlet pressure.

Figure 17 shows distributions of velocities, turbulent kinetic energy, and pressure on the cross-section of $X_2 =$ 1.4 mm at 0.17 s, 0.22 s, and 0.27 s, with the inlet velocity of 0.869 m/s.

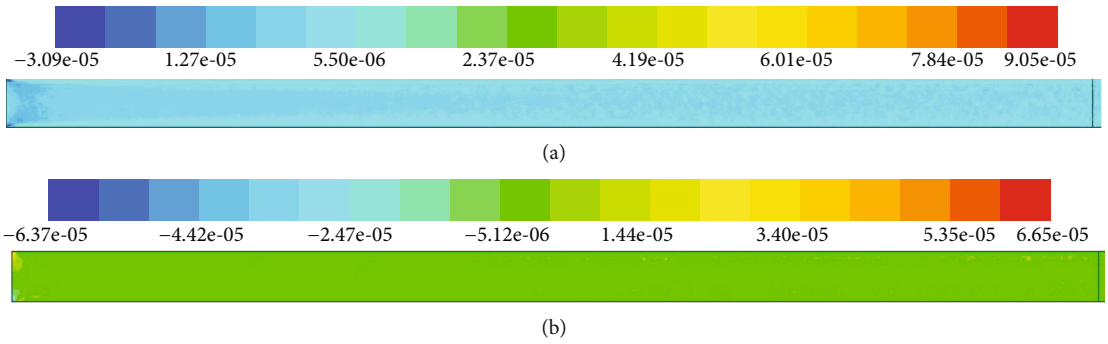

Figure 14: Distribution of the momentum source terms with 0 mm ≤ X_1 ≤ 40 mm in the discrete-phase model: (a) X_1 direction component; (b)X_2direction component.

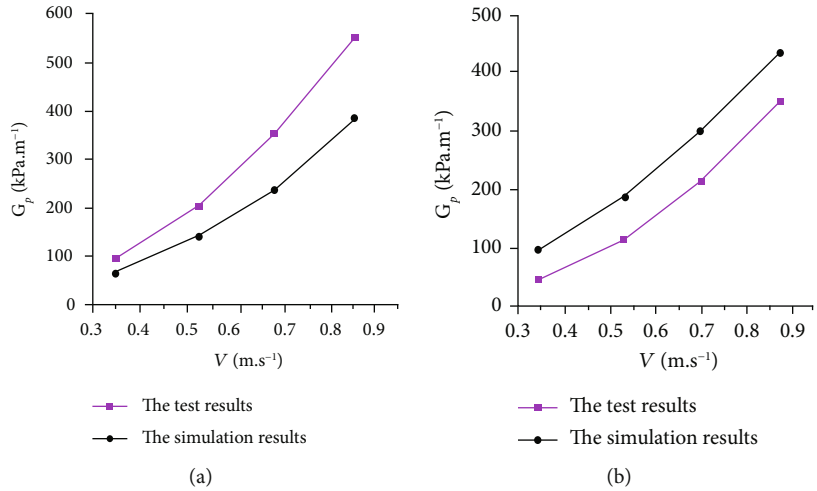

Figure 15: Comparison of the absolute value of the pressure gradient-seepage velocity curves: (a) single-phase flow; (b) water-sediment two-phase flow.

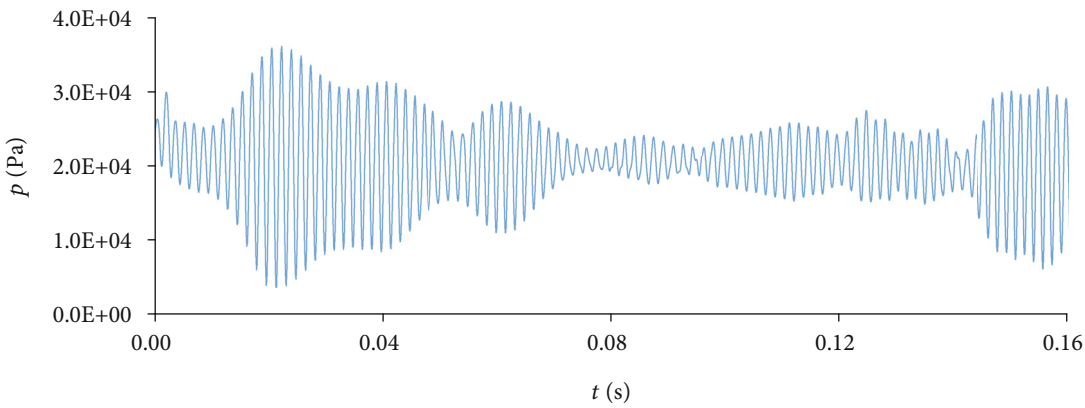

Figure 16: Average pressure-time curve at fracture inlet.

It could be found that when $X_1 \geq 2$ mm and the flow velocity fluctuated around 2.7 m/s, the difference between peak and valley values was small. The velocity curves do not match at different times, and there is no significant difference between the peak value and the valley value. When $X_2 \leq 2$ mm, the flow velocity increased sharply. This is because the inlet velocity was uniformly distributed. The fluid velocity recombined from the inlet and changes constantly during the flow through each section. It was decreased due to the viscosity at the walls. The fluid in the middle part outside the boundary layer accelerated.

In Figure 17(b), when $X_1 \geq 20$ mm, the turbulent kinetic energy fluctuated violently between 0.03 m^2/s^2 and 0.07 m^2/s^2, which reflected the basic properties of turbulence. When $X_1 \leq 20$ mm, it increased sharply, indicating that the fluid velocity recombined from the inlet and increased the

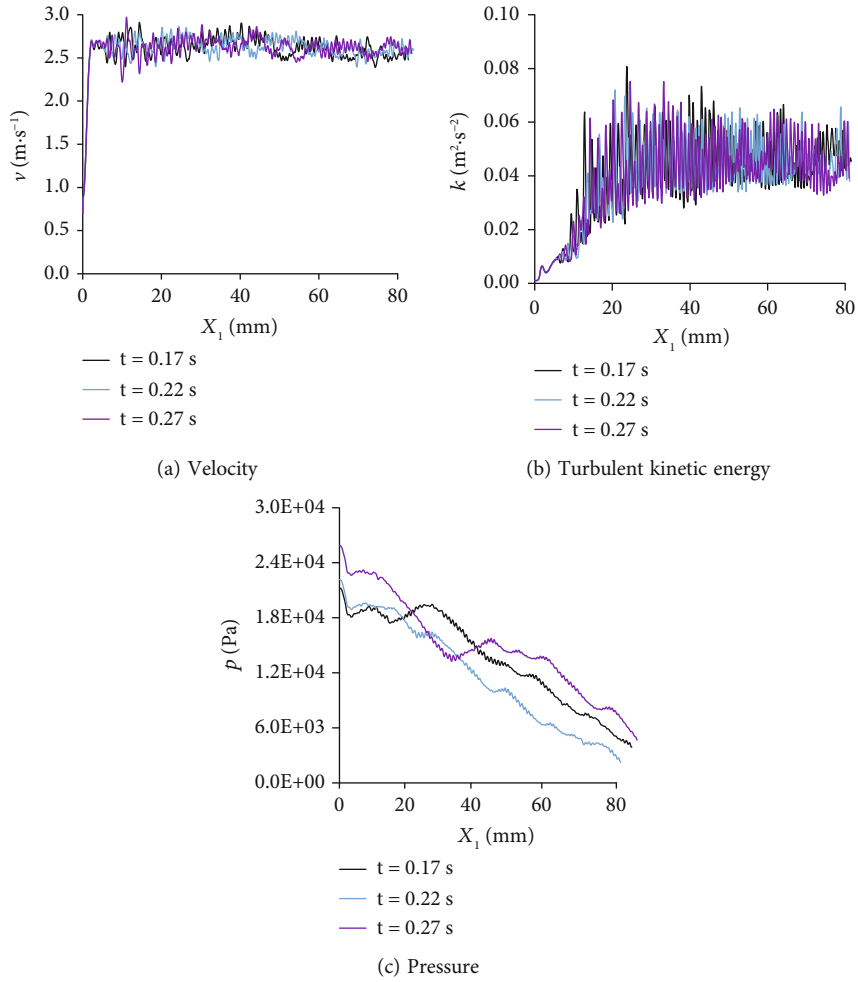

Figure 17: Distributions of physical quantities on the cross-section of $X_2 = 1.4$ mm.

turbulence intensity. There was no obvious difference between the peak values and valley values.

In Figure 17(c), the pressure fluctuates locally and the overall trend decreases linearly with X_1.

Figure 18 shows the distributions of velocity, turbulent kinetic energy, and pressure distribution on the cross-section of $X_1 = 40$ mm, at 0.17 s, 0.22 s, and 0.27 s, with the inlet velocity of 0.869 m/s. In Figure 18(a), the maximum water velocity was between 2.5 m/s and 3.0 m/s, and the corresponding position was between $X_2 = 2.2$ mm and $X_2 = 2.4$ mm. In Figure 18(b), the turbulent kinetic energy was very small near the wall, and the peak values and positions changed dramatically over time. In Figure 18(c), the pressure fluctuated smoothly along X_2 and changed greatly with time.

3.3.3. The Spatial Distribution Law of Physical Quantities in the Flow Fields. Figure 19 shows the pressure nephogram when $t = 0.27$ s, with the inlet velocity of 0.869 m/s. Many lamellate low-pressure and high-pressure areas could be observed in the flow fields. They mainly existed near the fracture tip, indicating that the roughness of the fracture surface increased the pressure loss of the flow field [34].

Figure 20 shows the flow-line diagram of the fracture segment from $X_1 = 30$ mm to $X_1 = 40$ mm when $t = 0.27$ s, with the inlet velocity of 0.869 m/s. The flow separated at the concave corners of the fracture. One or two clockwise-rotating vortices and one counterclockwise-rotating vortex were formed at the concave corners of the lower fracture surface, and one or two counterclockwise-rotating vortices and one clockwise-rotating vortex were formed at the upper fracture surface. Take the lower fracture surface as an example. The causes of the vortices were analyzed. The fluid flowed forward through the fracture. After flowing through the fracture tip, the flow cross-section expanded suddenly. It was impossible for the fluid to suddenly change the direction along the fracture surface due to the inertial force. At this point, smooth transitions of fluid occurred, manifesting that the main flow lines bent near the wall and the flow expanded. Some fluids did not flow forward with the main flow between the outer surface and the wall surface of the expanded part of the main flow. The expansion of the main flow cross-section decreased the flow velocity. At this point, the pressure gradually increased along the flow direction. Thus, the adverse pressure gradient was formed. Some fluids between the main flow and the wall flowed countercurrently along the wall, forming a clockwise vortex. The main flow continued to move forward. When it encountered the next fracture tip, the flow section suddenly shrank, and the main

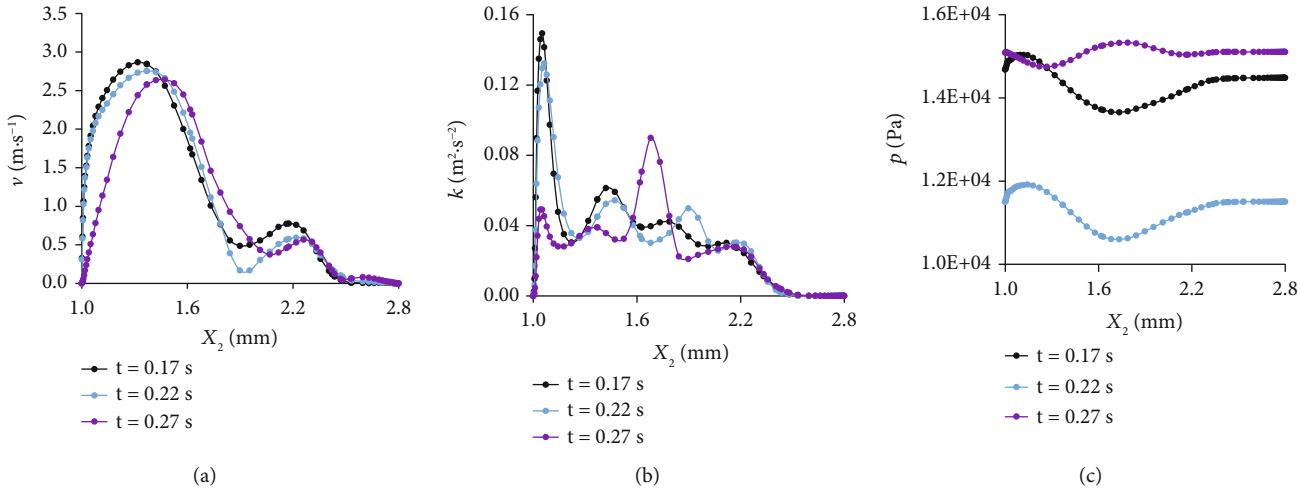

Figure 18: Distributions of physical quantities on the cross-section of $X_1 = 40$ mm: (a) velocity; (b) turbulent kinetic energy; (c) pressure.

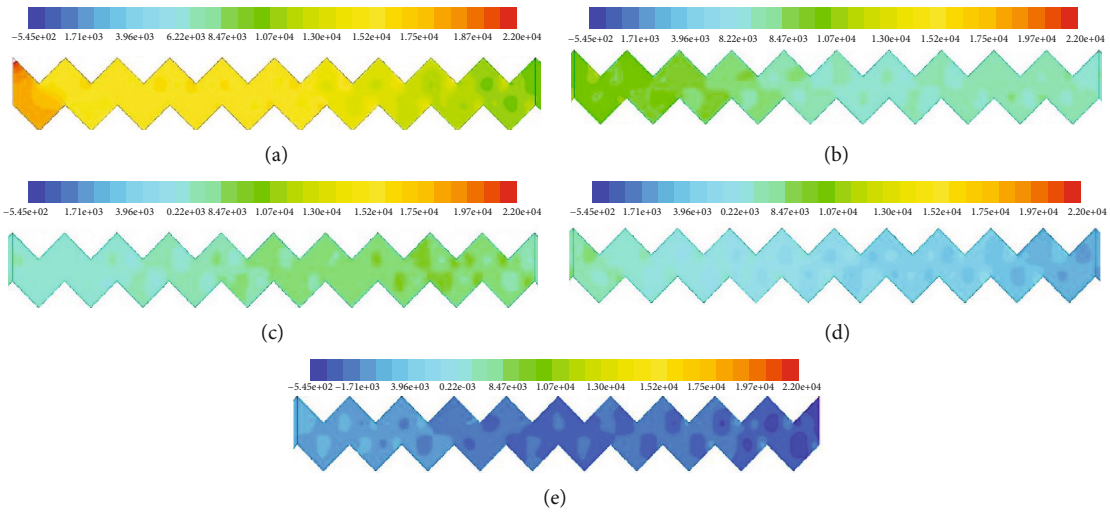

Figure 19: Pressure nephogram: (a) $X_1 = 0$ mm to $X_1 = 20$ mm fracture segment; (b) $X_1 = 20$ mm to $X_1 = 40$ mm fracture segment; (c) $X_1 = 40$ mm to $X_1 = 60$ mm fracture segment; (d) $X_1 = 60$ mm to $X_1 = 80$ mm fracture segment; (e) $X_1 = 80$ mm to $X_1 = 100$ mm fracture segment.

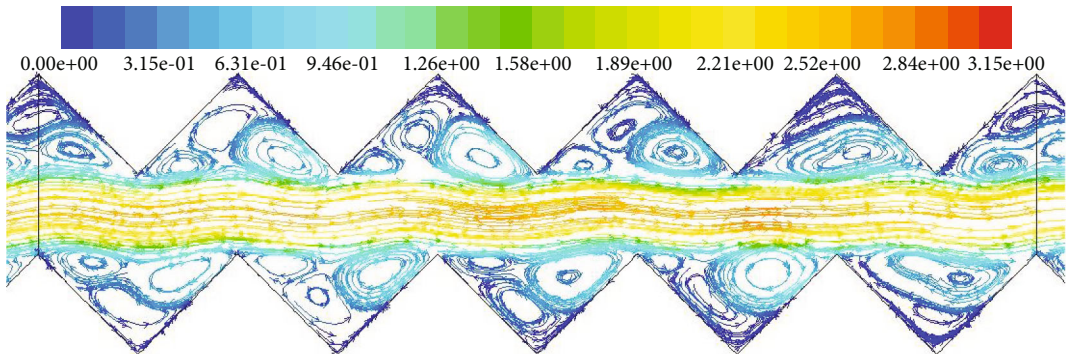

Figure 20: Flow-line diagram.

flow section also gradually shrank, forming a clockwise vortex at the wall. It could be found that the downstream vortex range was larger and the flow lines were denser, indicating that the downstream vortex was stronger. Two vortices merged at some concave corners of the fracture. There was a corner vortex rotating counterclockwise at the bottom of concave recessed corner of the fracture, which was formed by two vortices rotating clockwise. There were two types of

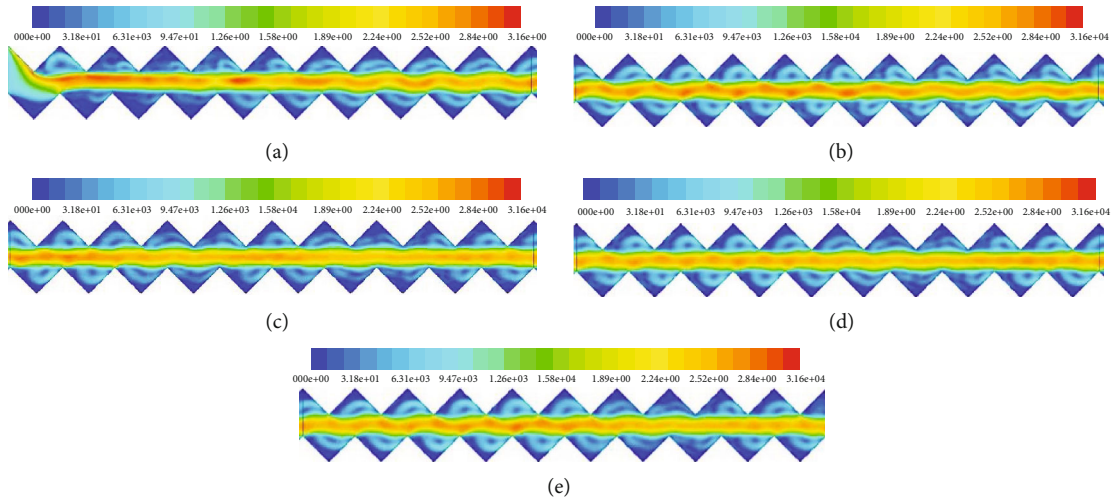

FIGURE 21: The velocity nephogram: (a) $X_1 = 0$ mm to $X_1 = 20$ mm; (b) $X_1 = 20$ mm to $X_1 = 40$ mm; (c) $X_1 = 40$ mm to $X_1 = 60$ mm; (d) $X_1 = 60$ mm to $X_1 = 80$ mm; (e) $X_1 = 80$ mm to $X_1 = 100$ mm.

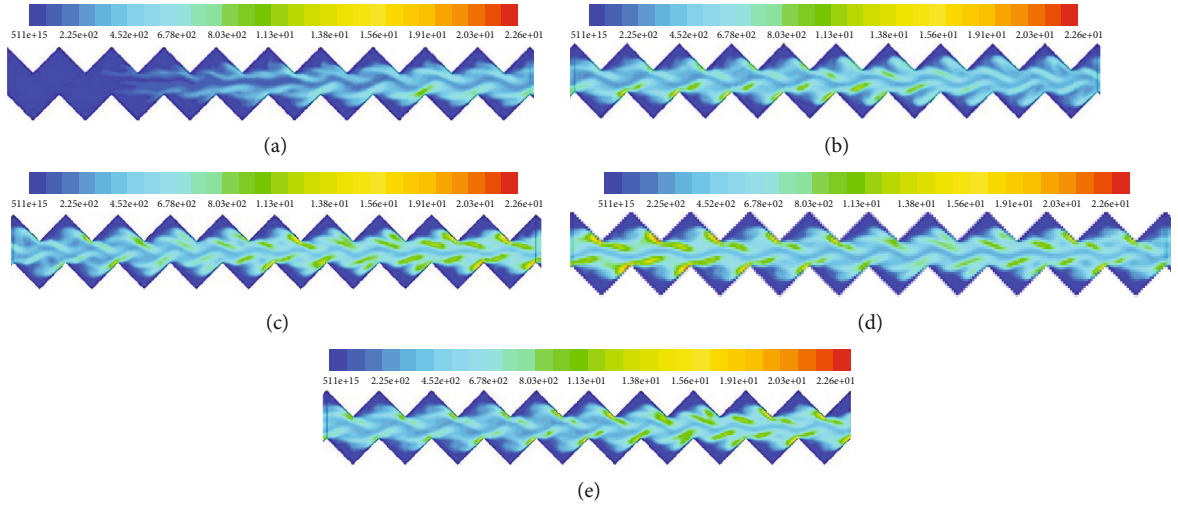

FIGURE 22: Turbulent kinetic energy nephogram: (a) $X_1 = 0$ mm to $X_1 = 20$ mm; (b) $X_1 = 20$ mm to $X_1 = 40$ mm; (c) $X_1 = 40$ mm to $X_1 = 60$ mm; (d) $X_1 = 60$ mm to $X_1 = 80$ mm; (e) $X_1 = 80$ mm to $X_1 = 100$ mm.

vortex structures in the flow field. One was the three-vortex structure composed of one large and two small vortices. The other was the double-vortex structure composed of one large and one small vortex. They were randomly distributed along the flow direction.

Figure 21 shows the velocity nephogram at $t = 0.27$ s, with the inlet velocity of 0.869 m/s. When the fluid entered the fracture, the velocity distribution changed drastically. The flow in the fracture was roughly divided into two parts. The main flow was between $X_2 = 1$ mm and $X_2 = 1.8$ mm, and the velocity was between 2.21 m/s and 3.16 m/s. There were many discontinuously distributed high-velocity areas. The main flow was bent at the fracture tip, which was unevenly distributed along the flow direction. The other part of the flow was in the vortex area at the concave corner of the fracture. The fluid velocity was relatively low in the center of the vortex and the boundary layer of the wall [33].

Figure 22 shows the turbulent kinetic energy nephogram at $t = 0.27$ s, with the inlet velocity of 0.869 m/s. It was relatively small at the inlet, because the inlet velocity was evenly distributed, and the flow was not fully developed. As the fluid flowed in the fracture, the turbulent kinetic energy gradually increased. There was a high turbulent kinetic energy region close to the wall at the fracture tip, due to strong collision between the fluid and the fracture tip and high fluctuating velocity. The turbulent kinetic energy was slightly lower near the center line $X_2 = 1.4$ mm. It was the lowest near the wall of the concave corner of the fracture. It was also randomly distributed along the flow.

Figure 23 shows the distribution of sand particles in the rough fracture at $t = 0.27$ s, with the inlet velocity of 0.869 m/s. In Figures 5–15, the sand particles were densely distributed and the velocity was higher with the 1 mm $\leq X_2 \leq$ 1.8 mm segment. The sand particle velocity was higher than the continuous-phase fluid velocity between 2.3 m/s and 3.29 m/s. The sand particle flow direction bent at the fracture tip. The volume concentration of the sand particles was relatively low from the main flow segment to the middle area of

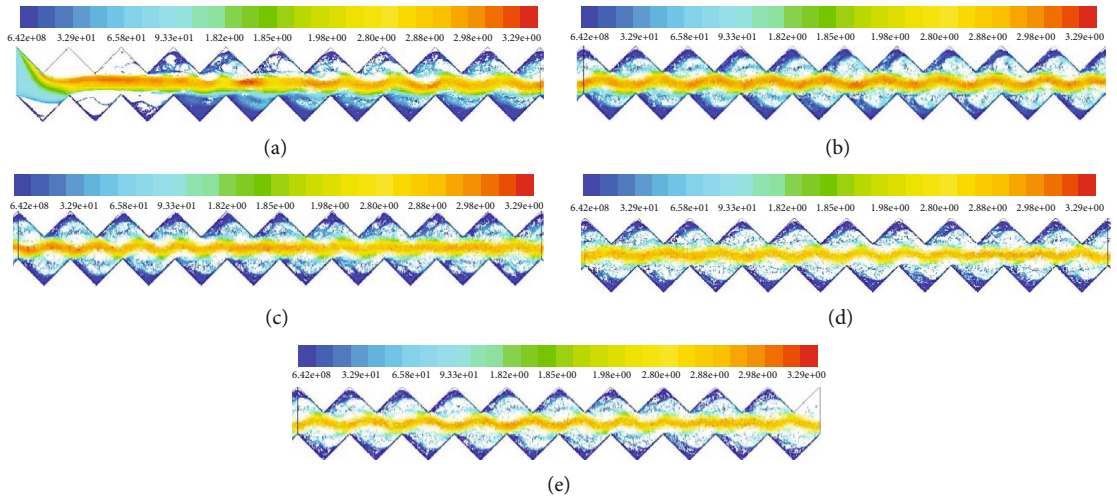

Figure 23: Distribution of sand particles: (a) $X_1 = 0$ mm to $X_1 = 20$ mm fracture segment; (b) $X_1 = 20$ mm to $X_1 = 40$ mm fracture segment; (c) $X_1 = 40$ mm to $X_1 = 60$ mm fracture segment; (d) $X_1 = 60$ mm to $X_1 = 80$ mm fracture segment; (e) $X_1 = 80$ mm to $X_1 = 100$ mm fracture segment.

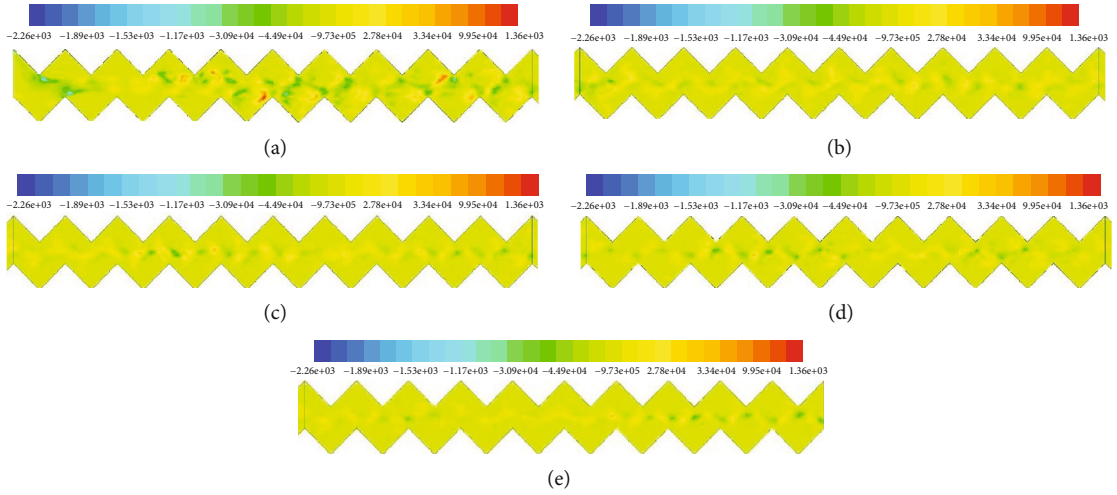

Figure 24: The momentum source term of the discrete-phase model in the X_1 direction component: (a) $X_1 = 0$ mm to $X_1 = 20$ mm; (b) $X_1 = 20$ mm to $X_1 = 40$ mm; (c) $X_1 = 40$ mm to $X_1 = 60$ mm; (d) $X_1 = 60$ mm to $X_1 = 80$ mm; (e) $X_1 = 80$ mm to $X_1 = 100$ mm.

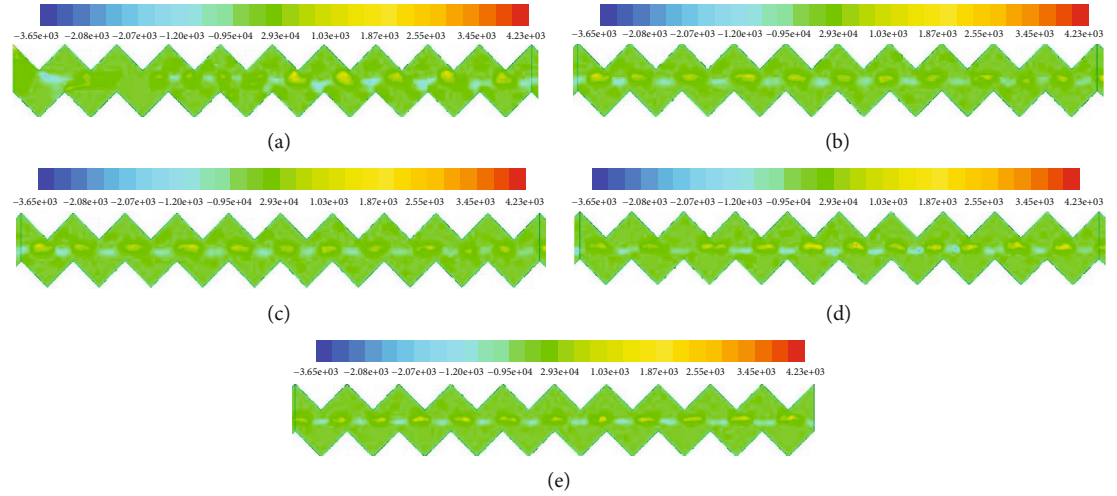

Figure 25: The momentum source term of the discrete-phase model in the X_2 direction component: (a) $X_1 = 0$ mm to $X_1 = 20$ mm; (b) $X_1 = 20$ mm to $X_1 = 40$ mm; (c) $X_1 = 40$ mm to $X_1 = 60$ mm; (d) $X_1 = 60$ mm to $X_1 = 80$ mm; (e) $X_1 = 80$ mm to $X_1 = 100$ mm.

the fracture wall. The sand particles were mainly distributed one upstream side of the wall, while the sand concentration was very low on the downstream side of the wall. Within the $0\,\text{mm} \le X_1 \le 20\,\text{mm}$ segment, the volume fraction of sand particles was relatively high in the lower fracture surface. This was because the flow at the inlet segment was not fully developed, and sand particles were prone to sedimentation due to force of gravity. With the development of flow, the distribution of sand particles tended to be even on the upper and lower fracture surfaces.

Figure 24 shows the distribution of the momentum source term of the discrete-phase model in the X_1 direction component at $t = 0.27$ s, with the inlet velocity of 0.869 m/s. Within the segment of $1\,\text{mm} \le X_2 \le 1.8\,\text{mm}$, the momentum source term was relatively large in the X_1 direction component, indicating that the force between the phases was large along the flow direction. Within the segment of $0\,\text{mm} \le X_1 \le 20\,\text{mm}$, the momentum source term was relatively large in the X_1 direction component, indicating that the momentum exchange between phases was large.

Figure 25 shows the momentum source term of the discrete-phase model in the X_2 direction component at $t = 0.27$ s, with the inlet velocity of 0.869 m/s. It could be found that it was relatively large when $X_2 = 1.4\,\text{mm}$. The area with higher absolute value was in a discontinuous and sheet distribution, and positive and negative values appeared alternatively. When the value was positive, the continuous-phase fluid had an upward force on discrete-phase sand particles. When the value was negative, there was a downward force.

4. Conclusions

In this paper, the water-sediment two-phase flow theory was used to establish the mechanical model of the water-sediment flow in the fractures. The numerical simulation software was used to simulate the water-sediment two-phase flow in smooth fractures and rough fractures. The conclusions are as follows:

(I) The RNG k-ε model, Realizable k-ε model, SST k-ω model, and Stress-Omega RSM and LES were used to simulate the continuous-phase flow in rough fractures. The simulated results were compared with the experimental data. The comparison results showed that Stress-Omega RSM could accurately calculate the pressure loss and simulate the flow field structures of rough fractures. Thus, it was chosen to simulate the continuous-phase flow in fractures

(II) The water-sediment two-phase flow theory was used to simulate the water-sediment two-phase flow in smooth and rough fractures. The sand density ρ_p was $2650\,\text{kg/m}^3$. The sand particle size D_p was 0.04 mm, and the volume fraction was $\Phi = 4.06\%$. The physical quantities such as pressure, velocity, and turbulence kinetic energy and the momentum source item, flow diagrams, and particle distributions were given with fracture inlet velocities of 0.349 m/s, 0.532 m/s, 0.697 m/s, and 0.869 m/s, respectively. The simulation results showed that the water-sediment two-phase flow pressure loss was basically the same with the experimental data, verifying the correctness of the numerical simulation method

(III) In the flow fields, the change law of the physical quantities with the time and the law of spatial distribution were analyzed in detail. The results indicated that they did not change with time in the smooth fractured flow fields, while changing continuously with time in the rough fractured flow fields and in a dynamic and stable state. In smooth fractures, there was an asymmetric spatial distribution of physical quantities due to the influence of gravity, while the flow field shows the randomness of spatial distribution in a rough fracture, because water-sediment flow was restrained by the walls

Data Availability

The data used to support the findings of this study are included within the article.

Conflicts of Interest

The authors declare that they have no conflicts of interest.

References

[1] F. Du, "Study on types and mechanism of water inrush and sand burst in western mining area".

[2] Z. Dou, S. Tang, X. Zhang et al., "Influence of shear displacement on fluid flow and solute transport in a 3D rough fracture," *Lithosphere*, vol. 2021, no. Special 4, p. 1569736, 2021.

[3] Z. Dou, Y. Liu, X. Zhang et al., "Influence of layer transition zone on rainfall-induced instability of multilayered slope," *Lithosphere*, vol. 2021, article 2277284, 2021.

[4] Y. Wang, H. Yang, J. Han, and C. Zhu, "Effect of rock bridge length on fracture and damage modelling in granite containing hole and fissures under cyclic uniaxial increasing-amplitude decreasing-frequency (CUIADF) loads," *International Journal of Fatigue*, vol. 158, article 106741, 2022.

[5] X. Shi and L. Li, "A study on prevention measures against water and sand inrush and their application in Shendong mining area," *Disaster Advances*, vol. 5, no. 4, pp. 1129–1135, 2012.

[6] G. Zhang, H. Wang, S. Yan, C. Jia, and X. Song, "Simulated experiment of water-sand inrush across overlying strata fissures caused by mining," *Geofluids*, vol. 2020, 11 pages, 2020.

[7] S. Wanghuacai and G. Qinghong, "Experimental research on critical percolation gradient of quicksand across overburden fissures due to coal mining near unconsolidated soil layers," *Chinese Journal of Rock Mechanics and Engineering*, vol. 26, no. 10, 2007.

[8] F. Liming, "Research progress of water inrush and sand-burst disaster in shallow coal seam".

[9] Y. Liu, S. Li, L. Ma, and N. Zhou, "Experimental study on non-Darcy seepage of water and sediment in fractured rock," *Meitan Xuebao/Journal China Coal Soc*, vol. 43, no. 8, pp. 2296–2303, 2018.

[10] X. Yang, Y. J. Liu, M. Xue, T. H. Yang, and B. Yang, "Experimental investigation of water–sand mixed fluid initiation and migration in porous skeleton during water and sand inrush," *Geofluids*, vol. 2020, 18 pages, 2020.

[11] Q. Liu and B. Liu, "Experiment study of the failure mechanism and evolution characteristics of water-sand inrush geo-hazards," *Applied sciences*, vol. 10, no. 10, 2020.

[12] B. Yang and T. Yang, "Experimental investigation of water-sand mixed fluid initiation and migration in filling fracture network during water inrush," *Advances in Civil Engineering*, vol. 2021, 20 pages, 2021.

[13] B. Zhang, Q. He, Z. Lin, and Z. Li, "Experimental study on the flow behaviour of water-sand mixtures in fractured rock specimens," *International Journal of Mining Science and Technology*, vol. 31, no. 3, pp. 377–385, 2021.

[14] J. Xu, H. Pu, J. Chen, and Z. Sha, "Experimental study on sand inrush Hazard of water-sand two-phase flow in broken rock mass," *Geofluids*, vol. 2021, 9 pages, 2021.

[15] M. Gao, J. Xie, Y. Gao et al., "Mechanical behavior of coal under different mining rates: a case study from laboratory experiments to field testing," *International Journal of Mining Science and Technology*, vol. 2021, no. 31, pp. 825–841, 2021.

[16] Y. Su, F. Gong, S. Luo, and Z. Liu, "Experimental study on energy storage and dissipation characteristics of granite under two-dimensional compression with constant confining pressure," *Journal of Central South University*, vol. 28, no. 3, pp. 848–865, 2021.

[17] Y. Chen, G. Zhao, S. Wang, H. Wu, and S. Wang, "A case study on the height of a water-flow fracture zone above undersea mining: Sanshandao Gold Mine, China," *Environmental Earth Sciences*, vol. 78, no. 4, 2019.

[18] F. Du, G. Jiang, and Z. Chen, "A numerical simulation study of the migration law of water-sand two-phase flow in broken rock mass," *Geofluids*, vol. 2018, 12 pages, 2018.

[19] H. Pu, "Characteristics of water-sand two-phase flow in weakly cemented fractured rock mass based on lattice Boltzmann theory".

[20] W. Guo, H. Wang, S. Chen, and J. Li, "Development and application of simulation test system for water and sand inrush across overburden fissures due to coal mining," *Chin J Rock Mech Eng*, vol. 35, no. 7, pp. 1415–1422, 2016.

[21] S. Lei, X. Feng, and W. Shidong, "Water-sand mixture inrush through weakly cemented overburden at a shallow depth in the Yili coal mining area.

[22] Z. Wu, Z. Wang, L. Fan, L. Weng, and Q. Liu, "Micro-failure process and failure mechanism of brittle rock under uniaxial compression using continuous real-time wave velocity measurement," *Journal of Central South University*, vol. 28, no. 2, pp. 556–571, 2021.

[23] Y. Zhao, Q. Liu, C. Zhang, J. Liao, H. Lin, and Y. Wang, "Coupled seepage-damage effect in fractured rock masses: model development and a case study," *International Journal of Rock Mechanics and Mining Sciences*, vol. 144, article 104822, 2021.

[24] Y. Zhao, L. Zhang, J. Liao, W. Wang, Q. Liu, and L. Tang, "Experimental study of fracture toughness and subcritical crack growth of three rocks under different environments," *International Journal of Geomechanics*, vol. 20, no. 8, p. 04020128, 2020.

[25] J. Smagorinsky, "General circulation experiments with the primitive equations," *Monthly Weather Review*, vol. 91, no. 3, pp. 99–164, 1963.

[26] B. J. Daly and F. H. Harlow, "Transport equations in turbulence," *Physics of Fluids*, vol. 13, no. 11, pp. 2634–2649, 1970.

[27] J. E. Matsson, *Ansys fluent 13 theory guide*, 2021.

[28] P. A. Cundall and O. D. L. Strack, "A discrete numerical model for granular assemblies," *geotechnique*, vol. 29, no. 1, 1979.

[29] K. Nazridoust, G. Ahmadi, and D. H. Smith, "A new friction factor correlation for laminar, single-phase flows through rock fractures," *Journal of Hydrology*, vol. 329, no. 1–2, pp. 315–328, 2006.

[30] Y. Zhao, Y. Wang, W. Wang, L. Tang, Q. Liu, and G. Cheng, "Modeling of rheological fracture behavior of rock cracks subjected to hydraulic pressure and far field stresses," *Theoretical and Applied Fracture Mechanics*, vol. 101, p. 59, 2019.

[31] K. Muralidhar and G. Biswas, "Advanced engineering fluid mechanics," 2006.

[32] C. Zhuoru, *Engineering Fluid Mechanics*, 2013.

[33] Y. Liu, S. Li, W. Li, Z. Luo, L. Wu, and Z. Xu, "Permeability characteristics of water-sand seepage in fracture by experiment," *Advances in Civil Engineering*, vol. 2021, 10 pages, 2021.

[34] Y. Zhao, C. Zhang, Y. Wang, and H. Lin, "Shear-related roughness classification and strength model of natural rock joint based on fuzzy comprehensive evaluation," *International Journal of Rock Mechanics and Mining Sciences*, vol. 137, article 104550, 2021.

Hindawi
Geofluids
Volume 2022, Article ID 8237954, 16 pages
https://doi.org/10.1155/2022/8237954

Research Article

Study on Deformation Mechanism and Control Measures of Tanziyan Landslide

Hai-chuan Tao,[1] Yuan Zhang,[1] Jia-xing Dong,[2] Zhi-qiang Zhou,[2] Xin-yue Gong,[2] and Sheng-wei Zhang[2]

[1]*Hydrogeology and Engineering Geology Brigade of Hubei Geological Bureau, Jingzhou 434020, China*
[2]*Faculty of Electric Power Engineering, Kunming University of Science and Technology, Kunming, Yunnan 650500, China*

Correspondence should be addressed to Jia-xing Dong; dong1986@kust.edu.cn

Received 10 January 2022; Revised 18 February 2022; Accepted 21 February 2022; Published 29 March 2022

Academic Editor: Long Yan

Studying the deformation and failure mechanism of the Tanziyan landslide in Yesanguan Town, Badong County, and designing the controlling measures are of great significance to ensure the sustainable development of urban planning and construction. In this paper, stability of Tanziyan landslide is analyzed using the calculation method of complex plane slip surface. After consideration of the essential characteristics of the disaster body,the deformation and failure mechanism of the landslide is studied, and the corresponding landslide treatment measures are presented. Results show stability state of the landslide is understable to unstable as a whole, and the development process can be roughly divided into three stages: sliding, bending and the cracks are connected. Finally, it is proposed to cut and reshape the slope from the crack groove on the slope top to the national highway, and thenlattice beams and anchor cables are presented to protect the reshaped slope surface. Ecological bags are used to stack and regreen between the lattice structures. A retaining wall is built on the inner side of the national highway at the bottom of the slope cutting area, an active protective net is laid on the east side of the crack groove, and monitoring works are set for potential deformation areas. In short, experiences of engineering practice in this landslidecan provide reference for similar projects.

1. Introduction

Landslide has always been a major type of geological disaster in mountainous areas. Landslide will lead to local traffic interruption, power facility damage, and villagers' forest land damage, threaten people's life safety, and cause serious economic losses. It is of great significance to find out the geological environmental conditions of landslides, clarify the deformation and failure mechanism, and put forward reasonable and scientific treatment measures for landslide prevention and control. In terms of landslide deformation and failure mechanism, many researchers start with engineering geological conditions, establish geological models, and deeply analyze its stability and deformation and failure mechanism. For example, Yao [1] took the Gedui village landslide in the Nujiang river basin as an example. Based on a geological survey, the whole process from landslide deformation accumulation to failure using discrete element numerical simulation technology was simulated. Liu et al. [2] found out the engineering geological conditions of landslide on the slope during the construction of the Zhuxi expressway. They analyzed the deformation, development, failure characteristics, and genetic mechanism of landslide in combination with geological mapping and survey. Zhang et al. [3] took the instability of sand mudstone-interbedded slope in road engineering as an example and comprehensively considered multiple factors such as slope structure, stratum structure, and microstructure. The deformation and failure mode of multifree surface combination and unequal thickness interbedded rock slope is analyzed. The corresponding treatment measures are put forward according to the deformation and failure mode. Zeng et al. [4] systematically studied the characteristics and deformation instability mechanism of Zhaojiagou landslide in Zhenxiong County based on the basic data obtained from several landslide field investigations and

exploration. Zhang et al. [5] used MIDAS/GTS software to conduct three-dimensional numerical simulation studies on the formation mechanism of the Liujiapo landslide. Xu [6] analyzed and summarized the deformation and failure behavior and deformation time curve of various landslides, combined with the rheological test results of rock and soil mass, and according to the characteristics of slope deformation curve with time changing, the landslides are divided into three types: stable type, gradual change type, and sudden type, and the mechanical conditions for these three types of deformation behavior are given. Hu et al. [7] analyzed the formation mechanism of the Baozha landslide based on the systematic study of the engineering geological conditions of the landslide. In addition, external factors such as dry-wet cycle, freeze-thaw cycle, and natural cracks have a significant impact on the deformation and failure of the slope. Under the influence of long-term rainfall and sunlight, the rock mass in nature will inevitably change its structure and develop cracks, thus affecting the stability of the slope. Li et al. [8, 9] studied sandstone's deformation and failure mechanism from the macro- and microperspectives by observing the microstructure of the specimen before and after failure through different dry-wet cycles of sandstone, followed by uniaxial compression test and direct shear test. Wang et al. [10] proposed a coupled damage model based on digital image processing technology, freeze-thaw cycle, and uniaxial cyclic load test, which can well describe the damage accumulation of rock, and the influence of natural cracks at rock deformation and failure is undeniable pronounced. Gao et al. [11, 12] carried out systematic field monitoring on a coal mine area and determined the evolution process of crack network in coal and rock mass by using fractal geometry and algorithm of predicting connectivity rate. At the same time, based on uniaxial compression test and digital image processing technology, it is pointed out that the tensile deformation of the original fracture can lead to fracture consolidation. Under high loading rate, the main reason for rock mass failure is fracture consolidation. Zhu et al. [13] studied the evolution process of intergranular cracks in granite with temperature from a microperspective. They pointed out that with the increase of temperature, the number of internal cracks increases, resulting in the gradual separation of mineral particles, that is, the internal structure of rock is broken, which affects the stability of slope. According to Chen et al. [14], the performance of the analytical solution is verified by comparing it with the results of numerical tests obtained using the three-dimensional distinct element code (3DEC), leading to a reasonably good agreement. The analytical solution quantitatively demonstrates that the equivalent elastic modulus increases substantially with an increase in confining stress. It is characterized by stress dependency. Zhu et al. [15] conducted 16 uniaxial cyclic loading simulations with distinct loading parameters related to reservoir conditions (loading frequency, amplitude level, and maximum stress level) and different water contents. The numerical results show that all these three loading parameters affect the failure characteristics of sandstone, including irreversible strain, damage evolution, strain behavior, and fatigue life.

In terms of landslide treatment, applicable conditions and applicability of various prevention and control measures should be analyzed in detail. The typical treatment schemes include bypassing the landslide area, weight reduction, back pressure, drainage, and retaining works [16–21] for many landslide treatment projects, which are often applied comprehensively. For example, according to Zhu et al. [22], constant resistance and large deformation bolt have excellent characteristics of high constant resistance force, large deformation, and high energy absorption and are thus widely used in the reinforcement and monitoring of roadway, tunnel, and slope engineering. Zou [23] designed antislide piles to stabilize the slope according to the stability calculation results and carried out landslide prevention and treatment by laying asphalt macadam in the middle and lower part of the landslide, placing gabion net in the middle and upper part of the landslide, and planting with full vegetation coverage. Huang [24], based on the landslide problem of Meihe expressway, analyzed the causes of slope landslide, puts forward the reinforcement scheme for anchor cable frames beam and anchor lattice beam, and puts forward the matters needing attention to drainage design and construction. Cao [25] studied the causes of the giant ancient landslide on the left bank on Xiluodu hydropower station and carried out construction and monitoring by taking engineering measures such as deep and shallow drainage, presser foot slope concrete, frame beam, and anchor cable foot fixation, to ensure the stability of the ancient landslide. Tao et al. [26] conducted the reinforcement mechanism test of layered anti-inclined slope based on physical model and determined the instability failure of anti-inclined slope reinforced with negative Poisson's ratio anchor. Li et al. [27] studied the mechanical behavior of surrounding rocks under prestressed anchor support, and a mechanical model is established. It is determined that the main controlling factors of the support effect are prestressing, anchor cable length, and anchor cable spacing. Similar simulation verification experiments further substantiated the accuracy of numerical simulation. The results indicate that the numerical simulation method of ubiquitous joint and DFN (discrete fracture network) can attain accurate results. Above all, controlling measures of the Tanziyan landslide should be designed after studying the deformation and failure mechanism.

2. Project Description

From June 19 to June 25, 2018, Tanziyan had a significant landslide risk. The accumulation caused by deformation and damage blocked about 100 m of the National Highway 318 (G318), resulting in damage to ancillary road facilities and transmission lines, with a direct economic loss of 6.425 million yuan. According to professional monitoring data, the Tanziyan landslide geological disaster has apparent mountain displacement and poor stability. Under the influence of continuous heavy rainfall, it is very likely to produce large-scale landslide deformation again, which will cause more severe consequences. If the Tanziyan landslide is unstable as a whole, many accumulations roll down at the bottom of the slope, blocking the Yuquan river and forming dammed lakes, and it will pose a significant threat to the downstream residents.

Therefore, once the Tanziyan landslide geological disaster is unstable, the loss is enormous. The potential catastrophe is highly unfavorable to the sustainable development of local economy and urban planning and construction. The comprehensive treatment of the Tanziyan landslide geological disaster is vital and urgent, with practical economic significance and important social significance.

2.1. Geographical Conditions. The study area is in Tanziyan, group 15, Tanjia village, Yesanguan Town, Badong County, Hubei Province (Figure 1), where the steep slope inside the K1420 + 000 − K1420 + 600 section of G318. The geographical coordinates are 30°38′57.5″N and 110°19′55.6″E, and village road and G318 are connected around the landslide site, with convenient transportation.

Tanziyan landslide geological hazard body is located on the hill from south to north, the bottom of the hill is Yuquan river, and the middle of the slope is G318, that is, the front edge of the landslide body. The rear rim is a ridge, the left side is a natural concave slope, and the new bedrock escarpment bounds the right side.

The exploration area is located on the right bank of the Yuquan river, with a peak elevation of 1100~1147 m and a relative elevation difference of 240~287 m. The microgeomorphic combination of the area is canyon steep slope. The sloped body is a clockwise slope composed of thick layer massive chert nodule limestone of Maokou Formation (P_1m) of Lower Permian system. The terrain is generally high in the south and low in the north. The lowest point is the bottom of the Yuquan river valley, with an elevation of 860 m. The valley profile presents an asymmetric "V" shape, and the left bank is a cliff, mainly formed by uncanny craft. The right bank slope is slightly slower than that of the left bank. The profile is linear with a steep bottom and soft folding top. The slope of the lower slope is 45~60°, and the slope of the upper slope is 30~45°. G318 runs parallel to the river valley in the middle of the proper bank slope, with an elevation of 1003-1009 m. The landslide area is located inside G318.

2.2. Geological Environment. According to relevant survey data, the working area belongs to structural erosion dissolution deep cutting medium mountain geomorphology, and the basic terrain configuration is platform mountain and deep valley. The terrain is high in the north and low in the south, the peak elevation is 1593~1100 m, and the cutting depth of the valley is 200~700 m. The southern part of the survey area is a ridge mountain canyon with the disintegration of the plateau, and the height decreases. The mountains are affected by the NE and EW structures of the region. Therefore, they generally extend along with the NE and EW directions.

Yangchang river anticline (Z1), Chenjiaya syncline (Z2), Yesanguan anticline (Z3), and Xiangbanxi syncline (Z4-1, 4-2, and 4-3) are mainly developed in the working area. Secondary small folds can be seen everywhere in the survey area, and joint fissures are relatively developed. The faults mainly include Zigui-Yesanguan fault, Yesanguan fault, general fault, and Yuejiahuang fault. Zigui Yesanguan fault and Yesanguan fault are close to the study area. The rock fissures are relatively developed, which has a significant impact on the integrity of nearby rock strata and slope stability. Other faults are far away from the study area and have a slight effect on the rock stratum in the working area, as shown in Figure 2. In short, fractures are highly developed due to the development of faults, anticlines, and other structures in the area. The fractures in the area are mainly inclined to the north, which is conducive to the development of slope unloading fracture structural plane through cutting layers, especially those whose tendency is consistent with the slope surface and whose inclination angle is close to or less than the slope angle having a significant impact on slope stability.

The lithology of the stratum in the area is single, mainly exposing upper Paleozoic carbonate strata, followed by quaternary eluvial, colluvial diluvial, and artificial accumulation. The surface water in the survey area is poor, mostly the surface flow and runoff formed by atmospheric precipitation quickly, which is discharged and collected down the Yuquan river along the mountain. The karst in the Yuquan river is developed, and the river bed is a dry ditch in arid season, so it is speculated that the groundwater is rich.

2.3. Basic Characteristics of Disaster Bodies. The plane shape of the Tanziyan landslide body is irregular armchair shape, with a longitudinal length of about 146 m, an average width of 250 m, and an area of about $3.65 \times 10^4\ m^2$, the average thickness is about 12.0 m, and the total volume is about $43 \times 10^4\ m^3$, which is a medium-sized geotechnical mixed landslide, with the main sliding direction of about 347°, as shown in Figure 3. At present, there are three small pitches and one collapse. Among them, three slopes are located on the inner side of the front national highway, arranged in a straight line from east to west, with deformation and failure volume of $750\ m^3$, $3500\ m^3$, and $7875\ m^3$, respectively. The collapse body is located near the top of the slope in the west, and the collapse volume is about $2460\ m^3$.

The boundary conditions of the Tanziyan landslide are apparent. The front edge is direct to G318, distributed in the northeast-southwest direction, with free conditions for landslide development. The trailing edge is bounded by the drawing crack trough at the ridge with 235° strike, with an elevation of 1115.7 m. The drawing crack trough is broad in the southwest and narrow in the northeast. The widest part of the tensile fracture groove is 5 m and 19.8 m deep. Its distribution direction is 235°. After pinching to the east, multiple intermittent tensile fractures are developed and distributed in the echelon. The left margin is bounded by a depression set in the southeast direction. The right boundary is determined by the arc cliff extending from northeast to near north.

Tanziyan landslide is divided into two areas according to the current deformation: deformation area and potential deformation area. The deformation area is located on the left side of the Tanziyan landslide. The width of the deformation area is about 120 m. The primary deformation is top collapse, ground crack, and bottom collapse deformation. The potential deformation area is located on the right where no obvious deformation has been found. Still according to the

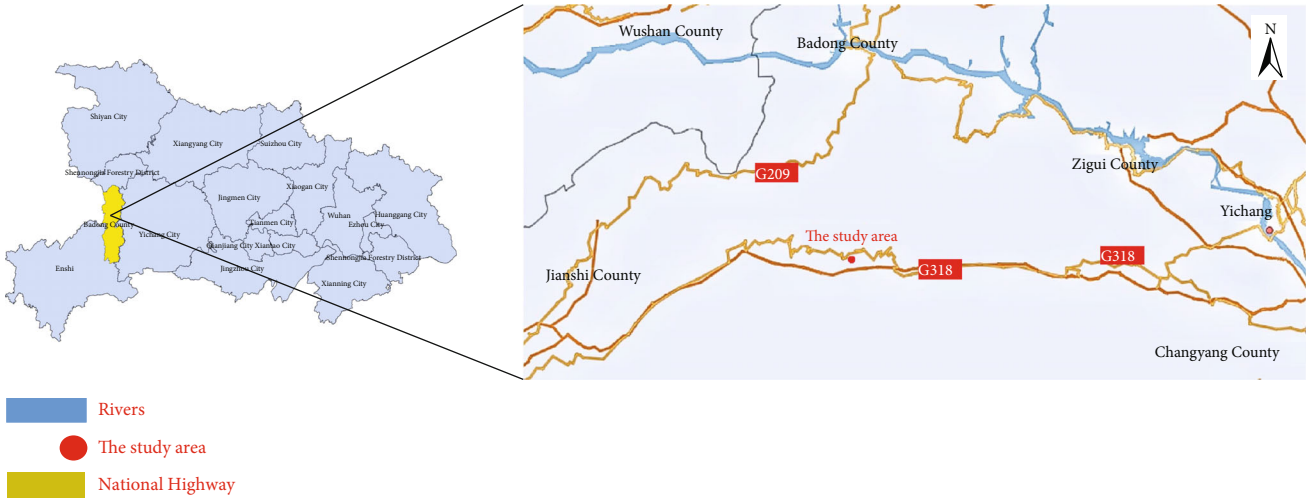

Figure 1: Geographical location of the study area.

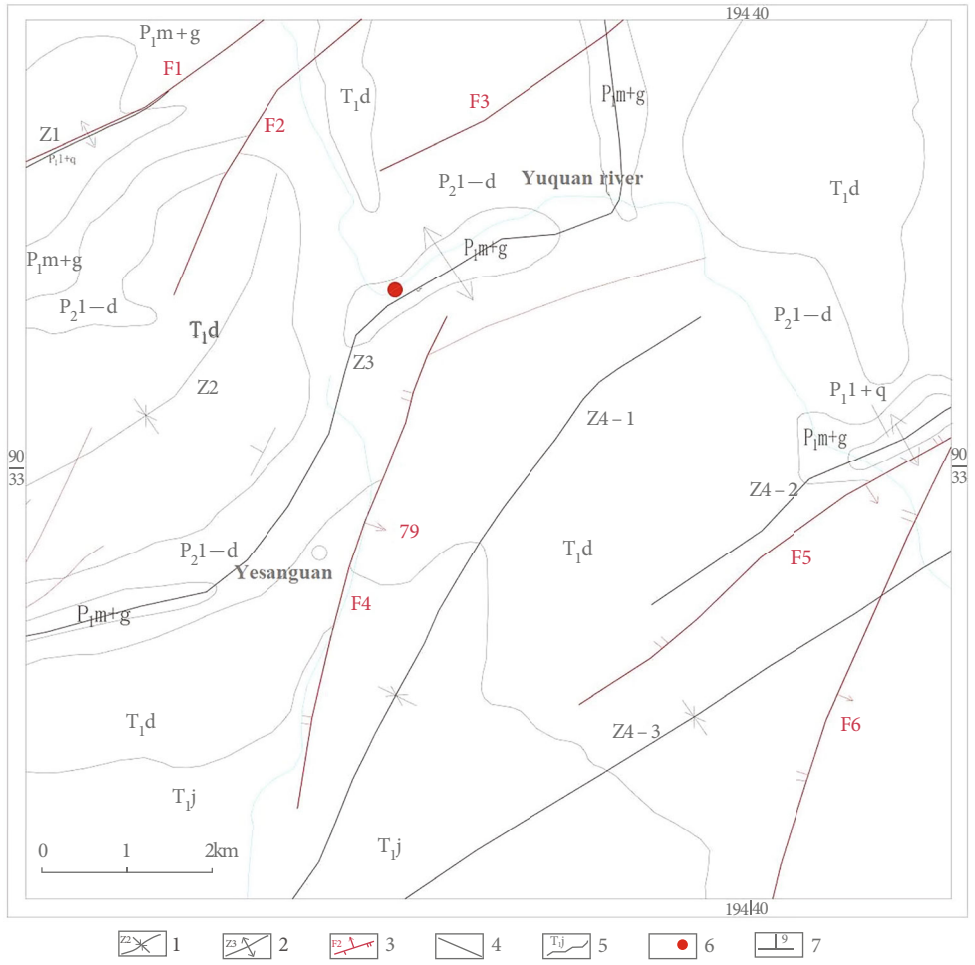

Figure 2: Outline map of geological structure of exploration area. 1, syncline and number; 2, anticline and number; 3, compressional torsional fault and its number; 4, general fault; 5, stratum code and boundary; 6, study area; 7, occurrence.

deformation mode of the Tanziyan landslide, the fracture will gradually develop to the northeast (right). The deformation zone is shown in Figure 4.

The collapse source area of the Tanziyan landslide is mainly the ghaut and the isolated peak at the top, and the depression on both sides is the potential deformation

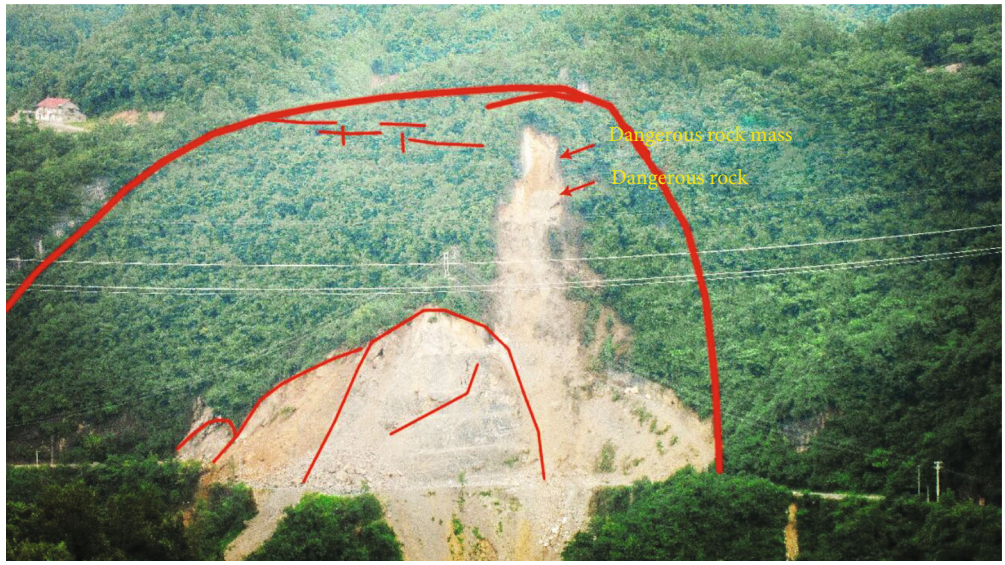

Figure 3: Overall view of Tanziyan landslide.

influence area. The collapse accumulation area is located along the national highway. Most of the deposits are distributed on the G318. A small part of the collapse block stones are scattered on the slopes and grooves above and below the national highway.

3. Deformation and Failure Mechanism

3.1. Deformation and Failure Phenomenon. The deformation of the Tanziyan landslide is mainly characterized by slides, mountain fissures, and collapse.

3.1.1. Sliding. The slide deformation occurs at the inner slope of G318 at the front edge of collapse, with a total of 3 places developed, namely, TH1, TH2, and TH3 (Figure 5), which are closely arranged from east to west. After the occurrence of slide TH1 and slide TH2, the professional monitoring of slide TH3 was focused. According to the professional deformation monitoring records, the displacement of collapse body was 0.3 m from June 30, 2018, to July 5, 2018 (Figure 6). In addition, from June 25, 2018, to June 30, 2018, the monitoring results of the high-pressure electrode slope on the upper part of the collapse TH3 were cracks, and the mountain displacement was 3.8 cm.

3.1.2. Mountain Fissures. Mountain fissure is one of the main deformations in the area, in which fissure LF2 and fissure LF3 are tension fissures and fissure LF1 is shear fissure. The fissure mentioned above LF3 with intense deformation forms a huge drawing crack trough at the ridge, showing a "thin strip of sky" landscape, which makes a vast rock mass wanting to separate from the rear mountain in the shape of a solitary peak. The three mountain fissures described in this paper are shown in Figure 7.

3.1.3. Collapse. Collapse is the primary deformation geological disaster in the area, with rich collapse source materials, poor integrity, high potential energy, and great harm. Affected by tectonism, the rock joints and fissures in this area are developed, and the cracks have apparent damage control on the rock mass. Five groups of fractures are mainly set in the study area, of which the rock stratum level and LX1 fracture (Figure 8(a)) are the principal structural planes of rock mass, with strong ductility. At the same time, it is cut by other groups of fractures, and the rock mass presents structural characteristics such as layered block fracture and rhombic wedge. As shown in Figure 8(b), LX2 and LX3 are conjugate fractures, developed in the shallow surface with good elasticity, with an extended height of 1.2-2.0 m, a length of 15 m can be seen locally, and the cutting layer is developed.

(1) Distribution of Dangerous Rock Mass. According to the field survey, after the collapse, two dangerous rock masses (W1 and W2) and one dangerous rock (W3) are mainly developed, of which dangerous rock masses W1 and W2 are distributed at the isolated peak at the trailing edge and dangerous rock mass W3 is distributed at the bottom of the cliff. According to relevant data statistics, the three dangerous rock masses all collapsed on June 25, 2018, with a total volume of about 2460 m^3, and there is a possibility of collapse again. The specific distribution is shown in Figure 9.

(2) Characteristics of Talus Slope. Most of the collapsed block stones in the area roll down to the Yuquan river valley (Figure 10(a)), with a volume of about 650m^3, a small part is accumulated at G318 (Figure 10(b)), and sporadic block stones are scattered on the groove slope. The plane of collapse accumulation body is long strip, with different thickness, thin at the top and thick at the bottom, with a thickness of 2.5-5 m. It is mainly composed of broken stones, with different diameters and angular shapes. The rock property of broken stones is flint nodule limestone.

(3) Deformation and Failure Characteristics. On June 25, 2018, Tanziyan landslide occurred and toppled northwestward. Blocked by the mountain mouth, it turned to the

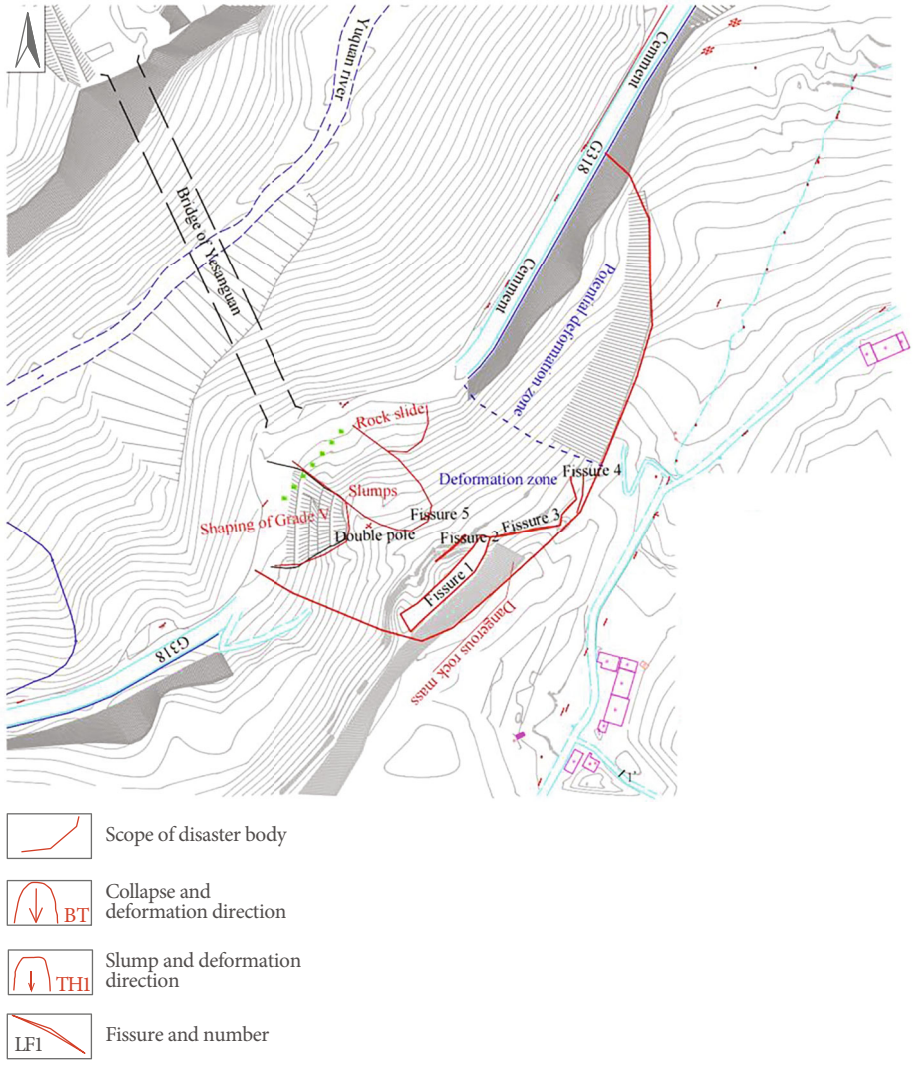

Figure 4: Plan diagram of Tanziyan landslide geological hazard.

(a) (b) (c)

Figure 5: Location distribution of slump cloth.

280° direction and rolled down with a high drop, with great potential energy and great damage. Nearly 60 m guardrails and embankments of the national highway were destroyed, and another culvert and 100 m drainage ditch were destroyed, resulting in the blockage of the national highway (Figure 10(b)).

3.2. Main Influencing Factors. According to the analysis of the characteristics of Tanziyan landslide and the main characteristics of recent deformation, the factors affecting the stability of collapse body can be divided into internal factors and external factors. The internal factors are related to the environmental geological conditions and their own characteristics of the

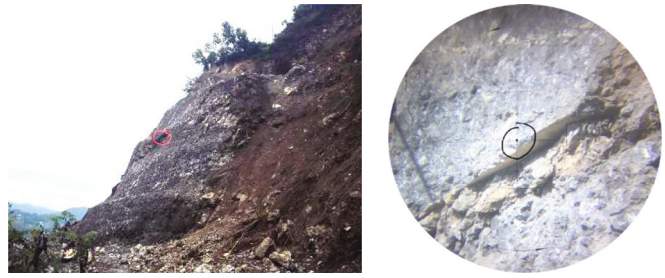

(a) (b)

Figure 6: Drawing and operation drawing of slide monitoring point.

(a) (b) (c)

Figure 7: Fissure of Tanziyan landslide geological disaster.

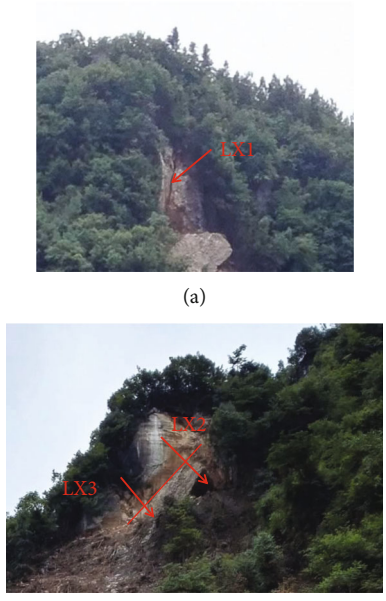

(a)

(b)

Figure 8: Distribution of joints and fissures in the investigation area.

collapse area, mainly including the geological structure, landform conditions, material structure conditions of the collapse body, and the vegetation coverage of the slope. The external factors are mainly atmospheric precipitation and human engineering activities.

3.2.1. Landform and Hydrology. The slope where the collapse area is located is steep, the height difference between the top and bottom of the collapse source is about 115.2 m, the collapse height difference is 237 m, and the slope is 37°~60°. The collapse source area has a good free surface (slope 60°). The mountain slope has good catchment conditions, and the surface water scouring is strong during rainfall. At the same time, the lush vegetation on the slope has obvious root splitting effect, which is easy to form a channel for atmospheric precipitation to infiltrate into the underground, and the underground water accelerates the weathering and dissolution of rock mass.

3.2.2. Stratigraphic and Structural Conditions. The formation lithology is mainly chert nodule limestone in Maokou Formation (P_1m) of Lower Permian system, followed by Quaternary eluvial deluvial deposit, colluvial deluvial deposit, and artificial accumulation. The rock stratum tends to northwest with an inclination of 34-37°. The slope is a clockwise slope. The material structure is as follows: the collapse area is mainly affected by structure, with broken rock mass and poor integrity. The shallow fractures of Maokou Formation (P_1m) of Lower Permian system are extremely developed, with many straight fracture surfaces and long extension, and karst fractures are also developed. The surface is covered with quaternary eluvial deluvial block stone and soil with loose structure, which is conducive to rainfall and surface water infiltration.

(a)

(b)

Figure 9: Distribution of dangerous rock masses in the survey area.

(a)

(b)

Figure 10: Distribution of colluvium block stones at river bottom (a) and G318 (b).

3.2.3. Rainfall. The infiltration of atmospheric rainfall will fill the relatively developed cracks and form hydrostatic pressure, which is very unfavorable to the stability of rock mass.

3.2.4. Human Engineering Activities. The national highway cut slope is built at the front edge to form a rock slope with a height of 10-25 m, which makes the free space conditions at the front edge well. In addition, recently human engineering activities have cleared the front edge dangerous rocks and cut the slope locally, which makes the slope stability worse.

3.3. Formation Mechanism. In the late 1970s, the slope cutting of G318 caused the rock mass at the top of the slope to crack and move down, with slight signs of deformation, but the cracks have occurred. In the long-term development process, the rainfall fills the cracks, the formed hydrostatic pressure is not conducive to the stability of the slope, the cracks continue to develop and expand, the mountains outside the cracks slowly incline outward, and the stress is concentrated at the foot of the slope. Recently, due to the slope cutting at the slope toe due to engineering construction, the state that has tended to be balanced has been broken. Recently, heavy rainfall has intensified the deformation, resulting in overall instability and collapse. The local collapse makes the whole in the limit equilibrium state again. On the whole, the slope rock mass fracture surface tracks the unloading surface and layer along the slope direction, forms a stepped fracture zone, and gradually develops into a weak surface. Once the weak surface is connected, driven by the upper rock mass, the rock mass slides along the weak surface, and a larger scale collapse will be formed.

The development process of Tanziyan collapse and slide can be roughly divided into three stages:

(1) Tensile deformation stage: when the slope toe is excavated, the massive rock mass tracks the structural cracks perpendicular to the slope direction, which produces tensile deformation. In the later stage, under the action of weathering and rainfall, the cracks gradually opens and expands, and the whole rock mass tilts outward slowly

(2) Bending deformation and failure stage: after the rock mass tilts outward, the stress concentration is formed at the weak part of the slope surface. Under the action of its own gravity, the stress gradually increases, and finally, the rock mass is unloaded and crushed in here, forming a weak broken structural plane between layers and slowly forming a sliding surface gradually penetrating from the layer surface and the unloading crack surface

(3) Cracked again to form a connected sliding surface and sliding stage: due to the recently slope cutting, the slope body temporarily in a stable state has lost its support end, and then, the upper rock mass tilts outward again and produces tensile deformation. The deep and long drawing crack trough at the rear edge is resurrected which is deepened, widened, and extended, and the upper rock mass is separated from the parent rock and has the potential of toppling and loading. Under its promotion, the early formed sliding surface tends to penetrate, and the rock mass is damaged along the sliding surface to form large-scale collapse

To sum up, the deformation and failure mode of Tanziyan landslide is fracture-bending-tensile fracture again and track the sliding failure of the weak surface. According to the deformation characteristics of the top drawing crack trough, it is wide at the top and slightly narrow at the bottom

and wide in the southwest and narrow in the northeast and gradually pinches out. It was analyzed that the rock mass outside the pull drawing crack trough is inclined outward and "tears" the mountain under the action of its own gravity. If the pull fracture continues to develop, it is bound to affect the potential deformation area and then form larger-scale deformation.

4. Stability Analysis

4.1. Calculation Method and Principle. The deformation and failure mode of Tanziyan landslide geological disaster is that the trailing edge unloading crack opens, topples outward under the influence of adverse factors such as rainfall, increases and deepens the crack opening, and finally produces overall sliding failure along the structural plane. Based on its deformation form and "Technical regulations for building slope engineering" (BG50330-2013), the stability of sliding along the structural plane is calculated. This example is more suitable for the calculation method of complex plane sliding surface, the calculation diagram is shown in Figure 11, and its calculation formula is as follows:

$$F_s = \frac{R}{T}, \tag{1}$$

$$R = [(G + G_b)\cos\theta - Q\sin\theta - V\sin\theta - U]\tan\varphi + cL, \tag{2}$$

$$T = [(G + G_b)\sin\theta + Q\cos\theta + \nu\cos\theta], \tag{3}$$

$$V = \frac{1}{2}\gamma_w h_w^2, \tag{4}$$

$$U = \frac{1}{2}\gamma_w h_w L. \tag{5}$$

In the above formulas, T is the sliding force caused by unit width strategy of sliding body and other external forces (KN/m); R is antisliding force caused by gravity per unit width of sliding body and other external forces (KN/m); C is cohesion of sliding surface (kPa); φ is internal friction angle of sliding surface (°); L is sliding surface length (m); G is dead weight per unit width of sliding body (KN/m); G_b is vertical additional load per unit width of sliding body (KN/m), taking positive value when pointing downward and negative value when pointing inward; θ is inclination angle of sliding surface (°); U is total water pressure per unit width of sliding surface (KN/m); V is total water pressure per unit width on the steep fracture surface at the trailing edge (KN/m); Q is horizontal load per unit width of sliding body (KN/m), taking a positive value when pointing to outside slope and a negative value when pointing to inside slope; h_w is the water filling height of the steep fracture at the trailing edge (m), and it is determined according to the crack conditions and catchment conditions.

4.2. Determination of Calculation Profile. Through the deformation range and stratum change delineated by the in situ ground engineering geological mapping, the deformation characteristics are analyzed structurally, and the section line is drawn in field, and the unit width is taken for research during calculation. According to the deformation, the stability is calculated as the 1-1′ longitudinal section and the G318 above section (Figure 12).

4.3. Calculation Parameters and Working Conditions

4.3.1. Calculation Parameters. The basic calculation parameters in this paper are taken according to the engineering geological survey report and the specification of "rock mechanics parameters manual" (water resources and Hydropower Press).

The natural density of rock is 2.69~2.71 g/cm^3, and the saturated density is 2.72~2.75 g/cm^3. The natural shear strength of medium thick layered limestone is as follows: C value is 1320 kPa, tgφ value is 1.43, and φ value is 55.03°. The deformation area of the project is affected by the structure, and the rock mass is relatively broken, so its strength should be much lower than that of the complete rock. According to the survey, the slope surface fractures are relatively developed and mostly open and the combination is poor. Two groups of "X" shaped main control fractures are developed in the rock mass and extend for a long time. The deformed area slides along the main control fractures. According to the geotechnical test results of the surrounding works and the reference empirical data, the complete chert nodule limestone exposed by the collapse is relatively hard rock, with saturated uniaxial compressive strength of 35 MPa and C value of more than 1000 kPa; φ value is 53°. However, the mechanical strength of the deformation and failure area is reduced due to the fracture of rock mass, which should be greatly reduced when the parameters are taken, so as to be more in line with the actual deformation situation. According to the technical code for building slope engineering, the shear strength of rock mass structural plane is taken as follows:

(1) Considering the importance of the slope, the standard value of shear strength is the corresponding value of "general combination": C value is 90 kPa and φ value is 35°

(2) The value of natural shear strength of potential slip surface is as follows: C value is 90 kPa and φ value is 35°; the saturated shear strength is multiplied by the reduction factor of 0.9, and the C value is 80 kPa and φ value is 32°

According to relevant data, the basic seismic intensity of Badong County is grade VI, and the peak ground acceleration is 0.05 g.

4.3.2. Calculation Conditions. According to the hydrogeological conditions, there is almost no water in the rock mass at ordinary times. The combination of calculation conditions is as follows: working condition 1: dead weight; working condition 2: dead weight+20-year rainstorm; and working condition 3: dead weight+earthquake (VI degree fortification).

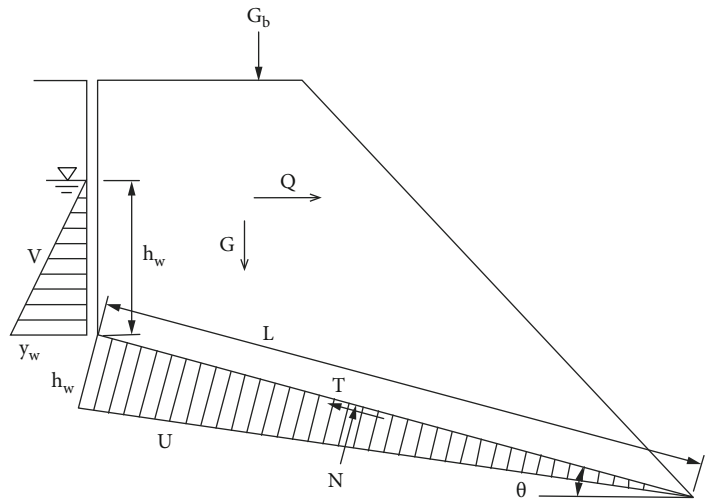

Figure 11: Structural plane stability calculation diagram.

4.4. Calculation Results and Analysis. According to the calculation model and parameters, the stability coefficient of disaster body under different working conditions is calculated. The calculation results are shown in Table 1. The evaluation shall refer to the provisions in relevant specifications.

The calculation results show that the stability coefficient of Tanziyan is 1.065 under condition 1, which is basically stable, and the safety margin is not high, indicating that Tanziyan is basically stable due to unloading under natural condition. It is in an unstable state under condition 2. Rainfall will fill the cracks on the top of the slope and form hydrostatic pressure, and the stability coefficient drops sharply, so that the slope is in an unstable state. Under condition 3, the stability coefficient is 1.038, which is understable. Considering various working conditions, the disaster body is from understable to unstable state, and engineering treatment is urgently needed to improve the stability coefficient.

5. Treatment Measures

According to the deformation characteristics and causes of Tanziyan landslide, slope cutting and shaping is adopted to eliminate dangerous rocks and improve the overall stability. For multiple cracks developed at the top, the form of crack sealing is adopted to prevent rainfall infiltration along the cracks. In order to further improve the overall stability, the construction method of lattice structure combined with anchor cable is adopted for anchoring.

5.1. Slope Cutting and Shaping

5.1.1. Conceptual Design. According to the height difference and slope of the landslide mass, the 1-1′, 2-2′, and 3-3′ sections in the deformation area are cut at a slope ratio of 1 : 1, as shown in Figure 13. And cut the slope at the slope ratio of 1 : 0.75 for sections 4-4′ and 5-5′, as shown in Figure 14. Each grade of slope is 15 m high and the middle berm is 2 m wide. The slope cutting and shaping area is 16210 m^2, and the slope cutting volume is about 104676 m^3.

The berm can be reasonably set according to the original landform of the northeast slope (potential deformation area). The north-east side of the slope cutting area shall be smoothly connected with the original landform, and the slope ratio shall be controlled at 1 : 2. If the smooth connection cannot be made due to the thick soil layer, the slope can be made according to the slope ratio of 1 : 1, and then, lattice anchor bolt shall be used for support. Although no one lives below the construction area, the bottom of the slope is the Yuquan river, and the waste slag cannot be rolled down arbitrarily to avoid blocking the river and forming a barrier lake. Before slope cutting, sand bags shall be stacked outside the national highway for buffer, with a length of 190 m, a height of 2 m, and a bottom width of 3 m. The waste slag shall be removed in time to ensure that the top is stable and cannot be carried out at the same time as slope cutting.

5.1.2. Stability Review. The slope cutting and shaping project basically eliminates the sliding deformation and failure controlled by the structural plane, but the downward extension distance of the crack is not clear in the top tensile crack groove. The rock mass after slope cutting forms a wedge under the joint action of the layer and the downward extension crack of the tensile crack groove, which may deform along the layer. Therefore, the bedding stability shall be rechecked according to the slope shape after slope cutting and shaping. The parameters are the same as above, and the calculation model is shown in Figure 15.

Through calculation, under condition 2, the stability factor is 1.017, which is in an unstable state and has not yet reached the safety factor of 1.1 required by the design. For the slope after shaping, other projects still need to be used for further support.

Through calculation, under condition 2, the stability factor is 1.017, which is in an unstable state and has not yet reached the safety factor of 1.1 required by the design. For the slope after shaping, other projects still need to be used for further support.

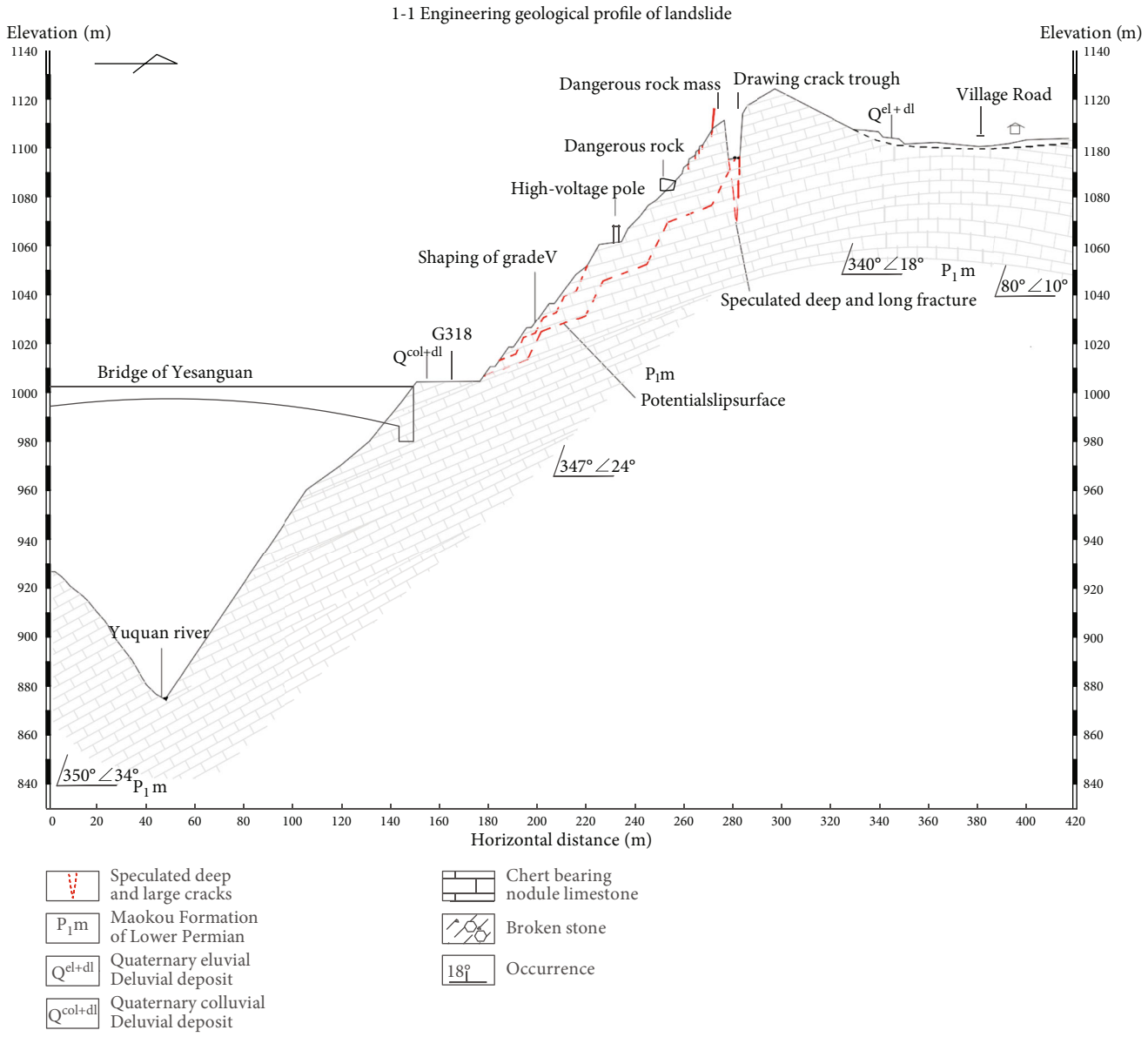

Figure 12: Calculation diagram of profile above G318.

Table 1: Stability calculation results of Tanziyan landslide geological hazard.

Profile number	Calculation condition	Stability factor Fs	Evaluate
1-1′	1	1.065	Basically stable
	2	0.895	Unstable
	3	1.038	Understable

Attention: stable, $Fs \geq 1.15$; basically stable, $1.05 \leq Fs < 1.15$; understable, $1.0 \leq Fs < 1.05$; unstable, $Fs < 1.0$.

5.1.3. Drawing Crack Trough Slope Cutting. The slope surface improves its own stability through slope cutting, but the rear edge wall of the cleavage groove after slope cutting forms a steep cliff with a height of nearly 20 m. Although the investigation shows that its stability is good at this stage and the crack cutting is not obvious, under the influence of long-term weathering, rainfall, and other adverse factors, it is inevitable that there will be block falling. If it is not treated, it will still become a hidden danger in the future. In combination with the landform developed by the tensile groove and the local construction planning for the area, it is proposed to eliminate the hidden danger by cutting the slope on the top of the mountain.

5.2. Crack Sealing. At present, many cracks are developed at the top of the slope. The maximum extension length of these cracks can reach more than 20 m and the opening width can reach 0.5 m. The development of cracks is very conducive to the infiltration of surface water formed by rainfall and is very unfavorable to the stability of the slope.

The method of clay compaction and concrete sealing is adopted in this paper. The slope excavation shall be carried

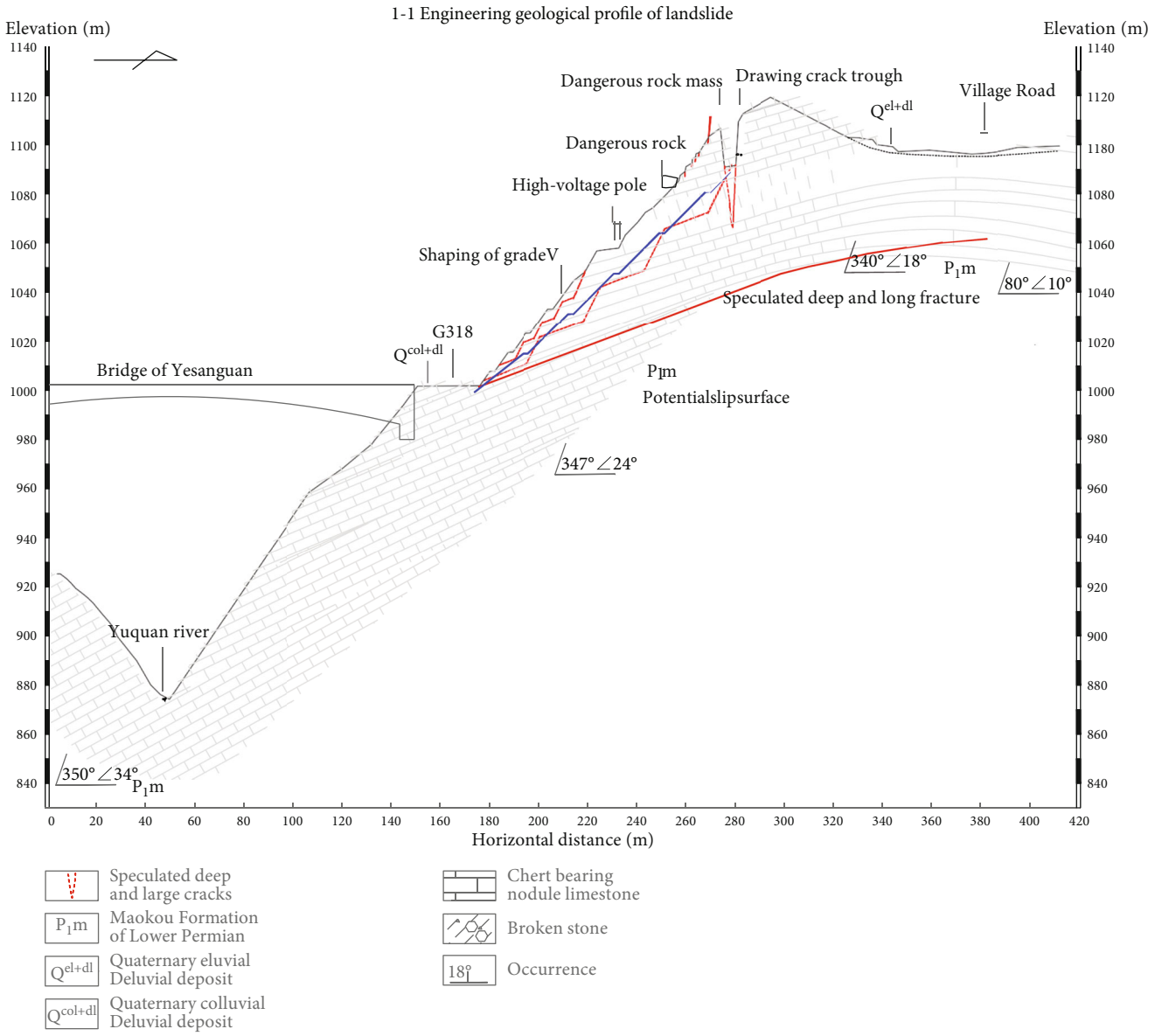

Figure 13: Schematic diagram of 1-1′ section slope cutting.

out on both sides of the existing crack according to 1 : 0.75, and the excavation depth shall not be less than 1 m, and then, the clay shall be backfilled and compacted by machinery. The top of the crack is sealed with concrete. The concrete slab is 0.3 m thick. It is cast in situ with C20 concrete. A steel nail is embedded on both sides of the concrete every 5 m. After the concrete curing, the steel nail is numbered for simple crack monitoring.

5.3. Lattice. The slope after slope cutting and shaping is further anchored with lattice anchor cable. The lattice is arranged at an elevation of 1000~1095 m, and edge sealing beams are used around and inside and outside the berm. The total area of the lattice structure is 16210 m^2, and the anchor cable is arranged at the intersection of the lattice structure, with the length of 20~55 m.

The slope protection adopts reinforced concrete lattice structure, the frame is arranged in a square shape, the side length is 4 m × 4 m, and the beam section is 50 cm × 65 cm (width × high). The bottom of the lattice structure is directly connected to the concrete retaining wall. A total of 12 rows of anchor cables are arranged at the intersection of the lattice structure of an elevation of 1920-1980 m, and grass is planted with the frame.

5.4. Anchor Cable and Rock Bolt. A total of 12 rows of anchor cables are arranged in the middle of the slope cutting and shaping area. The length of anchor cables is based on passing through the potential sliding surface and tensile crack groove. Eight kinds of anchor cable lengths are determined through calculation. Through engineering analogy and referring to relevant regulations, the length of anchor

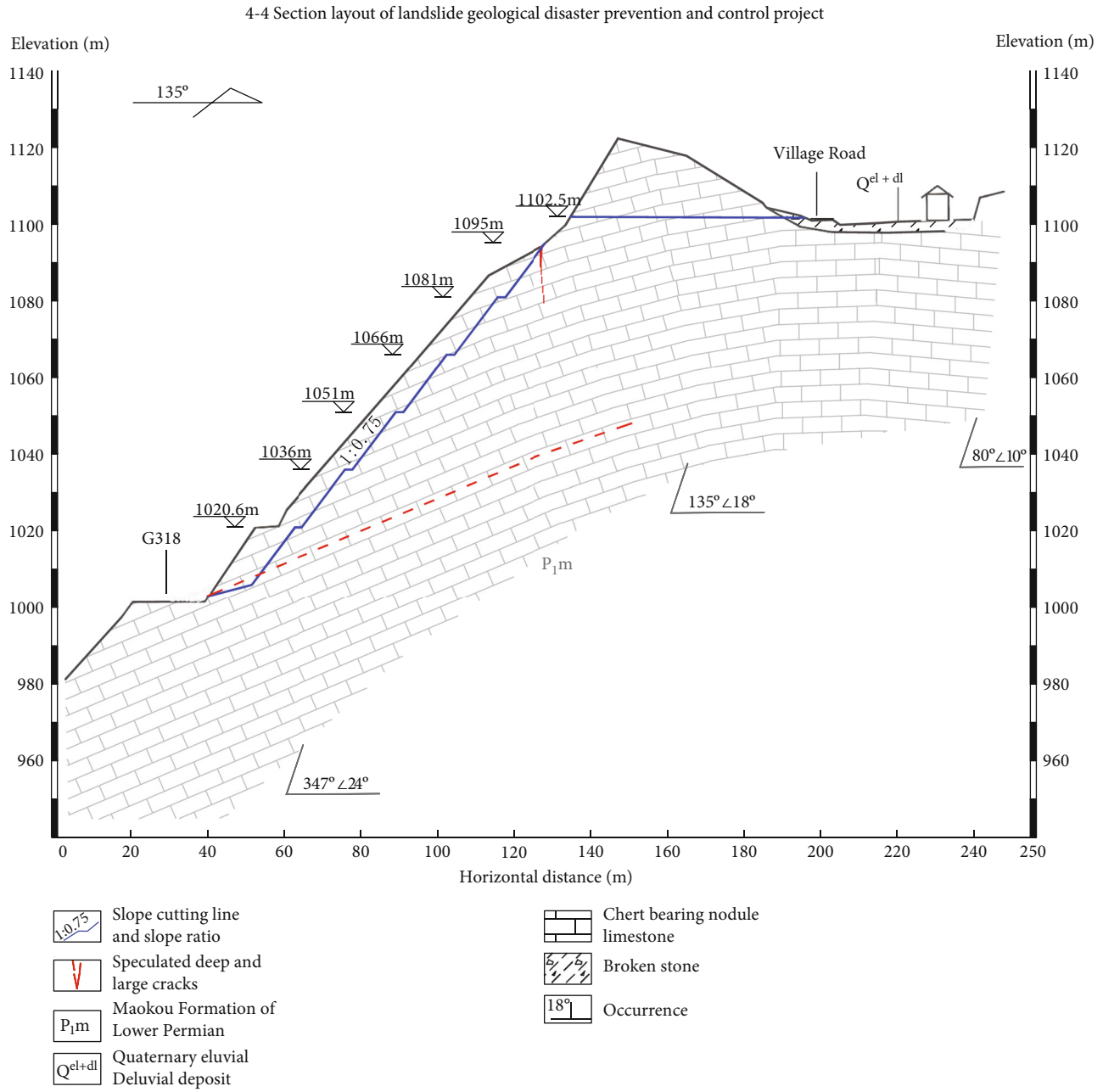

Figure 14: Schematic diagram of 4-4′ section slope cutting.

sections is 5 m. The nonfully bonded prestressed anchor cable is selected. The horizontal and vertical spacing of the anchor cable is 4 m. The shooting direction of the anchor cable is roughly perpendicular to the dip direction of the rock stratum, and the included angle between the incident angle and the horizontal angle is 25°. The anchor cable is arranged at the intersection of the lattice beam. The anchor pier is directly built on the lattice beam with concrete to form a table perpendicular to the incidence of the anchor cable. After the pretensioning of the anchor cable, the anchor head is poured with concrete.

Rock bolts are arranged at the intersection of anchor cables at the end of lattice beam. The rock bolts are made of C25 reinforcement. The rock bolts are 6 m and 9 m long, arranged alternately in quincunx shape, and the included angle between the incident angle of rock bolts and the horizontal angle is 25°. The rock bolts is of full bonding type and does not need to be pulled out.

5.5. Retaining Wall. There are 2 retaining walls, which are, respectively, arranged on the inside and outside of the highway. The retaining wall inside the highway can support the lattice beam and improve the overall aesthetics. The back side of the retaining wall in the nonlattice slope protection area does not need to be backfilled, and at least 2 m is reserved from the slope toe to form a rockfall groove. The retaining wall outside the highway is used to repair the damaged shoulder, and it shall be repaired according to the damage. The wall body is poured

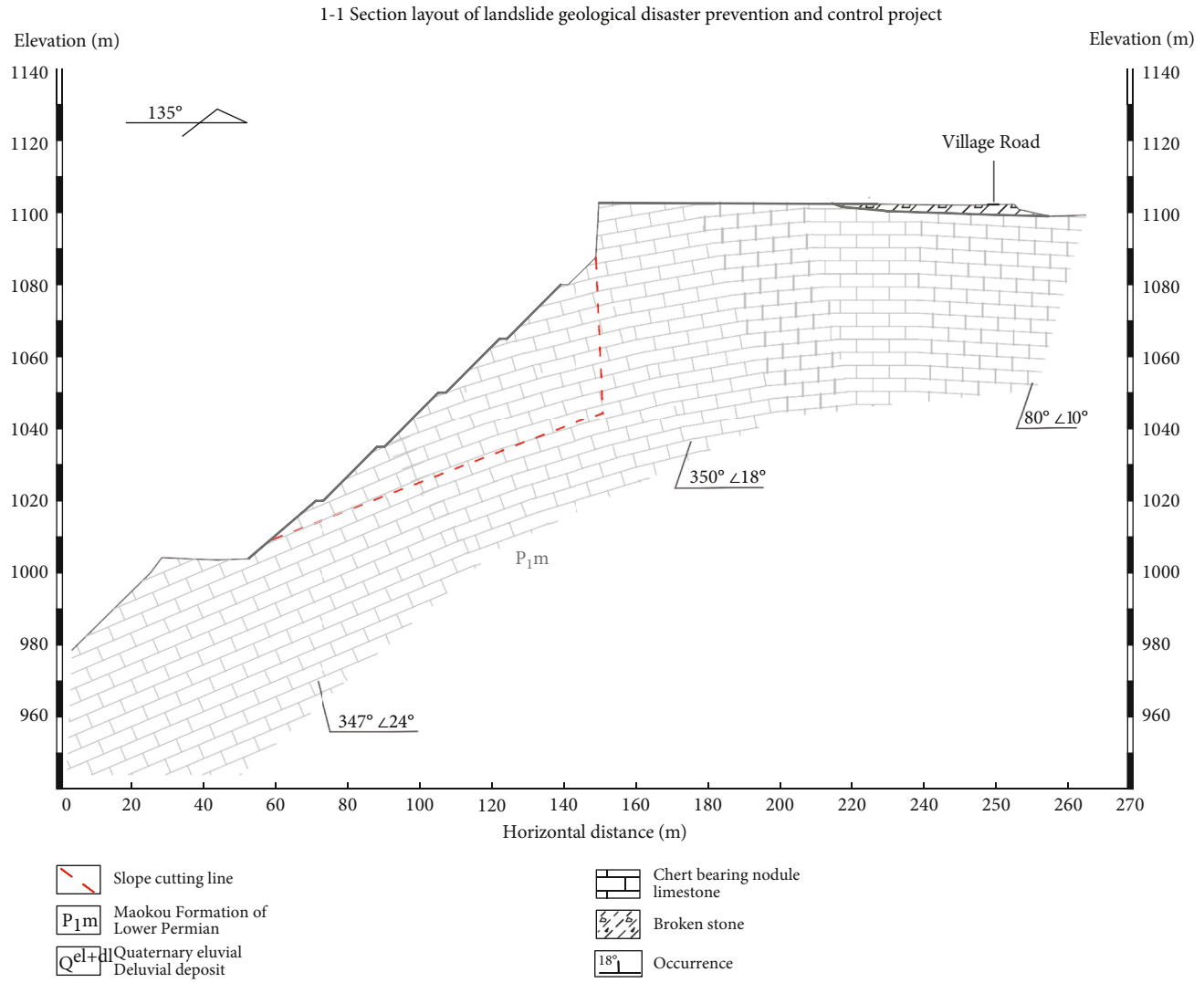

Figure 15: Stability calculation profile of 1-1′ section after slope cutting and shaping.

Table 2: Calculation results of retaining wall.

Retaining wall number	Antisliding K_c	Resistance to capsizing K_o	Foundation stress and eccentricity				Wall bottom section strength		
			e	σ_1 (kPa)	σ_2 (kPa)	σ (kPa)	$e1$	σ (kPa)	τ (kPa)
D01	2.076	4.013	0.129	96.537	42.648	69.592	0.129	96.537	-7.721
Repair the road shoulder	2.553	3.050	0.143	115.242	21.382	68.312	0.143	115.242	-11.269
Results evaluation	>1.3	>1.5	Comply with relevant specifications						

with C25 concrete, and expansion joints are set every 15 m. The foundation of the retaining wall and behind the wall is medium thick layered chert nodular limestone. There is no need to slope during foundation excavation. A drainage hole is set on the wall body, and the upstream side is wrapped with geotextile.

After checking and calculating a series of soil mechanics formulas, the antisliding stability, antioverturning stability, foundation bearing capacity, wall bottom section strength, and impact resistance of masonry retaining wall meet the planning requirements. The calculation results are shown in Table 2.

5.6. Slope Surface Greening. Vegetation restoration is carried out on the slope based on the principles of green treatment and ecological treatment. For slope greening, ecological bags are mainly placed in the lattice frame, and grass seeds are mixed in the soil, which is conducive to plant growth. With polypropylene as the main raw material, the ecological bag has the functions of antiultraviolet, antiacid, alkali and salt, antimicrobial erosion, and water and soil permeability, and the molding specification is $880 \times 300 \times 200$ (mm). The ecological bag is laid horizontally on the long side. After laying, the surface of the ecological

bag has a space of 10 cm from the top of the lattice beam to avoid unstable factors caused by the prominent lattice of the ecological bag.

5.7. Active Protective Net. After slope cutting and shaping, a 20 m high cliff is formed on the east side wall (parent rock) of the original tensile fracture groove. Although the whole is relatively complete and the fracture cutting degree is slight, under the action of long-term weathering, rainfall, and other adverse factors, blocks may fall off and pose a threat to the vehicles below. In order to prevent the slope from forming new dangerous rock disasters again after risk removal, STG-50 active protection system is designed to protect the rock wall.

The active flexible protective net covers the whole exposed slope, from the upper part to the cliff top and from the lower part to the lattice top beam in the slope cutting area. The slope area to be protected is 600 m^2, and 870 m^2 active protective net is laid.

6. Conclusions

Through geological investigation, this paper studied the stability, deformation, and failure characteristics of the disaster body in this area, puts forward corresponding treatment measures, and draws the following conclusions:

(1) The whole is from understable to unstable state

(2) The development process of Tanziyan landslide can be roughly divided into three stages, namely, tension fracture deformation stage, bending deformation failure stage, and retension fracture and forming a through sliding surface instability and sliding stage

(3) In view of the landslide situation in this paper, it is proposed to adopt slope cutting and shaping, crack sealing and filling, lattice structure, anchor cable, retaining wall, slope greening and active protection network, and combined with the monitoring scheme

With the current research, the research on landslide stability analysis method and deformation failure mode is relatively mature, and the materials and schemes for landslide control emerge endlessly. The complex plane sliding surface calculation method used in this paper is only one attempt. Some methods, theories, and treatment measures mentioned in Introduction, such as the application research of negative Poisson's ratio anchor cable, need more engineers and technicians to verify and develop.

Data Availability

The data that support the conclusions of this study are available from text and the corresponding author upon reasonable request.

Conflicts of Interest

There are no conflicts of interest with respect to the results of this paper.

Acknowledgments

This study is sponsored by the National Natural Science Foundation of China (No. 42162026).

References

[1] Y.-F. Yao, "Study on failure mode and development mechanism of anti-dip rock landslide," *Chemical Minerals and Processing*, vol. 50, no. 7, pp. 49–52, 2021.

[2] B.-F. Liu, X. Liang, and K. Zhou, "Study on the genetic mechanism and treatment scheme of a landslide," *Subgrade Engineering*, vol. 2, pp. 231–236, 2021.

[3] H.-T. Zhang, D.-C. Zhu, and P. Wang, "Analysis of deformation and failure mechanism of bedding rock slope," *Highway*, vol. 66, no. 3, pp. 67–71, 2021.

[4] Q.-L. Zeng, W.-F. Wang, and H.-Y. Chen, "Study on characteristics of Zhaojiagou landslide in Zhenxiong and instability mechanism based on slope structure," *Journal of Engineering Geology*, vol. 24, no. 4, pp. 510–518, 2016.

[5] Y. Zhang, S.-R. Su, and P. Li, "Study on landslide mechanism of fault control – taking Liujiapo landslide as an example," *Journal of Engineering Geology*, vol. 23, no. 6, pp. 1127–1137, 2015.

[6] Q. Xu, "Deformation and failure behavior and internal mechanism of landslide," *Journal of Engineering Geology*, vol. 20, no. 2, pp. 145–151, 2012.

[7] X.-L. Hu, H.-M. Tang, and C.-D. Li, "Study on deformation and failure mechanism of Baozha landslide based on parameter inversion," *Journal of Engineering Geology*, vol. 19, no. 6, pp. 795–801, 2011.

[8] X.-S. Li, K. Peng, J. Peng, and D. Hou, "Experimental investigation of cyclic wetting-drying effect on mechanical behavior of a medium-grained sandstone," *Engineering Geology*, vol. 293, article 106335, 2021.

[9] X.-S. Li, K. Peng, J. Peng, and H. Xu, "Effect of cyclic wetting-drying treatment on strength and failure behavior of two quartz-rich sandstones under direct shear," *Rock Mechanics and Rock Engineering*, vol. 54, no. 11, pp. 5953–5960, 2021.

[10] Y. Wang, B. Zhang, B. Li, and C.-H. Li, "A strain-based fatigue damage model for naturally fractured marble subjected to freeze-thaw and uniaxial cyclic loads," *International Journal of Damage Mechanics*, vol. 30, no. 10, pp. 1594–1616, 2021.

[11] M.-Z. Gao, J. Xie, Y.-N. Gao et al., "Mechanical behavior of coal under different mining rates: a case study from laboratory experiments to field testing," *International Journal of Mining Science and Technology*, vol. 2021, no. 31, pp. 825–841, 2021.

[12] M.-Z. Gao, J. Xie, J. Guo, Y.-Q. Lu, Z.-Q. He, and C. Li, "Fractal evolution and connectivity characteristics of mining-induced crack networks in coal masses at different depths," *Geomechanics and Geophysics for Geo-Energy and Geo-Resources*, vol. 7, no. 1, 2021.

[13] C. Zhu, Y. Lin, and G. Feng, "Influence of temperature on quantification of mesocracks: implications for physical properties of fine-grained granite," *Lithosphere*, vol. 2021, no. - Special 4, 2021.

[14] D.-H. Chen, H.-E. Chen, W. Zhang, J.-Q. Lou, and B. Shan, "An analytical solution of equivalent elastic modulus considering confining stress and its variables sensitivity analysis for fractured rock masses," *Journal of Rock Mechanics and Geotechnical Engineering*, 2021.

[15] C. Zhu, M.-C. He, B. Jiang, X.-Z. Qin, Q. Yin, and Y. Zhou, "Numerical investigation on the fatigue failure characteristics of water-bearing sandstone under cyclic loading," *Journal of Mountain Science*, vol. 18, no. 12, pp. 3348–3365, 2021.

[16] G.-X. Wang, "Current situation of landslide prevention engineering measures at home and abroad," *Chinese Journal of Geological Hazards and Prevention*, vol. 1, pp. 2–10, 1998.

[17] S.-D. Yin, X.-T. Feng, and Y.-L. Zhang, "Study on parallel evolutionary neural network method for optimization of landslide reinforcement scheme," *Journal of Rock Mechanics and Engineering*, vol. 16, pp. 2698–2702, 2004.

[18] G.-X. Wang, "Key technologies and treatment methods in landslide prevention and control," *Journal of Rock Mechanics and Engineering*, vol. 21, pp. 20–29, 2005.

[19] L.-Q. Wu, F. Zhang, and X.-C. Ling, "Stability analysis of high slope in Pingtou village, Wuyi, Zhejiang Province under heavy rainfall," *Journal of Rock Mechanics and Engineering*, vol. 28, no. 6, pp. 1193–1199, 2009.

[20] L. Ma, "Study on causes and treatment measures of landslide in waste dump in open pit mine," *Coal Technology*, vol. 35, no. 8, pp. 166–168, 2016.

[21] G.-X. Wang, "Selection and optimization of landslide control scheme," *Journal of rock Mechanics and Engineering*, vol. S2, pp. 3867–3873, 2006.

[22] C. Zhu, M.-C. He, X.-H. Zhang, Z.-G. Tao, Q. Yin, and L.-F. Li, "Nonlinear mechanical model of constant resistance and large deformation bolt and influence parameters analysis of constant resistance behavior," *Rock and Soil Mechanics*, vol. 42, no. 7, pp. 1911–1924, 2021.

[23] X.-W. Zou, "Stability analysis and treatment measures of high and steep slopes of Mombasa highway," *Engineering Construction*, vol. 53, no. 8, pp. 20–25, 2021.

[24] J.-Q. Huang, "Cause analysis and treatment measures of expressway slope landslide," *Engineering Construction and Design*, vol. 13, pp. 91–93, 2021.

[25] J.-H. Cao, "Stability analysis and treatment measures of ancient landslide of Xiluodu Hydropower Station," *Water Conservancy and Hydropower Technology*, vol. 47, no. 12, 2016.

[26] Z.-G. Tao, C. Zhu, M.-C. He, and M. Karakus, "A physical modeling-based study on the control mechanisms of negative Poisson's ratio anchor cable on the stratified toppling deformation of anti-inclined slopes," *International Journal of Rock Mechanics and Mining Sciences*, vol. 138, article 104632, 2021.

[27] G. Li, Y. Hu, S. M. Tian, M. weibin, H. L. Huang, and S.-M. Tian, "Analysis of deformation control mechanism of prestressed anchor on jointed soft rock in large cross-section tunnel," *Bulletin of Engineering Geology and the Environment*, vol. 80, no. 12, pp. 9089–9103, 2021.

Hindawi
Geofluids
Volume 2022, Article ID 5045961, 13 pages
https://doi.org/10.1155/2022/5045961

Research Article

Experimental Study on Energy Dissipation of Saturated Mudstone in Coal Mine under Impact Loading

Liangjie Guo[1,2] **and Yongyu Wang**[1]

[1]*Faculty of Engineering, China University of Geosciences, Wuhan 430074, China*
[2]*Engineering Research Center of Rock-Soil Drilling & Excavation and Protection, Ministry of Education, Wuhan 430074, China*

Correspondence should be addressed to Yongyu Wang; yywang@cug.edu.cn

Received 1 February 2022; Revised 26 February 2022; Accepted 28 February 2022; Published 17 March 2022

Academic Editor: Long Yan

The influence of blasting energy on blasting fragmentation and damage of reserved rock is important for safety and schedule of drill-blasting construction in coal mine. This study is aimed at investigating the dynamic mechanical properties of mudstone in coal mine using the energy characterization method, and their quantitative relation formula was also developed. The impact compression experiments of mudstone in Huainan mining area were conducted to study the saturated mudstone dynamic mechanism, crack properties, and energy dissipation law using the diameter 50 mm split Hopkinson pressure bar (SHPB). The results show that under the back-and-forth reflection of the stress wave, the saturated mudstone specimens are characterized by circumferential failure and axial splitting damage, which appear in the rock grain interface. By energy analysis, the energy dissipation per volume (EDV), energy dissipation per mass (EDM), and absorption impedance energy ratio (AIER) are used to represent the energy dissipation characteristic of mudstone. And the AIER is the best index. Additionally, there is the quadratic function relationship between three indexes and average strain ratio, showing the dependence of the strain ratio.

1. Introduction

Mudstone is widely distributed in coal measure strata, which is characterized by loose, poor cementation and low strength. Hence, mudstone is extremely sensitive to stress, moisture, temperature, and subsurface water [1, 2]. The mechanical property and inner structure of mudstone vary with the change of stress condition [3–5]. Many researchers studied the physical and mechanical properties and failure laws of mudstone in coal mine under complex natural environment conditions. The strength of mudstone is less than 30 MPa, reviewing the existing literature researches. And its strength would be lower when faced with water, temperature, weathering, and so on [6, 7]. Bhattarai et al. investigated the effect of chemical and physical weathering on the shear strength of the mudstone [8]. The results showed that the shear strength of fully weathered mudstone is 10 times larger than that of weak weathered mudstone. Huang et al. carried out a series of uniaxial compression experiments and creep experiments of mudstone specimens under different water contents and found that the rock strength and elastic modulus decreased rapidly with the increment of water content, and a nonlinear creep constitutive equation was established based on the experimental data [9]. Both Zhang et al. and Lu et al. studied the softening effect of mechanical properties of mudstone under high temperatures [10, 11]. High temperatures would cause thermal expansion of mudstone, and the expansion will increase with temperature increasing.

Due to the effects of impact loading, such as blasting and mechanical vibration in coal mine, the disturbance range of surrounding rock mass in roadway increases, yet the bearing capacity of rock mass decreases. Hence, the roof fall and rock bottom drum are easily happened [12–15]. The dynamic behavior of rock under impact loading is an important issue for coal mining [16, 17]. Some typical complete dynamic stress-strain curves for marble and granite using SHPB technique are given by Shan et al. [18], together with

an interpretative discussion on the shapes and meanings of the curves. Chen et al. tested the dynamic mechanical behavior of granite [19]. The results showed that impact dynamic strength increases as the precompression stress increases and can reach its maximum when the precompression stress is about 50% of the static tension strength. Liu et al. studied the mechanic properties of amphibolites, sericite-quartz schist, and sandstone under impact loading and analyzed the dynamic compressive strength, failure modes, and energy dissipation variation with the strain rate and the strain rate hardening effect from the perspective of sandstone microstructure [20]. Mardoukhi et al. used optical microscopy and profilometry to analyze the drop rate of tension strength and damage area of rock under impact loading using SHPB tests [21]. The dynamic mechanics of granitic specimens under different hydrostatic pressures were studied by Du et al., and the results showed that the dynamic strength of rock specimens increased with increasing the strain rate, while the rate sensitivity of rock strength decreased as the hydrostatic pressure increased [22]. The thermal effect on the dynamic properties of rock is another significant issue for deep coal mining. Fan et al. investigated the effects of high temperature on the dynamic behavior of granite using SEM and SHPB tests, and the results showed that both the dynamic strength and energy absorption capacity decreased as temperature increased [23].

Many researchers studied the failure morphology of rock specimens under impact loadings. And Chinese scientists have made tremendous achievements. Li et al. studied the impact failure characteristics of rock subjected to one-dimensional coupled static and dynamic loads [24]. Rock specimens will break with a shear failure model subjected to one-dimensional coupled static and dynamic loads, while the failure mode will be splitting faulting for conventional impact testing. Zhao et al. considered that the impact failure of rock consists of tensile strain failure, axial splitting tensile failure, and crushing failure [25]. Li et al. performed the numerical study on the failure of sandstone, limestone, and dolomite under impact loading [26]. The failure modes of rock are integrity, cleavage, and smashing.

Although many studies on mechanical properties of rock under impact loadings have been conducted [27–40], little attention was paid to the dynamic behavior of mudstone in coal mine. In consequence, this study is aimed at investigating the dynamic mechanical properties of mudstone in coal mine using the energy characterization method, and their quantitative relation formula was also developed. In the present study, a series of compression experiments of mudstone under different impact loadings from Huainan mining area, China, was conducted to study the mudstone dynamic behaviors, crack properties, and energy dissipation law using the diameter 50 mm SHPB test device. The relationships of crack and material composition of mudstone were determined. From the perspective of energy absorption, the deformation, failure, and energy dissipation of mudstone were described. The study provides good theoretical and technical supports for coal-rock roadway blasting excavation construction.

2. Theoretical Basis of SHPB Tests

In the conventional SHPB technique, the mudstone specimen is located in between the incident bar and the transmitted bar. The SHPB device is shown in Figure 1. When the striker bar hits the incident bar, a rectangular stress pulse is generated and travels along the incident bar until it strikes the specimen. Parts of the incident stress pulse reflect from the bar/specimen interface because of the material impedance mismatch. And part of it transmits through the specimen. The transmitted pulse emitted from the specimen travels along the transmitted bar until it strikes the end of the bar. The SHPB device is from Anhui University of Science and Technology. The length of the striker, incident bar, and transmitted bar is 0.60 m, 2.40 m, and 1.20 m, respectively. All the material of the bar is alloy steel. And the density of the bar is 7.8 g/cm^3, Young's modulus is 210 GPa, and longitudinal wave velocity is 5.19 km/s, respectively.

Under the failure of rock subjected to impact loading, rock constantly exchanges energy with the exotic environment. It is an evolutionary process that the microcracks vary from disorder to order and finally develop into macrocracks. The process from microdamage to macrofracture is the process of energy dissipation [41]. Hence, the failure mechanism can be easily revealed by energy analysis. In SHPB tests, both the stress and strain can be obtained in terms of the recorded strains of the incident and transmitted bars. During the impact loading, the incident energy $W_I(t)$, transmitted energy $W_R(t)$, and reflected energy $W_T(t)$ of specimens are as follows [12, 22, 32]:

$$W_I(t) = AEC_0 \int_0^t \varepsilon_I^2(t)dt, \tag{1}$$

$$W_R(t) = AEC_0 \int_0^t \varepsilon_R^2(t)dt, \tag{2}$$

$$W_T(t) = AEC_0 \int_0^t \varepsilon_T^2(t)dt, \tag{3}$$

where A is the section area of the bar, E is Young's modulus of the bar, and C_0 is the wave velocity of the bar. $\varepsilon_I(t)$, $\varepsilon_R(t)$, and $\varepsilon_T(t)$ are the strain of the incident wave, reflected wave, and transmitted wave at time t, respectively.

By omitting the wasted energy induced by the friction force between the specimen and incident bar, transmitted bar during the impact loadings, the absorbed energy of specimen $W_S(t)$ is

$$W_S(t) = W_I(t) - [W_R(t) + W_T(t)]. \tag{4}$$

3. Specimen Preparation and Physics

3.1. Preparation of Specimens. Located in the central of Anhui province, China, middle and lower reaches of Yangtze River (see in Figure 2), the Panyi mine is faced with the danger of high in situ stress, water pressure, and temperature in rock roadway construction. This mining area was in use in

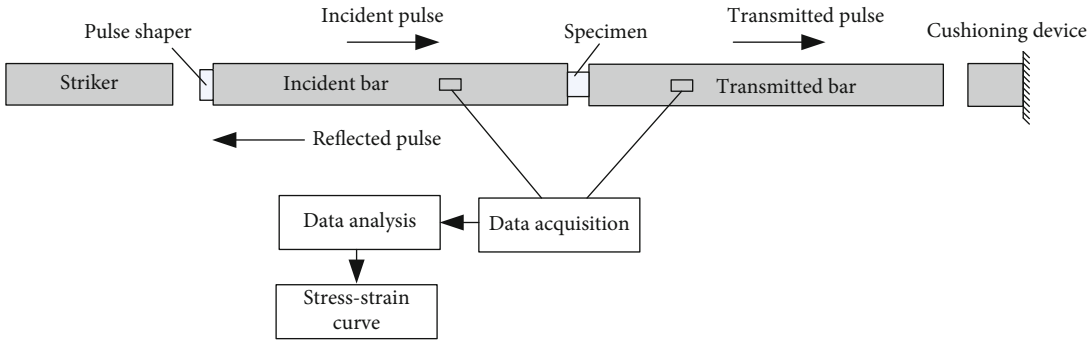

Figure 1: Structural constituents of SHPB device.

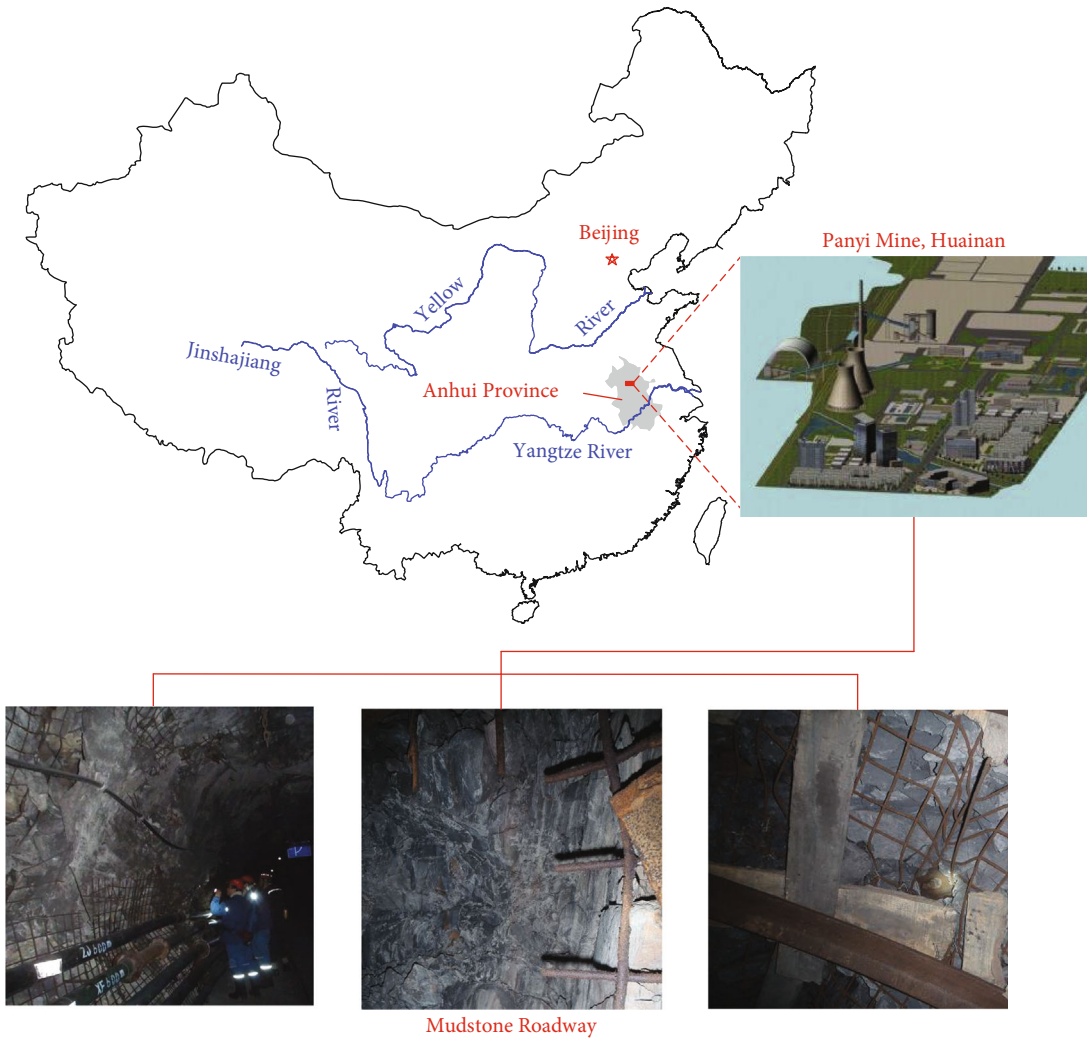

Figure 2: Specimen location: Panyi mining area, Huainan, China.

December 2016. The roadway floor heave and side extrusion deformation were found in 2017. The mudstone blocks, used to be in experiments, originated from the 800 m deep 5# coal seam mining area as shown in the geological section in Figure 3. The coal mine area consists of mudstone, sandstone, and coal formations dipping about 40° to the south in the area of interest. There are some faults passing through the mudstone-sand layers, easily leading to rock fall. The mudstone forms in the development period of continental strong tensional faulting and experienced main squeezing and luffing tectonic and hydrothermal alteration activity.

The cylindrical specimens are obtained by drilling, cutting, and grinding in the laboratory. In order to meet the assumption of one-dimensional stress wave propagation

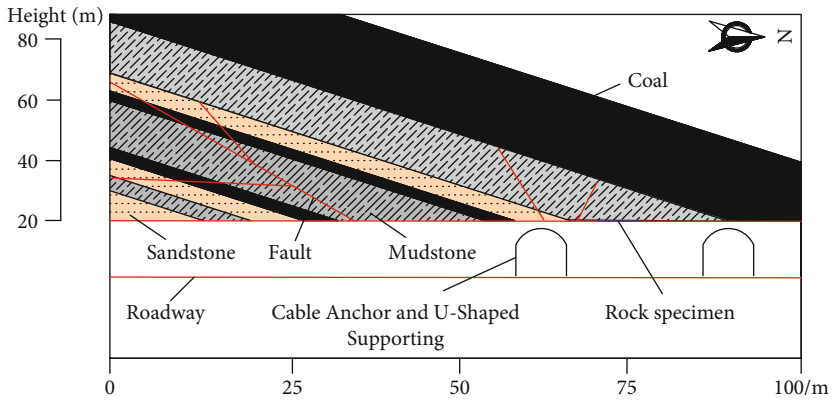

Figure 3: Geological section along 5# coal seam mining area. The obtained rock specimen is located within mudstone that dips approximately 40 deg south.

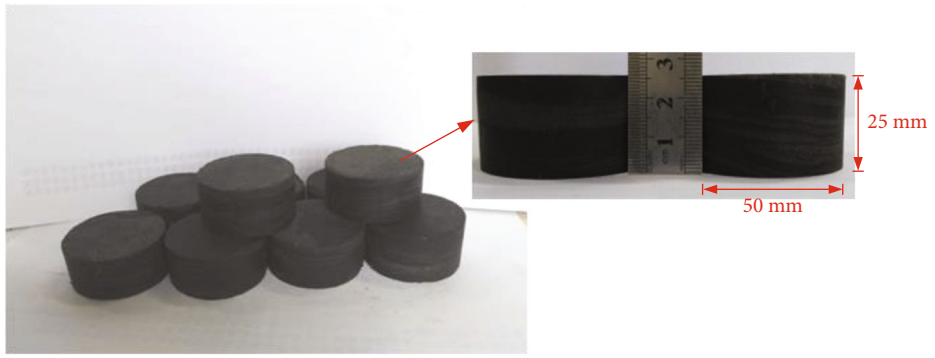

Figure 4: Mudstone specimen: diameter 50 mm and length 25 mm.

theory of SHPB and reduce the friction and axial inertia effect of the specimen, the length-diameter ratio of the prepared specimens is 0.5. Hence, the diameter of the specimen is 50 mm; the length of the specimen is 25 mm. No parallelism is within 0.05 mm on both ends of the specimen, and the roughness is within 0.02 mm. Those mudstone specimens in coal mine are shown in Figure 4.

Before testing, the process of saturating specimens with liquid was conducted using the vacuum saturation device (ZYB-IA, see Figure 5), by following the below procedure. Distilled water was used as a saturated liquid to avoid the potential influence of chemical factors.

(1) Put the dry mudstone specimen in a basket in the vacuum saturation device

(2) Vacuum the specimen storehouse until no air bubbles were generated in the liquid storage tank

(3) Switch on the specific valve; the distilled water in the liquid storage tank was sucked into the specimen storehouse

(4) The mudstone specimen was immersed in the distilled water (i.e., vacuum water-saturated environment) for 7 days, and the saturation pressure was set as 1.0 MPa

Figure 5: Vacuum saturation device (ZYB-IA).

(5) Take out the mudstone specimen for the next step of testing

3.2. Physics and Mechanical Properties of Mudstone Specimen. The chemical composition of mudstone has much effect on the macromechanical properties of mudstone specimens. The chemical composition of mudstone in coal mine was determined using X-ray fluorescence (XRF) and X-ray Diffraction (XRD) by grinding the mudstone specimen after

Table 1: The chemical composition of mudstone in coal mine.

Chemical component	Na_2O	MgO	Al_2O_3	SiO_2	K_2O	TiO_2	Fe_2O_3	CaO
Percent (%)	1.200	1.943	20.383	56.616	3.989	1.419	12.328	0.964

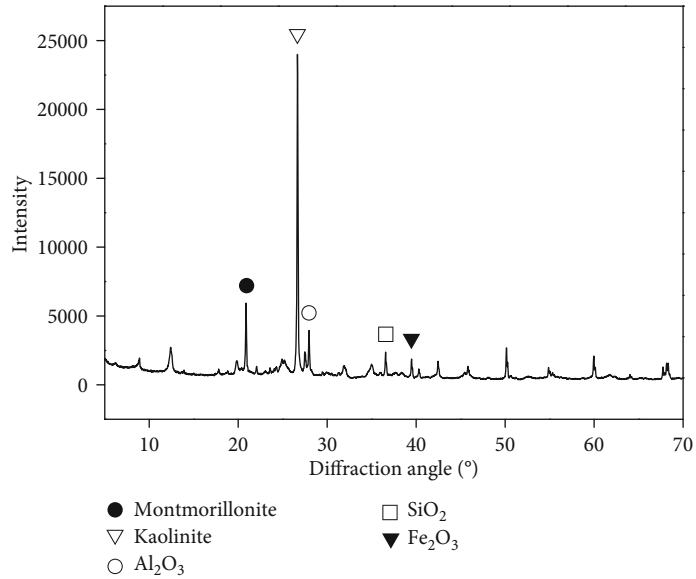

Figure 6: The XRD spectra of mudstone.

drying. The results of XRF and XRD are plotted in Table 1 and Figure 6. It is shown that a total of 8 components are identified in mudstone. The main products are silicon dioxide (SiO_2), aluminum oxide (Al_2O_3), and iron trioxide (Fe_2O_3), reaching 56.6%, 20.38%, and 12.32%, respectively. And sodium oxide (Na_2O) is the least of the ingredients. In terms of mineral composition, kaolinite is one of the largest minerals in mudstone. Hence, the strength of mudstone is low, compared with other rocks. The static mechanical properties of mudstone were also tested, which results are shown in Table 2. The compressive strength and tensile strength of mudstone specimens are 28.96 MPa and 2.16 MPa, respectively. Hence, the strength of mudstone is lower than that of other rocks from coal mine.

4. The Procedure of Tests

Three kinds of drive pressure were applied to saturated mudstone specimens in the SHPB tests. The impact pressure is 0.25 MPa, 0.30 MPa, and 0.40 MPa, respectively, used in the SHPB tests. An approximate uniform deformation of the rock specimen is a prerequisite of the valid dynamic uniaxial compression tests. Before the tests, the dynamic stresses on both ends of the specimen should be roughly identical. This can be checked by comparing the stress histories on both ends of the specimen during the dynamic tests. Figure 7 illustrates the dynamic stress balance on both ends of the specimen for the typical test. It is clear that in this test, the uniformity of the dynamic stress across the specimen has been achieved, and thus, the axial inertial effect has been reduced to a negligible level, verifying that the SHPB test

Table 2: Static mechanical properties of mudstone.

Density (g/cm^3)	Longitudinal wave velocity (m/s)	Compressive strength (MPa)	Tensile strength (MPa)	Poisson ratio
2.57	2176	28.96	2.16	0.23

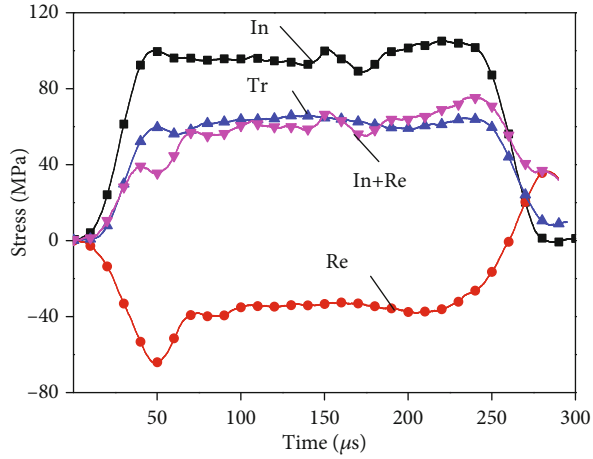

Figure 7: Strain balance check for a typical dynamic SHPB test with pulse shaping. In: incident wave; Re: reflected wave; Tr: transmitted wave.

conforms to the assumption of one-dimensional stress wave. With the dynamic stress balance, the stress-strain curves of rocks can be obtained under different drive pressures in

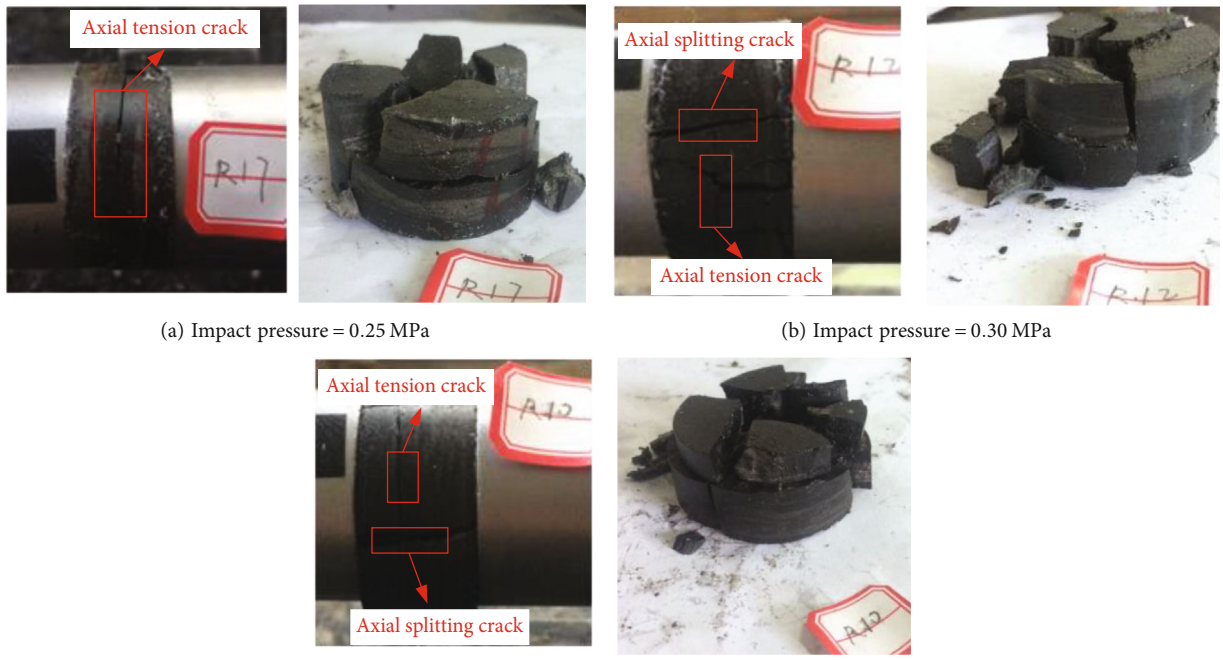

(a) Impact pressure = 0.25 MPa

(b) Impact pressure = 0.30 MPa

(c) Impact pressure = 0.40 MPa

Figure 8: Crack morphology of mudstone under different impact pressures.

the SHPB tests. After dynamic stress balance tests, a total of nine mudstone specimens were examined in the SHPB tests.

5. Results of SHPB Tests

5.1. Failure Mode of SHPB Tests. Figure 8 shows the failure models of saturated mudstone under different impact loadings. It is shown that as the impact pressure increases, both the length and aperture of cracks in the mudstone specimen increase. A main circular crack appears in the mudstone specimen when impact pressure is 0.25 MPa. The crack passes throughout the whole specimen, and the length and aperture further increase. There are other cracks along the axial of specimens, which length is small. The specimen is broken into large blocks, due to the circular and axial cracks. When the impact pressure reaches 0.30 MPa, the number of axial cracks increases and some cracks extend to circular cracks of specimens, which is shown in Figure 8(b). At the same time, many split cracks are found in the test, and the size of these split cracks is large. Under the 0.40 MPa impact pressure, the cracks along with the axial of the specimen further extend and finally pass throughout the whole specimen. And the aperture of circular and axial cracks increases. The specimen is broken into lots of smaller blocks.

5.2. Dynamic Stress-Strain Curve. The stress-strain curves of mudstone specimens under different impact loadings are shown in Figure 9. The dynamic stress-strain curve can be divided into four stages: (I) elastic stage, (II) crack expansion stage, (III) plastic deformation stage, and (IV) failure stage, seen in Figure 10. In the elastic stage, stress increases linearly with strain increasing. When reaching elastic limit stress, the microcrack will generate and expand. The plastic deformation stage will appear under the larger strain. In addition, the dynamic strength increases slowly in this stage. After yield stress, the stress dramatically decreases with an increase of strain. The specimen is finally destroyed. The failure model can be seen in Figure 8. Unlike the general relationships of stress and strain, there is no existence of the initial crack closure stage. The main reason is the fact that the high strain ratio leads the internal microcracks not to be closed in time and directly enter the elastic stage. It can be also inferred in Figure 9 that as the impact loading increases, the dynamic strength of the mudstone specimen increases.

5.3. Time-History Curve of Energy under Impact Loading. According to Equations (1), (2), (3), and (4), the incident energy, absorbed energy, transmitted energy, and reflected energy at any time can be obtained. The results are shown in Figure 11. It is illustrated that all the energy increases with an increase in time. The incident energy grows fastest. In addition, the intensity of incident energy is largest, the transmitted energy is second, and the reflected energy is smallest. The incident energy, absorbed energy, transmitted energy, and reflected energy at the final time are 103 J, 44.3 J, 42.2 J, and 16.5 J, respectively.

Combined with the crack morphology of the mudstone specimen shown in Figure 8, the energy absorption process of the mudstone specimen can be divided into three stages from the perspective of absorbed energy.

(1) *First Stage.* The absorbed energy increases during 0 to 50 μs. The mudstone specimen is at the elastic compressive deformation condition. The absorbed energy exists in the form of elastic energy.

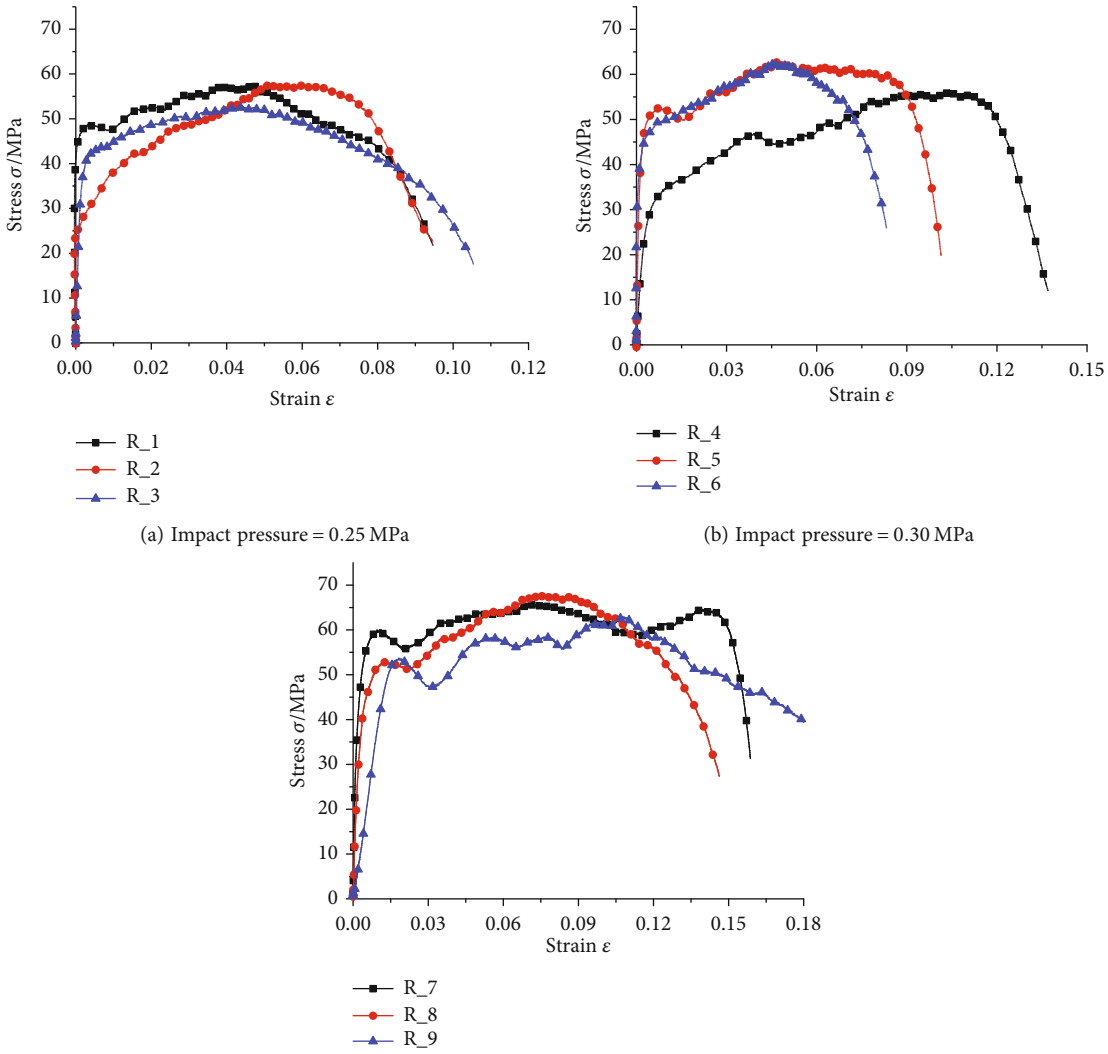

(a) Impact pressure = 0.25 MPa

(b) Impact pressure = 0.30 MPa

(c) Impact pressure = 0.40 MPa

Figure 9: Dynamic stress-strain curves of mudstone specimens under different impact loadings.

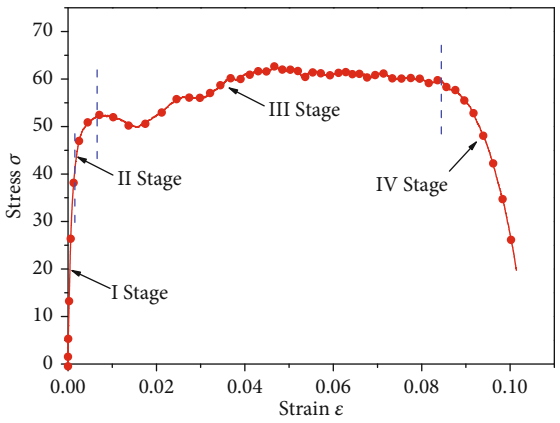

Figure 10: The typical stress-strain curve of mudstone under impact loading.

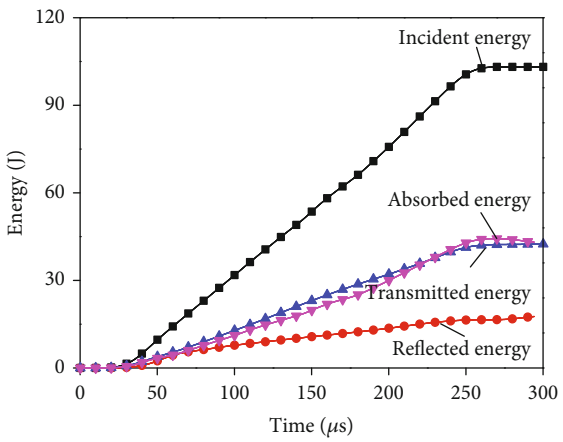

Figure 11: The time-history curve of energy under impact loading.

Table 3: Results of energy dissipation of mudstone under different impact loadings.

Number	Drive pressure (MPa)	Scale		Impedance (10^5 g/(cm^2 s))	Incident energy (J)	Transmitted energy (J)	Reflected energy (J)	Absorbed energy (J)	Energy dissipation density (J·cm^{-3})	Average strain ratio (s^{-1})	Dynamic compressive strength (MPa)	Peak strain
		Diameter (mm)	Length (mm)									
1	0.25	49.83	26.19	4.91	54.94	28.14	7.64	19.16	0.375	45	57.50	0.0099
2	0.25	49.95	26.11	5.59	52.53	26.19	12.93	13.44	0.262	47	56.65	0.0111
3	0.25	50.05	24.08	5.76	50.53	23.17	7.77	19.59	0.414	42	52.50	0.0117
4	0.3	49.64	25.56	4.40	60.37	30.01	9.88	20.48	0.414	53	55.32	0.0138
5	0.3	50.05	25.30	4.55	68.19	36.70	7.96	23.53	0.473	62	62.30	0.0103
6	0.3	49.88	26.76	5.16	61.80	33.7	7.10	21.00	0.404	60	62.13	0.0098
7	0.4	50.04	26.06	5.49	103.15	42.43	17.64	43.09	0.841	71	64.34	0.015
8	0.4	49.97	26.65	4.29	96.35	38.57	14.50	43.24	0.828	66	67.69	0.016
9	0.4	49.74	25.78	5.30	105.51	40.20	16.59	48.72	0.973	70	63.57	0.0212

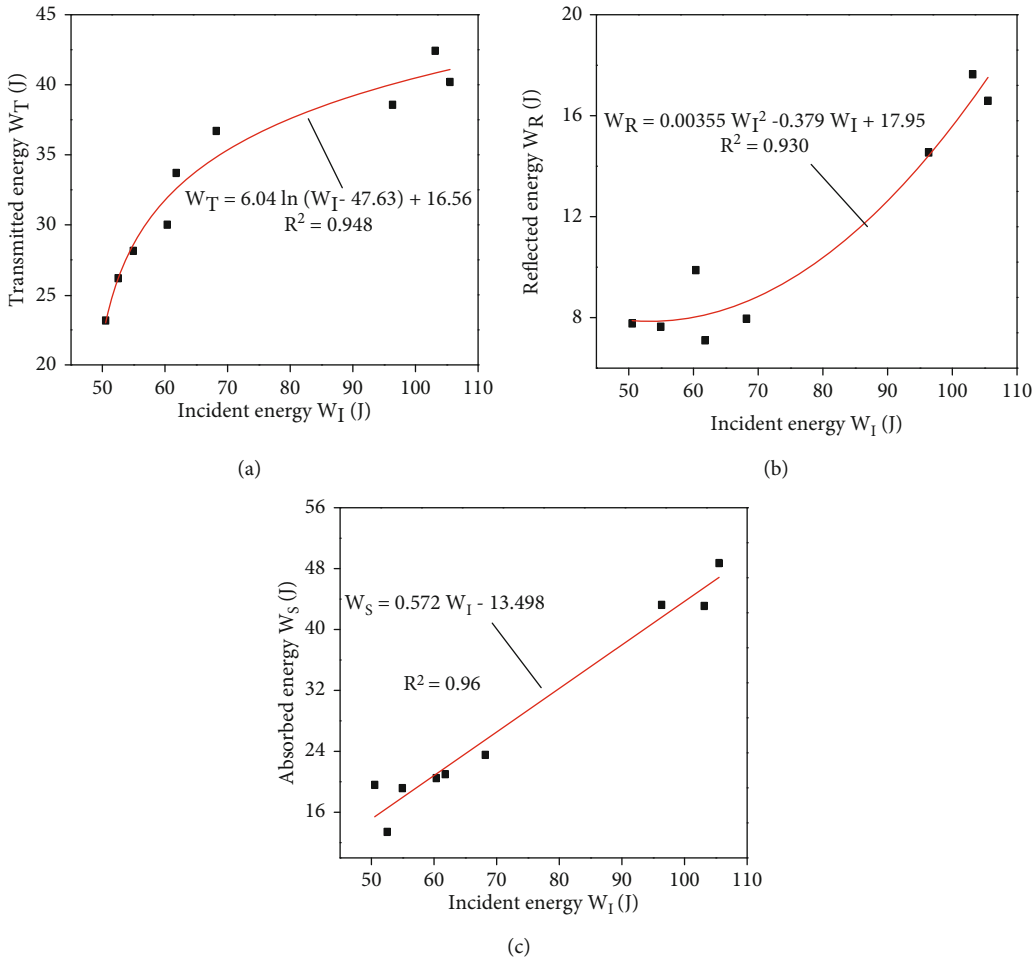

Figure 12: The relationships between incident energy and transmitted energy, reflected energy, and absorbed energy.

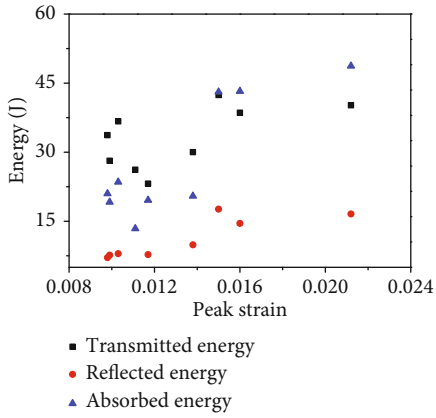

Figure 13: The relationship between energy and peak strain of mudstone specimens.

(2) *Second Stage*. This stage begins at 50 to 200 μs. The absorbed energy of the specimen is smaller than reflected energy in the earlier stage and then is larger than reflected energy after 80 μs. The main reason can be summarized as follows. The incident end surface of the specimen would generate reflected tensile stress and transfer reflected energy under incident stress waves, due to a mismatch between the wave impedance of the specimen and the bar. In this state, the absorbed energy is smaller than reflected energy. However, the contact surface will be smooth and the reflected energy will decrease under the incident bar continuously impacting. The circular crack will generate under the tensile stress wave. Subsequently, under the effect of high incident stress, the original microcracks inside the mudstone specimen extend, and a large number of new microcracks are generated at the same time, and the absorption energy continues to increase slowly.

(3) *Third Stage*. After 200 μs, the primary cracks in the mudstone specimen rapidly expand and new cracks will generate and pass through the specimen. And then, the axial cracks will be produced. Because there is no energy supplement, eventually, the energy tends to have a stable energy value.

5.4. The Relationships of Incident Energy and Transmitted Energy and Reflected Energy. The final incident energy,

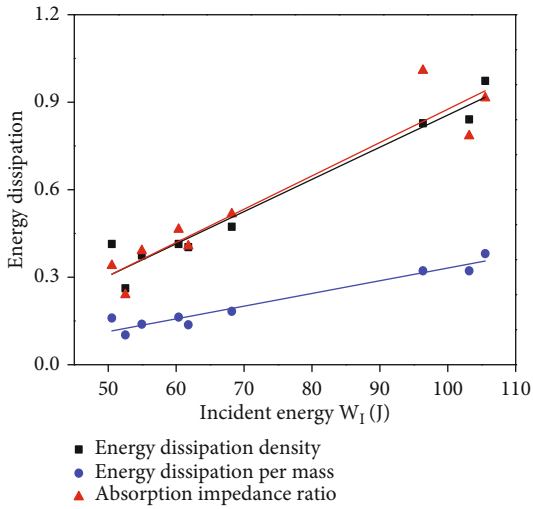

Figure 14: The relationship between energy indexes and incident energy.

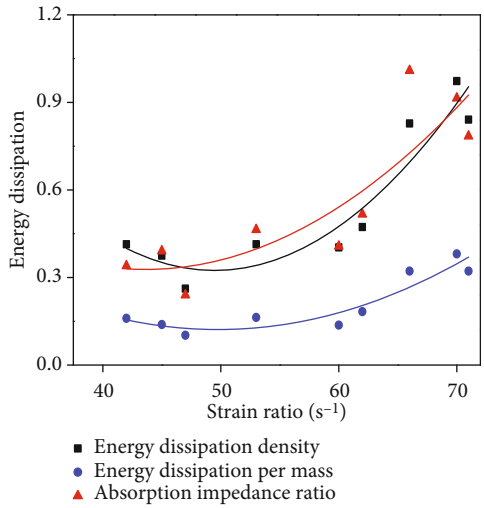

Figure 15: The relationship between energy indexes and average strain rate.

absorbed energy, transmitted energy, and reflected energy time can be obtained using Equations (1), (2), (3), and (4). The relationships of all the energy are shown in Table 3 and Figure 12.

It is indicated from Figure 12(a) that when the incident energy is smaller, the transmission energy increases with the increase of the incident energy. When the incident energy is larger, the transmission energy increment decreases with the increase of the incident energy. For the lower incidence energy, the mudstone specimen is in the elastic stage. With the increase of the incident energy, the mudstone is in the plastic stage, the inner primary microcrack growth and the new microcrack are produced, and the transmission of the transmission wave is weakened.

As shown in Figure 12(b), when the incident energy is small, the reflected energy increases slowly with the increase of the incident energy. When the incident energy exceeds 70 J, the reflected energy increases faster; the transmission energy tends to be stable. It is known from Figure 12(c) that the absorbed energy of the specimen increases linearly with the increase of the incident energy, and the absorbed energy is less than 0.5 times the incident energy. It is indicated that more than half of the energy of the impact incident can be dissipated in the form of an elastic wave of the bars.

5.5. The Relationships of Absorbed Energy, Transmitted Energy, and Reflected Energy between Peak Strains. The energy transmission is related to the deformation of mudstone specimens. Hence, the relationships of absorbed energy, transmitted energy, and reflected energy between peak strains are plotted in Figure 13. It is shown that as the peak strain increases, the absorbed energy, transmitted energy, and reflected energy increase. However, the increases are different among the absorbed energy, transmitted energy, and reflected energy, and there is some volatility during the increases. And the largest growth in energy is absorbed energy. The reason is that the deformation increments of mudstone specimens need more energy.

5.6. EDV, EDM, and AIER. Three energy dissipation indexes were introduced to represent the energy absorption characteristics of mudstone specimens. One is absorbed energy per volume (EDV) w_d, which is defined as follows:

$$w_d = \frac{W_s}{V_s}, \tag{5}$$

where V_s is the volume of rock specimens. Considering the effect of mass, the second index is defined as absorbed energy per mass (EDM) m_d. The formula is

$$m_d = \frac{W_s}{M_s}, \tag{6}$$

where M_s is the volume of rock specimens. The impedance of mudstone specimens is closely related to the energy transfer efficiency. Hence, introducing the impedance, the third index is defined as

$$Z_w = \frac{W_s}{\rho C_s}, \tag{7}$$

where Z_w is absorption impedance energy ratio (AIER).

The relationships between three indexes and incident energy are plotted in Figure 14. Also plotted in Figure 14 are the best-fitted curves for the data using the linear function, implying that the linear relationship between the three indexes and incident energy fits the flow data very well for most of the data points. Comparing with the fitting coefficient (R^2) of three indexes (w_d,m_d ,Z_w), the best fitting is the relationship of AIER and incident energy, and this fitting coefficient is 0.936. It is indicated that AIER Z_w, which takes into account the wave impedance property, can more effectively reflect the energy

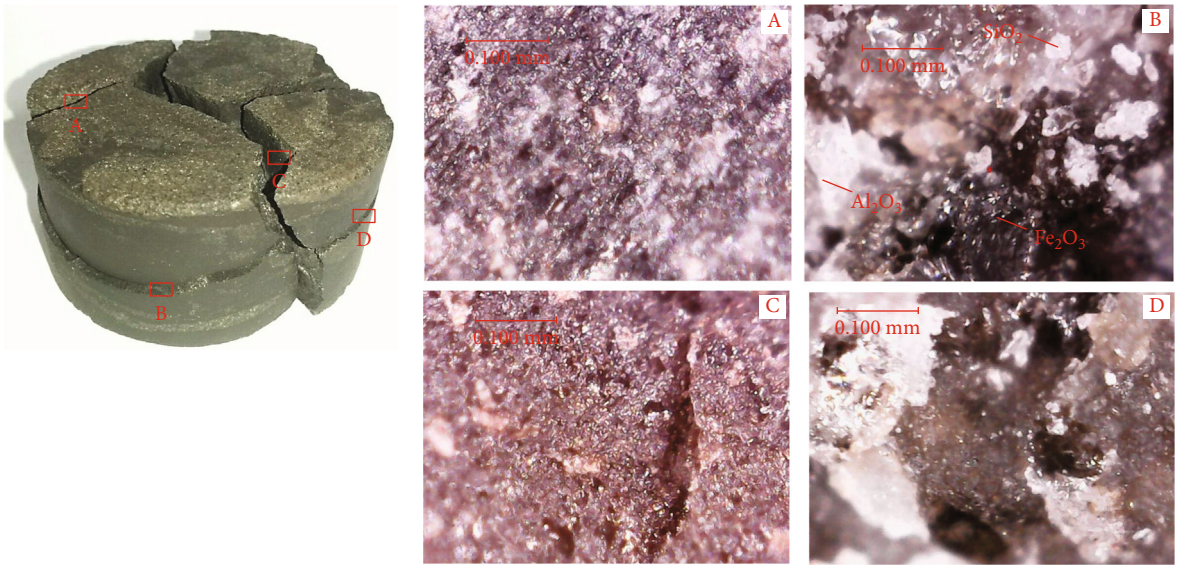

(a) (b)

Figure 16: The crack characteristic of mudstone under impact loading: (a) axial splitting and axial tension crack locations numbered as A, B, C, and D, respectively; (b) crack micrograph under electron digital microscope (× 1000).

absorption of mudstone specimens:

$$\begin{aligned} w_d &= 0.011W_I - 0.247\ (R^2 = 0.848), \\ m_d &= 0.004W_I - 0.104\ (R^2 = 0.836), \\ Z_w &= 0.114W_I - 0.267\ (R^2 = 0.936). \end{aligned} \tag{8}$$

5.7. The Effect of Energy Dissipation on Strain Ratio. The relationships between EDV, EDM, and AIER and average strain ratio ε are plotted in Figure 15. The quadratic function can be used to describe the relationships between three indexes and average strain ratio. When the strain rate is low, the absorbed energy causes mudstone with many internal defects. When the strain rate increases, the increase of the absorbed energy of the specimen will cause the new microcracks to generate in the mudstone specimens. When the strain rate is high, the original microcracks in the mudstone expand and pass through the mudstone specimens. And the specimen is crushed and broken finally:

$$\begin{aligned} w_d &= 0.0041\dot{\varepsilon}^2 - 0.134\dot{\varepsilon} + 3.65\ (R^2 = 0.855), \\ m_d &= 0.0005\dot{\varepsilon}^2 - 0.055\dot{\varepsilon} + 1.49\ (R^2 = 0.827), \\ Z_d &= 0.0008\dot{\varepsilon}^2 - 0.069\dot{\varepsilon} + 1.85\ (R^2 = 0.678). \end{aligned} \tag{9}$$

6. Discussion

In order to understand the fact that chemical components and microstructures lead to the macrocrack phenomenon of saturated mudstone specimens under impact loading, the crack morphology was observed using the BIST digital microscope. Two axial and two circular crack surfaces of the typical broken mudstone specimen were selected to examine and numbered A, B, C, and D. Obvious roughness characteristics are easily observed in two kinds of crack surfaces, shown in Figure 16. But the roughness of the circular surface is greater than that of the axial surface. The main reason is that the axial crack surface (A and C) is caused by shear slip and wearing, and the stress wave tension results in the circular crack surface (B and D) under impact loadings. In addition, from Table 1, SiO_2 is one of the main components in mudstone, followed by Al_2O_3 and Fe_2O_3. Their grain distribution is shown in Figure 8(b). And it is concluded that both the axial and circular cracks mainly occur in the grain interface, because it is a weak area in rock.

Combining the one-dimensional stress wave propagation theory and physics component of mudstone, the reason for the generation of circular and axial cracks in specimens under impact loadings is as follows. Mudstone is characterized by viscoplasticity, softening, and low structural strength. The microstructure of mudstone will change when suffering from impact loading. The microparticle of mudstone is redistributed along with forced direction from the free condition. In the SHPB test, the incident stress reflects and transmits to tensile stress when the stress transmits to the contact surface between transmitted bar and specimen. The tensile stress causes the circular crack due to the low tensile strength of the mudstone in the coal mine specimen. Meanwhile, under the continuous action of the incident compression stress wave, the specimen is subjected to axial splitting failure.

Drill-blasting is the main way for roadway tunneling in coal mine. Generally, the cylindrical charge is used for blasting holes, and the surrounding rock is in a one-dimensional compression situation. In addition, the effect of blasting energy on blasting fragmentation and damage of reserved rock is important for drill-blasting, especially for mudstone

with low strength. Hence, the energy dissipation law and failure mechanism of mudstone under impact loading provide strong support for mining blasting safety.

7. Conclusions

In this paper, the dynamic mechanical properties of mudstone in coal mine are investigated using the energy characterization method, and their quantitative relation formula is also developed. Therefore, a series of compression experiments of mudstone under different impact loadings are conducted to study the mudstone dynamic behaviors, crack properties, and energy dissipation law using the diameter 50 mm SHPB test device. The above analyses support the following conclusions:

(1) The axial splitting failure and circular tensile failure are observed in mudstone specimens during the test. It is because the tensile stress would be generated and easily cause circular tensile failure for low strength rock due to the reflection and transmission effect of the transmitted bar. Additionally, continuous compressive stress leads to axial splitting failure

(2) It is shown from the crack micromorphology that the failure surface appears in the mudstone grain interface, and the roughness of the tensile failure surface is greater than that of the splitting surface

(3) The absorbed energy, transmitted energy, and reflected energy of mudstone increase with the increase of incident energy, showing linear, logarithmic, and quadratic functions, respectively

(4) Comparing the three energy dissipation indexes (EDV, EDM, and AIER) with incident energy, the AIER is more a reflection of the energy dissipation of mudstone. The quadratic function relationship between three energy dissipation indexes and average strain rate of mudstone specimen shows a strong dependence of strain rate

Data Availability

The datasets used or analyzed during the current study are available from the corresponding author on reasonable request.

Conflicts of Interest

The authors declare no conflicts of interest.

Authors' Contributions

Both Liangjie Guo and Yongyu Wang proposed the research. Liangjie Guo contributed to the SHPB tests and writing the manuscript; Yongyu Wang contributed to the specimen preparation and revision of the manuscript.

Acknowledgments

This research was financially supported by the National Natural Science Foundation of China (51904281). This support is gratefully acknowledged.

References

[1] F. R. Ma and P. L. Li, "Experiment analysis on the mechanical properties of the horizontally stratified mudstone," *Advanced Materials Research*, vol. 1065-1069, pp. 31–34, 2014.

[2] L. Zhang, X. Mao, and R. Liu, "The impact of loading rate on mechanical property of mudstone at high temperatures," *Electronic Journal of Geotechnical Engineering*, vol. 19, pp. 3019–3027, 2014.

[3] A. G. Corkum and C. D. Martin, "The mechanical behaviour of weak mudstone (Opalinus clay) at low stresses," *International Journal of Rock Mechanics and Mining Sciences*, vol. 44, no. 2, pp. 196–209, 2007.

[4] A. Taheri and K. Tani, "Use of down-hole triaxial apparatus to estimate the mechanical properties of heterogeneous mudstone," *International Journal of Rock Mechanics and Mining Sciences*, vol. 45, no. 8, pp. 1390–1402, 2008.

[5] L. A. N. R. Douma, M. I. W. Primarini, M. E. Houben, and A. Barnhoorn, "The validity of generic trends on multiple scales in rock-physical and rock- mechanical properties of the Whitby Mudstone, United Kingdom," *Marine and Petroleum Geology*, vol. 84, pp. 135–147, 2017.

[6] X. L. Lei, O. Nishizawa, K. Kusunose, A. Cho, T. Satoh, and O. Nishizawa, "Compressive failure of mudstone samples containing quartz veins using rapid AE monitoring: the role of asperities," *Tectonophysics*, vol. 328, no. 3–4, pp. 329–340, 2000.

[7] J. Luo and L. Wang, "High-temperature mechanical properties of mudstone in the process of underground coal gasification," *Rock Mechanics and Rock Engineering*, vol. 44, no. 6, pp. 749–754, 2011.

[8] P. Bhattarai, H. Marui, B. Tiwari, N. Watanabe, G. R. Tuladhar, and K. Aoyama, "Influence of weathering on physical and mechanical properties of mudstone," *Physical Review B*, vol. 80, no. 23, pp. 308–310, 2006.

[9] X. Huang, J. Liu, C. Yang, and J. W. Chen, "Experimental investigation of Daqing Oilfield mudstone's creep characteristic under different water contents," *Journal Central University of Technology*, vol. 15, no. s1, pp. 471–474, 2008.

[10] L. Zhang, X. Mao, R. Liu, X. Guo, and D. Ma, "The mechanical properties of mudstone at high temperatures: an experimental study," *Rock Mechanics and Rock Engineering*, vol. 47, no. 4, pp. 1479–1484, 2014.

[11] Y. Lu, L. Wang, X. Sun, and J. Wang, "Experimental study of the influence of water and temperature on the mechanical behavior of mudstone and sandstone," *Bulletin of Engineering Geology and the Environment*, vol. 76, no. 2, pp. 1–16, 2016.

[12] Z. Zhou, X. Li, Z. Ye, and K. Liu, "Obtaining constitutive relationship for rate-dependent rock in SHPB tests," *Rock Mechanics and Rock Engineering*, vol. 43, no. 6, pp. 697–706, 2010.

[13] F. Dai, S. Huang, K. Xia, and Z. Tan, "Some fundamental issues in dynamic compression and tension tests of rocks using split Hopkinson pressure bar," *Rock Mechanics and Rock Engineering*, vol. 43, no. 6, pp. 657–666, 2010.

[14] C. Zou and L. N. Y. Wong, "Size and geometry effects on the mechanical properties of Carrara marble under dynamic loadings," *Rock Mechanics and Rock Engineering*, vol. 49, no. 5, pp. 1695–1708, 2016.

[15] Y. Chen, A. Lu, X. Mao, M. Li, and L. Zhang, "Nonlinear dynamics mechanism of rock burst induced by the instability of the layer-crack plate structure in the coal wall in deep coal mining," *Shock and Vibration*, vol. 2017, no. 10, Article ID 4051967, 2017.

[16] S. Demirdag, K. Tufekci, R. Kayacan, H. Yavuz, and R. Altindag, "Dynamic mechanical behavior of some carbonate rocks," *International Journal of Rock Mechanics and Mining Sciences*, vol. 47, no. 2, pp. 307–312, 2010.

[17] Y. Hao and H. Hao, "Numerical investigation of the dynamic compressive behaviour of rock materials at high strain rate," *Rock Mechanics and Rock Engineering*, vol. 46, no. 2, pp. 373–388, 2013.

[18] R. Shan, Y. Jiang, and B. Li, "Obtaining dynamic complete stress-strain curves for rock using the split Hopkinson pressure bar technique," *International Journal of Rock Mechanics and Mining Sciences*, vol. 37, no. 6, pp. 983–992, 2000.

[19] Z. M. Chen, Y. X. Li, and Z. Zhang, "Experimental study of dynamic mechanical properties of granite," *Applied Mechanics and Materials*, vol. 858, pp. 86–90, 2016.

[20] J. Z. Liu, J. Y. Xu, X. C. Lv, D. H. Zhao, and B. L. Leng, "Experimental study on dynamic mechanical properties of amphibolites, sericite-quartz schist and sandstone under impact loadings," *International Journal of Nonlinear Sciences and Numerical Simulation*, vol. 13, no. 2, pp. 209–217, 2012.

[21] A. Mardoukhi, Y. Mardoukhi, M. Hokka, and V. T. Kuokkala, "Effects of heat shock on the dynamic tensile behavior of granitic rocks," *Rock Mechanics and Rock Engineering*, vol. 50, no. 5, pp. 1171–1182, 2017.

[22] D. F. Du HB, Y. Xu, Y. Liu, and H. N. Xu, "Numerical investigation on the dynamic strength and failure behavior of rocks under hydrostatic confinement in SHPB testing," *International Journal of Rock Mechanics and Mining Sciences*, vol. 108, pp. 43–57, 2018.

[23] L. F. Fan, Z. J. Wu, Z. Wan, and J. W. Gao, "Experimental investigation of thermal effects on dynamic behavior of granite," *Applied Thermal Engineering*, vol. 125, pp. 94–103, 2017.

[24] X. Li, F. Gong, J. Zhao, K. Gao, and T. Yin, "Test study of impact failure of rock subjected to one-dimensional coupled static and dynamic loads," *Chinese Journal of Rock Mechanics and Engineering*, vol. 29, no. 2, pp. 251–260, 2010.

[25] G. M. Zhao, W. W. Ma, and X. R. Meng, "Damage models and energy characteristics of rock-like materials under dynamic load," *Rock and Soil Mechanics*, vol. 36, no. 12, pp. 3598–3605, 2015.

[26] X. Li, H. Li, K. Liu et al., "Dynamic properties and fracture characteristics of rocks subject to impact loading," *Chinese Journal of Rock Mechanics and Engineering*, vol. 36, no. 10, pp. 2393–2405, 2017.

[27] C. Li, Y. Xu, P. Chen, H. Li, and P. Lou, "Dynamic mechanical properties and fragment fractal characteristics of fractured coal–rock-like combined bodies in split Hopkinson pressure bar tests," *Natural Resources Research*, vol. 29, no. 5, pp. 3179–3195, 2020.

[28] T. Chakraborty, S. Mishra, J. Loukus, B. Halonen, and B. Bekkala, "Characterization of three Himalayan rocks using a split Hopkinson pressure bar," *International Journal of Rock Mechanics and Mining Sciences*, vol. 85, pp. 112–118, 2016.

[29] Z. Yan, F. Dai, Y. Liu, A. Li, and H. du, "Numerical assessment of the rate-dependent cracking behaviours of single- flawed rocks in split Hopkinson pressure bar tests," *Engineering Fracture Mechanics*, vol. 247, p. 107656, 2021.

[30] H. Wu, B. Dai, L. Cheng, R. Lu, G. Zhao, and W. Liang, "Experimental study of dynamic mechanical response and energy dissipation of rock having a circular opening under impact loading," *Mining, Metallurgy & Exploration*, vol. 38, no. 2, pp. 1111–1124, 2021.

[31] Y. Luo, G. Wang, X. Li et al., "Analysis of energy dissipation and crack evolution law of sandstone under impact load," *International Journal of Rock Mechanics and Mining Sciences*, vol. 132, article 104359, 2020.

[32] C. Zhu, M. C. He, X. H. Zhang, Z. G. Tao, Q. Yin, and L. F. Li, "Nonlinear mechanical model of constant resistance and large deformation bolt and influence parameters analysis of constant resistance behavior," *Rock and Soil Mechanics*, vol. 42, no. 7, pp. 1911–1924, 2021.

[33] C. Zhu, M. C. He, B. Jiang, X. Z. Qin, Q. Yin, and Y. Zhou, "Numerical investigation on the fatigue failure characteristics of water-bearing sandstone under cyclic loading," *Journal of Mountain Science*, vol. 18, no. 12, pp. 3348–3365, 2021.

[34] G. Li, Y. Hu, and T. Sm, "Analysis of deformation control mechanism of prestressed anchor on jointed soft rock in large cross-section tunnel," *Bulletin of Engineering Geology and the Environment*, vol. 80, no. 12, pp. 9089–9103, 2021.

[35] M. Z. Gao, J. Xie, Y. N. Gao et al., "Mechanical behavior of coal under different mining rates: a case study from laboratory experiments to field testing," *International Journal of Mining Science and Technology*, vol. 31, no. 5, pp. 825–841, 2021.

[36] M. Z. Gao, H. C. Hao, S. N. Xue et al., "Discing behavior and mechanism of cores extracted from Songke-2 well at depths below 4,500 m," *International Journal of Rock Mechanics and Mining Sciences*, vol. 149, article 104976, 2022.

[37] C. Cao, W. Zhang, J. Chen, B. Shan, S. Song, and J. Zhan, "Quantitative estimation of debris flow source materials by integrating multi- source data: a case study," *Engineering Geology*, vol. 291, article 106222, 2021.

[38] Z. Dou, S. X. Tang, X. Y. Zhang et al., "Influence of shear displacement on fluid flow and solute transport in a 3D rough fracture," *Lithosphere*, vol. 2021, no. Special 4, 2021.

[39] F. Xiong, Q. Jiang, and C. Xu, "Fast equivalent micro-scale pipe network representation of rock fractures obtained by computed tomography for fluid flow simulations," *Rock Mechanics and Rock Engineering*, vol. 54, no. 2, pp. 937–953, 2021.

[40] F. Xiong, H. Sun, Z. Ye, and Q. Zhang, "Heat extraction analysis for nonlinear heat flow in fractured geothermal reservoirs," *Computers and Geotechnics*, vol. 144, p. 104641, 2022.

[41] B. Xie, X. Wang, and P. Lv, "Dynamic properties of bedding coal and rock and the SHPB testing for its impact damage," *Journal of Vibration and Shock*, vol. 36, no. 21, pp. 117–124, 2017.

Hindawi
Geofluids
Volume 2022, Article ID 3889950, 9 pages
https://doi.org/10.1155/2022/3889950

Research Article

Influence of Water-Resisting Layer Thickness on Fracture Evolution in Karst Tunnel and Control Measures

Chun Liu and Congying Jiang

School of Civil Engineering and Architecture, Zhejiang Guangsha Vocational and Technical University of Construction, Dongyang 322100, China

Correspondence should be addressed to Congying Jiang; jiangcy@zjgsdx.edu.cn

Received 13 January 2022; Revised 6 February 2022; Accepted 11 February 2022; Published 7 March 2022

Academic Editor: Feng Xiong

In this paper, a series of studies are carried out on the hidden karst encountered in the excavation of Baziling tunnel. In this paper, the safe thickness of the water-resisting layer in a hidden karst cave and tunnel is studied by means of engineering geological investigation, numerical simulation, and neural network. The numerical calculation model is established through the geological survey. Innovate to use BP neural network and differentiation algorithm to inverse the rock mechanical parameters. By analyzing the influence of different thicknesses of the water-resisting layer on the deformation and failure of surrounding rock, the final thickness of the water-resisting layer is obtained. At the same time, the influence of water pressure on the thickness of the water-resisting layer is studied, and the treatment scheme under different water pressure is finally determined.

1. Introduction

Karst water inrush does great harm to tunnel construction. The development of the karst cave causes the instability of tunnel surrounding rock and the disaster of water and mud inrush, which is difficult to control. In the prediction of karst water inflow, many scholars at home and abroad have conducted extensive research, but there is little research on the safe thickness in front of the tunnel [1]. Li et al. [2] proposed an accurate and feasible systematic evaluation method for water inrush risk of karst tunnel. The confidence criterion is used to judge the risk level of water inrush. The calculation results of this method are compared with an example. The comparison results show that the evaluation results of this method are basically consistent with the field observation results. Li et al. [3] established a water inrush risk assessment software system by comprehensively considering 8 risk factors, such as groundwater level, unfavorable geology, formation lithology, terrain, formation dip angle, excavation, advanced geological prediction, and monitoring. Wang et al. [4] combined the weighting method with the normal cloud model and proposed a new water inrush evaluation method. Specifically, the evaluation index system is established, and each index is quantitatively divided into four levels. A comprehensive weighting algorithm is proposed, which combines the analytic hierarchy process, entropy method, and the statistical method to reasonably allocate index weight. Lin et al. [5] combined variable weight theory with cloud model theory to construct a calculation model for karst tunnel construction risk assessment.

Based on the extension evaluation method, Zhang et al. [6] proposed an improved water inrush risk evaluation system for carbonate karst tunnel. The system considers karst geological conditions and selects 9 main factors affecting tunnel water inrush as evaluation indexes. According to the value of the evaluation index or expert judgment, the evaluation index is quantitatively divided into four risk levels. Wang et al. [7] proposed a risk assessment method for water inrush and water inrush interval of karst tunnel. On this basis, the concept and calculation form of the risk assessment models are proposed, and the risk environment, construction factors, and feedback information are analyzed. Zhao et al. [8] classified the water and mud gushing of railway tunnels according to a large number of examples of

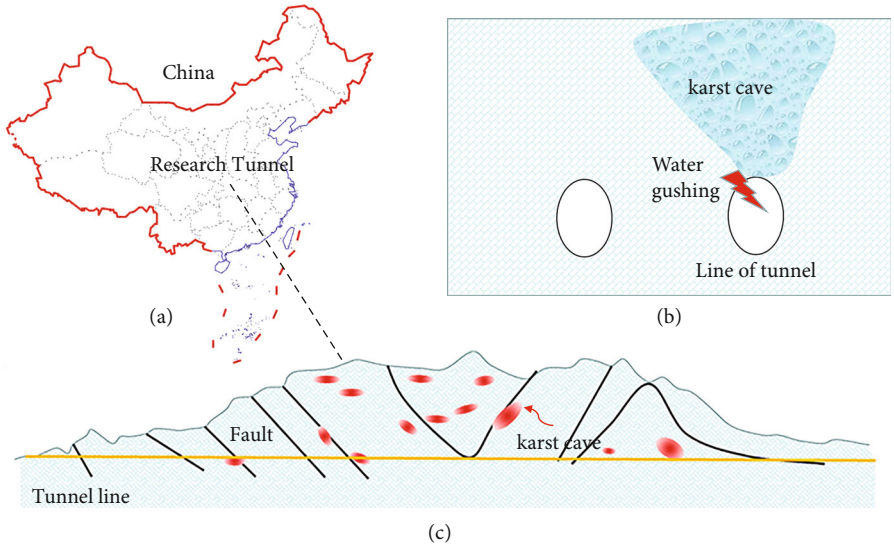

Figure 1: Overview of research target tunnel.

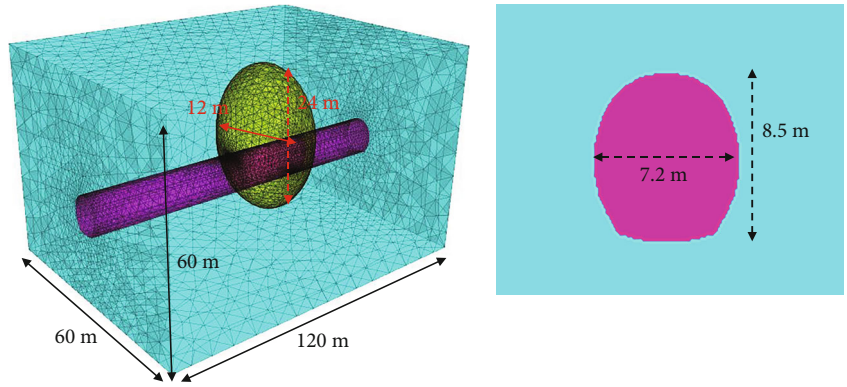

(a) Numerical calculation model (b) Tunnel excavation profile

Figure 2: Numerical calculation model.

water and mud gushing of the railway tunnels, combined with the surrounding rock conditions and meteorological factors of tunnel excavation. Combined with the macro and micro mechanisms, the causes of water inrush and mud inrush are summarized, and the targeted treatment methods are put forward. The treatment methods include selecting the advanced geological prediction method according to the risk degree of different sections of the tunnel, determining the prediction items, and selecting the appropriate methods, namely, drainage guidance method, blockage guidance method, or drainage blockage method. Li et al. [9] analyzed the transformation mechanism of water inrush and seepage caused by excavation disturbance and analyzed the potential water-bearing area of the tunnel by using the electromagnetic geophysical exploration method. The constitutive model of rock mass and grouting parameters is considered in the numerical simulation. The initiation and propagation laws of tunnel cracks under different curtain grouting parameters are put forward. The characteristics of seepage and water inrush caused by tunnel excavation are described. It is considered that the seepage characteristics of tunnel can be divided into incubation stage, sudden stage, and stable stage.

Liu et al. [10] selected a specific project and introduced the geological conditions, water inrush, mud inrush disasters, and subsequent prevention and control countermeasures. Then, the original grouting design and process as well as 25 grouting cycles and field operation of excavation are introduced to evaluate the grouting effect and suggestions for future grouting work. Based on the field investigation, the values of main grouting parameters are put forward. The grouting thickness is 5~8 m, the grouting length is 15~18 m (3~3.6 times the thickness), and the grouting amount per meter is 34.2 m^3. Wang et al. [11] proposed a new method of real-time monitoring and fusion early warning of tunnel water inrush. Zhu et al. [12] proposed a fuzzy comprehensive evaluation method for water inrush risk of tunnel water rich fault based on grey theory. The grey fuzzy method consists of two parts: one is the single factor evaluation matrix established by the evaluation index and the risk

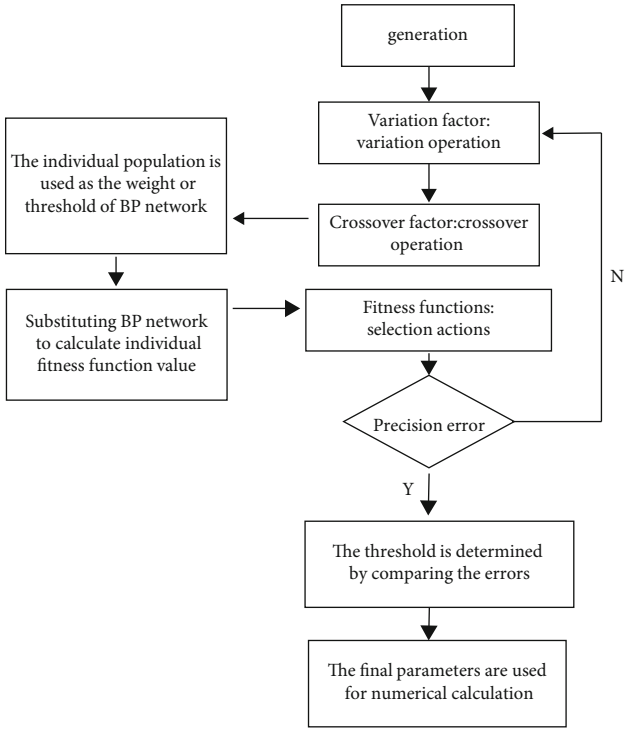

Figure 3: Algorithm flowchart.

grade membership function, and the other is to determine the weight of each evaluation index by using the norm grey correlation degree. From the aspects of formation lithology, geological structure, and hydrogeological conditions, five influencing factors such as fault dip angle, groundwater level, RMR, permeability, and formation dip angle are selected as evaluation indexes. Huang et al. [13] proposed a numerical method to study the influence of fractures on fluid flow, considering different types of discontinuities. The conceptual model of fractured water inrush focusing on the evolution of fracture connectivity is established, the seepage process of fluid in fractured rock mass is studied, and then, the water inrush mechanism is studied.

In tunnel engineering in karst area, when there are large karst caves in tunnel excavation, the checking calculation of tunnel safety thickness will be a key problem in engineering practice. The selection of its safe thickness is directly related to the project cost and project quality. Selecting an appropriate safe thickness will produce huge economic and social benefits for the whole project. However, due to many factors involved, there is no reliable analysis method for checking the safe thickness of the tunnel. In this paper, the influence of different isolation safety thickness on seepage is discussed by using the methods of engineering geological investigation, theoretical analysis, and numerical calculation. The reasonable safe thickness is determined, and the relevant advance grouting scheme is designed.

2. Engineering Geological Characteristics

2.1. Project Overview. Baziling tunnel of Yichang Wanzhou railway is located in Yesanguan Town, Changyang County, Yichang City, Hubei Province, China, with a design speed of 160 km/h, as shown in Figure 1. The total length of the tunnel is 5867 m, one side uphill, and the maximum buried depth is 695 m. The tunnel is located at the junction of the Yangtze River system, with dalupo syncline, jianshanling anticline, and chuanxinping syncline developed. The tunnel consists of Silurian, Devonian, Triassic, and Quaternary. The length of limestone stratum is 4464 m. The length of Silurian and Devonian fragments is 1550 m. Tunnel layer, two underground river systems around the tunnel. The area where most strata of the tunnel pass through is densely covered with karst and underground rivers are developed. The normal water inflow of the tunnel is 73000 m^3/d. The maximum water inflow is 302000 m^3/d.

2.2. Typical Karst Cave Characteristics. The revealed karst direction of DK 0+104 is NE80°, and the karst cavity gradually shrinks to both ends to form a fault structure. It is developed vertically, almost upright, and large-scale eroded stalactite suspension is developed upward and downward, with a small amount of dripping water. DK108+835.5 karst cave is 3 m long, 3.5 m wide, and 6 m high along the strike, filled with mud and stone, and collapsed during excavation. DK108+831 karst cave is 4.5 m wide, which is limestone, with relatively developed joint fissures, nearly horizontal karst cavity, vertical fissures, and relatively broken. The width of DK108+955 karst cavity is 6.2 m, and the karst cave is 4.5 m away from the top excavation contour line. The occurrence of some rocks in the karst cave is nearly horizontal, with vertical cracks and relatively broken. Dk108+698 dissolution fissure, 3 m in the transverse direction, 1.5 m in the longitudinal direction, and about 2.0 m high, gradually decreases upward, and the filling of the karst cave collapses. The filling is soil mixed with stone without water. Dk108 +683 crevice karst cave runs through the tunnel face, with a width of about 2.0 m. The filler is mud mixed with stone. The vertical joints around the karst cave are developed, with a joint spacing of about 2 m. The surrounding rock at the tunnel arch is relatively broken. DK109+039 reveals a fissured karst cave, which runs through more than 80% of the tunnel face from the left side of the line, is 1.0 m wide, soil mixed with stone, there is no water, and the fissures in the surrounding rock around the karst cave are developed. DK109+089 karst is about 1 m wide and 2.5 m deep. It runs along the tunnel line and is about 3 m long. The filling is clay with slight water seepage. The surrounding rock around the karst cave is broken, and there is a huge dangerous rock at the arch.

3. Numerical Calculation Model

3.1. Establish Numerical Calculation Model. The discrete element numerical calculation software is used for modeling, and the influence of model boundary is fully considered [14–16]. The model size is 60 m ∗ 60 m ∗ 120 m. The tunnel excavation contour span is 7.2 m, the height is 8.5 m, and the thickness of the secondary lining is 50 cm, as shown in Figure 2. The karst cave is simplified as an ellipsoid, with a long axis of 24 m and a short axis of 14 m. The karst cave

Table 1: Mechanical parameters of optimized rock mass.

Limestone rock parameters	Density (kg/m^3)	E (GPa)	Poisson's ratio	Cohesion (MPa)	Internal friction angle (°)	Tensile strength (MPa)
	2500	10	0.25	12	35	11
Limestone joint parameters	Normal stiffness (GPa)	Tangential stiffness (GPa)	Internal friction angle (°)			
	10	10	30			

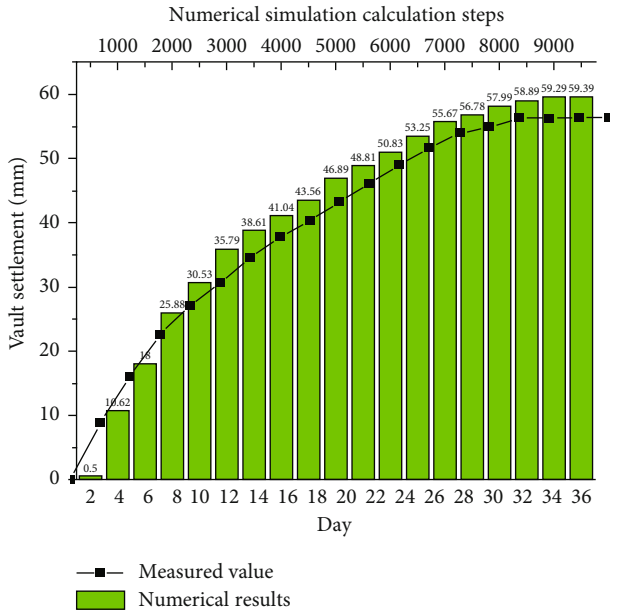

Figure 4: Comparison between numerical simulation and measured settlement of tunnel vault.

is located in front of the tunnel. The buried depth of the simulated tunnel is 600 m; the vertical stress only considers the unit weight of rock mass. The geological survey report shows that the study area lateral pressure coefficient is 1.4 under the influence of fault. The x-direction boundary, y-direction boundary, and z-direction boundary of the model are constrained by normal displacement. The water pressure inside the karst cavity acts directly on the interface.

3.2. Constitutive Model. The block element adopts a unified strength constitutive model, which considers the different effects of all stress components acting on the double shear element on the yield or failure of materials [17–21]. It is suitable for all kinds of tensile and compressive materials and is a collection of a series of linear strength criteria. The expression of principal stress of unified strength theory is the most widely used, which can directly reflect the influence of each principal stress on material strength. The expression of the principal stress form of unified strength theory is

$$\text{if } \sigma_2 \le \frac{\sigma_1 + \alpha\sigma_3}{1+\alpha}, \quad F = \sigma_1 - \frac{\alpha}{1+\mathrm{b}}(b\sigma_2 + \sigma_3) = f_t, \tag{1}$$

$$\text{if } \sigma_2 \ge \frac{\sigma_1 + \alpha\sigma_3}{1+\alpha}, \quad F' = \frac{1}{1+\mathrm{b}}(\sigma_1 + b\sigma_2) - \alpha\sigma_3 = f_t, \tag{2}$$

$$\alpha = \frac{(1-\sin\varphi)}{(1+\sin\varphi)}, \tag{3}$$

$$f_t = \frac{2c\cos\varphi}{(1+\sin\varphi)}. \tag{4}$$

In the formula, $\sigma_1, \sigma_2, \sigma_3$ represents the maximum principal stress, the intermediate principal stress, and the minimum principal stress, respectively; f_t is uniaxial tensile strength; α is tension compression strength ratio; b is the unified strength theoretical parameter, and $0 \le b \le 1$. c is cohesion and φ is internal friction angle. Coulomb sliding joint model can fully represent the joint shear failure, tension crack failure, compression shear failure, and tension shear failure in rock mass [22, 23]. In the elastic deformation stage of joints, the stress of joints follows

$$T_{\max} = -TA_c, \tag{5}$$

$$F^s_{\max} = cA_c + F^n \tan\varphi. \tag{6}$$

In the formula, F^n is the normal force; T is tensile strength; c is cohesion; φ is the internal friction angle.

The joint seepage in numerical calculation obeys the law of legislation. The expression is shown in

$$q = \frac{ge^3}{12v}J. \tag{7}$$

In the formula, q is the unit area seepage flow per unit time; J is hydraulic gradient; e is the crack opening; g is gravitational acceleration; v is the viscosity coefficient of water flow; when the water temperature is 15°, $v = 1.14 * 10^{-6}$ m^2/s.

3.3. Calculation Parameter Value. The field test and laboratory test cannot effectively determine the mechanical parameters of complex geotechnical media. Due to its nonuniformity, cracks, and other factors, the results of mechanical parameters have great randomness and limitations, and there is a large error with the field measured values. In order to make up for the shortcomings of the above methods, this paper uses the geotechnical back analysis method to obtain the parameter value in the numerical calculation [24, 25].

In this paper, the combination of BP neural network and differential evolution algorithm is used for inverse analysis to establish the nonlinear relationship between surrounding rock displacement and mechanical parameters as shown in

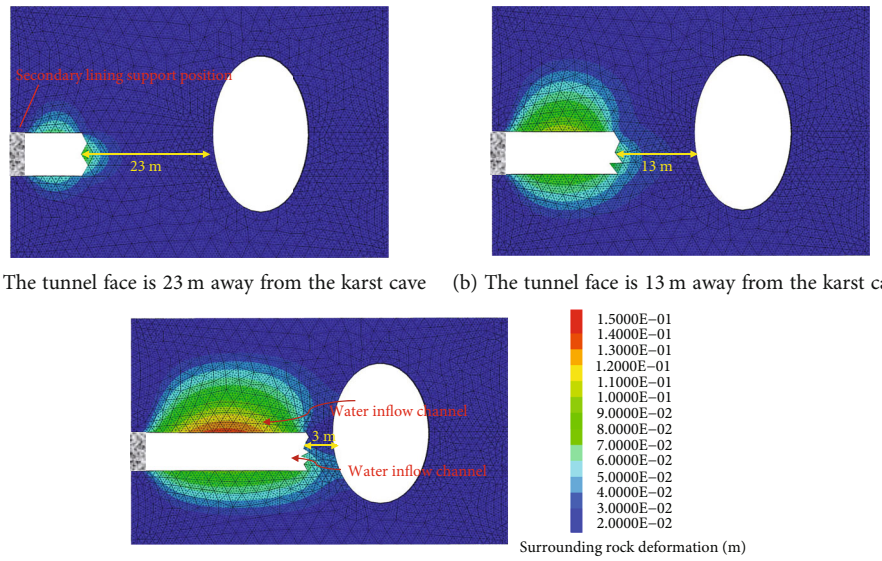

(a) The tunnel face is 23 m away from the karst cave (b) The tunnel face is 13 m away from the karst cave

(c) The tunnel face is 3 m away from the karst cave

Figure 5: Deformation characteristics of surrounding rock under different thickness of water-resisting layer.

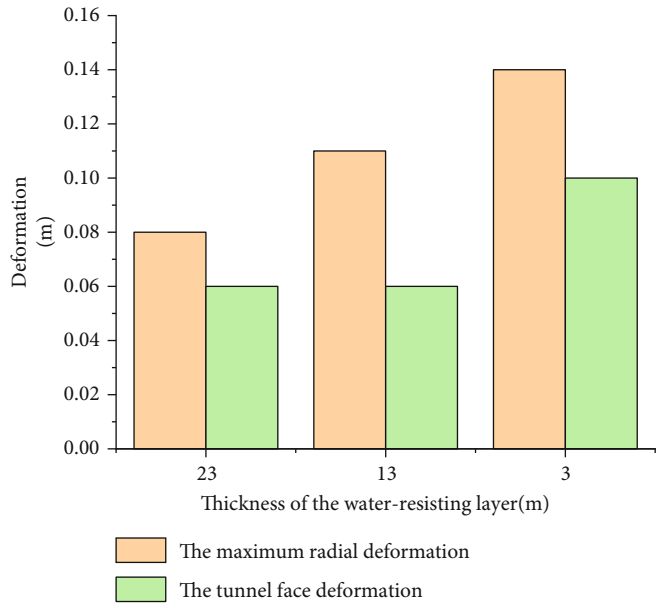

Figure 6: Deformation of tunnel under different thickness of water-resisting layer.

Figure 3. BP neural network is a complex and nonlinear dynamic analysis system, including input layer, hidden layer, and output layer. The network response corresponding to the input mode is transmitted from the input layer to the output layer through the middle layer. According to the error between the actual tunnel displacement value and the numerical simulation value, the connection weight is corrected from the output layer to the input layer through the hidden layer so that the difference between the actual value and the expected value is gradually reduced. However, BP neural network has some problems, such as slow convergence speed, poor network performance, uncertain learning rate, and easy to fall into local minimum. Different evolution can make up for the shortcomings of BP neural network. Differential evolution algorithm simulates the evolution of biological population and iterates repeatedly, so as to retain the individuals who meet the adaptation conditions. It retains the global search ability of genetic algorithm and has the robustness and strong global optimization ability.

Taking the surrounding rock parameters as the input layer vector and the displacement value as the output layer vector, the rock elastic modulus E, cohesion c, and internal friction angle φ are selected; joint shear stiffness k_s, joint normal stiffness k_n, joint internal friction angle k_φ, and joint

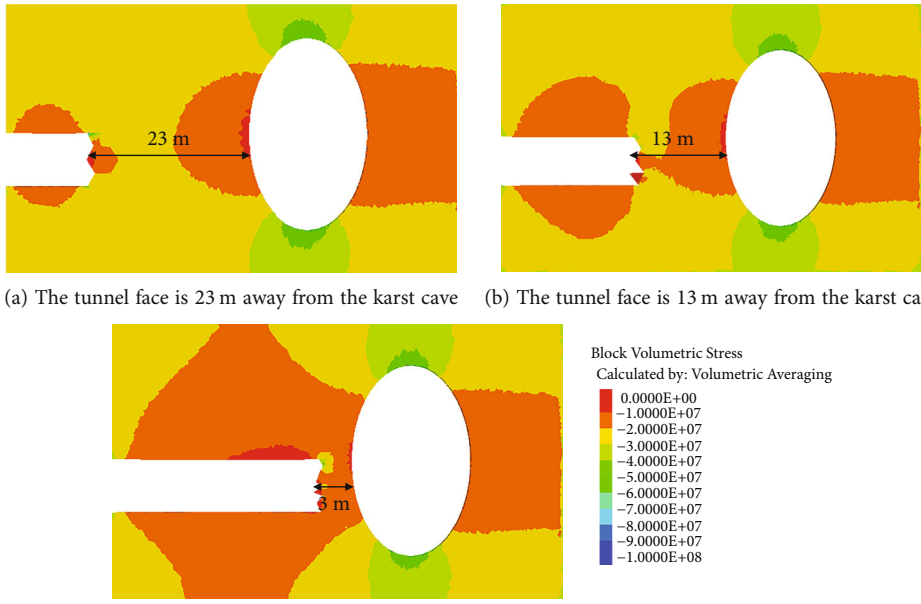

(a) The tunnel face is 23 m away from the karst cave (b) The tunnel face is 13 m away from the karst cave

(c) The tunnel face is 3 m away from the karst cave

Figure 7: Block volumetric stress of surrounding rock under different thickness of water-resisting layer.

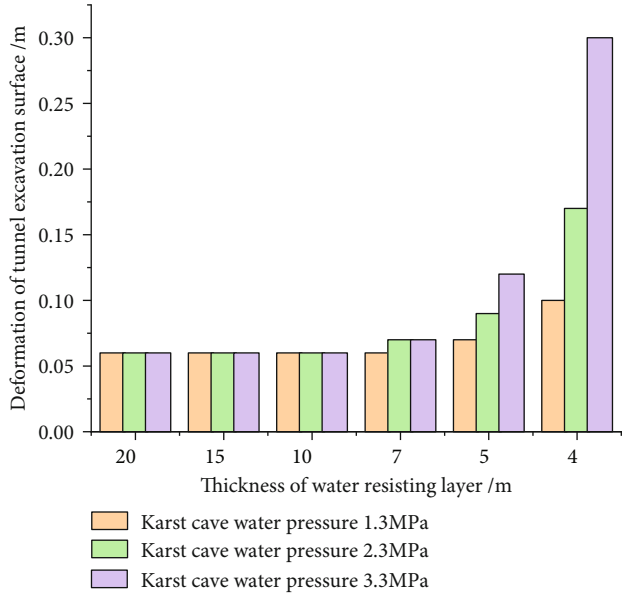

Figure 8: Displacement and deformation characteristics of tunnel face under different water pressure.

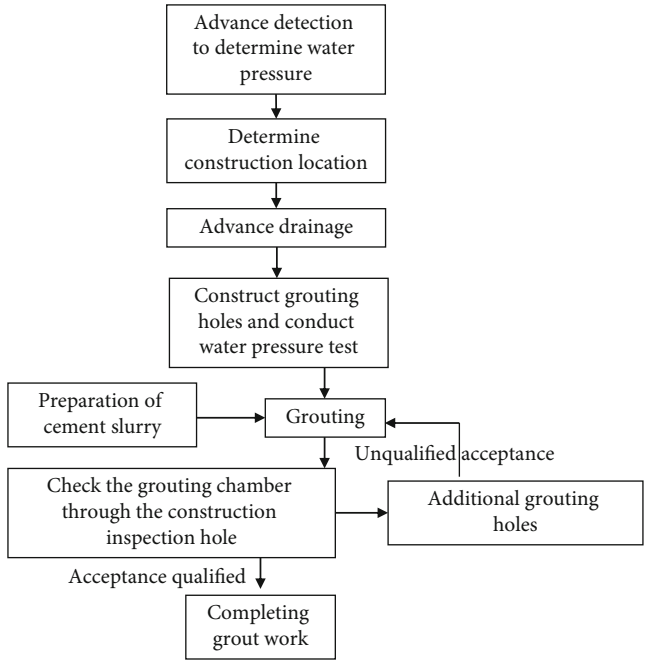

Figure 9: Curtain grouting process flowchart.

cohesion k_c are the input parameters, and the numerical simulation displacement value is the output parameter. The parameters shown in Table 1 are used to compare the measured value with the simulation value, as shown in Figure 4. The numerical calculation and analysis show that the calculation step is balanced at 9500 steps, and the maximum settlement of the arch crown is 59.39 m. The measured results show that the maximum settlement of arch crown is 55.3 mm, and the stability time is about 31 days after excavation. The numerical simulation can fully reflect the deformation characteristics of the surrounding rock, and the parameters obtained from inversion can be used for subsequent research.

4. Analysis of Numerical Results

4.1. Deformation Characteristics. Figures 5 and 6 show the influence of different water-resisting layer thicknesses on surrounding rock deformation and seepage when the water pressure in the karst cave is 2.3 MPa. The calculation shows that with the continuous advancement of the tunnel, the deformation and failure of surrounding rock are mainly

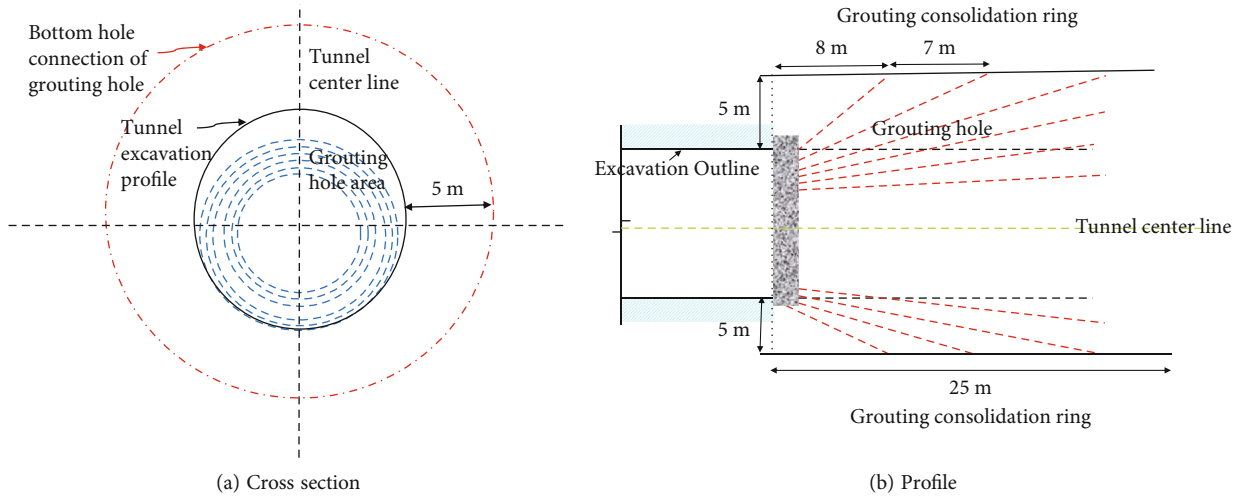

Figure 10: Design drawing of advance curtain grouting.

divided into two parts: radial development and advanced influence, and the radial deformation increases with the extension of the distance from the secondary lining. When 9 m away from the secondary lining, the thickness of the water-resisting layer is 23 m, the maximum radial deformation is 0.08 m, the tunnel face deformation is 0.06 m, and the advanced influence distance is 10 m. When 19 m away from the secondary lining, the thickness of the water-resisting layer is 13 m, the maximum radial deformation is 0.11 m, the tunnel face deformation remains 0.06 m, and the advance influence distance is 10 m. When 29 m away from the second lining, the thickness of the water-resisting layer is 3 m, the maximum radial deformation is 0.14 m, the maximum deformation of the tunnel face surges to 0.1 m, and a seepage channel is generated with the karst cave. The water in the solution cavity flows into the tunnel through the seepage channel, resulting in disasters. With the decrease of the safe thickness of the water-resisting layer, the advance stress caused by tunnel excavation is superimposed and coupled with the stress concentration around the karst cave, resulting in damage. Therefore, in order to ensure safe production, it is necessary to control the distance between the secondary lining and the tunnel face, analyze the minimum water-resisting layer thickness under different water pressure conditions, and advance grouting before reaching the minimum water-resisting layer thickness.

As shown in Figure 7, it shows the variation law of volume stress with the decrease of the thickness of the water-resisting layer during tunnel excavation. Volume stress can fully show the three-dimensional stress state of the unit body. With the decrease of the thickness of the water-resisting layer, the low stress area caused by tunnel excavation is fused with the low stress area caused by karst cave, which is easy to form a seepage channel.

4.2. Influence of Water Pressure in Karst Cave on Safe Thickness. When the water pressure of the karst cave is 1.3 MPa, 2.3 MPa, and 3.3 MPa, respectively, the displacement of excavation surface is shown in Figure 8. When the thickness of the water-resisting layer is more than 10 m, the change of water pressure in the karst cave has no impact on the tunnel face, and the deformation is 0.06 m. When the thickness of the water-resisting layer is 7 m, the water pressure is 2.3 MPa to 3.3 MPa, and the deformation increases by 25% compared with 1 MPa. When the thickness of the water-resisting layer is 5 m, it can be seen that the deformation increases sharply with the increase of water pressure. When the water pressure is 3.3 MPa, the deformation reaches 0.125 m. When the thickness of the water-resisting layer is 4 m and the water pressure is 3.3 MPa, the maximum deformation reaches 0.3 m. When the water pressure is 2.3 MPa, the deformation reaches 0.17 m. When the water pressure is 1.3 MPa, the deformation reaches 0.1 m. According to the above research, in order to ensure the safety of the tunnel during tunneling, the thickness of the water-resisting layer should be kept above 10 m, and then, the construction should be carried out by grouting in advance.

5. Control Measures and Effects

Advance drainage and curtain grouting are adopted for karst cave treatment to reduce water pressure and prevent outburst. Determine the water pressure in the karst cave according to the advanced geophysical exploration. When the water pressure is greater than 3.3 MPa, drainage and curtain grouting shall be carried out 10 m in advance. When the water pressure is greater than 2.3 MPa, drainage and curtain grouting shall be carried out 8 m in advance. When the water pressure is greater than 1.3 MPa, drainage and curtain grouting shall be carried out 6 m in advance. The treatment process flow is shown in Figure 9. Firstly, the solution cavity position and water pressure are determined by advanced geophysical exploration, so as to analyze the advanced control distance. Advance drilling shall be carried out to remove water pressure and curtain grouting shall be carried out.

The mixture of cement and water glass is used as grouting material. The water cement ratio of cement slurry is 1 : 1~1 : 1.5, the water glass concentration is 30~40 Baume degree, the cement water glass volume ratio is 1 : 0.3~1 : 1, and an appropriate amount of retarder is added as required.

The dosage is determined by test, generally 1%~3% of the dosage of cement. Through the analysis of the revealed geological conditions, after the advance curtain grouting construction is completed, the slurry fills the cracks more densely, reduces the formation permeability coefficient, and plays an effective role in water plugging.

Figure 10 shows the design of advance grouting, in which the advance reinforcement section is 25 m long. The thickness of grout stop wall is 2 m. The lateral reinforcement range is 5 m outside the contour line of the tunnel face. The slurry diffusion radius is 2.0 m. The spacing of final holes shall not exceed 3.0 m.

6. Conclusion

The stability of rock stratum between tunnel and karst cave is one of the main problems endangering safety in tunnel construction in karst area. During the construction of the tunnel through the karst area, the existing karst cave often leads to local collapse, block falling and rock falling during the tunnel excavation, especially the hidden karst cave that is not exposed during the excavation. Because the safety measures cannot be taken in advance, it is easy to be damaged out of guard, causing great potential safety hazards and great harm to the tunnel construction and operation. At present, there is a lack of systematic research on the impact of karst cave on tunnel construction in karst area. Therefore, it is necessary to systematically study the impact of karst cave on tunnel construction and explore its regularity, so as to carry out targeted treatment or pretreatment of karst cave in construction, ensuring the safety of tunnel construction in karst area. This paper studies the reasonable thickness of tunnel excavation surface and karst tunnel aquifuge and discusses the basic control methods. The specific conclusions are as follows:

(1) Through geological investigation and analysis, it is considered that the karst caves in the tunnel are densely distributed and the water content is huge. Therefore, the discrete element numerical calculation model is established, the unified constitutive model is adopted for the block, and the Coulomb slip model is adopted for the joint

(2) The method of back analysis of surrounding rock mechanical parameters through displacement is realized through neural network. It is considered that the combination of BP neural network and differential evolution algorithm can effectively reduce the simulation error

(3) When the water pressure is 1.3 MPa, the thickness of the water-resisting layer is too small, the deformation of the tunnel face increases sharply, and a seepage channel is generated with the karst cave. The advance stress caused by tunnel excavation is superimposed and coupled with the stress concentration around the karst cave, resulting in damage

(4) The increase of water pressure makes the thickness of the safety water-resisting layer increase accordingly. It is more reasonable to carry out advance grouting design according to different water pressure

Data Availability

The data used to support the findings of the study are available within the article.

Conflicts of Interest

The authors declare that they have no conflicts of interest.

Acknowledgments

This research was supported by the Project of Zhejiang Provincial Education Department (FX2019112).

References

[1] L. Li, W. Tu, S. Shi, J. Chen, and Y. Zhang, "Mechanism of water inrush in tunnel construction in karst area," *Geomatics, Natural Hazards and Risk*, vol. 7, no. sup1, pp. 35–46, 2016.

[2] S. Li, Z. Zhou, L. Li, Z. H. Xu, Q. Q. Zhang, and S. S. Shi, "Risk assessment of water inrush in karst tunnels based on attribute synthetic evaluation system," *Tunnelling and Underground Space Technology*, vol. 38, pp. 50–58, 2013.

[3] L. Li, T. Lei, S. Li et al., "Risk assessment of water inrush in karst tunnels and software development," *Arabian Journal of Geosciences*, vol. 8, no. 4, pp. 1843–1854, 2015.

[4] X. Wang, S. Li, Z. Xu, J. Hu, D. Pan, and Y. Xue, "Risk assessment of water inrush in karst tunnels excavation based on normal cloud model," *Bulletin of Engineering Geology and the Environment*, vol. 78, no. 5, pp. 3783–3798, 2019.

[5] C. Lin, M. Zhang, Z. Zhou et al., "A new quantitative method for risk assessment of water inrush in karst tunnels based on variable weight function and improved cloud model," *Tunnelling and Underground Space Technology*, vol. 95, p. 103136, 2020.

[6] K. Zhang, W. Zheng, C. Xu, and S. Chen, "An improved extension system for assessing risk of water inrush in tunnels in carbonate karst terrain," *KSCE Journal of Civil Engineering*, vol. 23, no. 5, pp. 2049–2064, 2019.

[7] X. Wang, S. Li, Z. Xu, X. Li, P. Lin, and C. Lin, "An interval risk assessment method and management of water inflow and inrush in course of karst tunnel excavation," *Tunnelling and Underground Space Technology*, vol. 92, p. 103033, 2019.

[8] Y. Zhao, P. Li, and S. Tian, "Prevention and treatment technologies of railway tunnel water inrush and mud gushing in China," *Journal of Rock Mechanics and Geotechnical Engineering*, vol. 5, no. 6, pp. 468–477, 2013.

[9] G. Li, W. Ma, S. Tian, Z. Hongbo, F. Huabin, and W. Zou, "Groundwater inrush control and parameters optimization of curtain grouting reinforcement for the Jingzhai tunnel," *Geofluids*, vol. 2021, 10 pages, 2021.

[10] J. Q. Liu, K. V. Yuen, W. Z. Chen, X. S. Zhou, and Wei-Wang, "Grouting for water and mud inrush control in weathered granite tunnel: a case study," *Engineering Geology*, vol. 279, p. 105896, 2020.

[11] S. Wang, L. Li, S. Cheng et al., "Study on an improved real-time monitoring and fusion prewarning method for water inrush in tunnels," *Tunnelling and Underground Space Technology*, vol. 112, p. 103884, 2021.

[12] B. Zhu, L. Wu, Y. Peng, W. Zhou, and C. Chen, "Risk assessment of water inrush in tunnel through water-rich fault," *Geotechnical and Geological Engineering*, vol. 36, no. 1, pp. 317–326, 2018.

[13] Z. Huang, K. Zhao, X. Li, W. Zhong, and Y. Wu, "Numerical characterization of groundwater flow and fracture-induced water inrush in tunnels," *Tunnelling and Underground Space Technology*, vol. 116, p. 104119, 2021.

[14] G. C. Shi, X. J. Yang, H. C. Yu, and C. Zhu, "Acoustic emission characteristics of creep fracture evolution in double- fracture fine sandstone under uniaxial compression," *Engineering Fracture Mechanics*, vol. 210, pp. 13–28, 2019.

[15] C. Zhu, M. C. He, B. Jiang, X. Z. Qin, Q. Yin, and Y. Zhou, "Numerical investigation on the fatigue failure characteristics of water-bearing sandstone under cyclic loading," *Journal of Mountain Science*, vol. 18, no. 12, pp. 3348–3365, 2021.

[16] G. Li, Y. Hu, S. M. Tian, M. Weibin, and H. L. Huang, "Analysis of deformation control mechanism of prestressed anchor on jointed soft rock in large cross-section tunnel," *Bulletin of Engineering Geology and the Environment*, vol. 80, no. 12, pp. 9089–9103, 2021.

[17] M. Z. Gao, J. Xie, Y. N. Gao et al., "Mechanical behavior of coal under different mining rates: a case study from laboratory experiments to field testing," *International Journal of Mining Science and Technology*, vol. 31, no. 5, pp. 825–841, 2021.

[18] M. Z. Gao, H. C. Hao, S. N. Xue et al., "Discing behavior and mechanism of cores extracted from Songke-2 well at depths below 4,500 m," *International Journal of Rock Mechanics and Mining Sciences*, vol. 149, p. 104976, 2022.

[19] C. Cao, W. Zhang, J. Chen, B. Shan, S. Song, and J. Zhan, "Quantitative estimation of debris flow source materials by integrating multi- source data: a case study," *Engineering Geology*, vol. 291, p. 106222, 2021.

[20] D. Chen, H. Chen, W. Zhang, J. Lou, and B. Shan, "An analytical solution of equivalent elastic modulus considering confining stress and its variables sensitivity analysis for fractured rock masses," *Journal of Rock Mechanics and Geotechnical Engineering*, vol. 2021, 2021.

[21] H. Liang, L. Wang, D. Xuaning, H. Wen, X. Yuan, and W. Zhang, "Similarity quantification of soil parametric data and sites using confidence ellipses," *Geoscience Frontiers*, vol. 13, no. 1, article 101280, 2022.

[22] C. Zhu, M. Karakus, M. He, Q. Meng, and Y. C. Yuan, "Flexural toppling mechanism and stability analysis of an anti-dip rock slope," *Rock Mechanics and Rock Engineering*, vol. 54, no. 8, pp. 3721–3735, 2021.

[23] B. D. Ding, Z. Y. Han, G. C. Zhang et al., "Volumetric deformation and damage evolution of Tibet interbedded skarn under multistage constant-amplitude-cyclic loading," *International Journal of Rock Mechanics and Mining Sciences*, vol. 152, p. 105066, 2022.

[24] Z. Dou, S. X. Tang, X. Y. Zhang et al., "Influence of shear displacement on fluid flow and solute transport in a 3D rough fracture," *Lithosphere*, vol. 2021, no. Special 4, p. 1569736, 2021.

[25] Z. Dou, Y. M. Liu, X. Y. Zhang et al., "Influence of layer transition zone on rainfall-induced instability of multilayered slope," *Lithosphere*, vol. 2021, no. Special 4, p. 2277284, 2021.

Hindawi
Geofluids
Volume 2022, Article ID 1568050, 16 pages
https://doi.org/10.1155/2022/1568050

WILEY | Hindawi

Research Article

Dynamic Prediction Method of 3D Spatial Information of Coal Mining Subsidence Water Area Integrated with Landsat Remote Sensing and Knothe Time Function

Hui Liu [1,2] **and Yu Li** [1,2]

[1] *School of Resources and Environmental Engineering, Anhui University, Hefei, Anhui Province 230601, China*
[2] *Anhui Province Mine Ecological Restoration Engineering Laboratory, Hefei, Anhui Province 230601, China*

Correspondence should be addressed to Hui Liu; lhui99@aliyun.com

Received 19 January 2022; Revised 5 February 2022; Accepted 8 February 2022; Published 1 March 2022

Academic Editor: Long Yan

Subsidence water disaster has become a major problem to the ecological environment because of the submerged villages, farmland destruction, and ecological destructive changes in the mining subsidence area of high-water level. Taking the 1031 working face of Wugou Coal Mine in Huaibei, Anhui, China, as the research subject, (1) a three-dimensional (3D) spatial information dynamic prediction method was proposed for high-water-level coal mining subsidence areas by combining the Knothe time function based on the probability integration method (PIM) and the principle of water balance. (2) The dynamic evolution law of the water accumulation area in the high-water-level coal mining subsidence area was studied. (3) The applicability of the dynamic prediction model of the water accumulation range in the high-water-level coal mining subsidence area was verified. The results showed that the dynamic prediction of the 3D spatial information of the high diving area is highly accurate and can be suitable for the dynamic prediction by comparison with the results of remote sensing monitoring and field measurement. As a result, technical reference and theoretical basis for the comprehensive assessment and remediation of the ecological environment of the high diving mining subsidence area were proposed.

1. Introduction

Coal is China's main energy source, accounting for approximately 70% of primary energy production and consumption [1,2]. It has an important position in the economy [3] and is an important factor that drives world economic development. With the rapid development of contemporary socioeconomic and industrial production, coal consumption as a conventional fuel is continuously growing [4]. According to the World Energy Yearbook, China's coal resource output reached 3846 billion tonnes in 2019, accounting for 47.3% of the global total output, remarkably higher than the world's average output level [5]. However, coal mining not only caused serious safety accidents [6–8] but also caused a range of profound environmental problems, such as decreased soil quality, ecosystem degradation, biodiversity loss, and landscape destruction [9]. Fractured rocks in the subsurface are ubiquitous, and the dynamics of mass transfer in the fractured rocks play an important role in understanding the problem in engineering geology and environmental geology [10]. Amongst them, underground coal mining directly causes large surface subsidence [11–13]. Subsidence and accumulated water disasters have become the primary ecological environment problems faced by coal mine subsidence areas with high phreatic levels. Village flooding, farmland damage, and disruptive changes in the ecosystem have brought great challenges to the construction of ecological civilization in the mining area [14,15], and these are the urgent problems in the coal mining areas that need to be addressed.

The negative impact of coal mining in the areas with high phreatic water levels in eastern China is particularly serious. This area has the characteristics of high phreatic level and thick loose layer coverage [16]. The mining area is an area

with coal resources. Diving is gravity water with a free surface above the first continuous aquifer below the surface. Its upper part has no continuous and complete waterproof top plate, and the diving water surface is a free water surface, called a diving surface. Any point on the diving surface is called the diving level according to the absolute height of the reference level. A high diving level, as the name suggests, is a higher level of diving underground. High-water-level mining areas are mainly distributed in the eastern part of China. High underground water level causes the surface to sink, and water is accumulated after coal mining, thus forming a unique ecological environment of the mining area with a combination of water and land.

Understanding in situ stress is the foundation of studying deep rock mechanics [17]. Generally, deformation, fracture propagation, and energy release are highly associated with mining-induced stress evolution [18]. When underground coal is extracted, the surrounding rock loses the original stress balance [19,20], causing stress redistribution. With the increasing maximum stress, the average stress applied and the duration of rock suffering from a high-stress increase. Therefore, reaching the strength limit becomes easier, and the fatigue life is shorter [21]. When the concentrated stress of the roadway roof exceeds the strength limit, roof layer deformation, fracture, and collapse [22] cause pressure subsidence and water consolidation subsidence. These conditions eventually cause the movement and deformation on the surface subsidence basin and produce a large number of cracks in high diving areas, where groundwater formation easily connects to the subsidence area. The water in the subsidence area mainly comes from atmospheric precipitation, surface runoff, surface water evaporation, and groundwater seepage. When the water input and output of various factors reach equilibrium, the range of water in the subsidence area remains unchanged. Figure 1 shows the image of the surface subsidence caused by coal mining in a typical high-water-level mining area of Lianghuai coal mines in China. The images on the left and right are the Huainan Guqiao Coal Mine and Huaibei Coal Mine, respectively. The subsidence water disaster has become a primary ecological environment problem because of the high diving mining subsidence areas, submerged villages, farmland damage, and disruptive changes to the ecosystem, causing great challenges to the sustainable development of the mining area. In the past 25 years, the water accumulation area in the coal mining subsidence area of Anhui Province has increased by approximately six times, from 18.95 km^2 to 118.09 km^2, with an annual growth of 3.97 km^2. In addition, some water areas account for 30% to 50% of the total coal mining subsidence area [23]. The large subsidence area gradually evolves from an original land ecosystem into a water land composite ecosystem, causing irreversible damage to the original local ecosystem balance. On the other hand, surface subsidence destroys large areas of cultivated land and prominent human and land contradictions, thereby seriously affecting the local economic development, social structure, and stability.

Surface subsidence caused by coal mining directly damages the ecological environment in the mining area. Especially in the areas with high diving sites, coal resource mining not only causes surface subsidence but also accumulates a large range of water in the subsidence area. As a result, the ecological environment is seriously damaged. In the view of the surface subsidence water in high diving mining subsidence area and a series of environmental problems, field mapping, mining subsidence estimation, and remote sensing monitoring have been widely used to obtain the geospatial information data of the coal mining subsidence area.

(1) Field surveying and mapping: the surface mobile observation station is set, a large number of measured data are collected, theoretical analysis is performed, the surface mobile data of different mining areas are obtained, and the surface deformation laws under different geological mining conditions are analyzed. The monitoring of water mainly uses the entire station instrument, theodolite, GPS, and other traditional measurement instruments. In accordance with the water characteristics, the characteristic point coordinates are measured, and then water statistics are obtained according to the internal industry treatment.

However, the surface form and water situation in the subsidence basin are dynamically affected by many factors. This method is suitable for small water areas with limited applicability.

(2) Mining subsidence is expected to happen because of the construction of underground mines. In recent years, with the further deepening of mining under different conditions, scholars have developed and established many new mining subsidence prediction methods, such as the Knothe surface subsidence prediction theory based on the traditional influence function method [24] and the mining subsidence prediction model based on spatial statistical methods. From the mechanical perspective, the linear elastic analysis principle and the surface element principle are introduced. Different geological conditions and mining methods have led to the development of the prediction theories and models of inclined coal seam surface subsidence prediction, surface settlement prediction of abandoned column old mining area, surface subsidence prediction of the shallow mining area, and surface subsidence prediction of chamber column mining.

However, in a special geological situation, the surface subsidence characteristics are different from the conventional mining subsidence characteristics. Thus, the conventional subsidence prediction model cannot fully apply to the surface subsidence prediction and needs further verification of the accuracy of the surface subsidence prediction model of coal seam mining.

(3) Remote sensing monitoring: in terms of water evolution, Suping et al. considered the Huainan mining area and used transmission electron

Figure 1: High-water-level coal mining subsidence area.

microscopy (TM) images to extract the information of water at different times using the method of principal component analysis and analyzed the changes in the water area [25]. With the development of remote sensing technology, domestic high-resolution satellite images have been used for monitoring the range of stagnant water and scope information extraction.

However, the surface form and water in the mining subsidence area are dynamically affected by many factors. The observation data obtained by the existing methods lack timeliness, thus making the timely prediction of the 3D spatial information of water in the surface subsidence area difficult and affecting the accuracy of the planning and design of the coal mining subsidence area.

Studies on the field mapping of the high mining subsidence, mining subsidence dynamic forecast, and remote sensing monitoring are abundant. However, the surface subsidence water and many factors, such as comprehensive mining subsidence, surface water range evolution, and water circulation, require further investigation. In addition, high mining subsidence and water range dynamic evolution law should be analyzed. (1) The dynamic evolution law of water in the subsidence area of the high diving level is still unclear. Restricted by the means of field mapping, the existing studies mainly targeted the range change of surface water before and after subsidence. However, studies on the production, increase, stability, and dynamic laws of surface water at different mining stages are limited. (2) The accuracy of the mining subsidence expected model should be verified. Further validation is expected for surface subsidence with special geological conditions. (3) The dynamic prediction of surface water range in high diving coal mining subsidence area is limited. Although the development of remote sensing technology has been relatively mature, most existing studies focus on a single mining area or a working surface, few large areas, and long-time effect of water dynamic evolution characteristics. In addition, the impact of the dynamic change of water analysis is less, the subsidence area evolution law analysis is not comprehensive, and the observation data could not be taken in a timely manner. Thus, satisfying the requirements of land reclamation and ecological restoration is difficult.

In this study, a dynamic prediction model of the water accumulation area in the high-water-level coal mining subsidence area was established. The equivalent relationship between the volume of the subsidence basin and the water accumulation in the subsidence basin was established using the probability integration method based on the Knothe time function and the principle of water balance in the coal mining subsidence area, combined with the main influencing factors of the evolution of the water accumulation area to determine the mining capacity of the working face. The dynamic evolution of the surface water range was predicted, and information, such as the range of water accumulation, the range of subsidence basins, the level of water accumulation, and the amount of water accumulation during the evolution of water accumulation is obtained. The general law of the evolution of the water accumulation area in the coal mining subsidence area was studied. The time of water accumulation in subsidence basins generally lags behind the mining of the working face. The evolution of surface water accumulation can be divided into four stages: unformed period, synchronous growth period, residual growth period, and relatively stable period. The accuracy of the model was analyzed.

Therefore, taking the working surface of Wugou Mine 1031 as the research area, the three-dimensional (3D) spatial information of the coal mining subsidence water accumulation area of 1031 was dynamically predicted, and the dynamic evolution law of the water accumulation range was analyzed. Initially, the study area overview, as shown in section 2, was introduced. Then, the overall idea of the dynamic prediction method was proposed, as shown in section 3. The complete dynamic prediction method of the 3D spatial information of high diving mining subsidence is introduced in section 4. Finally, in section 5, model evaluation and validation are described by the engineering example of 1031. This study provides a theoretical basis for land use planning, land reclamation, and the establishment of a land and water complex ecosystem in the subsidence area of high diving sites.

2. Overview of the Study Area

Wugou Coal Mine is the 10^{th} pair of mines developed and constructed by North Anhui Coal and Power Group. It is located in the Wugou Town, Suixi County, which is 50 km away from the Huaibei urban area, as shown in Figure 2. The

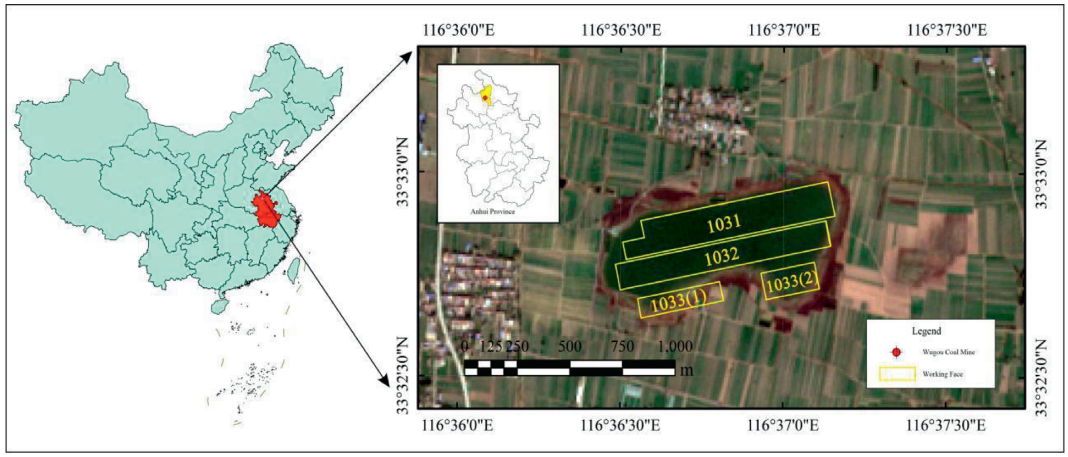

Figure 2: Location of the study area and current status of the water system.

underground diving level in the mining area is 1.5 m, which is a typical high diving level mining area. The coal-containing formation in this mine is carbonite-Permian system, mainly comprising four layers of coal seam (72, 81, 82, and 10 coal seams, with the average thicknesses of 1.80, 2.50, 2.53, and 3.86 m, respectively). The average recoverable total thickness is 10.69 m because the coal seam is seriously damaged by fault cutting. A considerable part of the shallow area is in the wind oxidation zone or waterproof coal column, resulting in the recoverable area of the coal seam. The total resource reserves of the entire well field are 137,304,600 tonnes, 125,910 million tonnes, and 40,339,500 tonnes, of which 10 coal seams' recoverable reserves are 25,956,200 tonnes, accounting for 64.3%.

The regional climate is mild. It is a monsoon warm temperate semihumid climate, mild spring and autumn rain, hot and rainy in summer, and cold and windy in winter. The annual average temperature is 14.1°C, the annual average sunshine is 2345.3 h, the average annual rainfall is 834 mm, the groundwater is buried at a depth range of 1.5–4 m, and the average annual buried depth of the water level is 2.48 m [25]. The rainfall is mostly concentrated in July and August, the annual evaporation is 1400 mm, the annual frost-free period is 208–220 days, and the freezing period is generally from early December to mid-February of the following year.

Figure 2 shows the location of the working surface and surface remote sensing images with a total length of 1136 and width of 180 m. The coal seam inclinations are from 3° to 16° and 8°. The coal seam average thickness is 3.8 m, and the average buried depth is 364 m. Figure 3 shows the loose layer at approximately 94 m, as shown in Figure 3. The working surface is flat with a surface elevation of 26.50 m to 27.56 m, with no large flow river on the surface. The water on the surface forms after the working surface mining because of the buried depth of the groundwater in the area, high rainfall, and the large subsidence coefficient of the surface.

3. Overall Idea of the Prediction Approach

3.1. Obtaining the Geological Mining Parameters. According to the working surface specifications of the mining area, the following parameters were established, namely mining promotion distance v, the tangent of major influence angle tan β, average mining thickness of the working surface m, coal bed pitch α, subsidence factor q, and major influence radius r. The 3D coordinate system of the mining subsidence space was established. The inflection point of the subsidence curve of the main section on the surface includes the coordinate origin o. The x-axis points along the surface toward the drain area are parallel to the coal seam direction. The y-axis over the coordinate origin leads straight down from the vertical z-axis of the x-axis. The Knothe time function was used to estimate the mining subsidence model.

3.2. Calculating the Subsidence Basin Volume. The dynamic subsidence was interpolated by the Kriging interpolation method, the contour of the subsidence basin of the coal mining subsidence area was generated successively, and the subsidence basin volume corresponding to different contour sections was calculated.

3.3. Calculating the Water Accumulation Volume in the Subsidence Basin. The hydrological and water resource data of the coal mining subsidence area were collected, and the water balance iterative equation was established according to the water balance principle to obtain the water volume at different times in the subsidence basin of the coal mining subsidence area.

3.4. Calculating the 3D Spatial Information. The water volume in different sinking basins was calculated according to the iterative equation of water balance. In addition, combined with the sinking basin volume corresponding to different contour sections at this time, the relationship between the subsidence basin volume and the volume of water in the basin was established.

This model was used to predict the 3D dynamic spatial information at different moments with the advancement of the working surface, including water depth, water area, water range, water volume, and maximum storage capacity.

The technical flow chart is shown in Figure 4.

Thickness (m)	Depth (m)	Lithology
270	270	Loose layer
8.5	278.5	Medium sandstone
25.74	304.24	Fine sandstone
18.13	322.37	Mudstone
20.56	342.93	Siltstone
5.80	348.73	Sand and mudstone interbed
6.68	355.41	Siltstone
9.37	364.78	Mudstone
3.8	368.58	10 Coal seam

Figure 3: Generalized columns of working faces for 1031.

4. Dynamic Prediction Method of 3D Spatial Information

4.1. Dynamic Sinking Is Expected

4.1.1. Random Medium Theory. The theoretical basis of the probability integration method is the stochastic medium theory. Thus, this method is also known as the stochastic medium method. Littvinishen, the founder of random media theory, is a doctor in mathematics, who is familiar with probability theory. It is impossible to identify whether the rock mass medium is elastic, plastic, continuous, loose, or whole. The mine rock mass medium is generally called random medium. The basic assumptions and corollary of random medium theory indicate that the rock medium comprises many sufficiently small rock block particles. These particles are completely disconnected and can move relatively. Their movement is a stochastic process, as shown in Figure 5. The laws of rock strata and surface movement caused by mining are macroscopically similar to those described in the granular medium model acting as a random medium. The mutual verification of theory and practice was carried out, and the effect function based on the random medium theory is very similar to the one-Gaussian function of the Knott–Bradlake theory based on the measured data.

4.1.2. Probabilistic Integral Method. The randomastic medium theory was initially introduced into the rock layer movement study by the Polish scholar Li Tvinishen in the 1950s and was then developed into the probability integration method by Chinese scholars Liu Baochen and Liao Guohua. After more than 20 years of research by mining and subsidence workers in China, the probability integration

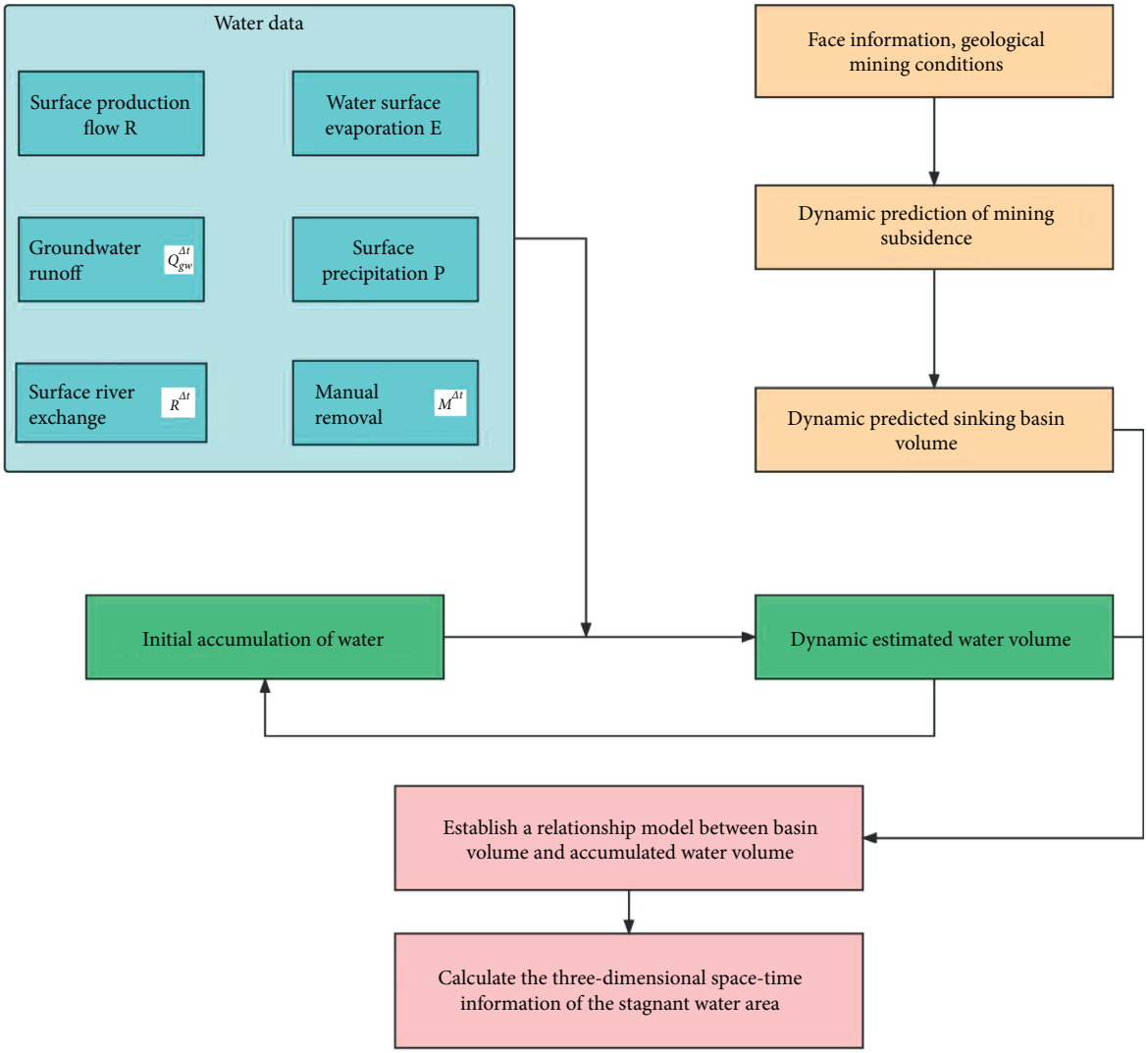

Figure 4: Technical flow chart.

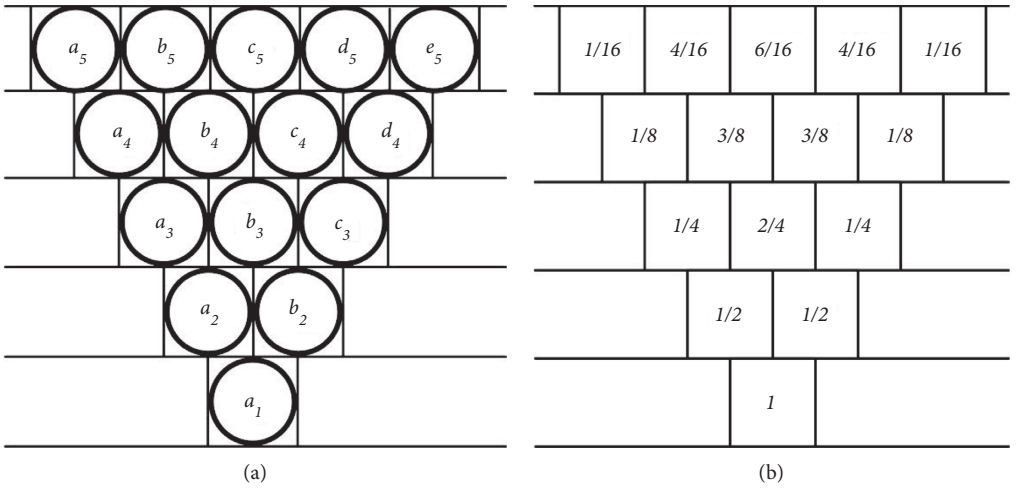

Figure 5: Random medium model. (a) Theoretical model. (b) Stochastic model of granular medium movement.

method has become one of the more mature and most widely used prediction methods in China. Probability integral is named after the probability integral (or its derivatives) in the movement and deformation prediction formula.

This method is based on the movement law of the surface and is generally similar to the random medium model. It is a comprehensive response to geographical and mining conditions to mining settlements, such as mining depth, mining thickness, rock mass properties, and coal seam inclination, regardless of the effect of special structures, such as faults, folds, and collapse columns.

The probabilistic integration model is one of the most widely used models in the field of mining subsidence currently as it can predict the degree of surface movement deformation through the working surface geological mining condition parameters and the expected parameters. The probability integral method model is represented by equation (1).

$$\begin{aligned} W(x,y) &= W_{\max} C_x C_y, \\ W_{\max} &= mq\cos\alpha, \\ C_x &= \frac{1}{2}\left[\frac{2}{\sqrt{\pi}}\int_0^{\sqrt{\pi}\,(x\cdot\tan\beta/H_0)} e^{-\lambda^2} d\lambda - \frac{2}{\sqrt{\pi}}\int_0^{\sqrt{\pi}\,((x-l)\cdot\tan\beta/H_0)} e^{-\lambda^2}\mathrm{d}\lambda\right], \\ C_y &= \frac{1}{2}\left[\frac{2}{\sqrt{\pi}}\int_0^{\sqrt{\pi}\,(y\cdot\tan\beta/H_1)} e^{-\lambda^2} d\lambda - \frac{2}{\sqrt{\pi}}\int_0^{\sqrt{\pi}\,((y-L)\cdot\tan\beta/H_0)} e^{-\lambda^2}\mathrm{d}\lambda\right], \\ l &= L_0 - S_1 - S_2, \\ L &= (L_1 - S_3 - S_4)\times(\cos\alpha + \sin\alpha\cdot\cot\theta_0), \end{aligned} \tag{1}$$

where x and y are the coordinates of any point in the working surface coordinate system within the influence range of underground mining, and $W(x, y)$ is the final sinking amount of the point (x,y) in the working surface coordinate system. $W_{\max}$ is the surface maximum subsidence, when the goaf is critical or supercritical in size [26]. m is the mining thickness. q is the sinking coefficient. H_1 and H_2 are the mining depths of downhill and uphill direction, respectively. H_0 is the average mining depth. θ_0 indicates the propagation angle influence.tanβ is the positive tangent value of the main influence angle. L_0 and L_1 are the working surface direction and tendency length, respectively. S_1, S_2, S_3, and S_4 are the inflection point deviation distances corresponding to both ends of the uphill and downhill directions. α is the seam inclination, and the practical significance of the parameters can be used. The parameters m, H_0, H_1, H_2, L_0, L_1, and α are called geological mining condition parameters and are generally provided by the production unit, and they are the known quantities: q, θ, tanβ, S_1, S_2, S_3, and S_4 are the expected parameters of the probability integration method, and they can be obtained from the measured data. With the known geological mining condition parameters of the working surface, the sinking amount of any point in the working surface can be expected by equation (1) as long as the rate integration prediction parameter is accounted into the model.

4.1.3. Knothe Time Function. To more accurately reverse and predict the dynamic process of surface subsidence, mine staff and scholars attempt to simulate the process of the dynamic subsidence of surface points using mathematical models, amongst which the most widely used model is the Knothe function of time. According to the working surface information of the mining area, the dynamic subsidence in the basin was obtained by the probability integration method based on the Knothe time function.

In 1952, the Polish scholar Knothe established the Knothe time function by analyzing the relationship between the sinking speed at a certain surface point and the sinking amount at the final subsidence at that time. This function can partly reflect the relationship between the surface subsidence and time [24]. The Knothe model represents the relationship between the surface subsidence velocity and subsidence volume, as expressed by equation (2).

$$\frac{\mathrm{d}W(t)}{\mathrm{d}t} = v(t) = C\left(W_0 - W(t)\right), \tag{2}$$

where t is the surface subsidence moment, W_0 is the final surface subsidence amount, $W(t)$ is the subsidence amount of the surface at time t and $V(t)$ is the subsidence speed of the surface point at time t, C is the time factor influence coefficient or lithology factor and is generally considered to be related to the mechanical nature of the overlying rock layer [27].

The surface sink is 0 at $t = 0$, namely, $W(0) = 0$. Thus, equation (3) was integrated with respect to t as follows:

$$W(t) = W_0\left(1 - e^{-Ct}\right), \tag{3}$$

where t is the independent variable, representing the time calculated from the moment the surface begins to sink, W_0 is

the final amount of surface subsidence and can be obtained or estimated by the probabilistic integration model, C value is the time factor influence coefficient and is related to the geological mining conditions of the working surface, and equation (3) is the Knothe time function. Substituting the final surface subsidence W_0 and the time factor influence coefficient C into equation (3) can lead to the surface subsidence at any time. In addition, the horizontal movement, slope, and parameters like curvature can be calculated.

When t tends to zero, $W(t) = 0$; when $t \longrightarrow \infty$, $W(t) = W_0$. Thus, W_0 controls the upper and lower boundary limits of the Knothe time function and is obtained by changing the time factor. C is the Knothe time function impact factor.

4.1.4. Dynamic Sinking Is Expected. The probability integral method is based on the Knothe time function, and geological mining condition parameters and equation (3) are used to calculate the dynamic subsidence prediction value of the subsidence basin, which is represented as follows:

$$w(x_i, y_i, T) = \frac{mq\cos\alpha}{r^2} \cdot \left(1 - e^{-cT}\right) \cdot \iint_D e^{-\pi\left((x_i-\varsigma)^2+(y_i-\tau)^2/r^2\right)} \mathrm{d}\varsigma\mathrm{d}\tau, \tag{4}$$

where $w(x_i, y_i, T)$ is the expected value of the dynamic subsidence at any point T on the surface of the subsidence basin, m is the average thickness of the working surface per m, α is the inclined angle of the coal seam, q is the sinking coefficient, r is the main influence radius and is measured per meter, c is the time coefficient, e is the natural constant and is approximately 2.718, d^{ξ} and d^{ξ} are the binary integral variables, ξ and τ are the integral variables in the s and y directions, respectively, and D is the range of the sinking basin at time T.

4.2. Volume Calculation of the Subsidence Basin. The Kriging interpolation method is an unbiased optimal estimation of regionalization variables in finite regions based on the variant function theory and structural analysis [27] and was established back in the 1950s with the prototype algorithm and is expressed as follows:

$$\hat{z}_0 = \sum_{i=0}^{n} \lambda_i z_i, \tag{5}$$

where z_0 is the value of the estimated point and z_i is the actual measurement of the interpolation element at point i. λ_i = the unknown weight of the actual measurement at the position. The weights are not only related to the distance between the measurement points and the predicted location but also based on the overall spatial arrangement of the measurement points. In the Kriging method, weight λ_i is a fit model of the optimal set of coefficients that can satisfy the smallest difference between the estimates and the actual values at the unknown point, satisfying the unbiased estimation conditions, depending on the spatial relationship amongst the measured points, the distance of the predicted position, and the measurements around the predicted location [27]. Therefore, the Kriging interpolation method considers not only the known relationships of the points to be estimated but also the spatial correlations of the variables. At present, this interpolation method can theoretically estimate the model error point-by-point without using the error test model, and it is not theoretically possible by other interpolation methods [28].

According to the expected value of the subsidence basin, the interpolation method initially uses formula (6) to calculate the difference between the bottom of the sinking basin and the lowest horizontal section in the basin d', as follows:

$$d' = W_m - (10 + nd), \tag{6}$$

where n is the number of horizontal sections, except the edge of the sinking basin, W_m is the maximum subsidence value of the surface at any time, and the contour value of 10, $10 + d$, $10 + 2d$, . . ., $10 + nd$ in mm corresponds to the equal section area of different sinking basins S, S_1, S_2, S_3, . . ., S_n. The volume of the sinking basin corresponding to the different contour sections was calculated using the area of the isoline section of each sinking basin.

Secondly, as shown in Figure 6(a), V is the volume of the entire sinking basin, V_1 is the volume between S and S_1, and V_2 is the volume between S_1 and S_2. V_n is the sinking volume between S_{n-1} and S_n, and V' is the sinking volume between S_n and W_m. Thus, the volume of the sinking basin with different contour cross-sections can be obtained, $V^T_{\max}$ is the maximum volume of the basin that can be obtained by formula (7).

$$\begin{aligned} V^T_{\max} &= V_1 + V_2 + V_3 + \cdots + V_n + V' = \frac{d}{2}S + dS_1 + dS_2 + \cdots + dS_n + \left(\frac{d}{2} + \frac{d'}{3}\right)S_n, \\ V^k_b &= V' + V_n + V_{n-1} + V_{n-2} + \cdots + V_k = \left(\frac{d}{2} + \frac{d'}{3}\right)S_n + dS_{n-1} + \cdots + \frac{d}{2}S_k, \quad 1 \le k \le n, \end{aligned} \tag{7}$$

where $V^T_{\max}$ is the maximum volume of the basin, V^k_b is the sinking basin volume corresponding to the cross-section of the contour $10 + (k-1)d$, V_1 is the volume between the contour 10 and the contour $10 + d$ is the cross-section, V_2 is

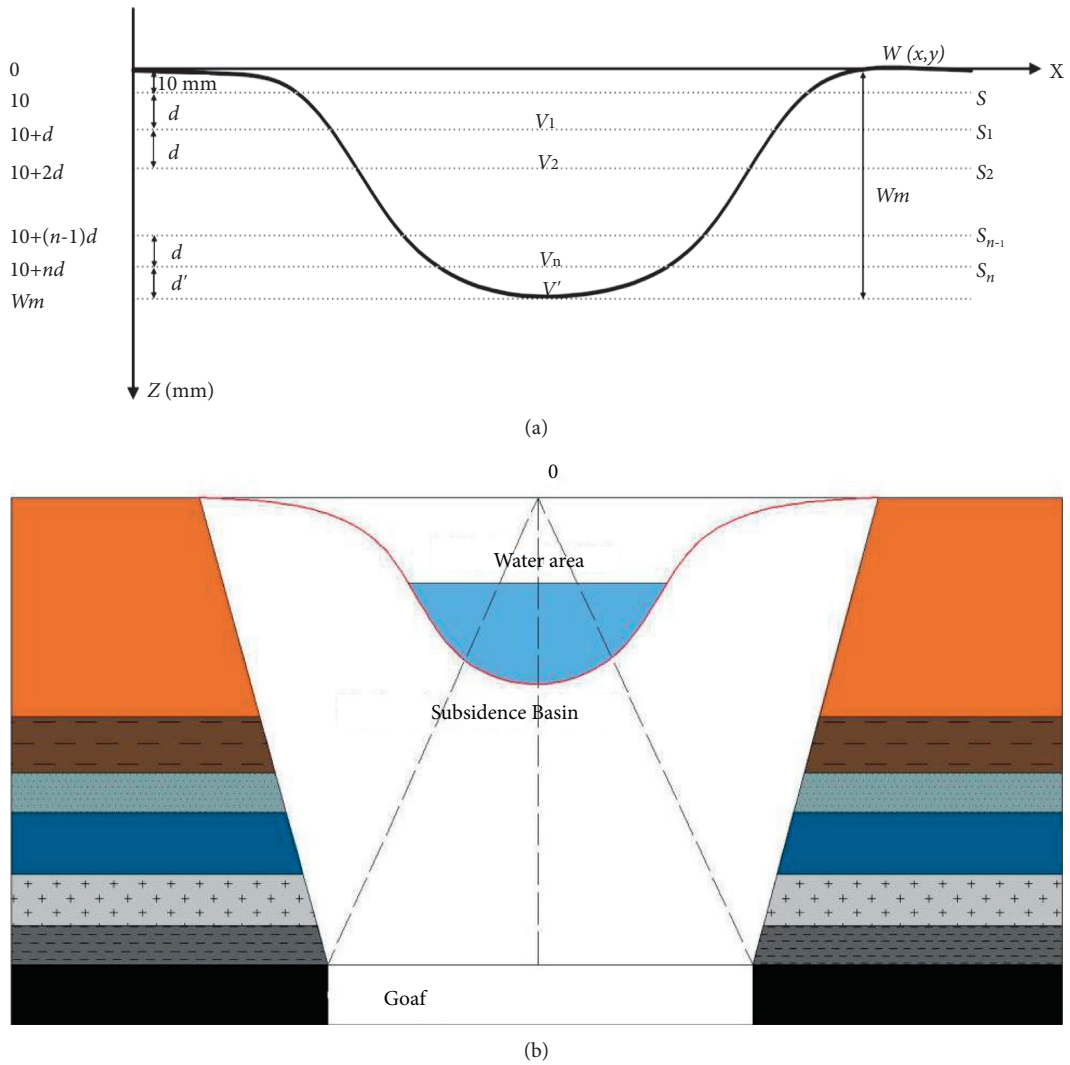

Figure 6: (a) Volume calculation of subsidence basin. (b) Schematic diagram of the working surface.

the volume between the contour $10 + d$ and the contour $10 + 2d$ cross-section, V_n is the volume between the contour $10 + (n - 1)d$ and the contour $10 + nd$ cross-section, V' is the volume between the contour of $10 + nd$ and the maximum sinking point W_m.

As the face advances, the newly mined rock begins to move. When the scope of the goaf is large enough after the impact of mining reaches the surface, the ground affected by the mining will sink down from the original elevation, thereby the surface above the goaf will form a much larger depression than the area of the goaf. Such depressions are often called surface mobile basins or ground subsidences, as shown in Figure 6(b).

Finally, the horizontal cross-sectional area of each contour of the sinking basin is calculated using formula (8), as follows:

$$S_n = \frac{1}{2}\sum_{i=1}^{N}\left(x_i^{10+nd} \cdot y_{i+1}^{10+nd} - x_{i+1}^{10+nd} \cdot y_i^{10+n\,d}\right), \tag{8}$$

where x_i^{10+nd} and y_i^{10+nd} are the contour point coordinates of the sink basin boundary of the sink value $10 + nd$ (n is a positive integer in unit mm).

4.3. Calculation of Water Accumulation in the Subsidence Basin. The supplementary and the excretion items are mainly considered when calculating the water volume changes in the basin, and the factors with less influence on the evolution of the water range are not considered. Supplementary items include water surface precipitation, surface runoff, and groundwater recharge. Excretion items include water surface evaporation and permeable water volume.

(1) Water face precipitation refers to the amount of water that directly falls in the water surface area during the atmospheric precipitation process, and this water is directly supplied to the atmospheric precipitation area, and the water surface precipitation can be determined according to the product of the water area and precipitation, which is as follows:

$$P = \frac{S_{\text{water}} \cdot P_{\text{day}} \cdot t}{1000}, \tag{9}$$

where P is the water surface precipitation/m^3, S_{water} is the water surface area/m^2, P_{day} is the daily precipitation/mm, and t is the duration/d.

(2) Surface runoff refers to the water flowing into the basin during the atmospheric precipitation. The flow area of the subsidence basin and the flow coefficient of the flow area of the basin and the study area were obtained as follows:

$$R = \frac{\left(S_{\text{basin}} - S_{\text{water}}\right) \cdot P_{day} \cdot \alpha \cdot t}{1000}, \tag{10}$$

where R is the surface production flow/m^3 in the unflooded area, S_{basin} is the sinking basin area/m^2, S_{water} is the water surface area/m^2, P_{day} is the daily precipitation/mm, and α is the surface runoff coefficient. According to the relevant hydrological data in the literature [29], the surface runoff coefficient in Huaibei area is about 0.15–0.25. According to the actual situation of the study area, the underlying surface of the mining area is mainly farmland, crops, and vegetation, and there are small areas of the hardened surface. The surface runoff coefficient is taken as 0.2 based on the actual situation, and t is the number of days/d.

(3) Groundwater replenishment refers to the process of an aquifer or an aquifer system acquiring water from the outside world, which is represented as follows:

$$W_{\text{underground}} = 0.042 \cdot (P + R), \tag{11}$$

where P is the water precipitation/m^3 and R is the surface production flow/m^3 in the unflooded area.

(4) Water evaporation refers to the evaporation of the water area in the subsidence basin. The product of the water area and evaporation is obtained as follows:

$$E = \frac{S_{\text{water}} \cdot E_{\text{day}} \cdot t}{1000}, \tag{12}$$

where E is the water evaporation/m^3, S_{water} is the water surface area/m^2, E_{day} is the daily evaporation/mm, and t is the number of days/d.

(5) Water leakage from the subsidence basin into the groundwater is computed as follows:

$$Q_{\text{seepage}} = 0.09E = \frac{S_{\text{water}} \cdot E_{day} \cdot t}{1000} \cdot 0.09, \tag{13}$$

where Q_{seepage} is the water seepage (m^3), E is the water evaporation (m^3), E_{day} is the daily evaporation (mm), S_{water} is the water surface area (m^2), and t is the days (d).

Supplementary items and excretion items (also known as expenses and receipts) are the principles of water balance. Water balance refers to the difference between the amount of water in revenue and the amount of expenditure in any area (or water body) during any period of time, and it is equal to the amount of change in water storage, as shown in formula (14).

$$V_{\text{ponding}} = V + P + R + W_{\text{underground}} - E, \tag{14}$$

where V is the original water amount, P is the water surface precipitation, R is the surface runoff, $W_{\text{underground}}$ is the groundwater recharge, and E is the water surface evaporation amount.

The iterative model of water balance was established using the principle of water balance, as shown in formula (15), to calculate the volume of water accumulation at different times T in the coal mining subsidence area, which is as follows:

$$\begin{aligned} V_w^{T+\Delta t} = {} & V_w^T + S_w^T \Delta P \Delta t + \alpha\left(S_b^T - S_w^T\right)\Delta P \Delta t \\ & + Q_{gw}^{\Delta t} + R^{\Delta t} - S_w^T \Delta E \Delta t - M^{\Delta t}, \end{aligned} \tag{15}$$

where $V_w^{T+\Delta t}$ is the expected water volume in the subsidence basin in cubic meter, V_w^T is the original water volume in the subsidence basin, Δt is the time interval, ΔP is the daily precipitation per meter, ΔE is the daily evaporation quantity in meter, α is the surface runoff coefficient, S_b^T is the subsidence basin boundary contour section area of 10 mm, its unit is square, S_w^T is the water area in the subsidence basin, its unit is square, $Q_{gw}^{\Delta t}$ is the groundwater seepage, its unit is cubic meter, $R^{\Delta t}$ is the surface river and subsidence area water exchange, its unit is cubic meter, and $M^{\Delta t}$ is the manually extracted volume in cubic meter.

4.4. 3D Dynamic Spatial Information Calculation. According to the water volume in the sinking basin at different times corresponding to different contour line sections, the relationship between the subsidence basin volume and water volume was established. The contours of the sinking basin are equal to the volume of the accumulated water in the sinking basin. Three-dimensional dynamic spatial information, such as water depth, water area, water range, water volume, and maximum storage capacity of the subsidence basin at different times T as the working surface is predicted, as shown in Figure 7.

According to the water volume in the sinking basin at different times and the sinking basin volume corresponding to the different contour sections, a mathematical relationship between the volume of the subsidence basin and the water volume in the basin was established as follows:

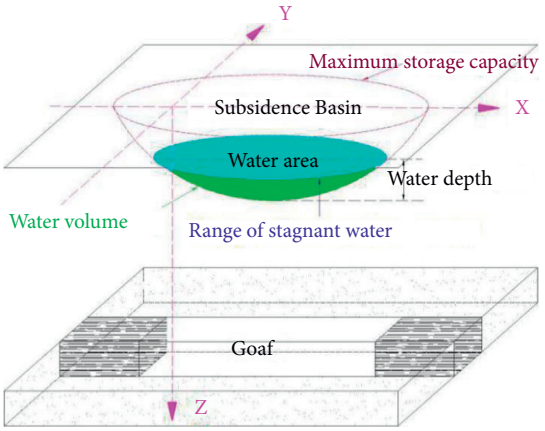

Figure 7: Schematic diagram of spatial three-dimensional coordinate system.

$$\begin{aligned} V_w^{T+\Delta t} &= V_w^T + S_w^T \Delta P \Delta t + \alpha\left(S_b^T - S_w^T\right)\Delta P \Delta t + Q_{gw}^{\Delta t} + R^{\Delta t} - S_w^T \Delta E \Delta t - M^{\Delta t} \\ &= \left(\frac{d}{2} + \frac{d'}{3}\right) \cdot S_n + d \cdot S_{n-1} + \ldots + \frac{d}{2} \cdot S_k = V_b^k, \quad 1 \le k \le n, \end{aligned} \tag{16}$$

where $V_w^{T+\Delta t}$ is the expected water volume in the sink basin, (m^3) and V_b^k is the sink basin volume corresponding to the contour $10 + (k-1)d$ section, (m^3). From $V_W^{T+\Delta t} = V_b^k$, the contour of the sinking basin $10 + (k-1)d$ is equal to the volume of water in the sinking basin.

Therefore, the 3D spatial information of the surface water area at different times T as the working surface advances was obtained by formula (17).

$$\begin{cases} H_w^T = W_m - 10 - (k-1)d, \\ S_w^T = \dfrac{1}{2}\displaystyle\sum_{i=1}^{N}\left(x_i^{10+(k-1)d} \cdot y_{i+1}^{10+(k-1)d} - x_{i+1}^{10+(k-1)d} \cdot y_i^{10+(k-1)d}\right), \\ V_w^{T+\Delta t} = V_w^T + S_w^T \Delta P \Delta t + \alpha\left(S_b^T - S_w^T\right)\Delta P \Delta t + Q_{gw}^{\Delta t} + R^{\Delta t} - S_w^T \Delta E \Delta t - M^{\Delta t}, \\ V_{\max}^T = V_1 + V_2 + V_3 + \ldots + V_n + V' = \dfrac{d}{2}S + dS_1 + dS_2 \ldots + dS_n + \left(\dfrac{d}{2} + \dfrac{d'}{3}\right)S_n, \end{cases} \tag{17}$$

where H_w^T is the water depth of the subsidence basin at dynamically predicted time T, (m), W_m is the maximum sinking value of the sinking basin at time T, (m), S_w^T is the water area and unit square of the subsidence basin at dynamically predicted time T, $x_i^{10+(k-1)d}$ and $y_i^{10+(k-1)d}$ are the contour point coordinates with a sinking value of $10 + (k-1)d$, $V_w^{T+\Delta t}$ is the expected water volume in the subsidence basin, (m^3), V_w^T is the original water volume of the subsidence basin, (m^3), Δt is the time interval, ΔP is the daily average precipitation, (mm), ΔE is the daily average evaporation, (m), α is the surface runoff coefficient, S_b^T is the cross-sectional area of the boundary contour of the subsidence basin with a subsidence of 10 mm, (m^2), S_w^T is the area of water in the subsidence basin, (m^2), $Q_{gw}^{\Delta t}$ is the groundwater seepage flow, (m^3), $R^{\Delta t}$ is the exchange volume of the surface river with the accumulated water in the subsidence area, (m^3), $M^{\Delta t}$ is the manual withdrawal volume, (m^3), $V_{\max}^T$ is the maximum reservoir capacity of the subsidence basin at the dynamic predicted time T, (m^3), V_1 is the volume between S and S_1, V_2 is the volume between S_1 and S_2, V_n is the volume between S_{n-1} and S_n, and V' is S_n the volume between the maximum sinking points W_m. The boundary of the stagnant water range is the curve enclosed by the coordinate points $x_i^{10+(k-1)d}$ and $y_i^{10+(k-1)d}$ on the isoline with a sinking value of $10 + (k-1)d$.

5. Engineering Application

Multiple remote sensing monitoring and field measurement results were used to verify and comprehensively analyze the practicability, accuracy, and application scope of the

dynamic prediction model, evaluate the estimated accuracy, and provide scientific basis and technical reference for land reclamation and ecological planning in high diving site coal mining subsidence areas.

5.1. Remote Sensing Monitoring and Field Measurement. The surface water in the mining area is spread on long range and for a long period of time, and the location is inconvenient for transportation. Conventional observation methods cannot easily obtain large-scale, long-time series, complete, and unified evolution data of the water range, whereas remote sensing observation methods have short observation periods and large amounts of data and high accuracy. Therefore, remote sensing data are selected as the data source to extract the range of surface water in the coal mining subsidence area [30].

The mining time of the study area No. 1031 was from October 2013 to March 2015, and the surface water basin was unaffected by other working surface mining as of October 2016. Thus, the remote sensing images obtained from Landsat-8 from 2013 to 2016 were selected. The remote sensing images generated by a sensor exhibits radiation distortion and geometric distortion because of the change in the satellite operation state, aerosol refraction, random noise in the image generation process, and other factors. This condition affects the quality and application of the image. The preprocessing of remote sensing images, with steps including radiation calibration, atmospheric correction, geometric correction, and cropping, is required to eliminate these errors.

(1) Radiation calibration: Radiation calibration is the process of converting the digital quantitative value (DN) of the image into the radiation luminance value or physical quantities, such as reflectivity or surface temperature. The universal radiation calibration tool (Radiometric Calibration) in ENVI software is used to read the radiation calibration parameters in the landsat-8 remote sensing image metadata and complete the radiation calibration by the radiation luminance method.

(2) Atmospheric correction: Atmospheric correction eliminates the radiation error caused by the atmospheric influence and reverses the real surface reflectivity of the Earth. Initially, the radiation target data is input into the FLAASH module in ENVI to set the sensor-related parameters. Then, the corresponding atmospheric model is selected according to the latitude and imaging time, where the tropical (T) model was selected from July 2014 to September 2014 and the midlatitude summer (MLS) model for the rest of the months. According to the environment of the study area, the rural (R) mode was selected for the aerosol model, and the 2-band (K-T) was selected for the aerosol inversion method. Finally, the remaining relevant parameters were set, and the FLAASH module was run to determine the atmospheric correction results.

(3) Geometry correction: Geometry correction uses ground control points and geometric correction mathematical models to correct the errors caused by nonsystematic factors. The coordinate system is endowed to the image data during the correction process, which includes geographic coding. This step uses the geometry correction module in ENVI. The benchmark image is input, and the images corrected more than three image points of the same name are manually selected. Then, the automatic extraction function extracts more than 50 image points with the same image. The same name image point with the root mean square greater than 1 is eliminated, and the geometric correction module output file is finally run.

(4) Cropping: The appropriate size of the image output is cut according to the position of the study area to obtain the final image.

Secondly, the reflection characteristics of water to different bands are determined by the water body index method. The principle of the method is to place the band with the strongest reflectivity and the weakest reflectance in the molecule and denominator, respectively. Then, the characteristics of the ratio operation are enlarged, while the characteristics of other objects are inhibited. Finally, water extraction is achieved [31]. At present, the more commonly used water index is normalized difference water index (NDWI) [32], and the improved normalized differential water index [31] is modified normalized difference water index (MNDWI).

NDWI takes advantage of the high reflectivity in visible bands and low reflectivity in near-infrared and the range of midinfrared bands to highlight water information using ratio operation. In addition, attributing to the strong reflectivity of the vegetation in the near-infrared band, the water information in the green light band and the near-infrared band is used to calculate the simultaneously suppressed vegetation information, as shown by formula (18).

$$\mathrm{NDWI} = \frac{\mathrm{Green} - \mathrm{NIR}}{\mathrm{Green} + \mathrm{NIR}}, \tag{18}$$

where Green refers to the green light band reflectivity, and NIR refers to the near-infrared band reflectivity.

The remote sensing images are processed using the MNDWI index to avoid miscalculation and improve the accuracy of water extraction. According to the characteristics of water in the image, the water boundary was visually checked. After determining the accuracy of the extraction results, the threshold was set, the water area was calculated, and the water boundary was converted to a vector file output [32]. Soil and buildings have similar spectral characteristics in the green and near-infrared bands. Thus, the mid-near-infrared band (NIR) in formula (18) is replaced by the midinfrared band (MIR) to obtain MNDWI. This method avoids the misjudgment of soil and buildings as water bodies when calculating the normalized water index band. MNDWI is obtained as follows:

$$\mathrm{MNDWI} = \frac{\mathrm{Green} - \mathrm{MIR}}{\mathrm{Green} + \mathrm{MIR}}, \quad (19)$$

where Green refers to the green optical band reflectivity, and MIR refers to the midinfrared band reflectivity.

Considering the 1031 working face of Huaibei Wugou Coal Mine to be the research object, through remote sensing monitoring and on-site measurement, the evolution of the water accumulation area in the coal mining subsidence area with high phreatic level is divided into four periods to facilitate the study of the factors affecting the evolution process. The four stages include the unformed period, the synchronous growth period, the residual growth period, and the relatively stable period, as shown in Figure 8.

(1) Unformed period: This stage is the beginning of the working surface mining to the surface water formation period, and in this period, the surface water does not form.

(2) Synchronous growth period: In this stage, the water on the surface stopped flowing to the working surface for the first time and expanded rapidly along the propulsion direction of the working surface, and the water area on the water surface grew rapidly.

(3) Residual growth period: In this stage, the cessation of mining took approximately five months from the working surface after the shutdown. The water slowly expanded along the propulsion direction of the working surface, slightly increasing the water area.

(4) Relative stability period: In this stage, approximately five months after the working surface stops mining, the boundary of water no longer expands along the mining direction, and the overall water area becomes stable [33].

5.2. Combining the Actual Measurement and the Model. Figure 9 shows the comparison of the predicted water accumulation area and the measured water accumulation area of the inland water accumulation area from 2014 to 2017.

5.2.1. Unformed Period. According to the image, the measured data did not include water observation in the study area before March 2014, the model forecast water range was approximately 3000 m^2, and the water area in the two observation periods was small. Combined with the measured data, the surface of the mining area is mainly farmland, and the surface runoff in the subsidence basin is affected by soil leakage, evaporation, and other factors. In addition, the remote sensing images could not show the water range. The expected result is consistent with the measured results because of the small range of predicted water accumulation, considering the actual situation.

5.2.2. Synchronous Growth Period. Water was observed in the measured data for the first time in March 2014. The water area was 11,000 m^2, the model expected the water range in March 2014 to be 12,615 m^2, and the difference was approximately 1615 m^2, with an error of approximately 10%. According to the prediction results, the range of water in February 2014 is similar to that in March 2014 and the area of water accumulation is 12,812m2, indicating that a certain range of water may have been already present in the subsidence basin before the water was initially observed.

From April 2014 to March 2015, the predicted range of water coincided well with the measured value, and the difference between those did not exceed 10% of the water area. Among them, the predicted result from September to November 2014 was because of the precipitation in September, which was 280 mm, leading to the rapid increase in the water level. Although numerous studies have paid significant attention to rainfall-induced instability of multilayer slopes, the interface between the layers is generally considered to be "zero thickness," and the layer transition zone between the layers is neglected [10]. From October 2014 to November 2014, the water area decreased, and this observation was consistent with the measured value. The results obtained in December 2014 and March 2015 were greater than the predicted value, with a difference of approximately 1. At 5000 m^2, the meteorological data of Huaibei City indicate that the winter temperature is less than 0°C, and the low temperatures result in a reduction in actual evaporation. Thus, the observation value is less than that predicted by the dynamic prediction model.

5.2.3. Residual Growth Period. The measured data in April 2015 and October 2015 were 15,000 and 17,400 m^2 and 157,839 and 181,655 m^2. The prediction error did not exceed 10% of the measured value. The water range in July 2015 was from 171,000 m^2 to 191,8941 m^2. The difference accounted for approximately 11% of the meteorological data of the research area. During the July 2015 period, no precipitation occurred, and the highest daily temperature exceeded 30°C. In addition, the evaporation amount was large. As a result, the measured value of water is in the range of the model predictive value with a very low error.

5.2.4. Relative Stability Period. After October 2015, the surface of the coal mining subsidence area became stable. Figure 9 shows that the range of water accumulation in this stage was generally stable, and the predicted value has the same trend as the measured value. Considering the increase in human activity after the stability of the surface subsidence basin, a large difference was found between the predicted value and the measured value. For example, from March 2016 to June 2016, the measured area of the basin is greater than the predicted value, with an approximate difference of 20,000 m^2. The water from the surrounding farmland irrigation converges into the water area affected by topography and permeability, and the new water supply increases. Thus, the measured value is greater than the model predicted value.

In conclusion, the 3D spatial information dynamic prediction method predicts the evolution of the water area,

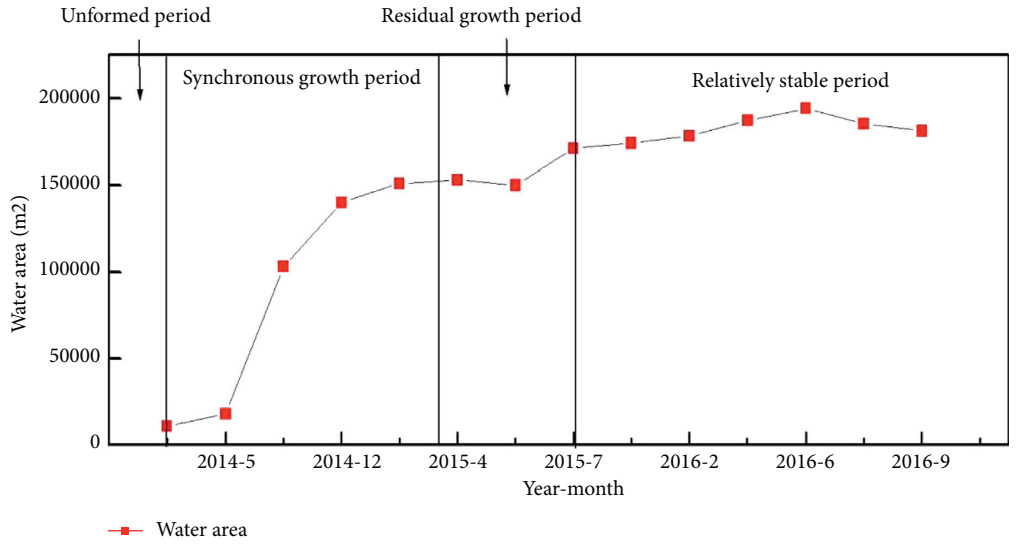

Figure 8: Evolution of the water range of 1031 working area.

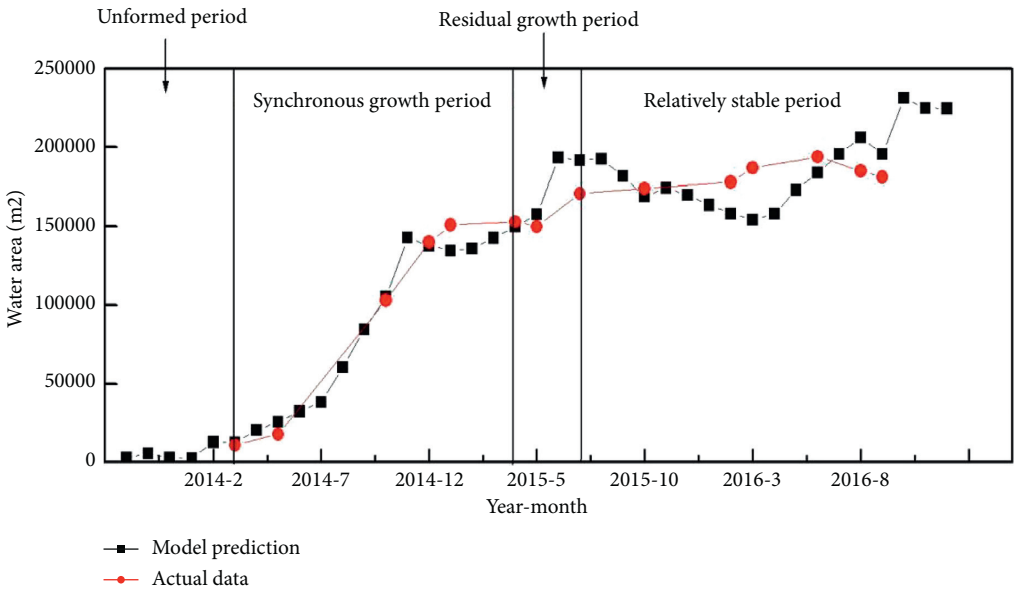

Figure 9: Comparison of the evolution of the measured and simulated water accumulation area.

and the water range predicted by the dynamic prediction model of the high diving position coal mining subsidence area is consistent with the measured results. In the period, when stagnant water is not formed, the predicted value of the model is basically consistent with the measured value, the error between the predicted value of the model, and the measured value in the synchronous growth period and the residual growth period is about 10%. Since the empirical data of groundwater exchange and ponding water leakage are all used in this study, the dynamic changes of groundwater depth and ponding leakage are not considered, causing some systematic errors that are difficult to eliminate in the model. In addition, there are still some inevitable errors in the method because of the lack of research data. During the relatively stable period, the prediction results of the model are consistent with the change trend of the measured ponding range. Thus, the model accuracy is high and can be used to predict the dynamic evolution of water in high diving mining subsidence areas.

6. Conclusion

(1) In view of addressing the problem of water accumulation in the surface subsidence basin, a dynamic prediction model of the water accumulation area in the high-water-level coal mining subsidence area was constructed by combining the dynamic prediction of the coal mining subsidence area based on the probability integral method of the Knothe time function and the principle of water balance in coal mining subsidence water area. Dynamically

predicting the depth, area, volume, maximum storage capacity, and scope of the basin became possible with the advancement of the working face and the passage of time. The prediction results have certain timeliness and can effectively avoid the failure of real-time follow-up or repeated management of the comprehensive treatment of subsidence basins because of the lack of timeliness of the data.

(2) Taking the 1031 working face of Wugou Mine as an example, the applicability of the dynamic prediction model of the water accumulation area in the high-water-level coal mining subsidence area was verified. The error between the predicted value of the model and the measured value is approximately 10%. This newly developed model showed high accuracy and thus can be used for predicting the dynamic evolution of water range in high diving mining subsidence areas.

(3) In the dynamic prediction of the 3D spatial information of the coal mining subsidence water area, the acquired hydraulic information in the coal mining subsidence water area basin can provide a reference for the comprehensive management of the coal mining subsidence area and can also assist in protecting the ecology and surrounding geography. Environment and mining subsidence dynamic prediction results can serve as a guide for mining area reclamation. The predicted water range and water depth can provide data for the establishment of lakes and wetland ecosystem in the coal mining subsidence area. A water storage project can be established using the subsidence basin volume. A widely applicable dynamic prediction model of surface subsidence was constructed in the mining areas with high phreatic levels, and reliable technical support is provided for land reclamation and ecological planning in similar mining areas.

(4) The dynamic prediction model of the water accumulation area in the high-water-level coal mining subsidence area needs to be further improved. The water accumulation area in the subsidence area of high-water-water mining established in this study only considers the flat surface and is only affected by the mining of a single working face. The water volume of the recharge term was calculated, and the mutual conversion between these recharge terms and excretion terms was not analyzed in depth. In addition, the influencing factors, such as human activities and surrounding water systems, are not taken into account in the model. Therefore, this model still needs to be further improved, accounting for many influencing factors to accurately predict the surface water range in the high-water-level coal mining subsidence area with a larger area, undulating terrain, and complex hydrogeological conditions.

Data Availability

The data used to support the findings of this study are available from the corresponding author upon request.

Conflicts of Interest

The authors declare that there are no conflicts of interest.

Acknowledgments

The authors acknowledge the financial supports from the National Nature Science Fund Subsidized Project (CN) (52174156), the National Nature Science Fund Subsidized Project (CN) (51874005), and the Anhui University Collaborative Innovation Project Fund Subsidized Project (GXXT-2020-055).

References

[1] H. Bloch, S. Rafiq, and S. Ruhul, "Coal consumption, CO_2 emission and economic growth in China: empirical evidence and policy responses," *Energy Economist*, vol. 34, pp. 518–528, 2012.

[2] M. Bhattacharya, S. Rafiq, and S. Bhattacharya, "The role of technology on the dynamics of coal consumption-economic growth: new evidence from China," *Applied Energy*, vol. 154, no. 154, pp. 686–695, 2015.

[3] M. He, Q. Wang, and Q. Wu, "Innovation and future of mining rock mechanics," *Journal of Rock Mechanics and Geotechnical Engineering*, vol. 13, no. 1, pp. 1–21, 2021.

[4] N. Apergisa and J. E. Payneb, "The causal dynamics between coal consumption and growth: evidence from emerging market economies," *Applied Energy*, vol. 87, pp. 1972–1977, 2010.

[5] W. Guo, B. Hu, J. Zhang, Q. Chen, X. Jia, and J. Li, "Research on the settlement regulation and stability of large building foundation over gobs: a case study in the xiangcheng coal mine, China," *Shock and Vibration*, vol. 2021, Article ID 5533098, 17 pages, 2021.

[6] Q. Wang, Z. Jiang, B. Jiang, H. Gao, Y. Huang, and P. Zhang, "Research on an automatic roadway formation method in deep mining areas by roof cutting with high-strength bolt-grouting," *International Journal of Rock Mechanics and Mining Sciences*, vol. 128, Article ID 104264, 2020.

[7] Q. Wang, M. He, and S. Li, "Comparative study of model tests on automatically formed roadway and gob-side entry driving in deep coal mines," *International Journal of Mining Science and Technology*, vol. 31, no. 4, pp. 591–601, 2021a.

[8] Q. Wang, P. Zhang, and Z. Jiang, "Automatic roadway formation method by roof cutting with high strength bolt-grouting in deep coal mine and its validation," *Journal of China Coal Society*, vol. 46, no. 2, pp. 382–397, 2021b, in Chinese.

[9] L. M. Kurth, M. McCawley, M. Hendryx, and S. Lusk, "Atmospheric particulate matter size distribution and concentration in West Virginia coal mining and non-mining areas," *Journal of Exposure Science and Environmental Epidemiology*, vol. 24, pp. 405–411, 2014.

[10] Z. Dou, S. Tang, X. Zhang et al., "Influence of shear displacement on fluid flow and solute transport in a 3D rough fracture," *Lithosphere*, vol. 2021, no. 4, Article ID 1569736, 2021.

[11] M. Grzovic and A. Ghulam, "Evaluation of land subsidence from underground coal mining using TimeSAR (SBAS and PSI) in Springfield, Illinois, USA," *Natural Hazards*, vol. 79, pp. 1739–1751, 2015.

[12] A. Muntean, V. Mocanu, and B. A. Ambrosius, "GPS study of land subsidence in the Petrosani (Romania) coal mining area," *Natural Hazards*, vol. 80, pp. 797–810, 2016.

[13] Q. Wang, M. He, J. Yang, H. Gao, B. Jiang, and H. Yu, "Study of a no-pillar mining technique with automatically formed gob-side entry retaining for longwall mining in coal mines," *International Journal of Rock Mechanics and Mining Sciences*, vol. 110, pp. 1–8, 2018.

[14] Y. P. Chugh, "Concurrent mining and reclamation for underground coal mining subsidence impacts in China," *International Journal of Coal Science & Technology*, vol. 5, no. 1, pp. 18–35, 2018.

[15] R. Dhakate, D. Modi, and V. V. S. G. Rao, "Impact assessment of coal mining on river water and groundwater and its interaction through hydrological, isotopic characteristics, and simulation flow modeling," *Arabian Journal of Geosciences*, vol. 12, no. 1, p. 8, 2019.

[16] H. Liu, M. Zhang, L. Su, X. Chen, C. Liu, and A. Sun, "A boundary model of terrain reconstruction in a coal-mining subsidence waterlogged area," *Environmental Earth Sciences*, vol. 80, no. 5, 2021.

[17] M. Z. Gao, H. C. Hao, S. N. Xue et al., "Discing behavior and mechanism of cores extracted from Songke-2 well at depths below 4,500 m," *International Journal of Rock Mechanics and Mining Sciences*, vol. 149, p. 104976, 2022.

[18] M. Z. Gao, J. Xie, Y. N. Gao et al., "Mechanical behavior of coal under different mining rates: a case study from laboratory experiments to field testing," *International Journal of Mining Science and Technology*, vol. 31, no. 2021, pp. 825–841, 2021.

[19] Q. Wang, H. Gao, and Z. Jiang, "Development and application of a surrounding rock digital drilling test system of underground engineering," *Chinese Journal of Rock Mechanics and Engineering*, vol. 39, no. 2, pp. 301–310, 2020b, in Chinese.

[20] Q. Wang, H. Gao, B. Jiang, S. Li, M. He, and Q. Qin, "In-situ test and bolt-grouting design evaluation method of underground engineering based on digital drilling," *International Journal of Rock Mechanics and Mining Sciences*, vol. 138, Article ID 104575, 2021.

[21] C. Zhu, M.-c. He, B. Jiang, X.-z. Qin, Q. Yin, and Y. Zhou, "Numerical investigation on the fatigue failure characteristics of water-bearing sandstone under cyclic loading," *Journal of Mountain Science*, vol. 18, no. 12, pp. 3348–3365, 2021.

[22] Q. Wang, Y. Wang, M. He et al., "Experimental research and application of automatically formed roadway without advance tunneling," *Tunnelling and Underground Space Technology*, vol. 114, Article ID 103999, 2021.

[23] Kuiyang, *Research On Surface Deformation Parameters of Repeated Mining under Thick Loose layers_Kuiyang*, Anhui University, Anhui, China, 2018.

[24] S. Knothe, "Time influence on a formation of a subsidence surface," *Archiwum Górnictwai Hutnictwa, Kraków (in Polish)*, vol. 1, no. 1, pp. 120–132, 1952.

[25] J. Ma, S. Huang, and Z. Xu, "Dynamic monitoring and analysis of lake area in Wuhan from 1973 to 2015 based on remote sensing," *Journal of Hydraulic Engineering*, vol. 48, no. 8, pp. 903–913, 2017.

[26] H. Liu, K. Deng, X. Zhu, and C. Jiang, "Effects of mining speed on the developmental features of mining-induced ground fissures," *Bulletin of Engineering Geology and the Environment*, vol. 78, no. 8, pp. 6297–6309, 2019.

[27] B. Selby and K. M. Kockelman, "Spatial prediction of traffic levels in unmeasured locations: applications of universal kriging and geographically weighted regression," *Journal of Transport Geography*, vol. 29, pp. 24–32, 2013.

[28] B. Zou, X. U. Shan, and Z. Jing, "Spatial variation analysis of urban air pollution using GIS: a land use perspective," *Geomatics and Information Science of Wuhan University*, vol. 42, no. 2, pp. 216–222, 2017.

[29] F. Tao, Q. Sun, and L. Jin, "Analysis of runoff law in typical areas on the north bank of the middle reaches of the Huaihe River," *Hydropower and Energy Science*, vol. 33, no. 9, pp. 12–16, 2015.

[30] C. Cao, W. Zhang, J. Chen, B. Shan, S. Song, and J. Zhan, "Quantitative estimation of debris flow source materials by integrating multi-source data: a case study," *Engineering Geology*, vol. 291, Article ID 106222, 2021.

[31] H. Xu, "Research on extracting water body information using improved normalized difference water index (MNDWI)," *Journal of Remote Sensing*, vol. 5, pp. 589–595, 2005, in Chinese.

[32] S. K. McFeeters, "The use of the normalized difference water index (NDWI) in the delineation of open water features," *International Journal of Remote Sensing*, vol. 17, no. 7, pp. 1425–1432, 1996.

[33] X. Chen, W. Zhang, and X. Zhu, "Dynamic evolution law of water accumulation range in coal mining subsidence area with high phreatic level," *Coal Geology and Prospecting*, vol. 48, no. 2, pp. 126–133, 2020, in Chinese.